TU WIEN

TECHNISCHE UNIVERSITÄT WIEN

Vienna University of Technology

DISSERTATION

Abrasion/Korrosion an metallischen Werkstoffen in besonderen Umgebungsbedingungen

ausgeführt bei
AC²T research GmbH
Viktor-Kaplan-Straße 2C
2700 Wiener Neustadt

und am
Institut für chemische Technologien und Analytik
Technische Universität Wien
Getreidemarkt 9/164-CT
1060 Wien

unter Anleitung von Ao. Prof. DI Dr. Roland Haubner

durch

Dipl.-Ing. Nina ZWAZL

Maria-Theresiagasse 4
2620 Neunkirchen

Wien, September 2014

DOCTORAL THESIS

Abrasion/Corrosion of metallic materials used in extreme environment

performed at
AC²T research GmbH
Viktor-Kaplan-Straße 2C
2700 Wiener Neustadt

and

University of Technology Vienna,
Institute of Chemical Technologies and Analytics
Getreidemarkt 9/164-CT
A-1060 Vienna

supervised by Ao. Prof. DI Dr. Roland Haubner

by

Nina ZWAZL, MSc

Maria-Theresiagasse 4
2620 Neunkirchen

Vienna, September 2014

DANKSAGUNG / ACKNOWLEDGMENT

I would like to thank all the people who made it possible for this work to be written. These people are my family, my mother and my father, who did not only make my existence possible, they also helped me through my university life through financial support.

For special mental support, I would like to thank my sister, who was always there for me. Also I would like to offer special thanks to my partner, who moved heaven and earth to support me in each phase of my work.

Special thanks deserves Prof. Haubner, who was not only my advisor and scientific support of this work. Also, his effort for rendering this work possible has to be credited, alongside with the support of Prof. Mori for scientific supervision and Prof. Danninger, together with Prof. Franek for organizational support.

Special honor to my beloved friends on the university, the bird and the cat, which were always there for me with their words of wisdom.

KURZFASSUNG

Die Versagensmechanismen von tribologisch belasteten Werkstoffen, welche gleichzeitig mit hochkorrosiven Flüssigkeiten in Kontakt kommen, sind bisher nicht eindeutig unterscheidbar, bzw. der Versagenszeitpunkt voraussagbar. Besonders da die in diesen Medien weitgehend eingesetzten Kohlenstoffstähle, die sich in ihrer mikrostrukturellen Zusammensetzung unterscheiden, mehr oder weniger variieren. Dieses fehlende Wissen erfordert daher einen hohen Material- und Instandhaltungsaufwand durch die undefinierte Versagenswahrscheinlichkeit der Werkstoffe.

Die gegenständliche Arbeit verfolgt daher das Ziel tribologische sowie korrosive Effekte an diesen Stählen im Kontakt mit einem Gegenkörper auf Nickelbasis zu charakterisieren und eine Korrelation dieser Abrasions- und Korrosionseffekte mit der tribologischen Belastung, der chemischen Zusammensetzung der Materialien und des korrosiven Mediums, der Mikrostruktur und der Wärmebehandlung der eingesetzten Werkstoffe zu ermitteln. Die in der Praxis auftretenden spezifischen Umgebungsbedingungen werden im Labortest simuliert.

Darüber hinaus wurde ein Testgerät entwickelt, welches die Einflüsse von Verschleiß und Korrosion unter CO_2 Bedingungen simultan testet. Mit diesem System wurden die Unterschiede zwischen einem ferritisch/perlitischen und einem martensitischen Werkstoff, sowie Unterschiede zu den Ergebnissen der tribologischen und korrosiven Tests untersucht. Der Abrasions-Korrosions-Tribotester zeigt eine gute Vergleichbarkeit und hat daher großes Potential als Verschleißtester unter korrosiven Bedingungen.

ABSTRACT

The failure mechanisms of tribologically stressed materials, which are also in contact with highly corrosive fluids, are at present not definitely distinguishable, or in other words, the time of failure is not predictable. In particular, the equipped carbon steel materials, which differ in their microstructural composition, are more or less varying. The lack of knowledge in this field is resulting in high costs of materials and maintenance due to the undefined failure probability of the materials.

The aim of the present work is the characterization of tribological and corrosive effects on commonly equipped steel materials in contact with a nickel base counter body. A correlation between abrasive and corrosive effects under tribological stress, the chemical composition of the materials and the corrosive medium, the microstructure and the heat treatment process of the equipped materials are the topics of these investigations. The conditions predominant in practical applications are simulated in lab-scale experiments.

Further on, a test principle was established in order to investigate the influences of wear and corrosion under CO_2 conditions simultaneously. With this system, the differences between a ferritic/pearlitic and a martensitic steel sample were investigated and also compared to the results for the tribological and corrosive tests. The sliding corrosion test rig shows a good comparability and therefore offers a high potential as wear tester under corrosive conditions.

TABLE OF CONTENTS

1. Introduction

The thesis is divided in several sections, which are necessary in order to gain understanding in the field of CO_2 tribocorrosion of selected materials for specific applications.

At first, the damage mechanisms occurring under aggressive CO_2 corrosion conditions on steel materials, which are worn by Ni-base counter bodies, was investigated on real system parts. Such mechanisms might occur in the field of geological investigations. A variety of tests has been performed in order to investigate optical alteration on the material and also on the composition of formed corrosion products.

In this work, the effects of the material pairing steel and Ni-base material are investigated, on one side, under abrasive (sand particles) conditions. On the other side, the tribobehavior of both materials is evaluated. For that purpose, the running-in behavior of the Ni-base material on the steel surface and also on an oxide layer, which is equivalent to a layer achieved for a ready-to-use field material, on the steel surface is studied. The influence of the surface roughness and the hardness of the Ni-base material beyond the running-in state is also a topic of this work. The influence of the hardness and microstructure of the steel material is studied on the base of a carbon steel material, which undergoes different heat treatment processes in order to generate different steel grades. Further on, corrosion experiments under CO_2 conditions in saline media on unworn and pre-worn steel samples are carried out in order to investigate the influence of the steel grade and the tribological damage on CO_2 corrosion.

As experiments, the tribocontact of carbon steel samples with moveable Ni-base counter bodies in aggressive media is simulated in lab-scale testing. For the characterization of tribological effects, sliding wear tests using a steel-wheel and a pin-on-disc tribometer are performed. For the corrosion studies, static corrosion tests in simulated liquid corrosive media under CO_2 gas flow are performed in order to understand the mechanisms and kinetics of CO_2 corrosion and also the performance of different carbon steel materials.

As there are mostly both processes happening within application, the influences of both of these processes have to be understood. A test facility for the investigation of both effects simultaneously was equipped within this work and tested on ferritic/pearlitic and martensitic

materials. The so called sliding corrosion test rig is equipped with an extensive measurement system, able to record the oxygen concentration, pH value, conductivity and the system pressure. With this system, the testing time such as the tested load cycles can be selected, in order to set testing conditions close to application specific parameters. The results are compared to those achieved by sequential wear and corrosion testing and also to the mechanisms investigated on real application samples.

2. Literature

Corrosive mechanisms of CO_2 corrosion, wear mechanisms and synergistic mechanisms are the main research topics for the present study, together with other relevant sources of information about oxidative processes during heat treatment processes and the influence of sodium chloride on the tribological behavior.

In general, this literature study represents a summary of the information found in the single references mentioned in the square brackets. The statement is valid for the respective reference for the whole text from the beginning of a new citation to its end, which is marked with the respective citation in the bracket.

2.1. Corrosion mechanisms

Corrosion can be understood as the processes between the chemical components of materials and the medium in between, which is enabling the transport reactions of the substances through the phase barriers of the corrosion partners (materials). These reactions can lead to material failure. Corrosion can be divided into three basic corrosion mechanisms, electrochemical corrosion, high temperature corrosion and metal physical corrosion (diffusion of material into another material, accompanied by the formation of new phases or material separation). In this work, the first mechanism is important. [1]

In electrochemical corrosion, the material is processed by electrochemical reactions into its respective corrosion products. For this type of corrosion to be performed, two areas, where one has the function of the cathode and the other of the anode, connected by a, mostly liquid, electrolyte to enable a transport of charged species (electrons, ions). A prominent example is the oxidative corrosion of iron in aqueous medium (rusting).

Anodic reactions:	$Fe \rightarrow Fe^{2+} + 2\ e^-$	(1)
	$Fe^{2+} \rightarrow Fe^{3+} + e^-$	(2)
Cathodic reaction:	$O_2 + 2\ H_2O + 4\ e^- \rightarrow 4\ OH^-$	(1)
Sum reaction:	$4\ Fe^{2+} + O_2 + 2\ H_2O + 4\ OH^- \rightarrow 4\ Fe(OH)_3$	(1)
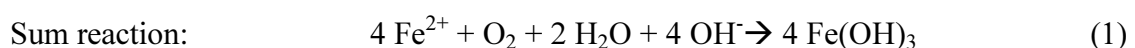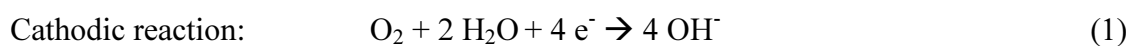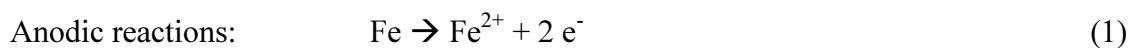
The iron hydroxide species then forms other products as the orange FeOOH and the iron oxide Fe_2O_3 (haematite). The corrosion reactions are forming a redox system, where the anodic reaction is the oxidative reaction and the cathodic reaction is the reductive reaction. [1]

2.2. CO$_2$ corrosion

CO$_2$ corrosion is one corrosive mechanism often occurring in applications using carbon steel materials with Ni-base material counter bodies. Therefore the investigation of the mechanism happening is crucial together with the factors influencing these reactions. The following chapters deal with the topic of CO$_2$ corrosion and its influencing factors.

2.2.1. Chemical reactions in contact with steel materials

A better understanding of the tribocorrosion mechanisms under CO$_2$ environment and the occurring damage is the first step towards better performing steel grades and lower life cycle costs of components in application.

Within the application system, oxygen free conditions are predominant. A deaerated aqueous solution of CO$_2$ is formed. The corrosion mechanism can be described in the following reaction steps [2]. At first, the carbon dioxide is dissolved forming carbonic acid (1).

$$CO_2(g) + H_2O(l) \rightarrow H_2CO_3(aq) \tag{1}$$

The main corrosion process can be categorized as a type of acid corrosion and summarized in three cathodic (2, 3, 4) and one anodic reactions (5) [3, 4].

Cathodic reactions:
$$2\ H_2CO_3 + 2\ e^- \rightarrow H_2 + 2\ HCO_3^- \tag{2}$$
$$2\ HCO_3^- + 2\ e^- \rightarrow H_2 + 2\ CO_3^{2-} \tag{3}$$
$$2\ H^+ + 2\ e^- \rightarrow H_2 \tag{4}$$

Anodic reaction:
$$Fe \rightarrow Fe^{2+} + 2\ e^- \tag{5}$$

The ions, which are generated this way, are reacting forming a corrosion layer on the steel matrix according to the following reactions (6, 7, 8) [4].

$$Fe^{2+} + CO_3^{2-} \rightarrow FeCO_3 \tag{6}$$
$$Fe^{2+} + 2\ HCO_3^- \rightarrow Fe(HCO_3)_2 \tag{7}$$
$$Fe(HCO_3)_2 \rightarrow FeCO_3 + CO_2 + H_2O \tag{8}$$

In a work on the fundamentals of chemical precipitation [5], a table for the solubility constant for various metal species is given. For $FeCO_3$, $Fe(OH)_2$ and $Fe(OH)_3$, the respective K_{sp} values for 25°C in water are given as $3.5 \cdot 10^{-11}$, $8 \cdot 10^{-16}$ and $4 \cdot 10^{-38}$. A more detailed table on solubility constants is given in another work [6], where the constant of the respective possible reaction is given in Table 2.1:

Table 2.1: Solubility constants Ksp for various iron species and reactions [6]

Solution/Precipitation rate	Solubility constant K_{sp} at 25°C
$Fe(OH)_2 \leftrightarrow Fe^{2+} + 2\ OH^-$	$8 \cdot 10^{-16}$
$Fe(OH)_2 \leftrightarrow Fe(OH)^+ + OH^-$	$4 \cdot 10^{-10}$
$FeCO_3 \leftrightarrow Fe^{2+} + CO_3^{2-}$	$2.1 \cdot 10^{-11}$
$Fe(OH)_3 \leftrightarrow Fe^{3+} + 3\ OH^-$	ca. 10^{-36}
$Fe(OH)_3 \leftrightarrow Fe(OH)_2^+ + OH^-$	$1.7 \cdot 10^{-15}$
$Fe(OH)_3 \leftrightarrow Fe(OH)^{2+} + 2\ OH^-$	$6.8 \cdot 10^{-25}$

2.2.2. CO_2 in aqueous solutions

An important factor for these reactions is the solubility of CO_2 in saline aqueous solutions. For the solubility of carbon dioxide (CO_2) in water, a suitable model was established by Duan et al. [7]. The solubility for carbon dioxide is calculated to be ~ 0.0803 mol per kg for 60°C, 5 bar and no salinity and for the same temperature and pressure, the solubility is ~ 0.0674 mol/kg for 1 mol, 0.0572 mol/kg for 2 mol and 0.0428 mol/kg for 4 mol NaCl in water.

The solubility of CO_2 in water rises with increasing pressure and decreases with ascending temperature and salinity of the solution. For higher pressure values, the solubility experiences a minimum for a certain temperature value and the solubility rises again with an increase of the temperature (Fig. 2.1). [7,8]

In general, the solubility of different substances (gases, proteins, etc.) in aqueous solutions usually decreases after adding inorganic salts. This is called the salting-out-effect. Therefore, the reduction of the CO_2 solubility is due to the salting-out-effect. The reason is the ions which are solvated and the water used for the solvation is therefore no more available for the solution of CO_2. The salting-out-effects of the three mentioned salts are from high to low: NaCl > $CaCl_2$ > KCl. This is because the hydration action on K^+ is smaller as on Na^+ and therefore there are more H_2O molecules free for the interaction with CO_2 in the KCl solution compared to the NaCl solution. Comparing the Ca^{2+} ion with the Na^+ ion, it is difficult to say which one leads to a

higher salting-out-effect. Ca^{2+} has two positive charges, which enhances the effect. Na^+ and Ca^{2+} have almost the same size and the molecular weight of $CaCl_2$ is twice as much as of NaCl. Therefore, there are more Cl^- ions in the $CaCl_2$ solution, which enhances the salting-out-effect of this solution. These effects compensate each other in the comparison of the NaCl solution with the $CaCl_2$ solution so that these salts have similar salting-out-effects. [7, 8]
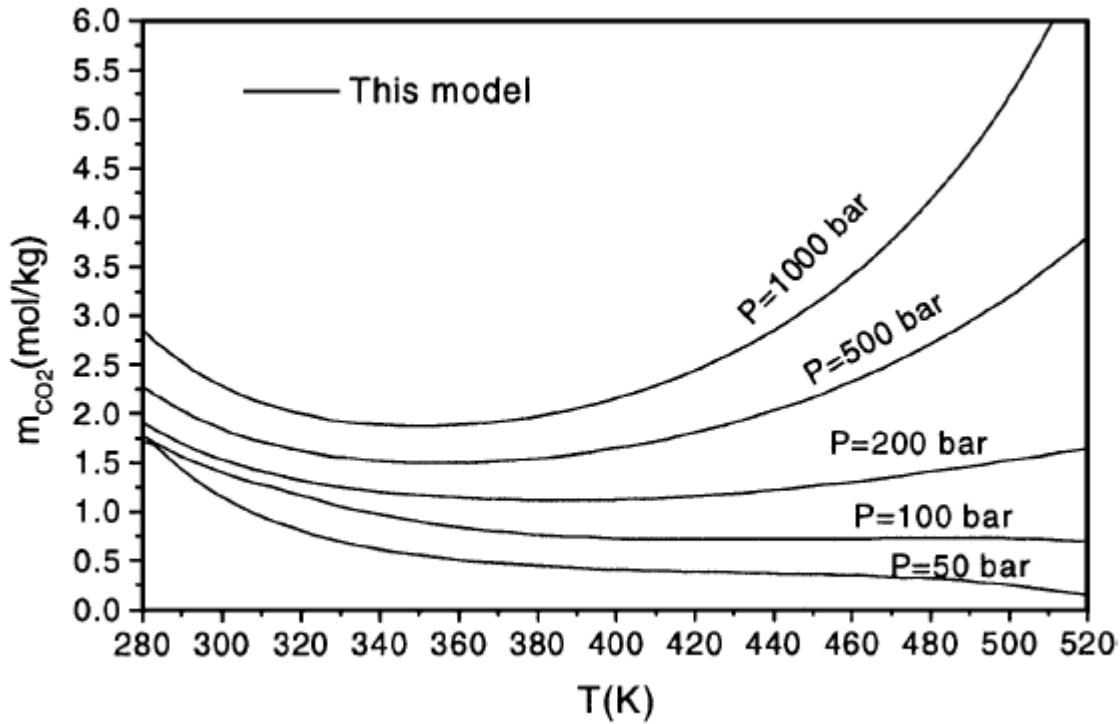
Fig. 2.1: The isobaric minimum solubilities of CO_2 in pure water [7]

2.2.3.   Layer formation on steels during CO_2 corrosion

The formation of $FeCO_3$ layers is performed over a crystallization process. The mechanism and kinetics of crystalline film growth is described as quadratic dependence on the supersaturation with R_{gr} as growth rate and k_{gr} as growth rate constant (9; 10). [9]

$$R_{gr} = k_{gr} \ (S\text{-}1)^2 \tag{9}$$

And supersaturation S as (with K_{sp} as solubility product)

$$S = \frac{(cFe^{2+} \cdot cCO_3^{2-})}{K_{sp}} \tag{10}$$

In order to achieve acceptable precipitation rates, S and k_{gr} have to be large. The formation of the iron carbonate layer is either porous and unprotective, or dense and protective, or the conditions are insufficient for layer formation. In the latter case, corrosion by the solution of iron ions from the steel surface takes place. High temperatures (~ 80°C or higher) and high pH values (> 5) lead to the formation of a dense and protective layer, lower temperatures (ca. 60°C) and pH values lead to porous and unprotective layer formation [10-12]. These factors favoring the formation of a dense layer lead to high S, and higher temperatures lead to high k_{gr}. At room temperature, only little or no iron carbonate film forms, even at high supersaturation values, as a result of the slow kinetics of the precipitation reaction (low k_{gr}). Protective iron carbonate films are also likely to be observed in systems with high Fe^{2+} concentrations and high CO_2 partial pressure (p_{CO2}). The scaling tendency ST describes the likeliness of film formation (CR = corrosion rate) (11).

$$ST = \frac{R_{gr}}{CR} \tag{11}$$

Higher ST values mean that the formation of a dense protective iron carbonate film is likely to occur [13]. The solubility of iron carbonate plays a major role for scale formation processes. The less soluble iron carbonate becomes, the more probable is a formation of a protective layer. An important factor in this is the pH value. The solubility of $FeCO_3$ decreases with a factor of 100 when the solution pH increases from 5 to 6 in this pH region (Fig. 2.2). [14]

According to Engels [15], CO_2 corrosion of carbon steel in oxygen free solutions can be separated in three different zones depending on the temperature. At low temperature, only dissolution of Fe^{2+} is likely to happen and no protective layer is formed. For elevated temperatures, a porous layer is formed, together with occurring pitting corrosion. Only at higher temperatures a protective siderite layer is able to be formed (Fig. 2.3).

In situ measurements on the growth of $FeCO_3$ layers has been performed by B. Ingham et al. [16] using synchrotron X-ray diffraction at pH 6.3 in CO_2-saturated brine in temperature ranges between 40 and 90°C on 0.19 C-0,39 Mn-Steel with ferritic/pearlitic structure. With that setup, it was possible to investigate the scale formation process. The formed scales became increasingly protective at temperatures above 60°C and were thin and dense when formed at 90°C. At 40°C, porous and non-protective scales were formed. At temperatures between 40 and 90°C, X-ray diffraction investigations showed that siderite is the primary phase formed. In addition to siderite, the formation of two yet-unidentified minor phases was also observed, one phase was

observed at 40°C, the other at 90°C. The lower temperature phase grows at the beginning of scale formation, and afterwards siderite formation can be observed, at slower rates. The higher temperature phase grows after siderite formation can be observed in slow rates. At temperatures 60 and 80°C, only siderite formation was observed (Fig. 2.4).

The scale forms more quickly at higher temperatures, but the scale growth rate is decreasing with time. The nucleation stage shows a clear trend with temperature; the higher the temperature, the shorter the nucleation time. The maximum growth rate is slow for 40°C and almost the same for the other temperatures until a plateau is reached.
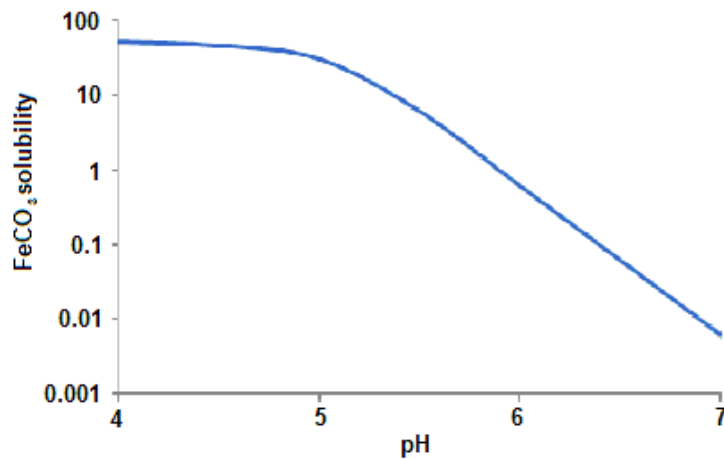
Fig. 2.2: Dependency of $FeCO_3$ solubility on pH value [14]
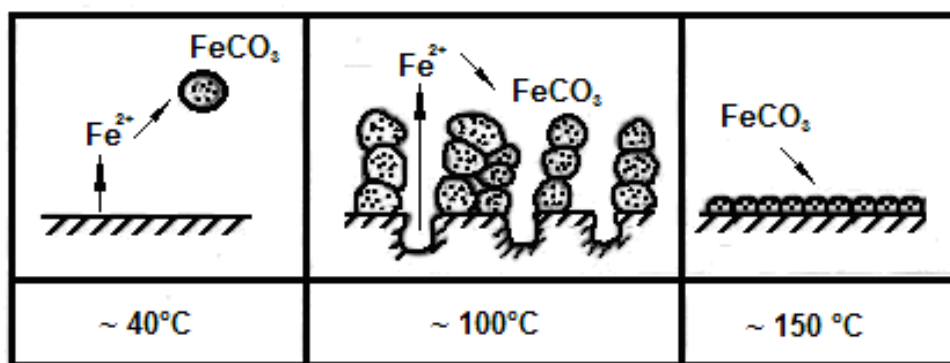
Fig. 2.3: Formation of siderite layer depending on temperature [16]
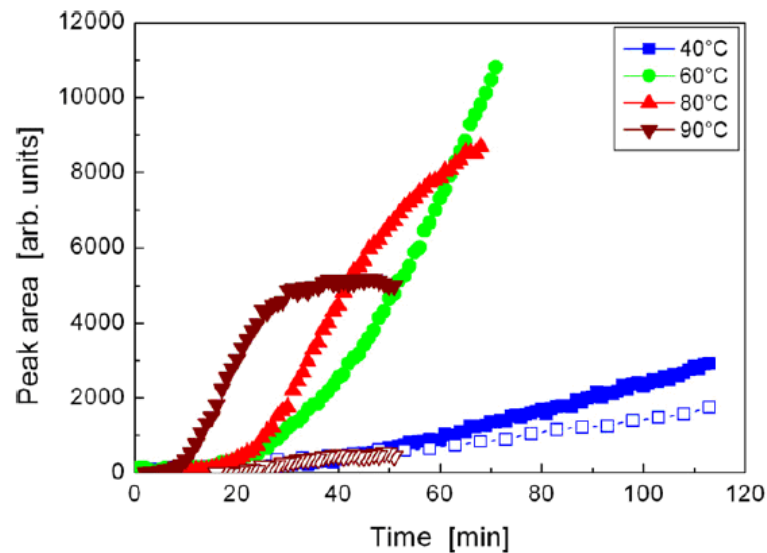
Fig. 2.4: Growth curves for siderite and the two minor unidentified phases for various temperatures (Closed symbols: siderite; open symbols: minor phases) [16]

2.2.4. Macroscopical effect of single parameters on CO_2 corrosion

The corrosion rate of low carbon steels depends on the protectiveness of the formed scale, which itself depends on the nature of the base material (composition, microstructure) and on the properties of the environment. The latter one is mainly influenced by the pH value, temperature, CO_2 partial pressure, Fe^{2+} concentration and the flow velocity of the medium. In macroscopic scale, a detailed study was mainly performed by Nesic et al. [17], who performed model calculations for carbon mild steels, which will be summarized in the following paragraphs.

2.2.4.1. Effect of pH value

High pH values lead to a decreased solubility of siderite ($FeCO_3$) and to a higher precipitation rate of the protective layer. Therefore, the corrosion rate decreases with increasing pH over time. The resulting protective film for higher pH values does not increase much in its thickness compared to lower pH values, but its density is higher. For the abrasive tests, where the steel surface is constantly renewed, only the region close to zero hours is important, where almost no precipitation reactions took place. From this point of view, pH values higher than 6.0 lead to an increase of the corrosion. Fig. 2.5 shows the correlation of the corrosion rate and the pH value. [17]

2.2.4.2. *Effect of temperature*

Increased temperature supports the formation of the protective film by an acceleration of the precipitation reactions. For 80°C, the protective film grows very fast and dense compared to 65°C and 55°C, where the kinetics of film formation are much slower. At 50°C, the film formation was so slow that there was only a porous layer of iron carbonate which offers little protection against the corrosion process. At temperatures higher than 50°C it comes to an increase of a corrosion and abrasion synergy similar to pH values higher than 6.0 as mentioned above. Fig. 2.6 shows the correlation of the corrosion rate and the temperature. From the abrasive aspect, lower temperatures lead to lower corrosion rates. [17]

In the work of López et al., it is stated that going from low temperatures to temperatures higher than 60°C, the corrosion rate increases, where it experiences a maximum at ~ 80°C. The position of this maximum depends on the factors of the system, like the CO_2 partial pressure or the flow velocity of the medium. A further increase of the temperature leads to a decrease of the corrosion rate, because the higher the temperature, the easier is the formation of the protective layer. That maximum is also called the scaling temperature (Fig. 2.7) effect. [18, 19]

2.2.4.3. *Effect of CO_2 partial pressure*

An increase of the CO_2 partial pressure increases the corrosion rate. When it comes to the formation of a protective film, a higher p_{CO2} can aid the film growth. Prior to film formation, an increase of the p_{CO2} leads to a higher corrosion rate. In case of abrasion, the precipitation of a protective layer is hindered by the constant removal of the first layers of the steel. The freshly available steel surface again underlies the initial CO_2 corrosion process. Therefore, an increase of the corrosion rate is the main result of an increase of the CO_2 partial pressure for that case. Fig. 2.8 shows the influence of the CO_2 partial pressure. [17]

2.2.4.4. *Effect of Fe^{2+} concentration*

The increase of the Fe^{2+} concentration leads to a higher supersaturation of the Fe^{2+} ions, leading to an acceleration of the precipitation rate of the iron carbonate. For long term applications, this effect leads to a reduced corrosion rate. For the abrasive application, the Fe^{2+} concentration shows no significant impact. Fig. 2.9 shows the influence of the Fe^{2+} concentration on the corrosion rate. [17]

2.2.4.5. *Effect of flow velocity*

Higher flow velocities lead to higher turbulence and therefore to a higher mixing of the solution. Prior to any film formation, higher velocities increase the corrosion rate, because the transport of the cathodic species towards the steel surface and the Fe^{2+} ions away from the steel surface is enhanced. A lower Fe^{2+} concentration near the steel surface leads to a lower surface supersaturation and therefore to a lower film precipitation, entailing a porous and unprotective layer formation at higher velocities. Even for non-abrasive systems, an increase of the velocity leads to a severe rise of the corrosion rate. Fig. 2.10 shows the influence of the flow velocity on the corrosion rate. [17]
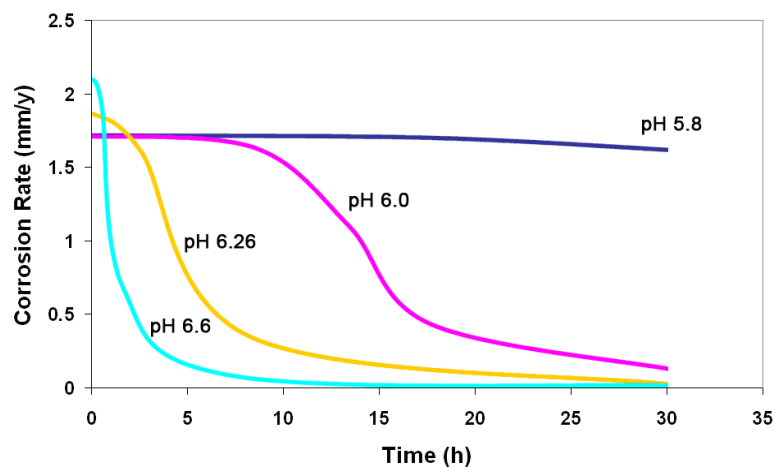
Fig. 2.5: Influence of the pH value on the corrosion rate

$(T = 80°C; p_{CO2} = 0.54 \text{ bar}; cFe^{2+} = 250 \text{ ppm and } v = 1 \text{ m/s})$ [17]
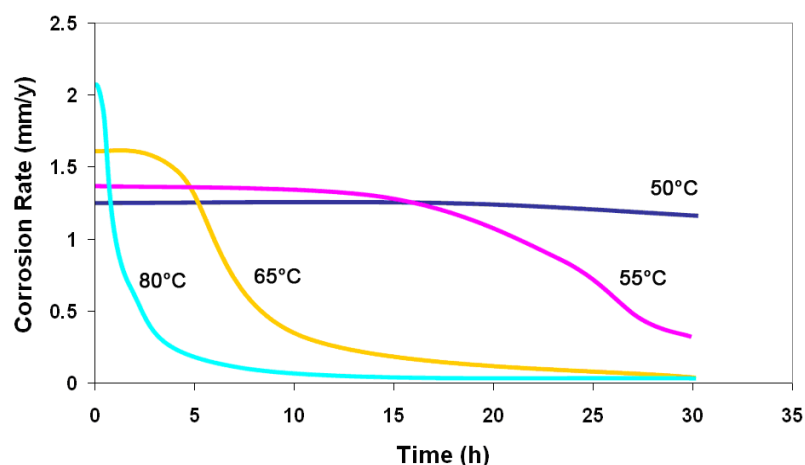
Fig. 2.6: Influence of the temperature on the corrosion rate

$(pH = 6.6; p_{CO2} = 0.54 \text{ bar}; cFe^{2+} = 250 \text{ ppm and } v = 1 \text{ m/s})$ [17]
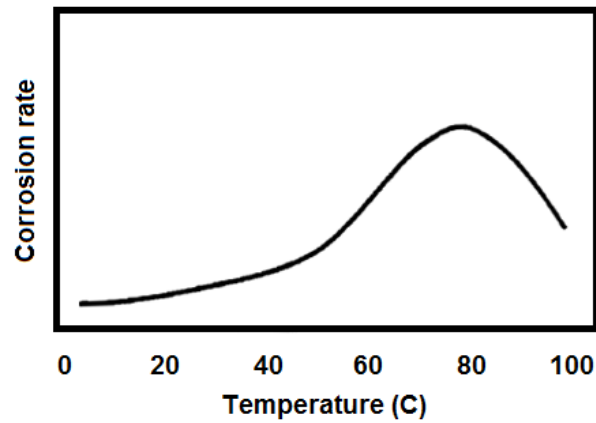
Fig. 2.7: Diagram showing the change of the corrosion rate with the temperature;
Maximum (scaling temperature) at ~ 80°C on carbon steel [19]
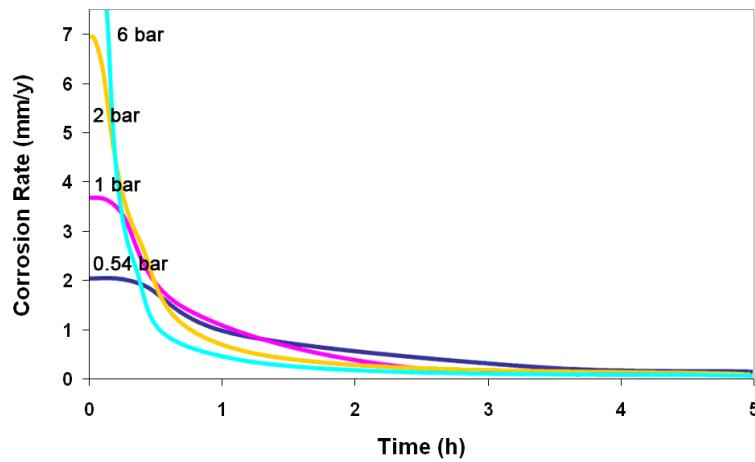
Fig. 2.8: Influence of the partial pressure on the corrosion rate
(pH = 6.6; T = 80°C; cFe^{2+} = 250 ppm and v = 1 m/s) [17]
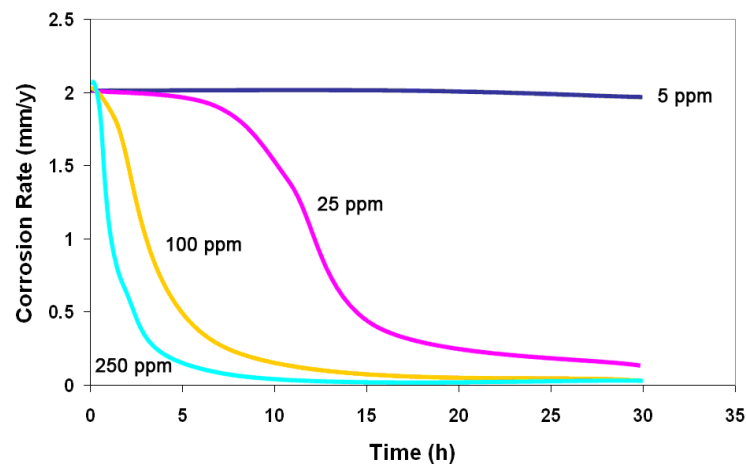
Fig. 2.9: Influence of the Fe^{2+} concentration on the corrosion rate
(pH = 6.6; T = 80°C; p_{CO2} = 0.54 bar and v = 1 m/s) [17]
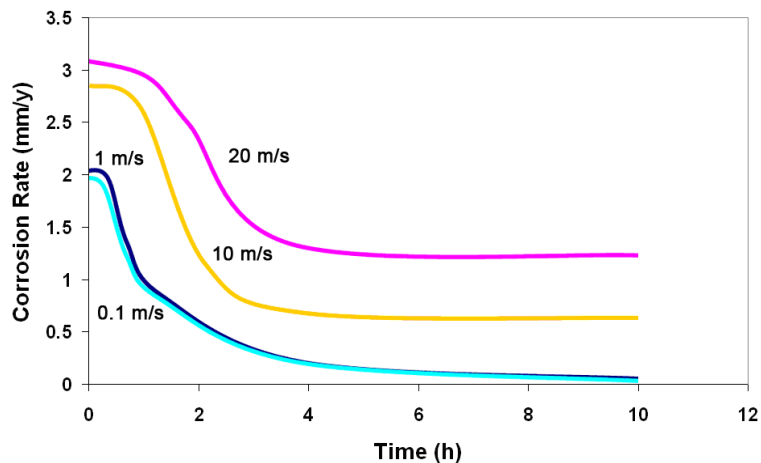
Fig. 2.10: Influence of the flow velocity on the corrosion rate
(pH = 6.6; T = 80°C; p_{CO2} = 0.54 bar and cFe^{2+} = 250 ppm) [17]

2.2.5. Effect of single parameters on CO_2 corrosion close to the material surface

The descriptions above were made for the whole corrosion system, the close-to-surface area and the principal solution together. These effects have also been studied intensely on the distance close to the metal layer, where the reactions occur. Directly on the layer of corrosion products, the parameters often show a different influence as for the principal solution. [13]

2.2.5.1. Close-to-layer effect of pH

To form iron carbonate films in CO_2 corrosion, the pH has to exceed a critical value, which depends on temperature, Fe^{2+} concentration, ionic strength, etc. Above the critical pH, saturation is exceeded and precipitation starts.

In experiments (20°C, 1 bar p_{CO2}, 1 m/s, principal solution pH 6) the pH on the steel surface was higher than for the principal solution due to the corrosion process. This effect leads to a reduced solubility of iron carbonate, increasing the level of supersaturation and therefore aiding the precipitation (Fig. 2.11). [13]

2.2.5.2. Close-to-layer effect of CO_2 partial pressure

The total pressure is the sum of CO_2 partial pressure and water vapor pressure. Increasing temperature leads to rapid film formation, but it is often overseen that this is always accompanied by a significant increase in water vapor partial pressure. Therefore, increasing temperature leads to decreasing CO_2 partial pressure in the gas phase. Hence, the amount of dissolved CO_2 in water also decreases according to Henrys law. Further, the concentration of

CO_3^{2-} is also reduced. Increasing temperature leads to two opposing effects. One is the increase of the precipitation kinetics; the other is the reduction of the supersaturation. Close-to-layer effect of temperature

For the formation of protective films, the temperature has to be elevated. On the iron surface, the supersaturation stays at lower values even for higher temperatures and lower iron carbonate solubilities. The reason for this is the fast precipitation process, which depletes the surface layer of Fe^{2+} and CO_3^{2-} ions maintaining a relatively low supersaturation. [13]

2.2.5.3.   Close-to-layer effect of Fe^{2+} concentration

Higher c_{Fe2+} leads to higher supersaturation and therefore to a higher precipitation rate and also a higher scaling tendency. In most closed laboratory systems (glass cells, autoclaves, and flow loops), rise of c_{Fe2+} in the solution is almost inevitable unless special measures are taken to remove Fe^{2+}. However, in once-through systems found in practice, and particularly in gas-condensate systems involving high rates of condensation, c_{Fe2+} may never reach the critical value.

Calculations show that rapid precipitation at the surface occurring at very high c_{Fe2+} can lead to a reduction of the surface pH compared to the principal solution pH and an increased corrosion rate. Offering extra iron ions increases the precipitation of a protective layer, but initially the corrosion rate temporarily increases due to this surface acidification effect for the beginning of film formation.

For $T = 50°C$, pH 6, $c_{Fe2+} = 1$ ppm, $v = 1$ m/s, it was found that for $p_{CO2} \leq 1$ bar, the resulting precipitation will not be sufficient to form protective films. On the other hand, when $p_{CO2} \geq 2$ bar, surface supersaturation increases leading to rapid precipitation and protective film formation.

As p_{CO2} is increased the pH at the surface initially increases due to corrosion and release of Fe^{2+} ions, and then decreases due to rapid precipitation.

CO_2 corrosion becomes more aggressive at higher CO_2 partial pressures, but the rate of precipitation also increases. [13]
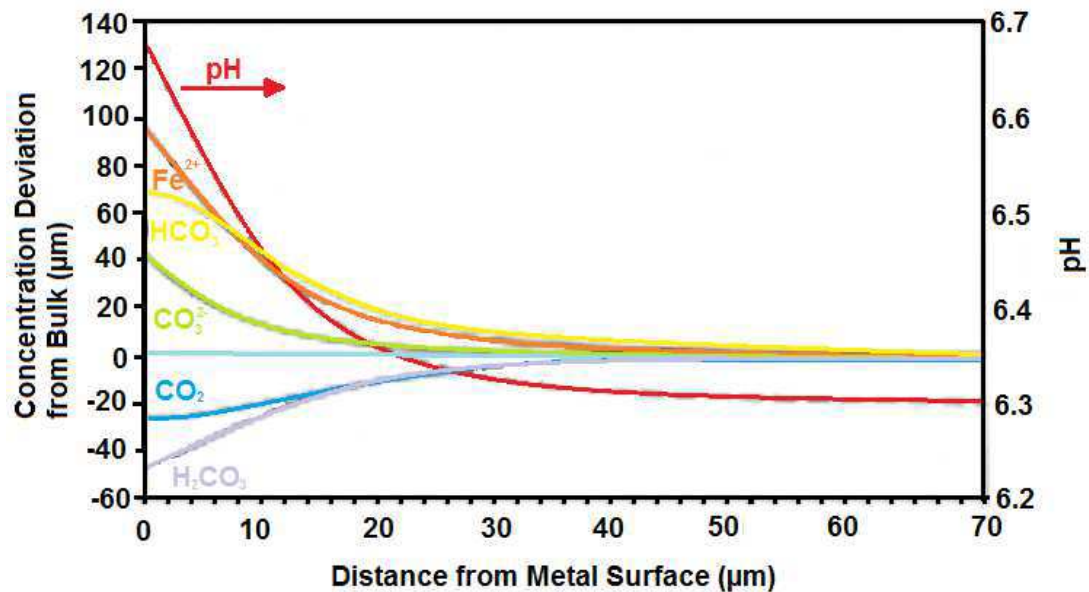
Fig. 2.11: Concentration profiles for the main dissolved species in the CO_2 solution
shown as the deviation from the principal solution equilibrium conditions
(T = 20°C, principal solution pH 6.3, p_{CO2} = 1 bar, c_{Fe2+} = 1 ppm, v = 1 m/s) [13]

2.2.5.4. *Close-to-layer effect of flow velocity*

Once a protective layer is formed, flow velocity can affect this layer through removal mechanically through erosion (improbable), chemically by dissolution (more probable), or a combination of both. If no protective layer was formed, it can affect the conditions on the beginning of corrosion and/or film formation by altering the mass transfer of dissolved species toward and away from the surface.

As the corrosion rate does not depend significantly on the velocity, the precipitation rate drops rapidly with increasing velocity. At low velocities, the precipitation rate is higher than the corrosion rate, leading to a high scaling tendency. Therefore, rapid formation of protective films is likely to occur. Above a threshold value, formation of protective films seems unlikely, due to a thinning of the mass transfer boundary layer. Higher velocities lead to more intensive mixing of the near-wall area with the principal solution, the Fe^{2+} ions are swept away from the surface before the can precipitate as protective film. [13]

2.2.6. Effect of an existing corrosion layer on further CO$_2$ corrosion process

For a present corrosion layer, the effect of its thickness, porosity and morphology are important.

2.2.6.1. Effect of film thickness

Macroscopic protective surface films are behaving like a diffusion barrier for species involved in corrosion. The diffusion is hindered the denser the layer, due to the necessity to get through a tangled maze of pores instead of directly diffusing to the metal surface. If the layer is porous, the barrier function to further corrosion is small and therefore there is no significant change in the corrosion rate. Otherwise, even for thin films, the corrosion rate can be reduced significantly, due to the so-called "surface coverage" effect, which is when parts of the surface under the film become unavailable for the corrosion. [13]

2.2.6.2. Effect of film porosity

Both corrosion and precipitation rate decreases as film density increases through a hindering of the flux of the species towards and from the metal surface. For very dense films, the fluxes of the single species are reduced, except for dissolved CO$_2$.

Only about a fifth of the H$_2$CO$_3$, which is consumed by the corrosion process as the main cathodic species, diffuses from the principal solution through the mass-transfer boundary layer. The rest is "produced locally" by direct hydration of dissolved CO$_2$ in a layer near the corroding steel surface.

In the case of a very thick and dense layer, almost all of the H$_2$CO$_3$ is produced locally in the thin chemical reaction boundary layer within the film. Outside this layer, and the rest of the film and in the mass-transfer boundary layer, the flux of all species other than dissolved CO$_2$ is very small, meaning that diffusion of dissolved CO$_2$ through the dense film is the main mechanism of providing the reactants to the corrosion reaction at the metal surface. [13]

2.2.6.3. Effect of film morphology

Detached 1% porous films performed similar as nine times more porous attached films, therefore the adherence of the protective layer it is very important for the corrosion performance. It is there-fore stated, that the main effect of protective iron carbonate films is to cover the metal surface and make it unavailable for further corrosion rather than an effective diffusion barrier. [13]

2.2.7. Morphology of formed FeCO₃ corrosion layers

In general, for conditions which led to scale formation, two types of scales were observed [10]:

Type I scales: thick with poor bonding between scale and metal, which gives the corrosive solution access to extended areas below the scale through cracks and pores, enabling corrosion reactions below the scale. These scales offer little protection due to complicating the mass transfer of reactants and products between the solution and the metal surface.

Type II scales: a very protective iron carbonate layer, which is thin, compact, non-porous and adherent to the metal surface. This scale offers a good isolation of the metal from the corrosive solution. Table 2.2 shows for which conditions scale formation was achieved and which scale type was observed. [10]

Other studies on the film formation showed that the CO_2 corrosion film can be classified in four main groups: transparent films, which is reported to not contain carbonate but iron and oxygen in the ratio of 1:2, iron carbide (Fe_3C) films, which is formed when anodic dissolution of iron ions is leaving behind some uncorroded steel cementite, iron carbonate ($FeCO_3$) films and iron carbonate plus iron carbide films. Table 2.3 gives the description of these classes. [20]

Table 2.2: Tested conditions and the type of layer obtained:
NP: non-protective or no layer, I: Type I, II: Type II layer [cf. 10]

	P_{CO2} = 241 kPa vel. = 1.5 m/s				P_{CO2} = 241 kPa vel. = 3.0 m/s		
pH	49°C	71°C	93°C	pH	49°C	71°C	93°C
4.5			NP	4.5			NP
5.0		NP	NP	5.0		NP	NP
5.5	NP	I	II	5.5	NP	NP	II
6.0	NP	I	II	6.0	NP	I	II
	P_{CO2} = 448 kPa vel. = 1.5 m/s				P_{CO2} = 448 kPa vel. = 3.0 m/s		
pH	49°C	71°C	93°C	pH	49°C	71°C	93°C
4.5			NP	4.5			NP
5.0	NP	NP	I	5.0	NP	NP	NP
5.5	NP	I	II	5.5	NP	I	II
6.0	NP	I	II	6.0	NP	I	II

Table 2.3: Tested conditions and the type of layer obtained; NP: non-protective or no layer, I: Type I, II: Type II layer [cf. 20]

Corrosion Film Class	Temperature Range of Formation (°C)	Characteristics/Nature	Growth Habit and Composition
Transparent	Forms at room temperature and below	<1 μm thick, transparent – once formed, it is very protective	Forming fast as temperature reduces to < room temperature mainly consisting of Fe and oxygen
Iron carbide	No range	<100 μm thick, metallic, conductive, and non-adherent	Spongy and brittle, consisting of Fe and C
Iron carbonate	Min. required in laboratory conditions 50°C to 70°C	Adherent, protective, and nonconductive	Cubic morphology, consisting of Fe, C, and O
Iron carbonate + iron carbide	Maximum 150°C (higher temperatures not studied)	All depends on how $FeCO_3$ is blended with Fe_3C	Consisting of ferrous carbide and ferrous carbonate

2.2.8. Influences of steel material parameters on CO_2 corrosion

2.2.8.1. Influences of steel microstructure on CO_2 corrosion

The influence of the microstructure on corrosion has been studied especially for the difference between ferritic/pearlitic and martensitic steel materials [20-22]. Ferritic/pearlitic J55 shows a good localized corrosion resistance lamellar cementite remaining in corrosion products. As the steel corrodes away, the lamellar cementite is left behind and acts as cathodic side accelerating the dissolution of iron. A local flow stagnation of higher local Fe^{2+} concentrations leads to $FeCO_3$ formation between the lamellar cementites, which help to anchor the corrosion product. If partial peeling off occurs, the layer heals due to this mechanism. This is why J55 shows a good localized-corrosion resistance. Martensitic steels like N80 have homogeneous dispersed-cementite to act as cathodic side, which accelerates CO_2 corrosion product formation, but the corrosion product peels of partially because of not having the anchoring effect as for J55. Therefore, N80 suffers from severe corrosion on locations with peeled-off layer. Initially, the ferritic/pearlitic structure is leading to higher corrosion rates. After the dissolution of iron ions, an empty cementite network is left behind, which forms a conductive porous sponge layer, in which cathodic reactions take place, thus leading to higher corrosion rates. As the $FeCO_3$ layer forms on this network, the anchoring effect as previously described, comes into effect. [20]

2.2.8.2. Influences of steel chemistry on CO_2 corrosion

A detailed study on alloying elements and their effects was performed by M. B. Kermani et al. [23] about the testing of low-carbon steels with microalloying additions of strong carbide-

forming elements (V, Ti, Mo and Nb). The purpose of the use of these elements is their combination with the carbon in the steel, leaving Cr uncombined in the ferrite to provide enhanced corrosion resistance. Si was added to provoke bainite formation under normalized conditions. Together with Ni it was used to bring back the strength which was lost due to carbon loss. The requirement of strength and toughness was met through grain size refinement, the promotion of bainitic microstructure and precipitation strengthening by carbides.

For **Chromium (Cr)**, 3 wt% Cr content showed the target reduction in corrosion rate of a 3-4 times improvement compared to commonly used carbon steel grades. 1.5 wt% Cr was not sufficient to reach this resistance level. The optimum level of Cr addition is supposed to be between 2 or 3 wt%.

Vanadium (V) showed a major beneficial effect on reducing the corrosion rate and is recommended to be added at ~ 50 wt% over stoichiometry with carbon, to give the best combination of corrosion resistance and mechanical properties. The improved corrosion resistance is maintained over a range of carbon contents.

Titan (Ti) has a beneficial effect on the corrosion behavior, but showed unsatisfactory effects on mechanical properties, which proved to be difficult to control. At pH 4.5-5, there is no difference to Ti and V containing steels, at pH 5 V shows a small beneficial effect giving more adherent corrosion films than Ti.

The microalloying elements **Si, Cu and Mo** showed beneficial effects on CO_2 corrosion complementary to the effect of Cr. Low-alloyed steels with 3 wt% Cr showed formation of Cr-rich films at conditions in which iron carbonate films are barely stable, and they grow at least down to pH 5. These films lead to a 3-10 times lower corrosion rate compared to non-alloyed reference steels. For Mo no effect was measurable.

A V microalloyed steel containing Cr, Si, Mo, and Cu showed to be the most promising composition in terms of corrosion resistance and mechanical properties, except for weldability, which makes this steel only suitable for downhole applications using screwed connections. Also, reference steel grades X70 and X65 showed an increase of corrosion rate over time, where the new composition steels showed reduced corrosion rate with time stabilizing after initial exposure, which indicates the formation of a protective film. The following composition range was found to offer superior CO_2 corrosion resistance (values for N, Al, S and P can be understood as maximum values (Table 2.4).

Table 2.4: Composition of alloying elements for superior CO_2 corrosion resistance

(values and standard deviations as mentioned in reference) [cf. 23]

Element	wt%
C	0.045 ± 0.015
Mn	0.550 ± 0.100
Si	0.600 ± 0.050
Cr	3.000 ± 0.200
Mo	0.300 ± 0.050
V	0.350 ± 0.100
N	0.005 ± 0.002
Al	0.030 ± 0.010
Cu	0.250 ± 0.010
Ti	0.400 ± 0.020

The level of microalloying should not be less than 1.5 times the stoichiometric ratio for the appropriate carbide. This work was the base for the investigation of the production of a commercially available CO_2 corrosion resistant steel grade. The outcome of these tests exceeded the target expectation of 3-4 times improved corrosion resistance at a cost of no more than 1.5 times of conventional oilfield steel grades by a factor of 3-10. Fig. 2.12 shows an overall graph for the effects of microalloying elements. [20]
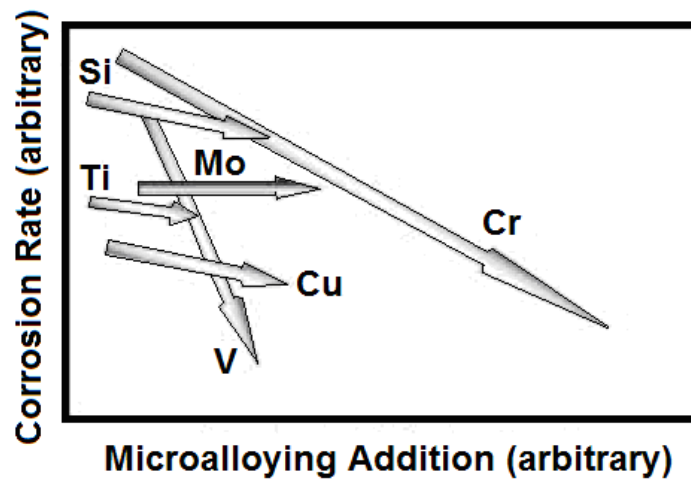
Fig. 2.12: Influence of the microalloying elements on CO_2 corrosion rate [cf. 20]

2.2.9. Corrosion models

2.2.9.1. DeWaard-Milliams equation

A simple model for the calculation of the corrosion rate is the DeWaard-Milliams equation [24, 25], which is given in Eq. 9. A plot for the results for the parameters of interest ($T = 0\text{-}100°C$ and $p_{CO2} = 0\text{-}5$ bar) is shown in Fig. 2.13.

$$\log V_{corr} = 5.8 - \frac{1710}{273 + T} + 0.67 \cdot \log(pCO_2) \tag{12}$$

This model is simple, but has the disadvantages of high estimations of the corrosion rates. Also the described maximum corrosion temperature is not visible in the results and salt solutions can not be considered.

With this equation, calculating for the experimental parameters of 60°C, 3 bar CO_2 and total pressure and 0.6 m/s velocity, a value of 9.7 mm/y corrosion was calculated for the initial phase of bare steel corrosion. These parameters represent environmental conditions present in field application. Assuming one cycle with a duration of 6 seconds, a corrosion rate of 1.8 nm was calculated, which is an influence of a few atom layers per cycle. Assuming a continuous friction leading to constant bare metal surfaces, the corrosion loss influence was calculated as 0.13 mm after an experimental duration of 5 days, which shows severe influence of the corrosion on the material loss according to these calculations.

Fig. 2.13: Calculated corrosion rates for CO_2 partial pressure values from 0 to 5 bar and temperatures from 0 to 100°C using the De Waard-Milliams equation [cf. 24, 25]

For the situation of the formation of a protective iron carbonate layer, a scale factor (F_{scale}) is taken into account, which is multiplied with the corrosion rate obtained from the De Waard-Milliams equation [25]. For temperatures below 60°C, this factor is taken as 1, as there is no protective layer formation. For higher temperatures, the scale factor is calculated using (13)

$$\log F_{scale} = \frac{2400}{T} - 0.6 \cdot \log(f_{CO_2}) - 6.7 \tag{13}$$

with T as temperature in K and f_{CO2} as fugacity of CO_2 gas calculated by multiplying the CO_2 partial pressure with the fugacity coefficient a calculated with

$$a = 10^{P \cdot (0.0031 - 1.4/T)} \tag{14}$$

with P as pressure in bar and T as temperature in K [26]. For the scaling factor results, the maximum value obtained is 1. If higher values are obtained, F_{scale} is set to 1. Another factor is the scaling temperature T_{scale}, in which the corrosion rate goes through a maximum and $F_{scale} = 0$. This scaling temperature decreases with increasing temperature (Fig. 2.14). For temperature/pressure combinations which lie below their respective scaling temperature, the corrosion rate does not need to be corrected, which means, no scaling factor has to be calculated and applied [25]. For a CO_2 partial pressure of 3 bar and 60°C temperature, the result lies below the scaling temperature and therefore does not need to be corrected. For 80°C, the scaling factor would be 0.65 and the value calculated for 3 bar p_{CO2} with De Waard-Milliams equation of 18.9 mm/y would change to 12.4 mm/y.
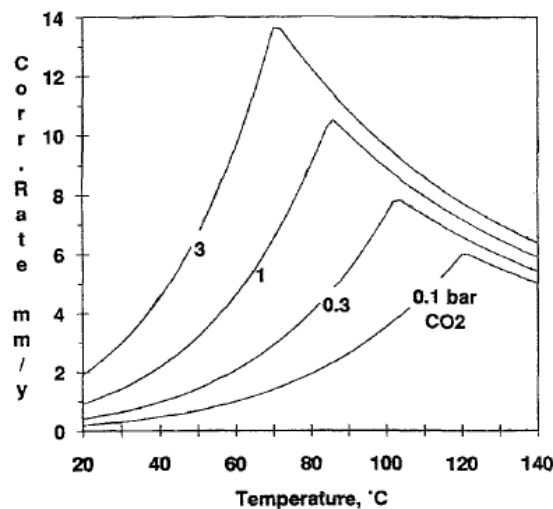
Fig. 2.14: Scaling temperature (peak) depending on CO_2 partial pressure [25]

2.2.9.2. NORSOK model

A widely used model is the NORSOK model [26]. It is an empirical model which was established based on laboratory data for low temperatures combined with field data for temperatures above 100 °C. The model has been developed by the Norwegian oil companies Statoil, Norsk Hydro and Saga Petroleum and is used as a standard for the Norwegian oil industry. The model puts a higher emphasis on the effect of protective corrosion films and therefore predicts lower corrosion rates at higher temperatures and higher pH values than the De Waard-Milliams model [27]. An advantage is that the pipe roughness is also considered. Also, the maximum corrosion temperature is shown in the calculated corrosion rates (Fig. 2.15). A disadvantage is, as for the De Waard-Milliams model, the missing saltwater influence for corrosion rate calculations.

The NORSOK equation is based on an empirical model for the calculation of aqueous CO_2 corrosion in petroleum industry. The parameters considered in this model are the temperature (range 5 to 160°C), pH value, CO_2 fugacity and the wall shear stress. For 60°C temperature, the equation is given as:

$$CR_t = K_t \cdot f_{CO2}^{0.62} \cdot (S/19)^{0.146+0.0324\log(fCO2)} \cdot f(pH)_t \qquad (15)$$

With CR_t as corrosion rate at temperature t, K_t as constant at temperature t (10.695 for 60°C), S as wall shear stress, f_{CO2} as CO_2 fugacity and $f(pH)_t$ as function of the pH value. The pH function for pH values in between 4.6 and 6.5 is given as:

$$f(pH) = 15.444 - (6.1291 \cdot pH) + (0.8204 \cdot pH^2) - (0.0371 \cdot pH^3) \qquad (16)$$

With pH as predominating pH value. The fugacity is calculated using:

$$f_{CO2} = a \cdot p_{CO2} \qquad (17)$$

With a as activity and p_{CO2} as CO_2 partial pressure. The activity a is calculated using:

$$a = 10^{P \cdot (0.0031 - 1.4/T)} \qquad (18)$$

for P as absolute pressure under 250 bar and T as temperature in K. The wall shear stress S is calculated using:

$$S = 0,5 \cdot \rho_m \cdot f \cdot u_m^2 \qquad (19)$$

With ρ_m as mixed density in kg/m^3, f as friction factor and u_m as mixed velocity in m/s. The friction factor was calculated using:

$$f = 0.001375 \left[1 + \left(20000 \frac{k}{D} + 10^6 \frac{\mu_m}{\rho_m u_m D} \right)^{0.33} \right] \tag{20}$$

With D as pipe diameter in mm and k as pipe roughness in m. Calculating for the case of experiments for 60°C, 3 bar CO_2 and total pressure and 0.6 m/s velocity, a value of 5.47 mm/y corrosion were calculated for the initial phase of bare steel corrosion. Assuming one cycle with a duration of 6 seconds, a corrosion rate of 1 nm per cycle was calculated. Assuming a continuous friction leading to constant bare metal surfaces, the corrosion loss influence was calculated as 0.12 mm after an experimental duration of 5 days. Hence also this model predicts severe corrosion loss.

2.2.9.3.   Model established by Han et al.

As model taking the salt concentration into account, the work of Han et al. [28] has to be mentioned. This model is for the calculation of the corrosion rate in the initial state of CO_2 corrosion, when the bare steel surface comes into contact with the corrosive medium. With this model, the corrosion rate for 60°C, 3 bar CO_2 and 3 wt% NaCl content was calculated to be 8.83 mm/y, which is significantly higher the NORSOK result, indicating the high influence of initial corrosion. The influence after 6 seconds cycle duration would be 1.7 nm, after 5 days it would be 0.12 mm, which would also indicate a severe influence. As it is an initial corrosion rate model, the maximum corrosion temperature observed for the NORSOK model is not included in the Han calculations. Also, the salt influence is not high within this model, for the corrosion rate calculated for 0 wt% NaCl is 8.76 mm/y, which is not significantly lower than with 3 wt% NaCl. The findings for the salt influence within this model are against the common knowledge for severe differences for salt concentrations from 0 to 5 wt% NaCl, where the maximum corrosion rate value lies around 3 wt% NaCl, which is the sea water salt concentration (Fig. 2.16; [29]). Fig. 2.17 and Fig. 2.18 show the results for the calculations using the HAN model.
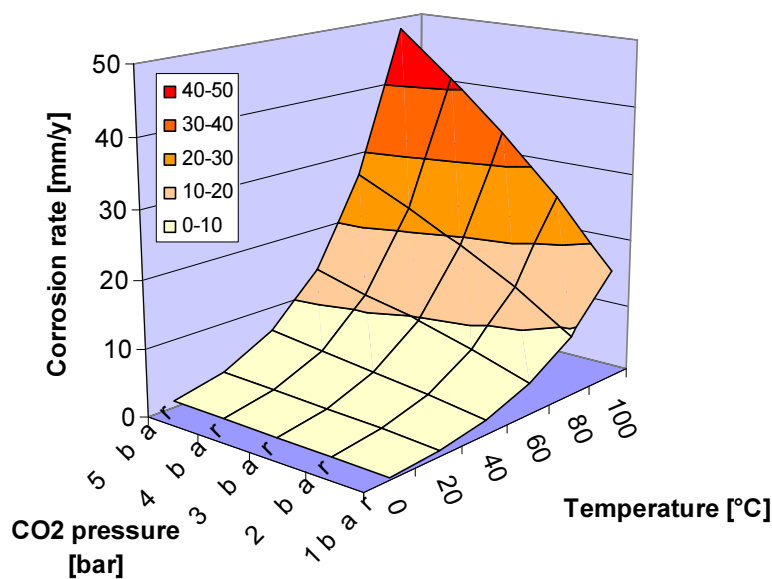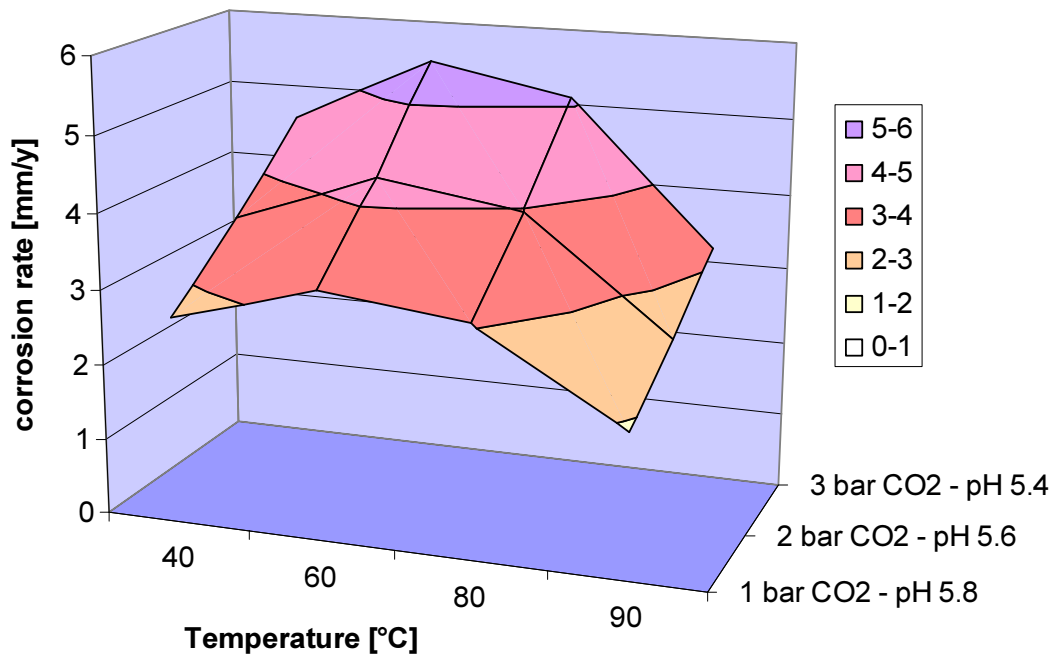
Fig. 2.15: Calculated corrosion rates for CO_2 partial pressure values from 0 to 5 bar and temperatures from 0 to 100°C using the NORSOK model mentioned in the literature [cf. 26]
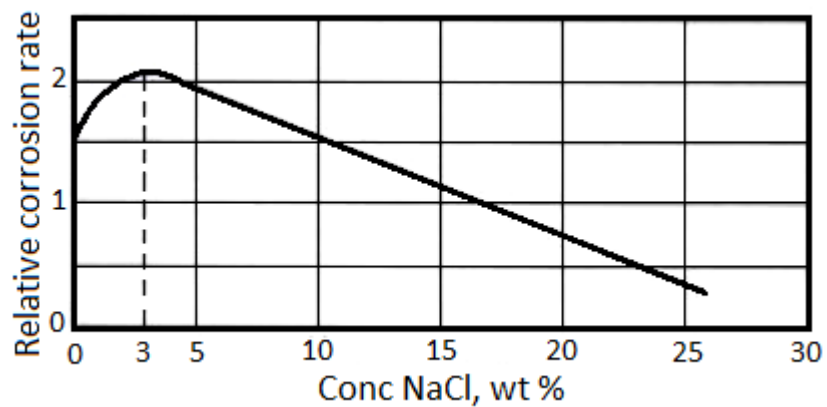
Fig. 2.16: Corrosion rate dependant on NaCl concentration in medium [cf. 29]
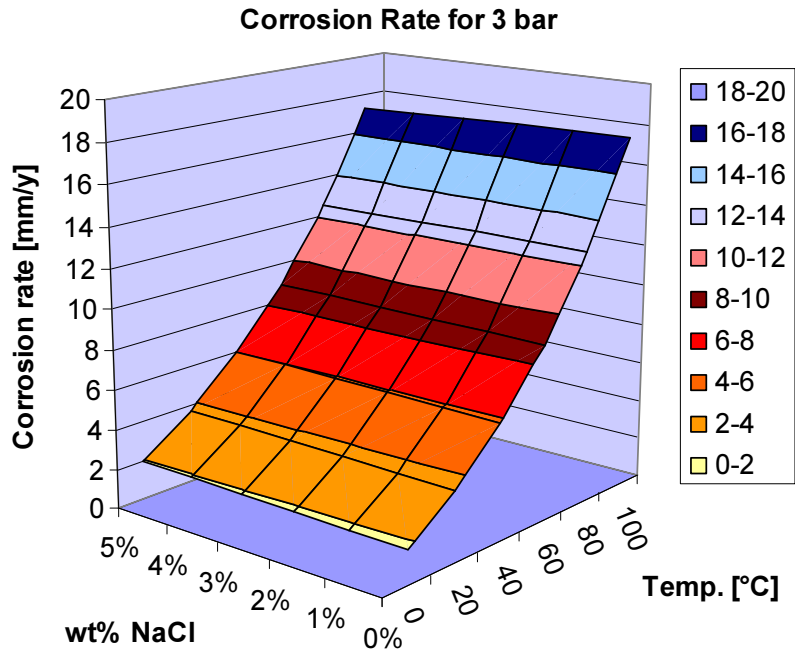
Fig. 2.17: Calculated corrosion rates for CO_2 partial pressure of 3 bar, for wt% NaCl values from 0 to 5 and temperatures from 0 to 100°C using the HAN model [cf. 28]
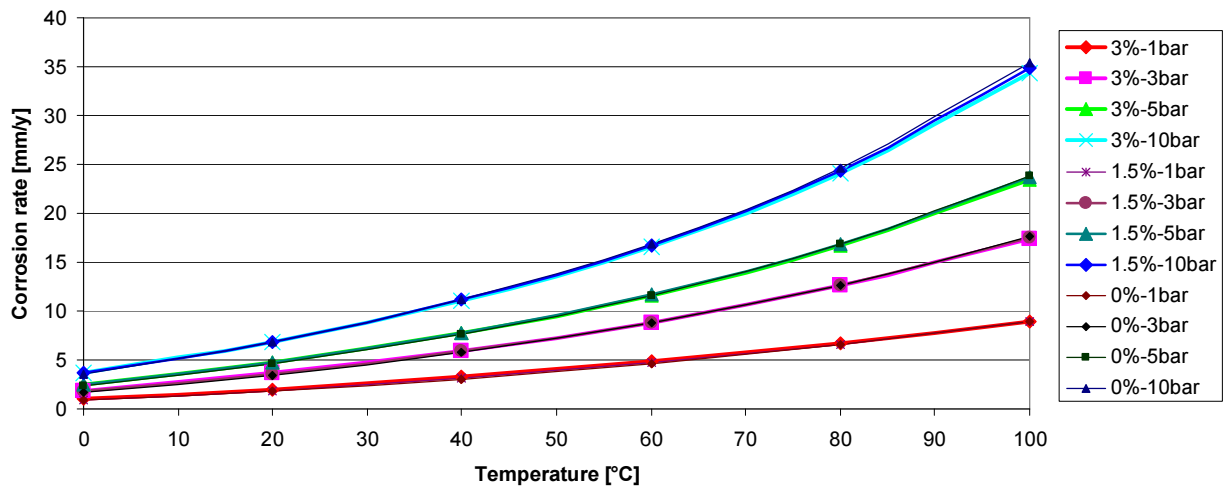
Fig. 2.18: Calculated corrosion rates for CO_2 partial pressure values from 0 to 10 bar, for NaCl values of 0, 1.5 and 3 wt%; and temperatures from 0 to 100°C using the HAN model [cf. 28]

2.2.10. Corrosion of Ni alloys

Ni-base materials are reported to show superior behavior in saline seawaters. Testing at 60°C in natural seawater containing 1 to 2 ppm free chlorine for 60 days, the tested alloys showed no detectable corrosion loss. Alloy 686 (19-23 Cr, 15-17 Mo, 3-4.4 W [wt%]) also showed no crevice corrosion. [30]

Pure nickel shows superior corrosion resistance in distilled water (only $3 \cdot 10^{-5}$ mm/y), and also in domestic hot water at 93°C (maximum $5 \cdot 10^{-3}$ mm/y) [31]. In distilled water saturated 50:50 with CO_2 at 71°C, the corrosion rate is ~ 0.03 mm/y. Also the MONEL alloys show similar behavior. INCONEL alloys are superior in aqueous solutions also containing CO_2, although they show a low tendency to pitting in chlorine containing fresh waters. MONEL alloys show less than 0.03 mm/y corrosion loss in flowing seawater. INCONEL alloy 625 (21.5 Cr, 9 Mo, 2.5 Fe, 3.6 Nb-stabilized [wt%]) shows no significant corrosive attack in seawater, the other alloys tested (INCOLOY 825, MONEL K-500 and 400) showed ~ 0.1 mm/y exposed to seawater under ambient conditions.

2.3. Wear

The term "wear" is known as ongoing material loss of the surface of a solid body (base body), provoked by mechanical causes, such as contact- and relative motion against a solid, liquid or gaseous counter acting body or substance. This wear of the surface of a solid body is called tribological wear.

Depending on the contact situation of the wear bodies (base and counter acting body), the following systems are distinguished [32]:

Solid/solid contact – solid wear
Solid/lubricant(in liquid or solid state)/solid contact – wear under mixed or boundary friction

Another classification of wear can be performed using the descriptions of the wear mechanism and wear types. The physical and chemical processes, which are occurring during wear contact, can be understood as wear mechanisms, which are, for instance, sliding wear, rolling wear, impact wear, oscillating wear etc.

For the wear measurement and the measurement of the results of wear processes it is crucial to know the wear measuring quantity (measured values which mark the alternation in shape or mass

of a worn body) and the wear appearance (alternation of worn surface and/or type and shape of wear particles). Measuring quantities can be given in different dimensions; wear length as one-dimensional, wear area as two-dimensional and wear volume as three-dimensional value.

Due to the complexity of wear in general it is hard to theoretically calculate these values. It is necessary to perform wear measurement through suitable measurement and testing techniques. [32]

2.3.1.   Wear mechanisms

Wear can occur as material loss and/or surface damage. It can be categorized in four main wear mechanisms (Fig. 2.19; [33]) [32]:

Adhesion – formation and breaking of interfacial adhesive bonds

Abrasion – removal of material due to scratching

Surface fatigue – fatigue and formation of cracks in surface regions due to tribological stress cycles that result in separation of materials

Tribochemical reactions – formation of chemical reaction products as a result of chemical interactions between the elements of a tribosystem initiated by tribological action
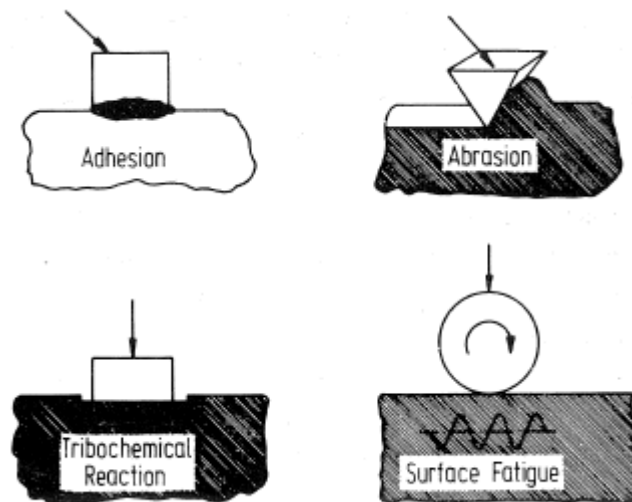
Fig. 2.19: Main forms of wear: adhesion, abrasion, tribochemical reaction and surface fatigue [33]

2.3.1.1. *Adhesive wear*

Adhesive wear can occur when surfaces slide against each other. High local pressure between contacting materials lead to plastic deformation, adhesion and, as a consequence, the formation of local junctions. Relative sliding between the materials causes ruptures of these junctions and as a result to material transfer from one surface to the other. With increasing damage or overloading due to stress, sliding speed or temperature, adhesion may result in scuffing, which is connected with increasing friction coefficient and wear. [33]

2.3.1.2. *Abrasive wear*

Abrasion can be understood as displacement of material under the influence of hard particles. These hard particles can be embedded in one or both surfaces, which are in relative motion or can be present as hard protuberances on one or both surfaces. A "hard particle" can result from the process as fragment of the materials themselves or can come from "outside" in form of dirt particles, sand etc. Protuberances can act as hard particles if the surface of this material is much harder than the counter surface. [33]

Abrasive wear occurs if the counter body is harder and rougher as the worn base body (2-body abrasive wear) or hard particles are located between the two bodies (3-body abrasive wear). Abrasive wear can occur due to different forms of interaction between the abrasive body and the worn body. The main forms are (Fig. 2.20) [32]:

- Micro ploughing – often occurring for ductile materials; due to plastic deformation, the worn body is pressed away by the abrasive counter body (Fig. 2.20 a).
- Micro chipping – in front of the abrasive particle, a chip is formed, which is ideally the same volume of the formed wear groove. (Fig. 2.20 b).
- Micro fatigue – material removal as result of local fatigue processes for repeated micro ploughing wear on the surface through multiple abrasive particles (Fig. 2.20 c).
- Micro cracking – often occurring for hard materials; occurs if applied load is higher than critical load of material, resulting in crack formation and propagation, which lead to major material disruptions alongside the wear groove (Fig. 2.20 d).
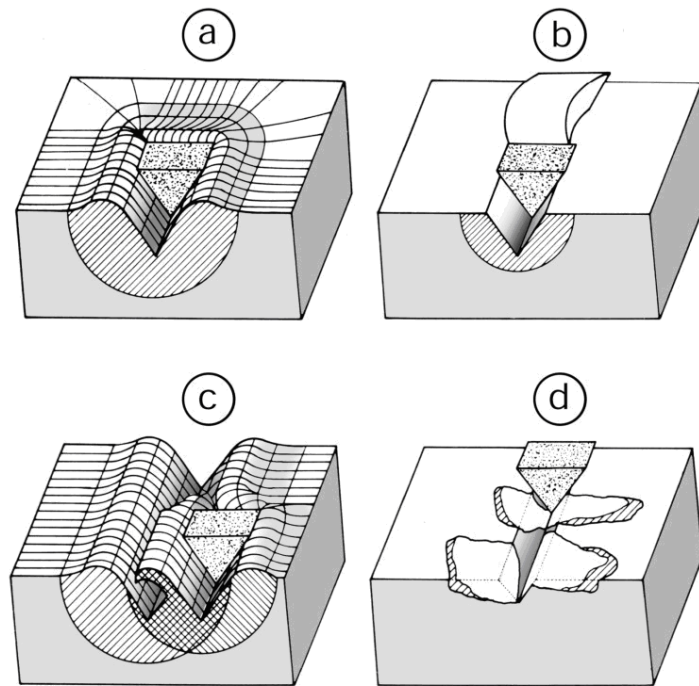
Fig. 2.20: Main forms of abrasive wear: a) micro ploughing, b) micro chipping,
c) micro fatigue, d) micro cracking [32]

2.3.1.3. Surface fatigue wear

Wear due to surface fatigue happens as crack formation and flaking of material as a result of repeated alternating loading of solid surfaces. Rolling and/or sliding contact on surfaces or the impact contact of solids or liquids can lead to cyclic surface stressing. Typical systems in which surface fatigue often occurs are e.g. rail and wheel systems or rollers for cold and hot rolling.

2.3.1.4. Tribochemical wear

Tribochemical wear can be understood as rubbing contact between two solid surfaces which react with the environment. The corrosive environment can be gaseous or liquid. The wear process proceeds by continuous removal of a formed corrosive layer and the reformation of this layer on the freshly uncovered surface. In the presence of oxygen, the formed layers consist mainly of oxides. [33]

Tribochemical wear results the removal of metal and chemical reaction products from the contact surfaces and can be divided into four processes [33]:

a) Metallic contact between surface asperities which leads to the removal of material due to adhesion. The small metallic wear debris, which is formed, may be oxidized

b) Chemical reactions of the metals with the environment lead to the formation of protective surface layers that reduce metallic contact

c) Cracking of these protective surface layers due to locally high pressure or micro fatigue leads to non-metallic wear debris

d) Metallic and non-metallic wear debris can also act as an abrasive and roughen the contacting surfaces.

Damage and mass loss are a result of the repeated occurrence of these four processes. Tribochemical wear is strongly influenced by the kinetics of the layer formation and their properties, which determine their resistance to removal (ductility, strength, adhesion to base material). Tribochemical layer resistance to cracking is increased by a sufficient strength of the base material (Fig. 2.21). [33]
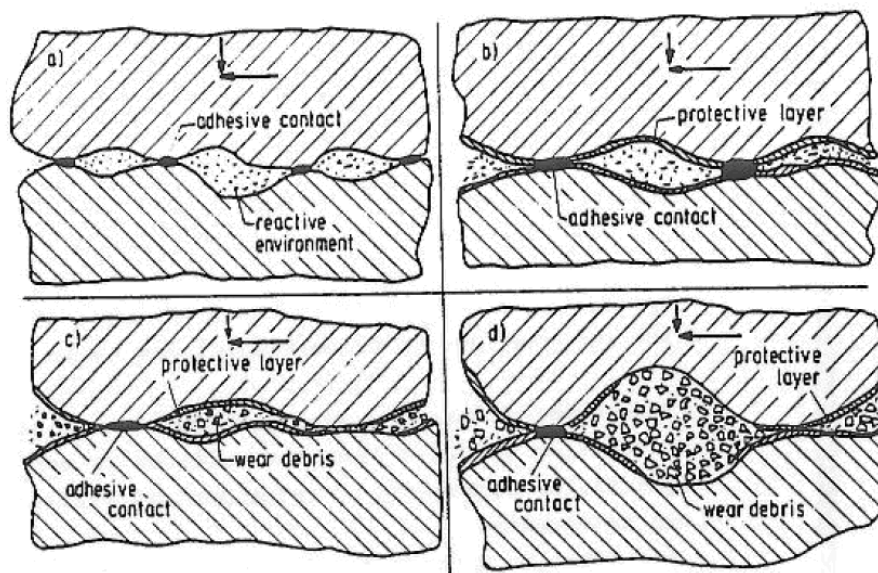
Fig. 2.21: Wear by tribochemical reaction – a) formation of oxide islands; b) and c) growth of oxide islands; d) destruction of primary oxide islands and forming of new islands [33]

2.3.2.   Effect of different microstructures in sliding wear contact

Considering the effect of different microstructures in sliding wear contact, ferritic/pearlitic materials perform better than martensitic because the cementite plates lead to more wear resistance compared to the martensite structure. [34]

A possible explanation for this effect of the better performance of the ferritic/pearlitic material can be linked to the content of the cementite phases, as it was investigated by Fontalvo et al. [35] for 0.35 wt% containing steels. It was found that adhesive wear depends on two factors: the carbide content and the distance between these carbides. The carbide content determines the probability a junction of the real area of contact is formed over a carbide, and therefore the probability of adhesive effects. Increasing carbide content reduces adhesive wear. This effect is influenced by the distance of the carbides. A close carbide network is more effective to prevent adhesive effects than distant carbides offering wide areas in between.

In wear tests using grinding balls out of steel of different microstructures, the as-quenched martensite structure resulted to have the highest hardness and the lowest wear rate. Tempered martensitic samples showed decreasing wear resistance with decreasing hardness [36, 37].

Investigations on martensitic and ferritic/pearlitic materials performed by Bermúdez et al. [38] showed a better wear behavior of the martensitic microstructure. Investigations in friction frequency (1 to 8 Hz) wear testing for different microstructures of low alloyed carbon (0.38 wt% C) steel showed that quenched and tempered martensitic microstructures show high wear resistance for low and high frequency testing. Annealed ferritic/pearlitic samples exhibit higher wear rates with increasing frequency. For this material, a transition from abrasive and oxidative wear to an adhesive mechanism was observed with increasing frequency, which is supposed to come from thermal softening [38]. The difference between the findings of [34] and [38] may be a result of the effect described in [35].

2.4. Wear and corrosion

Wear and corrosion synergy happens under the influence of wear attack on the surface, activating the surface by abrading an existing protective layer or a formed more or less protective corrosion layer. Abrasion under corrosive conditions allows the corrosive media to attack the freshly exposed material surface. This coaction of these processes lead to enhanced material damage through wear and corrosion synergy.

Wear and corrosion synergy can be found for example for abrasion-corrosion of passive stainless steels in acidic media [39] or in NaCl solutions [40].

2.4.1. Wear and corrosion synergy under CO_2 corrosive conditions

Synergy effects of erosion/abrasion and CO_2 corrosion leading to higher mass loss than the single effects have been verified in various works [41-46].

X. Hu et al. [42] performed erosion and corrosion tests as well as separated tests for erosion and corrosion. These effects were tested investigating erosion using test solutions of different sand amounts on X65 pipeline steel with an impact angle of 90°. The test apparatus was purged with CO_2 to generate an oxygen-poor atmosphere. The parameters varied were the impingement velocity (7-20 m/s), temperature (20-70°C) and the solid loading (30-200 mg/l). Synergistic effects were determined by comparing the measurement results for the total weight loss with the weight loss of pure erosion and corrosion as thickness loss in mm/y.

The values for the pure erosion and pure corrosion tests are minimal compared to the results for the tests for both effects combined. According to these results it can be assumed that the synergy of erosion and corrosion plays a major role. The increase of the thickness loss with rising temperature is assumed to result from a faster film growth rate for increased temperatures. Fig. 2.23 shows the results for different impingement velocities and sand loads.

Higher impingement velocities and higher sand loadings are leading to a higher thickness loss. The higher the flow velocity is the higher becomes the dependency on the sand loading.

For the combined effect of the flow velocity V, temperature T and solid loading S, an empirical model was established, which is used for the calculation of the total thickness loss TTS of erosion-corrosion (Eq. 21).

$$TTS = S^{\alpha} \cdot \exp(\beta \cdot V + \gamma T)$$

(21)

Where α, β and γ are constants which are derived from linear regression method of the experimentally acquired data.
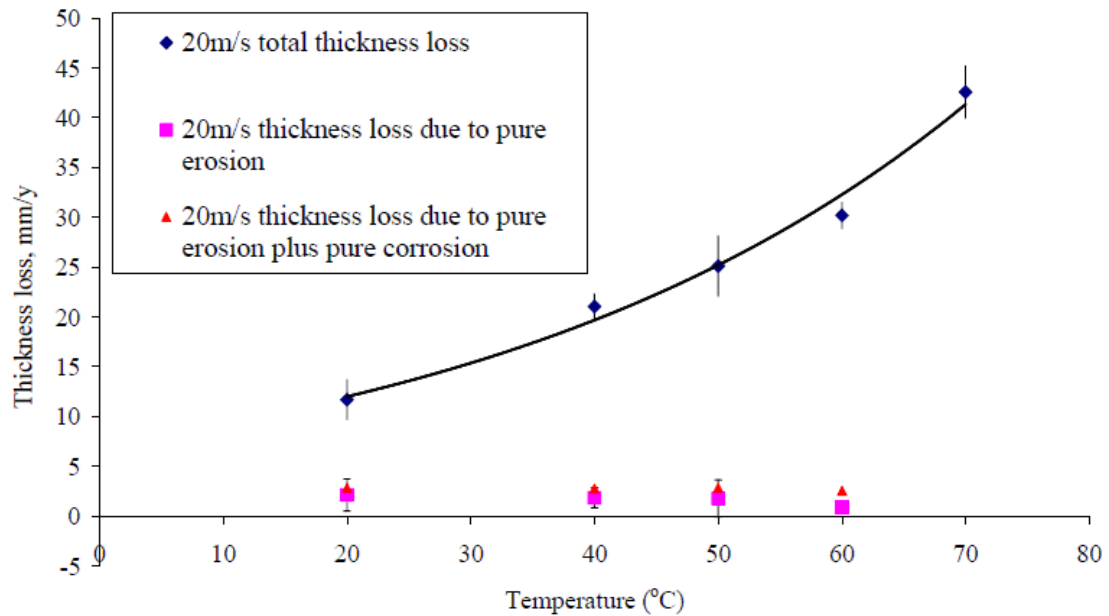
Fig. 2.22: Results for the erosion, corrosion and erosion-corrosion synergy shown as thickness loss in mm/y for 20 m/s impingement velocity using 200 mg/l sand loading for a temperature variation from 20-70°C [42]
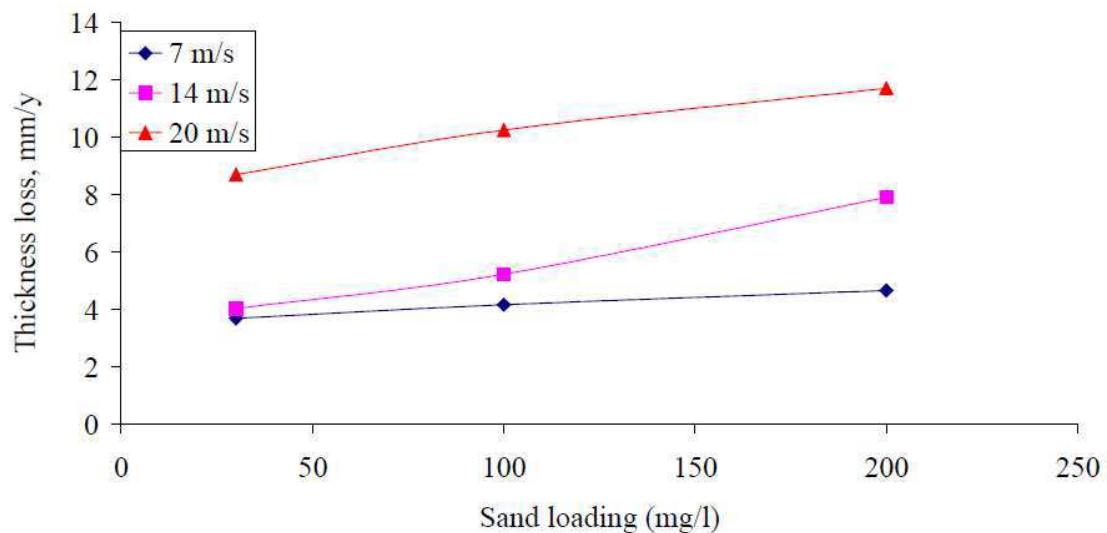
Fig. 2.23: Results for thickness loss as a function of sand loading and impingement velocity at 20°C for erosive-corrosive tests [42]

Erosion-corrosion tests were performed by Feyerl et al. [45] on ferritic/pearlitic J55 material and martensitic C95 material in an artificial brine of water with 27 g/l NaCl saturated with CO_2 gas with silica sand particles. The material degeneration showed an increase with increasing flow velocity for both materials. In the artificial brine, it comes to siderite formation, which is then eroded by impact of sand and water droplets. The ferritic/pearlitic material showed a deeper attack than the martensitic material. For the ferritic/pearlitic material, it is supposed to show a galvanic effect between the carbide phases in the formed siderite layer and the ferrite phase of the steel material. The martensitic material showed lower degeneration rates compared to the ferritic/pearlitic material, on one side, due to its higher hardness and on the other side due to weaker cathodes formed with the spherical carbides of the martensitic material.

Also, erosion, e.g. from sand particles, have found to have a severe effect on material damage on highly alloyed materials. These materials do not show damage in corrosion only conditions. With additional erosion, the passive layer of these materials is harmed. Since these mechanical defects are not able to repassivate, pits are propagated by the impact of sand particles. [46]

A detailed work on erosion-corrosion synergy was performed by Stack et al. [47], where erosion-corrosion synergy is described using the equation (22)

$$K_{WC} = K_W + K_C \tag{22}$$

with K_{WC} as the total wear-corrosion rate, K_C as total corrosion rate and K_W as total wear rate. K_W can be written as $K_{WO} + \Delta K_W$ where K_{WO} is the wear rate in absence of corrosion and ΔK_W can be seen as the "synergistic" contribution to the total wear rate. The same can be written for the total corrosion rate K_C as $K_{CO} + \Delta K_C$, where K_{CO} is the corrosion rate in absence of wear and ΔK_C as the enhancement of corrosion due to wear, also called "additive" effect. Another important factor is the formation of passive films during tribocorrosion, which has been investigated for oxide formation in aqueous solutions [48]. In the presence of passive films, the steel material experienced, depending on the nature of the solution, plastic flow accompanied by particle detachment or subsurface cracking and delamination.

On the strength of the formed $FeCO_3$ layer formed on mild steel, it was found out that the mechanical strength is ~ 10 MPa, which is many orders of magnitude higher than typical values found in turbulent flow [49]. The adhesive strength of the formed layer to the steel base material

appeared even larger. Flow shear stress up to 20 Pa did not harm the protective layer. The investigated layer was formed using a 1 wt% NaCl solution, deoxygenated with CO_2 purging and a temperature of 80°C electrochemically by applying a galvanostatic current equivalent to ~ 1 mm/year corrosion rate for 24 hours.

Tests on a similar formed $FeCO_3$ layer were performed on a rotating sample. Rotation speeds from 1000 to 7000 rpm generated wall shear stresses from 2 to 45 Pa. Over a time of ~ 4 hours, the corrosion rate rose to 0.8 mm/y for 1,000 rpm and to 1.1 mm/y for 7000 rpm. The initially formed protective scale had been partially removed in both cases, leading to higher corrosion rates by offering fresh steel surface to be corroded. The hypothesis taken prior to the tests, which the formed iron carbonate layer can not only be removed by hydrodynamic forces alone, seems not to be valid for higher velocities. [43]

Tests performed on chemical removal at 100 rpm and in an undersaturated solution showed that the scale was dissoluted immediately leading to a rise in the corrosion rate to 0.8 mm/y for pH of 5.8 after 4 hours.

For the investigation of erosion-corrosion synergy effects, low undersaturation and medium velocity (1000 rpm) at pH of 5.8 and high undersaturation at high velocity (7000 rpm) at pH of 5.6 were tested. Corrosion rates increased to 1.0 mm/y after 2 hours for the first and to 1.7 mm/y after 1.5 hours for the second conditions. In both cases, only very little from the original iron carbonate scale and an initiation of localized corrosion of the underlying steel was observable. It is supposed that the partial removal of the iron carbonate scale may lead to a galvanic effect, which would cause localized corrosion. It was measured that for the mechanical and chemical removal tests compared to the results of the chemo-mechanical removal tests, the results for the chemo-mechanical tests were higher than for the sum of chemical and mechanical tests. [43]

A very detailed work in the field of abrasion and corrosion synergy was performed by A. Hedayat et al. [50], where different steel types with different microstructures after quenching and tempering were tested on corrosion and abrasion using a test apparatus, which was built consisting of a round turnable counter body against a tube sample half pipe (Fig. 2.24).
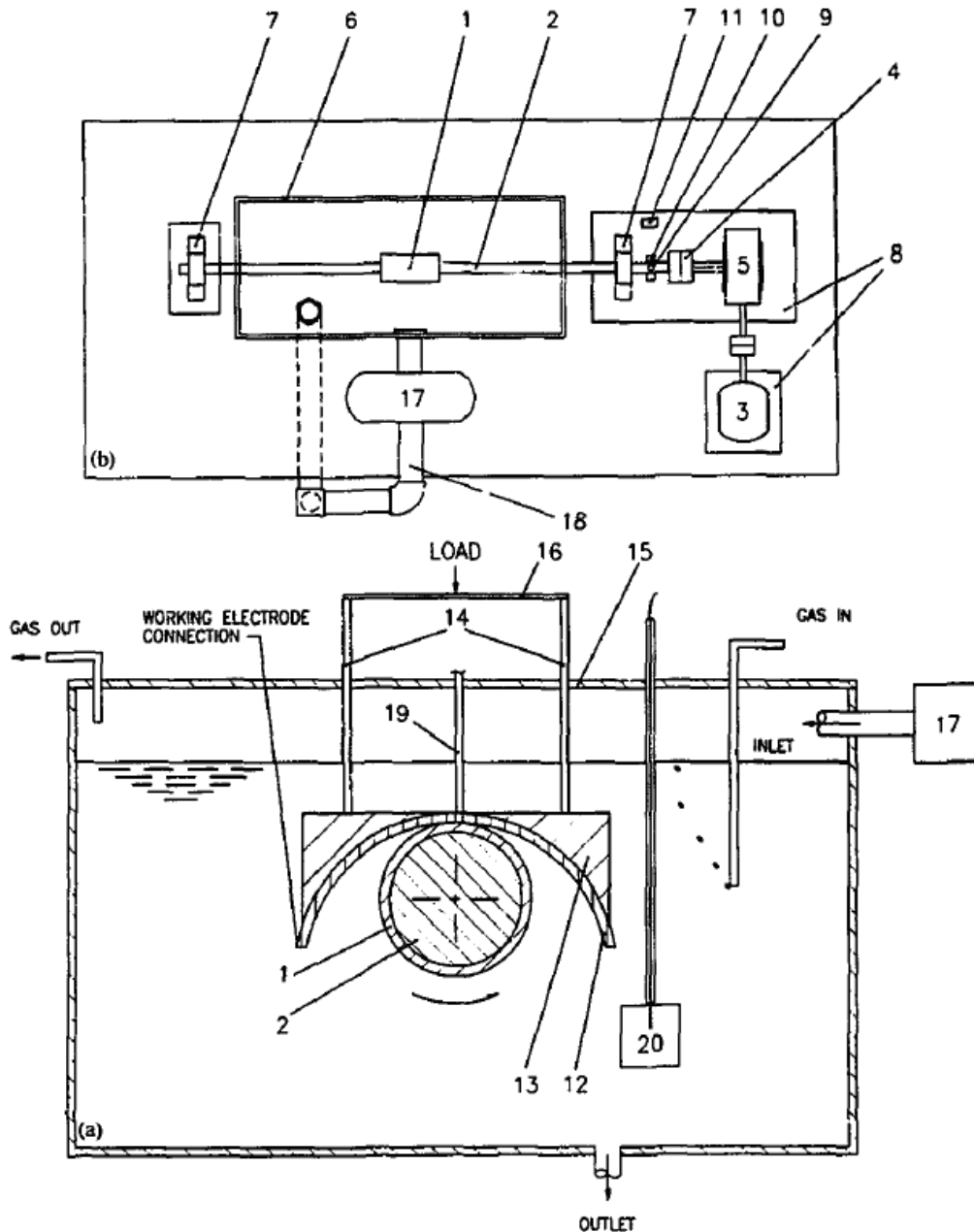
Fig. 2.24: Test apparatus used by A. Hedayat et al.; most important parts: 1) counter body,
2) 304 stainless steel shaft, 12) tubing half pipe, 13) 304 stainless steel plate [50]

As materials tested, AISI 1010, L80, N80 and P110 steel grades, using quenched and tempered (Q&T) as heat treatment, and the tubing material and AISI 1030 as counter body material were used. Also, a spray coated metal was tested as counter body material.

The L80 and N80 grade tubings had a bainite microstructure, while the P110 tubing had a tempered martensite microstructure. The hardness of these samples from highest to lowest were P110 > AISI 1010 > N80 > L80. The L80, N80 and P110 tubing contain approximately the same amount of carbon (~ 0.3 wt%). The different hardness values were achieved by phase

transformation. The spray coated metal also showed bainitic structure due to the different cooling treatment of the coating process. The tests were performed in a mixture of oil/water/sand in the ratio of 68:30:2. This mixture was purged with CO_2 gas.

In their tests, a harder counter body (spray coated hard metal instead of the softer AISI 1030 as counter body material) led to greater tubing thickness loss. But on the other side, the harder coating suffered less loss than the softer counter body material. The most damage was done on the L80 and the least damage on the P110 tubings. The increase in hardness by phase transformation led to a higher resistance against combined corrosion and wear effects. Inversely, the counter bodies tested against the soft L80 tubing material suffered less wear-corrosion than against the harder materials.

To the N-80 materials, small amounts of Cr (0.77 wt%) showed a beneficial effect against tribocorrosion which was higher than the positive influence achieved by solely hardening the material through phase transformation. The chromium added to the bainitc N80 material shows its beneficial effects as a carbon affine element by forming stable carbides in form of spheroids, which are increasing the tribocorrosion resistance. Also, some alloying elements such as Mn, Cr, Si or Mo have beneficial effects due to solid solution hardening.
The low alloyed steels with bainitic microstructure yielded less tribocorrosion than plain carbon steel hardened by phase transformation, although their tempered martensite structure is harder than of the bainite samples.

Not only the CO_2 itself has an influence on the corrosion; also the salt content has an influence on wear. On one side, it is reported that enhanced salt contents result in severe pittings in slurry tests [51]. It should be noted that these tests were performed with high salt contents (5 wt%) and durations of 2 hours testing time. On the other side, it is reported [52] that saline media are reducing the friction coefficient due to boundary effects with increasing salt concentration, until reaching a plateau. This lubrication effect is a result of hydrated anion repulsion, which increases the minimum distance between the contact bodies, and an enhanced local viscosity on the surfaces. Another work [53] performing 3.5 wt% sodium chloride medium tests on a pin-on-disc tribometer reported a lubricative effect compared to dry tribotests. The surface of worn carbon steel samples show the formation of plate-like debris on the surface, which is an indicator for a delamination wear process. Under corrosive conditions, a network of surface cracks is present on the carbon steel sample. A formation of galvanic cells might be responsible for these cracks. It is

supposed that these cells were formed due to the abrasion using the abraded area on the surface as anode and the undamaged area as cathode. Despite of the formation of these cracks due to synergism effects, the total weight loss under corrosive environment is less than for dry tests because the NaCl solution served as a lubricant reducing the friction between the substrate and the counter-face. Other studies [54] in a flow loop on carbon steel with similar sand load (1 wt%) and rising NaCl content from 3 to 18 wt% resulted in decreasing the sand erosion due to increasing density and viscosity of the solution. These tests were already performed in deaerated solutions purged with CO_2 gas at 75°C and are a good representation for synergistic effects of salt and CO_2 corrosion together. Also the corrosion rate decreased with increasing salt content.

2.4.2. Wear and corrosion testing

In order to test the wear and corrosion influence on carbon steel under CO_2 and saline influence, various methods have been taken into account. The following paragraphs offer a summary on these methods, which are mostly a modification of standard test methods on sliding wear (e.g. pin-on-disc or steel-wheel tribometer; description in experimental, chapter 3.2).

Modified standard tests (steel-wheel and pin-on-disc tribometer) – The idea of the respective authors was to equip a commercial steel-wheel or pin-on-disc tribometer with a sample chamber which can be filled with medium and purged with CO_2. The drawback of this method was the non-applicability of pressure (pressures of ~ 3 bar CO_2) on that sensitive system. Also the protection from corrosion of those sensitive parts was not possible within a reasonable effort. Ideas of such an application of steel-wheel tester for medium testing are presented in the literature [55-57] (Fig. 2.25, Fig. 2.26 and Fig. 2.27). These solutions do not conclude the applicability of higher pressure.
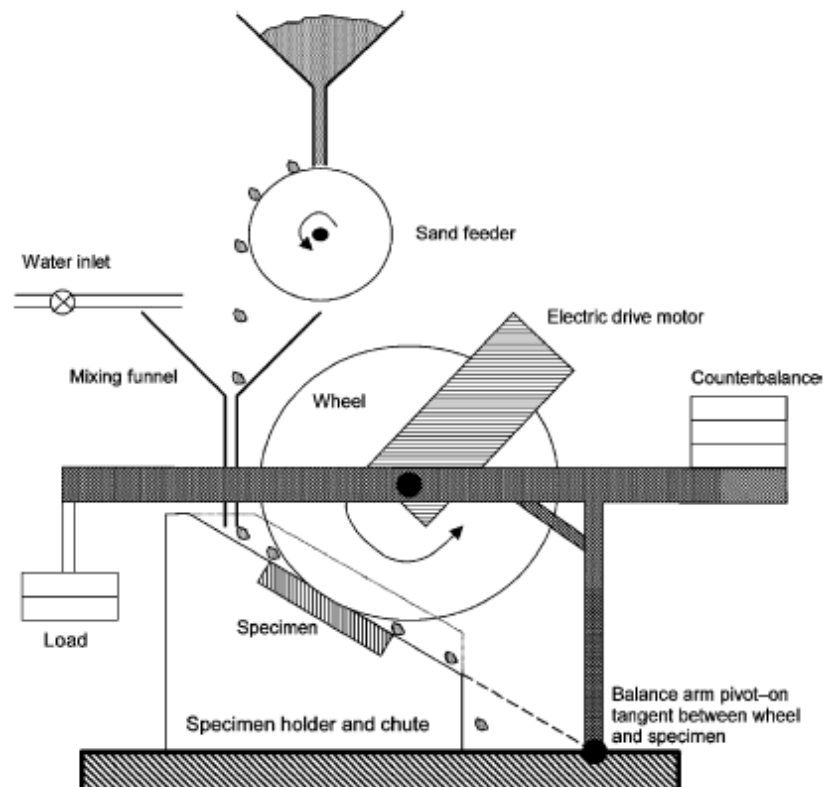
Fig. 2.25: Modified steel-wheel application found in the literature [55]
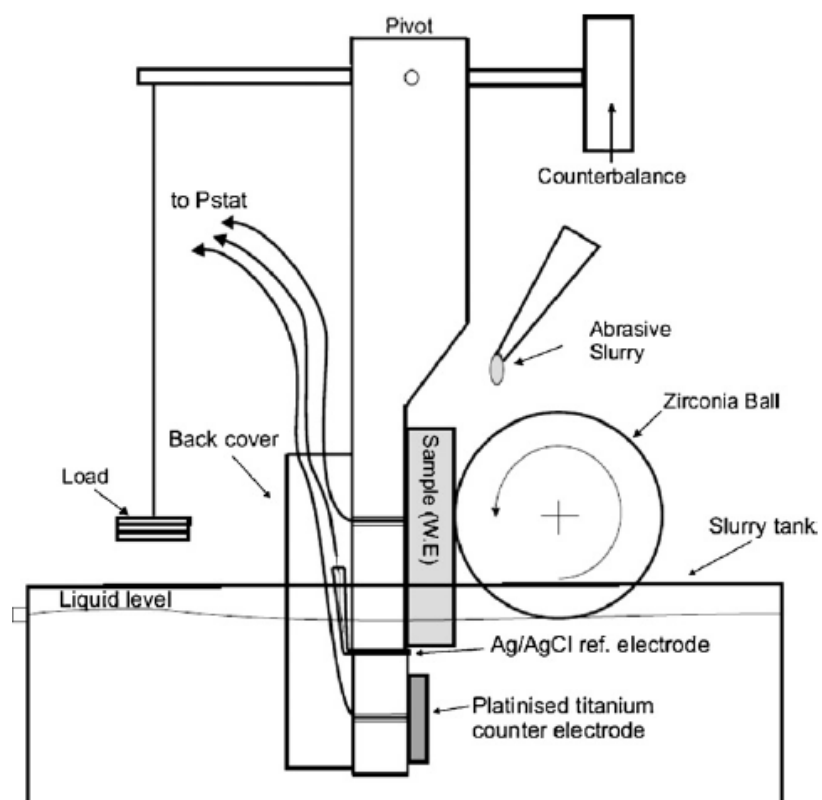
Fig. 2.26: Modified steel-wheel application found in the literature [56]
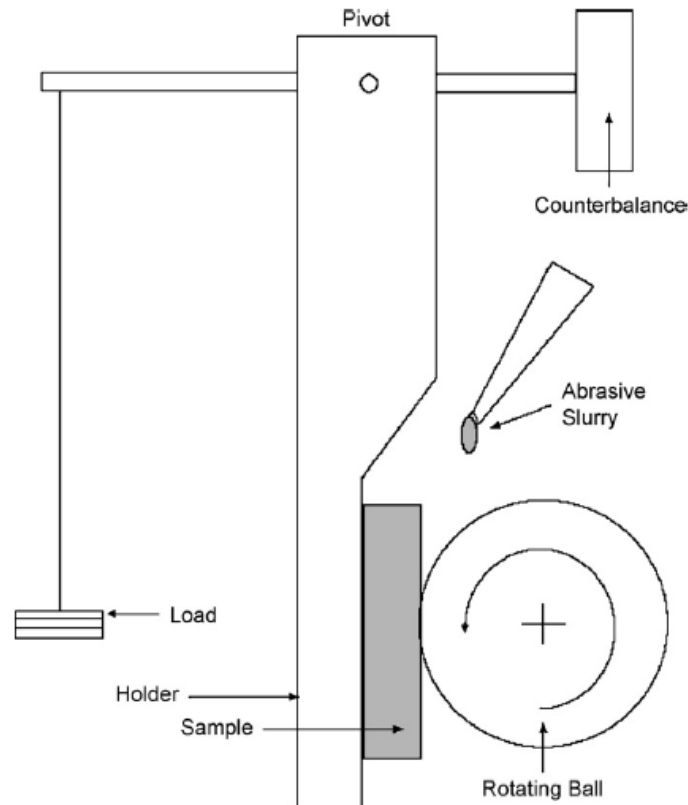
Fig. 2.27: Modified steel-wheel application found in the literature [57]

Cylinder against half pipe – This apparatus is closer described in the previous chapter and seen in Fig. 2.24. It consists of a counter body sample coated cylinder turning against a tubing sample half pipe. The part containing the samples is inside a closed tank filled with medium which is purged with CO_2 gas.

2.4.3. Influence of oxide layer and Ni-base counter body on wear process

2.4.3.1. Formation of oxide layers on steel surfaces due to heat treatment process

During oxidation process, the main phases formed during oxidation of iron are hematite (Fe_2O_3), magnetite (Fe_3O_4) and wustite (FeO). For low carbon steels, the oxidation rate reaches a plateau after ~ 30 min exposure time for temperatures between 650 and 1100°C. The obtained layer thickness increases with increasing temperature. [58]

The oxidation scale rapidly grows at the beginning of the process. After ~ 20 sec, the scale growth rate follows a parabolic law (Fig. 2.28) [59]. The oxidation process of carbon steel starts at ~ 400°C, where magnetite is formed at the surface. At around 500-600°C, hematite is formed, with the formation temperature dependant on the carbon content of the steel. Manganese as

alloying element has an influence on the magnetite formation, where increasing Mn contents retard the magnetite formation. Wustite was observed to be formed at temperatures between 750 and 850°C. [60]

Below 800°C, the oxide layer only grows to a thickness of around 30 µm. For higher temperatures (950°C), the thickness increases up to 150 µm due to an increase of the wustite formation. Wustite, which is thermodynamically stable at temperatures above 570°C, is likely to decompose to Fe_3O_4 and Fe during the cooling process. When FeO is rapidly quenched, the non-stoichiometric form can be obtained as a metastable phase at room temperature. [60]
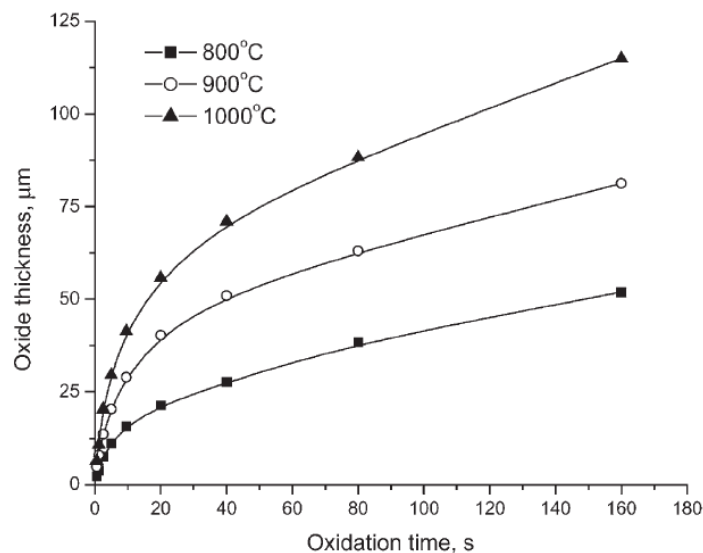
Fig. 2.28: Increase of oxidic layer thickness on low carbon steel for
800, 900 and 1000°C following a parabolic law

2.4.3.2.   Influence of oxide layer in sliding wear testing

It was found that the presence of iron oxide (Fe_2O_3) as particles increases the wear by acceleration of the transition from mild to severe wear in pin-on-disc tribotesting. This effect increases with increasing particle diameter and increasing normal load. The relative area of oxide films in tribocontact increases with normal load. It is suggested, that the transition from mild to severe wear occurs when the relative area of oxide film contact reaches a specific value, which is proportional to the area of real contact. [61]

For oxide formation on iron oxide in tribocontact, it was found for dry friction tests, that the formation of iron oxide products on the wear track are dominating the friction characteristics and induces a transition towards high friction. Adhesive wear occurs easier as the real contact increases, which is happening through increased normal loads. The oxide layer formation on the wear track occurs early due to the adhesive reaction combined with the reaction with environmental oxygen. [62]

2.4.3.3.   Influence of Ni-base counter body on sliding wear

Another important effect occurring in sliding wear testing is the effect of adhesive wear. Investigations were performed on Ni-based alloy coatings (10 mm Ni50 alloy powder deposited on 304L stainless steel) tested on a block-on-ring wear tester with applied normal loads of 30, 70 and 120 N. As counter body, the same material was applied. The coatings were observed to show abrasive wear at an initial stage of wear under low loads and adhesive wear under higher loads. After long-time wearing, the mechanisms are adhesive wear and oxidation wear under low load, and fatigue wear under high loads. [63]

2.4.3.4.   Wear-resistance of Ni-base materials

Ni-base materials are reported to show better wear performance than steel materials [64].Two Ni-base materials, which were built through electro spark deposition, with the composition of the main elements as shown in Table 2.5, were investigated. In comparison, the steel sample 1045 was also tested.

Table 2.5: Composition of tested Ni-base alloys [wt%]

	C	Si	Mn	Fe	Cr	W	Mo	Nb	Ni
Ni818	0.021	0.33	0.005	4.65	15.51	3.92	15.72	-	Base
Ni398	0.040	0.13	4.650	5.92	18.55	-	-	2.58	base

The used counterpart was a stainless steel ball of 2 mm in diameter, the load was 10 N, and the testing time was 30 min under dry friction conditions. Wear results showed that the friction coefficients for Ni-base materials are lower than for 1045 steel sample, and also the wear volume is significantly lower. The wear volume of Ni818 coating is only 1/6 of that for 1045 steel and 1/3 for Ni398 coating (Fig. 2.29).
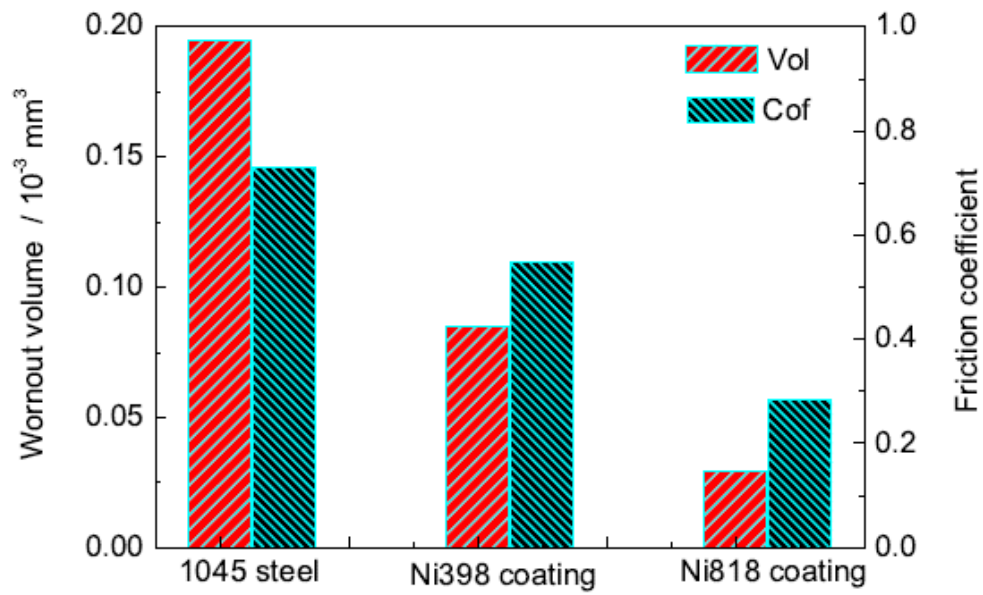
Fig. 2.29: Test results for wear volume (red) and friction coefficient (green) for tested Ni-base alloys and the 1045 steel sample [64]

3. Experimental

As first step before the performance of any experiments, a detailed analysis of worn samples from a real field application has been performed. The results of these investigations showed that abrasive sliding wear together with corrosion is predominant in field application. Hence there were simulated in lab-scale by slurry abrasion tests and pin-on-disc sliding wear test. A detailed summary of the field sample analysis is shown in detail in chapter 4.1. Based on the findings for this analysis, the lab-scale tests were processed. Results obtained for lab-scale tests have been compared to the found mechanisms from the real field application. Pin-on-disc sliding wear analyses were performed for many purposes. The influence of the oxide layer, which origins from processing and heat treatment at the production of steel materials, was investigated. Therefore, a heat treatment process was developed in order to achieve comparable oxide layers as they can be found on typical produced steel parts. As the heat treatment and the resulting steel qualities also have an influence on wear and corrosion performance, tests with exemplary heat treatments resulting in commonly used steel grades have also been performed. The influence of the Ni-base counter body was tested in two ways, on one side; the hardness influence was tested by comparison of a commonly used Ni-base grade compared to a softer Ni-base alloy.

As it is important to not only know the effects of wear and corrosion in separate, it is also necessary to investigate both effects simultaneously under defined conditions under typical applicative conditions. For the realization of these experiments, a test facility was established in which the steel samples can be equipped and tested under CO_2 corrosive conditions in oscillating sliding wear testing.

3.1. Description of basic body and counter body samples

As basic body samples, carbon steel samples were used where as counter body samples, Ni-base layer coated samples were tested, as these coatings are applied in field application. In a first set of experiments, the carbon steel samples have been manufactured and heat treated with a simple routine heat treatment set to the demands of ferritic/pearlitic and martensitic structures in order to gain an overview. Further on, specific heat treatment processes were defined and processed. The samples for the advanced test series have been prepared after heat treatment procedures which are also applied for materials equipped for real field application. Therefore, tests performed with the first set of materials can be seen as tests for the gaining of first experiences with the applied methods, where tests on materials of application material heat treatment can be seen as more application-specific tests. In order to preserve anonymity of the sample notation for

these samples, the original grade names are substituted by names which are describing the sample conditions.

3.1.1.   Steel samples used as basic body

The materials for the first set of experiments were processed out of an as-manufactured carbon steel material through lab routine heat treatment. The chemistry of the acquired steel material is listed in Table 3.1. As it was not yet clear which heat treatment procedures were selected for application material tests, lab-scale methods to produce two ferritic/pearlitic and two martensitic structures were chosen. Besides the "as received" material (N; ~200 HV1), for ferritic/pearlitic microstructure, two material grades were obtained through normalizing heat treatment, where one material was air cooled, achieving a hardness of ~200 HV1. The other one was furnace cooled, resulting in a hardness value lower than 180 HV1. Through Quenching and tempering, samples with martensitic microstructure were obtained. At higher tempering temperature, a hardness value around 240 HV1 were obtained, whereas for lower tempering temperatures, the material hardness was higher than 300 HV1 [76].

Table 3.1: Chemical composition of the base steel material in wt% [cf. 74]

Element	wt%
Carbon C	0.3
Manganese Mn	1.4
Chromium Cr	0.4
Iron Fe	base

The normalization process is performed by heating up into the austenitic area in the Iron carbon phase diagram as shown in Fig. 3.1 and is therefore austenitized. The essential part is the cooling phase, where the microstructure is able to re-form to a "normal state" as it is described in the Fe-C diagram. Fig. 3.1 shows the Fe-C-diagram. Typical holding times were about 1 hour.
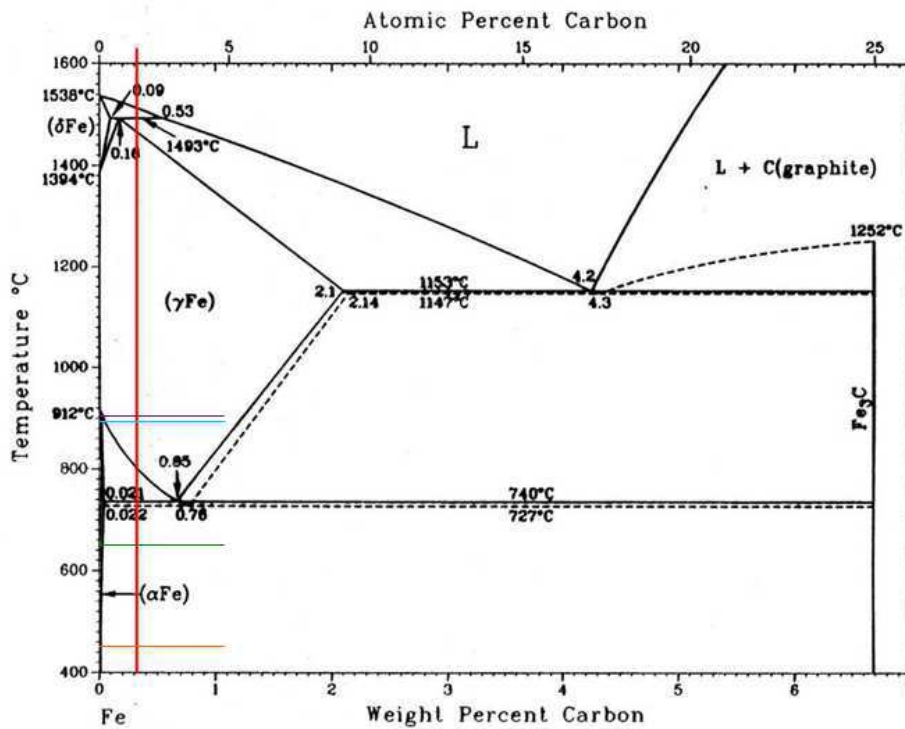
Fig. 3.1: Iron carbon phase diagram (red line: C-content of used steel material.
Blue line: Normalization temperature; Violet line: Q&T temperature;
Green line: tempering temperature V1; Orange line: tempering temperature V2 [cf. 65].

Cooling at air (N2) leads to a fine microstructure out of the "sub grains" (domains) existing in the grains of the material prior to the austenitization process. This leads to higher ductility with nearly unchanged hardness. Cooling in the furnace (N1) leads therefore to a coarse microstructure, because the grains are allowed to grow due to the slower cooling rate (longer times at temperature). The results for these heat treatments are given in chapter 4.2.

The used basic body materials for advanced tests according to field application are made from one obtained carbon steel material through different heat treatment and have therefore the same chemistry given in Table 3.1. Out of this material, the ferritic/pearlitic steel samples were manufactured similar as for the samples of the first set of experiments, where one material has a higher hardness (FP-H) than the other material (FP-S). Also, two martensitic steel grades were manufactured, were as for the FP samples, there is one "harder" (M-H) and one "softer" (M-S) material, which achieved similar results as were obtained for the lab-scale heat treatments. As "standard" material for the tests on the performance in sliding wear contact for various cycles,

the hard ferritic/pearlitic FP-H was tested. The results for these heat treatments are given in chapter 4.2.

3.1.2.   Counter body samples

As Ni-base materials, three alloy types were used to produce the coating layer, one spray coated layer and two built-up welding powders, one generating a "soft" layer containing ~10 wt% Cr with 535 ± 25 HV1. With 15 wt% Cr, the "hard" layer with 775 ± 37 HV1 was generated. The spray-coating layer had a hardness of 440 ± 45 HV1. Also containing ~ 10 wt% Cr, a spray-coated layer was used for the steel-wheel wear tests. For sliding wear tests, the welded layers were used. The microscopical images for the resulting welding layers are given in chapter 4.2. As substrate material, St37 steel with 10-12 mm thickness was chosen. [77]

3.1.3.   Sample preparation

For steel-wheel tests, the basic body sample parts were cut out of the basic body for the test geometry of about 70×25×7 mm.

For sliding wear tests, the Ni-base material was welded on a steel matrix. Then the pins were eroded to the necessary geometry of 6 mm diameter. It was desired to test these Ni-base layers on two roughness levels. The hard layer was grinded using a 120 grid for the rougher, and 1 μm diamond paste for the smoother surface. Roughness measurements showed a roughness R_a range of 0.15 to 0.25 μm for the smooth and 0.7 to 0.9 μm for the rougher surface [66, 67, 75]. In order to achieve these parameters for the softer material, it had to be grinded with grit 1000 for the smoother surface. For the rough conditions, there was no need for additional polishment, because the samples already had this roughness value. The roughness values R_a are referred in experiments as "polished" for the smooth surface and "grinded" for the rough surface, as these are the main manufacturing steps to achieve the measured roughness parameters.

For first tests using the Pin-on-Disc tribometer, the pin geometry was square shaped of 6 mm edge length for the contact surface, because this geometry was easy and cheap to manufacture. As in first tests, it was shown that this geometry leads to insufficient sample contact towards the steel disc, the geometry was switched to circular shape of 6 mm diameter. The pins have been manufactured by wire-electro discharge machining by Harald Umreich Ges.m.b.H. With this

approved setup, the influence of the adapted oxide layer and of the different material parameters after various heat treatment processes was studied.

The disc samples were made out of as-produced basic body material, which were heat treated to generate the desired steel grade. Also, the surface of the disc sample was prepared for metal-metal contact test (grinding off oxide layer) and oxide layer tests (keeping the layer produced by heat treatment). The results for the adapted heat treatments are given in chapter 4.2.

3.2. Test methods for fundamental wear and corrosion tests

For fundamental wear studies, test methods simulating sliding and abrasive wear were chosen. On one side, the steel-wheel tribometer was chosen in order to simulate three body wear with abrasive sand particles. Pin-on-disc sliding wear testing was chosen as suitable method for longer testing periods (up to 24 hours compared to 15 minutes of steel-wheel tribotesting).

For static corrosion testing, a test facility was established, which offers the opportunity to perform fast and easy corrosion tests under saline and CO_2 gas conditions.

3.2.1. Steel-wheel tribometer

The prepared basic body samples were worn using the steel-wheel test apparatus shown in Fig. 3.2. The procedure was derived from the G65 standard procedure [68].

The sample is fixed in upright position with the large side towards the steel-wheel, which forms the movable counterpart. The medium is added through the feed as slurry (abrasive mixture) or as (saline) aqueous solution. Applying a defined normal force, wheel and sample are pressed together. The slurry medium is mixed as a 50:50 mixture of abrasive (Ottawa sand SiO_2 of 3 mm grain size together with Ottawa sand flour) in aqueous and 1.5 wt% saline medium.

Through the slurry feed, the medium, which may be a saline solution and/or contain abrasive, is added. With this method, the influence of abrasives on wear was determined. These tests were carried out on the FP-H basic body material with a steel-wheel coated with the "soft" Ni-base layer as counter body material. The main test parameters are listed in Table 3.2.

For the evaluation of the test results, the samples were weighted before and after the test, using the scale mentioned in chapter 3.4.3 (which was used for all tests). This mass loss was used to calculate the wear rate in mm^3/m, which was calculated as following

$$WR = \frac{V_W}{d_W} = \frac{\left(\dfrac{m_W}{\rho} \cdot 1000\right)}{d_W} \tag{23}$$

with WR as wear rate, d_W for the sliding distance, V_W for the wear volume, M_W as the wear mass and ρ as the density of the steel, which is 7.80 g/cm^3 for the used samples.
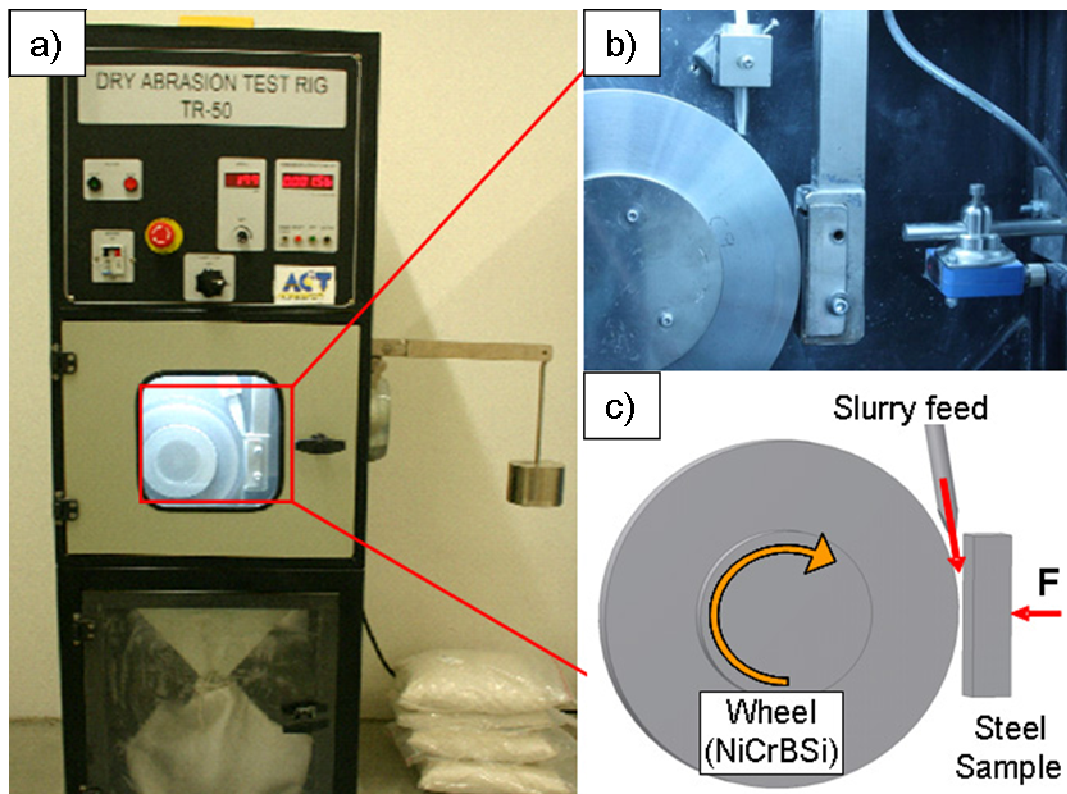

Fig. 3.2: Steel-wheel test facility: a) test apparatus, b) close-up of test chamber, c) schematic assembly of test principle [cf. 74]

Table 3.2: Main parameters used for the steel-wheel tests of the first heat treatment set (pre-tests) and of the applicative heat treatment (abrasive tests)

Parameter	Pre-tests	Abrasive tests
Steel-wheel	Ni-base coated steel wheel	Ni-base coated steel wheel
Wheel diameter [m]	0.232	0.232
Normal force [N]	45; 130	130
Sliding speed [m/s]	0.9; 0.6[1]	0.6
Test duration [min]	10; 30[1]	15
Salinity of medium [g/l NaCl]	15	0; 1.5
Abrasive content (Sand SiO_2) [wt%]	0.0; 0.1 and 60	0.1; 1; 5; 10, 20 and 60

[1] These parameters were only used for less abrasive tests

3.2.2. Pin-on-disc tribometer

For the simulation of the sliding wear between basic body and counter body, the pin-on-disc tribometer (Certony®) was applied (Fig. 3.3). The pin is pressed against the rotating disc with a defined normal force. The samples are flushed with tap water as aqueous medium. For the first tests using the pin-on-disc tribometer, the pin samples were made out of steel samples as used for the first tests on the steel-wheel tribometer (Fig. 3.4). The disc samples were Ni-base spray coated steel discs with the same Ni-base layer composition as used for the steel wheel tests (sectional cut image in Fig. 3.2). These tests were primarily performed to generate a damage image on the steel pin sample; therefore no tribotest curve was evaluated for this setup. For tests with the second heat treatment sample set, the oxide layer after heat treatment came into the focus of interest for further sliding wear tests. As the disc sample offers a higher surface for investigations, the samples were switched to steel disc and Ni-base layer pin samples. For the first test series, FP-H disc samples after double normalization were used with the oxide layer as received after heat treatment. Ni-base layer pin samples were cut in rectangular shape with 6 mm side length. For further tests, the heat treatment was optimized to achieve similar oxide layers as for the materials of the application. Fig. 3.4 shows images of the applied disc samples. Fig. 3.6 shows a side macro image of a rectangular pin sample as it was used for the first tests. The parameters used for the first damaging tests and sliding wear tests were derived from field application conditions and are listed in Table 3.3.
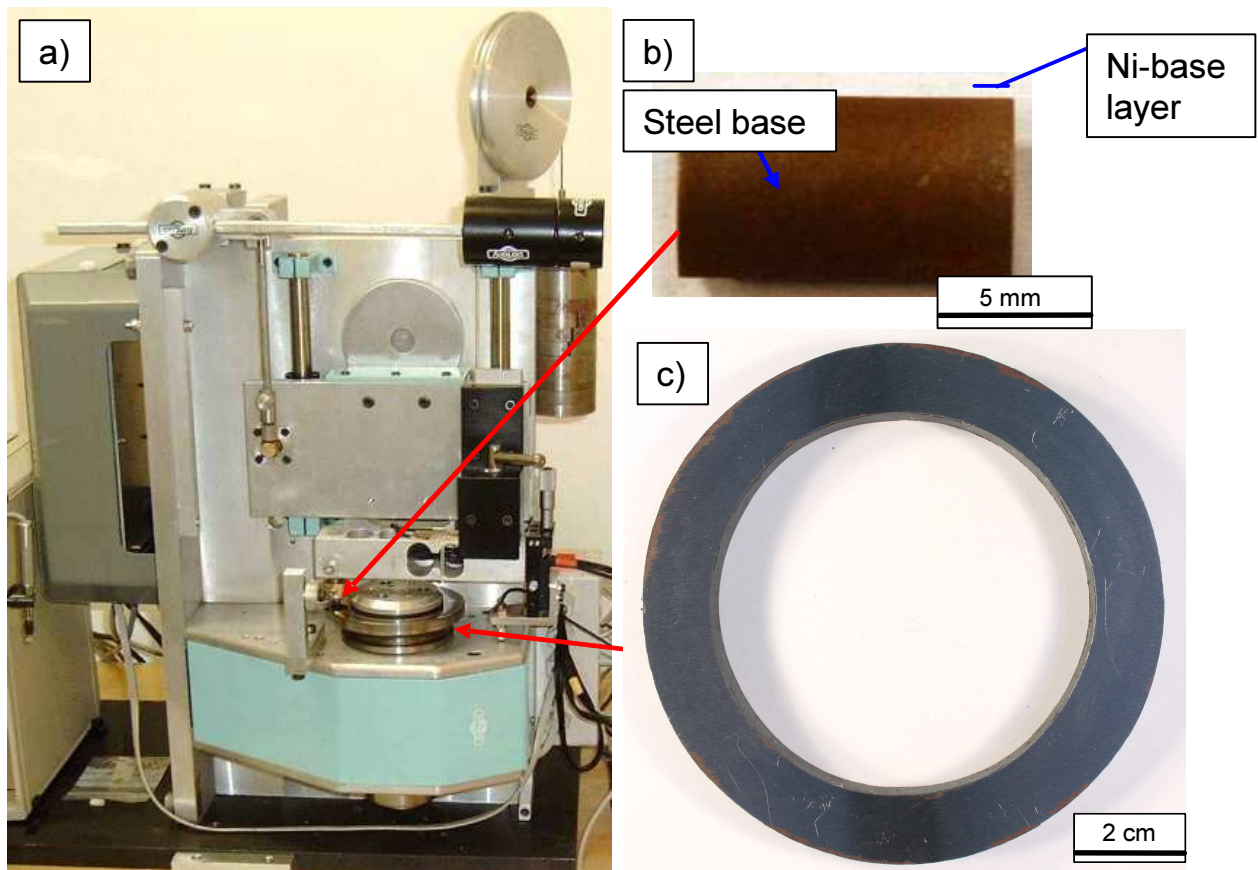
Fig. 3.3: a) Pin-on-disc tribometer together with applied samples,
b) pin sample from side view, c) steel disc sample [cf. 74]
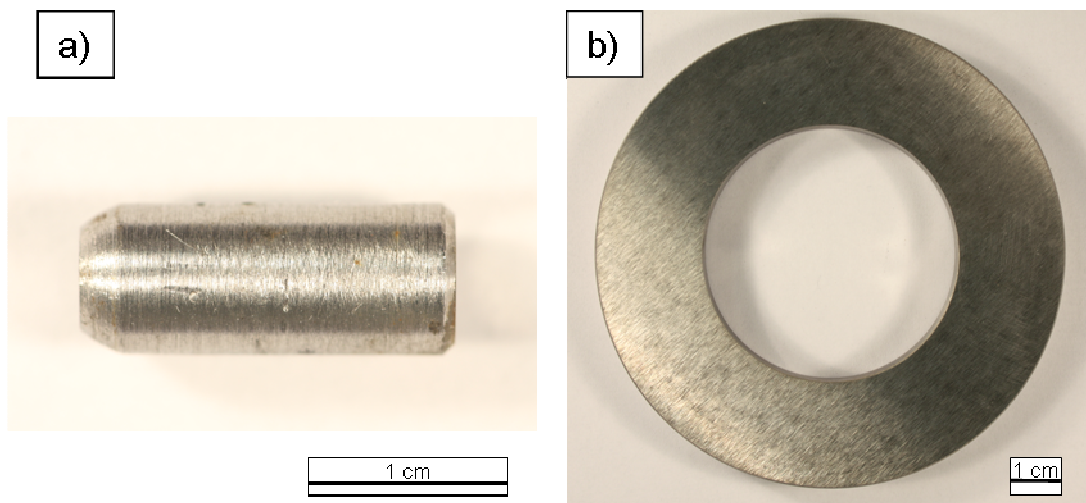
Fig. 3.4: Pin-on-disc samples for first tests: a) worn steel pin, b) unworn Ni-base coated disc
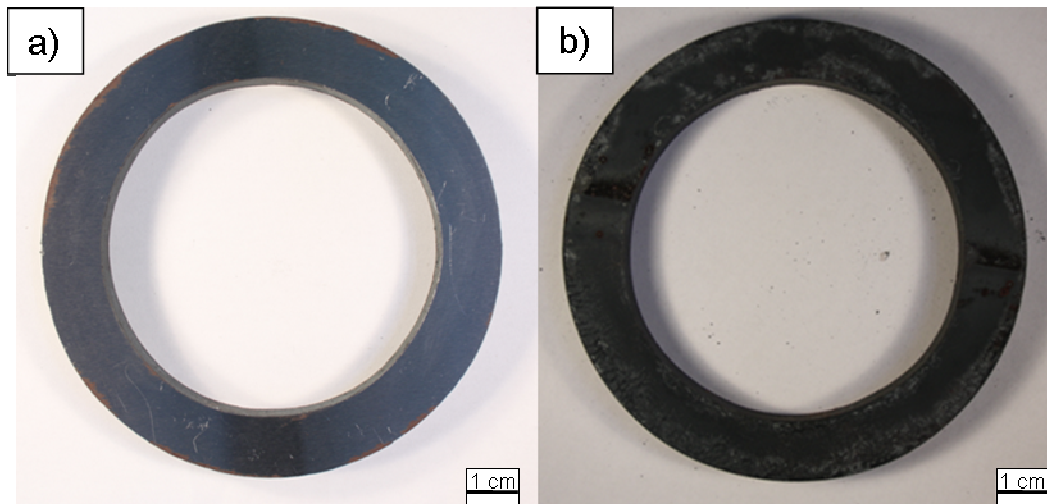
Fig. 3.5: Pictures of the disc samples. Left: without oxide layer; Right: with oxide layer [69]
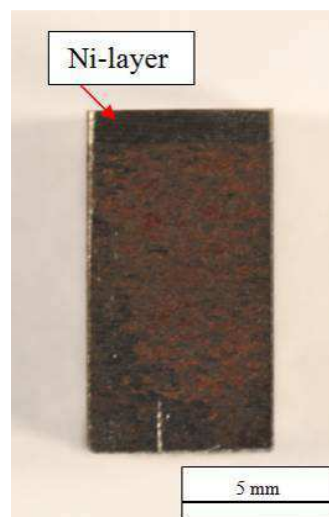
Fig. 3.6: Macro image of the rectangular Ni-base layer pin sample (side view) [69]

Table 3.3: Main parameters for sliding wear tests on pin-on-disc tribometer

Parameter	Initial tests	Sliding wear tests
Pin material	Steel of initial materials	Ni-base ("soft" and "hard")
Disc material	Ni-base spray coated layer	Steel grades of applicative samples
Disc diameter [mm]	110.0	114.3
Disc wall strength [mm]	25.0	15.6
Pin diameter [mm]	6	6
Pin length [mm]	17	12
Normal force [N]	11.5	21.6^{1}, (10 and)^{2} 70
Sliding speed [m/s]	0.6	0.6
Test duration [h]	2	2 – 24
Medium	tap water	tap water

[1] Adapted applied force for rectangular pin samples in order to apply the at first selected 0.6 N/mm^2
[2] Normal load of 10 N was used for tests of comparison of applied force in low cycle testing

Entire measurements during the test can be illustrated as tribotest curve showing the friction coefficient and the wear progress over time, an explanative image is introduced in Fig. 3.7. The orange line with violet curve fitting represents the friction coefficient over the testing period, which is typically constant and in between 0.1 and 0.5. The friction coefficient μ is a unit less value and is calculated by division of the resistance force, which acts against the movement, through the applied load. The blue curve shows the wear in μm over the testing period, measured as total wear loss, i.e. pin and disc wear. Ideally, it is a sloping linear function, where the wear rate can be calculated as slope of this curve. The illustration for the test plots (except for pre-tests) will be chosen with disc (basic body material) cycles (revolutions) instead of time in order to make conclusions for lifetime cycle tests. A two hour test is equivalent to 13,500 disc cycles. These values are displayed in cycles·1000, or cycles·10^3.
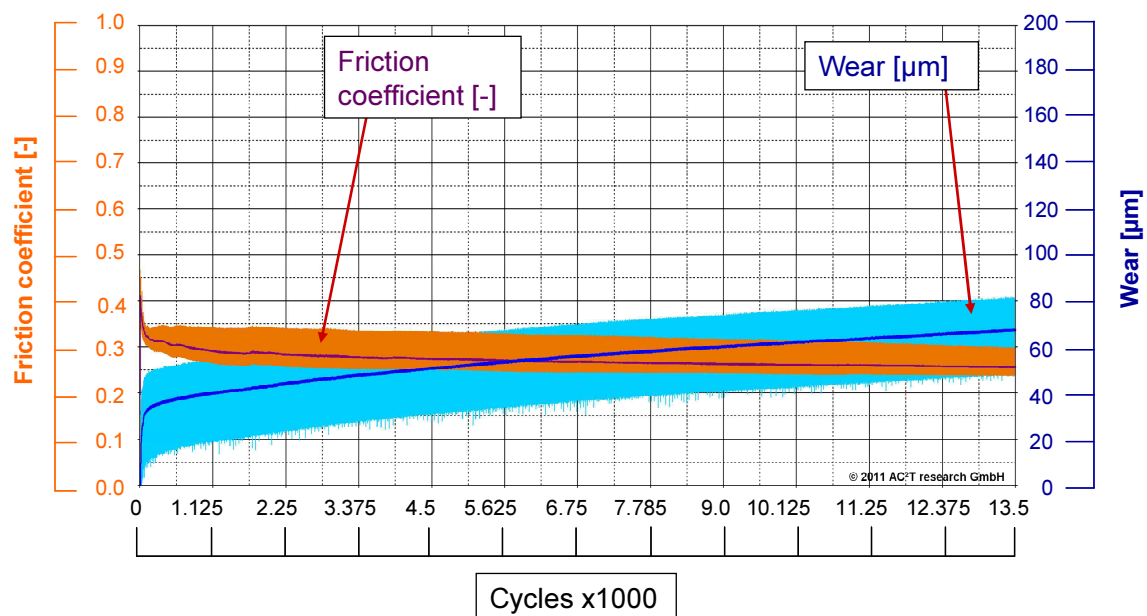
Fig. 3.7: Example of a tribotest curve as a result of the pin-on-disc sliding wear test [cf. 75]

Also, pin and disc wear were calculated separately. For pin wear, the mass loss of the pin sample after the experiment was measured. Through the density of the Ni-base layer (ca. 8.9 g/cm^3) and the mass loss, the wear volume was calculated. For the disc samples, the wear track was measured using the 3D confocal microscope (see chapter 3.4.3). Out of the obtained topography data, the wear volume was calculated (using MatLab® calculation software). LOM sectional cuts are performed to investigate the damage mechanisms alongside the wear track. The calculated values were set in relation to the processed cycles and are given in μm^3 per cycle·1000.

3.2.3. Static corrosion test

For these test, an apparatus consisting of a beaker, on oil heating bath, a cooler and hoses has been established. The setup is shown schematically in Fig. 3.8. The samples are placed on the bottom of the reactor unit (laboratory beaker). As medium, an aqueous solution, which contained NaCl from 0 to 3 wt% was filled inside the reactor and was purged constantly with CO_2 gas with a gas stream of 300 to 400 ml/min, in order to keep the solution free from oxygen, as CO_2 media in application are under nearly anaerobic conditions. The gas left the reactor through a cooler, also to prevent the aqueous solution to escape as vapor. The bath was tempered on 60°C. Corrosion time varied between 8 hours and five days. Before the test, the samples are weighted and the zones which should not be affected corrosively are covered with varnish. After the test, the samples were cleaned and weighted. The mass loss was taken as value of the corrosive attack. Out of the mass loss per sample and the area of the sample which was under corrosive attack, the corrosion rate was calculated for all samples according to equation 24. Also SEM analyses (see chapter 3.4.3) of the formed layers have been performed.

$$CorrosionRate\left[\frac{mm}{y}\right] = \frac{mass\_loss[g] \cdot 8760\left[\frac{h}{y}\right]}{surface[mm^2] \cdot exposure\_time[h] \cdot density\left[\frac{g}{mm^3}\right]} \tag{24}$$
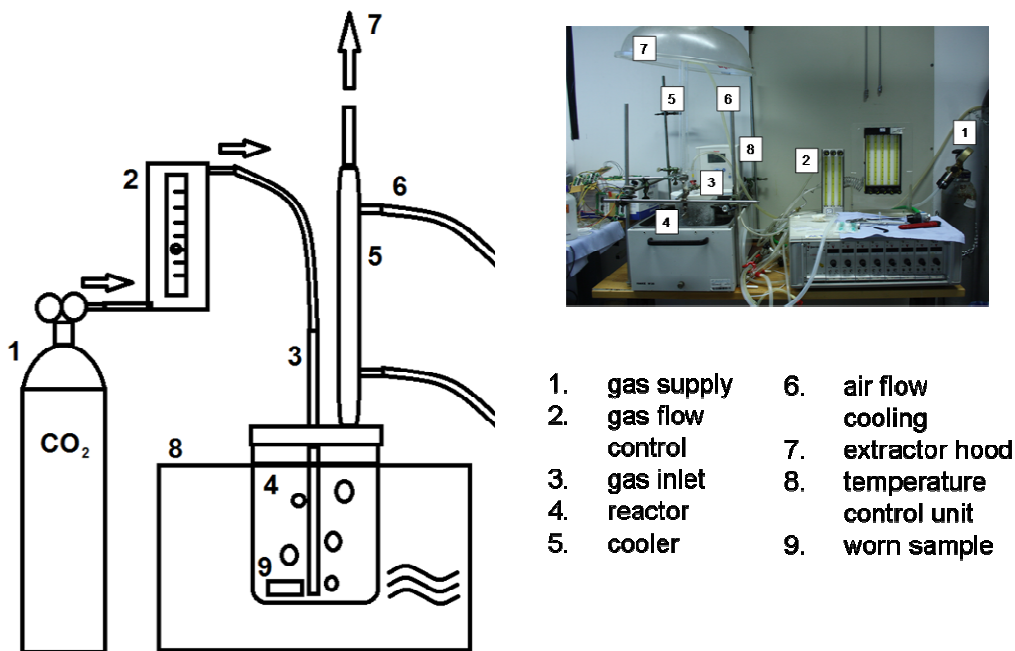
Fig. 3.8: Schematic image of corrosion setup together with a macro image and description of the main parts [cf. 74]

1. gas supply
2. gas flow control
3. gas inlet
4. reactor
5. cooler
6. air flow cooling
7. extractor hood
8. temperature control unit
9. worn sample

3.3. Sliding -corrosion test rig

3.3.1.   Description of Sliding-Corrosion-Test rig

The sliding-corrosion test rig (SCT) was built in order to simulate real field conditions for tribocorrosive applications in one test (Fig. 3.9). Therefore, the mode of actuation in some real applications, a moving part against a steel body, has to be simulated. The test chamber consists of a sample holding unit holding the steel samples of about 0.5 m length on the outer side, with the surface to be worn facing the center [76]. The counter body samples, which are coated with a similar Ni-base layer as used for the hard layer of the pin-on-disc tribotests, are placed on the inner side on a movable plunger, moving up and down against the steel samples (Fig. 3.10). The sample compartment is enclosed by a stainless steel tank. In this tank, the medium can be filled and purged with the CO_2 reaction gas. On top of the tank, sensors are placed in order to collect test data (e.g. temperature, O_2 content, inner pressure …). Furthermore, the friction force can be measured and then calculated to a friction coefficient. Wear measurement is performed by 3D topography measurements with additional calculations to obtain information, e.g. wear depth. Fig. 3.11 shows examples for the used samples in worn state. [cf. 70].

Fig. 3.9: Image of ready-to-use test facility [70]

Fig. 3.10: Scheme of test rig

Fig. 3.11: Image of worn basic body (upper image) and counter body (lower image) samples as they were equipped and tested in the abrasive-corrosive tribometer [cf. 70]

3.3.2.   Test operation on sliding corrosion test rig

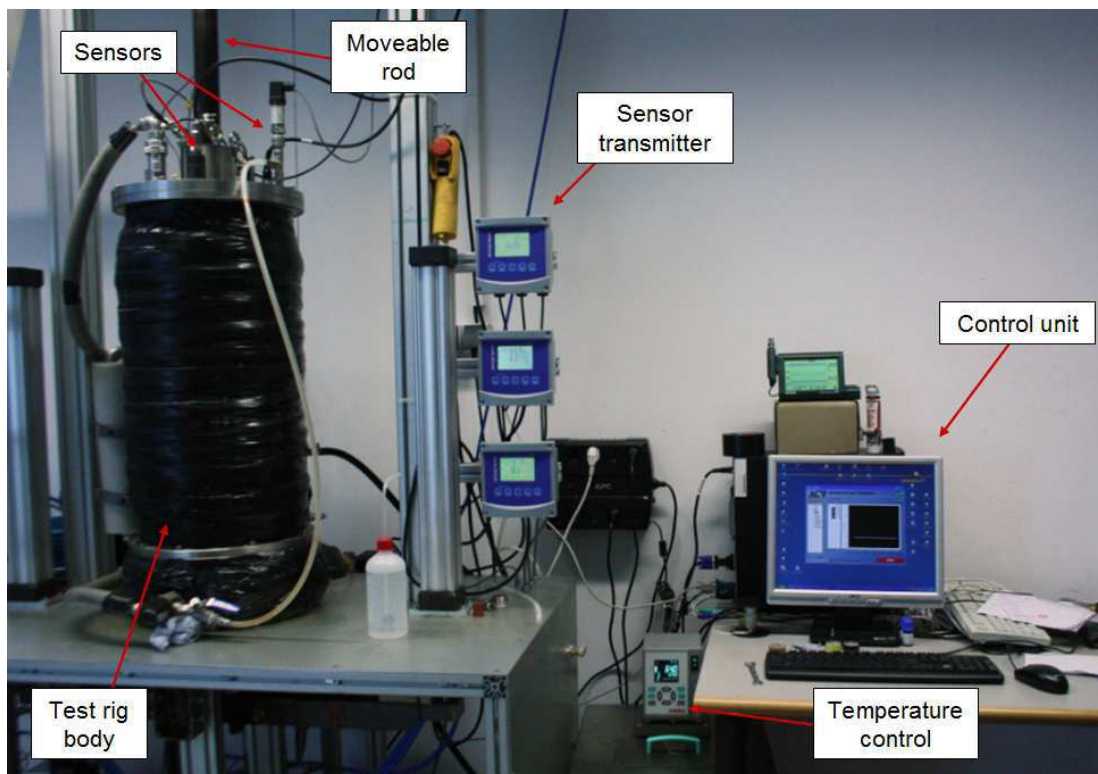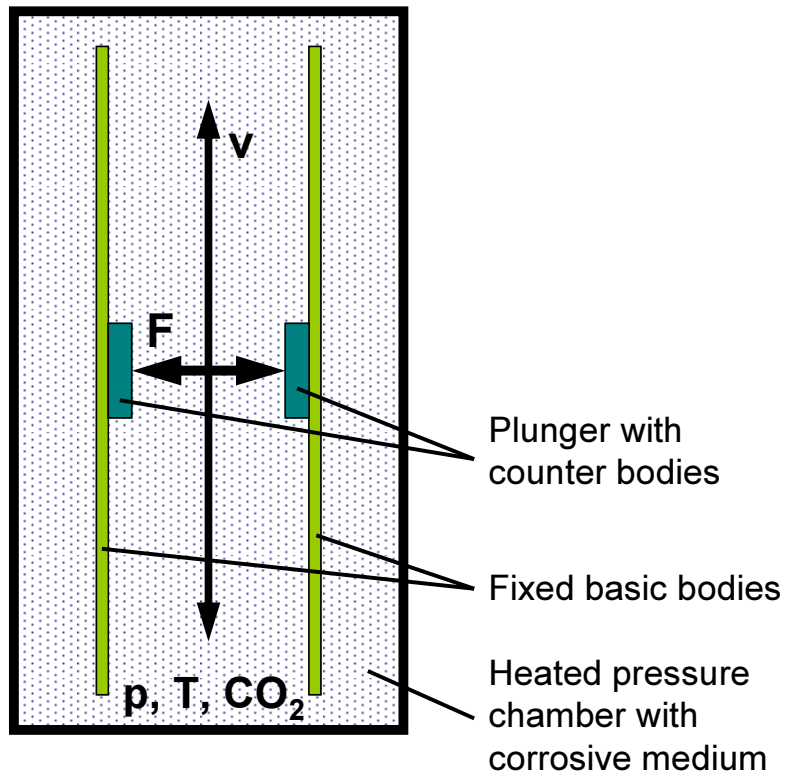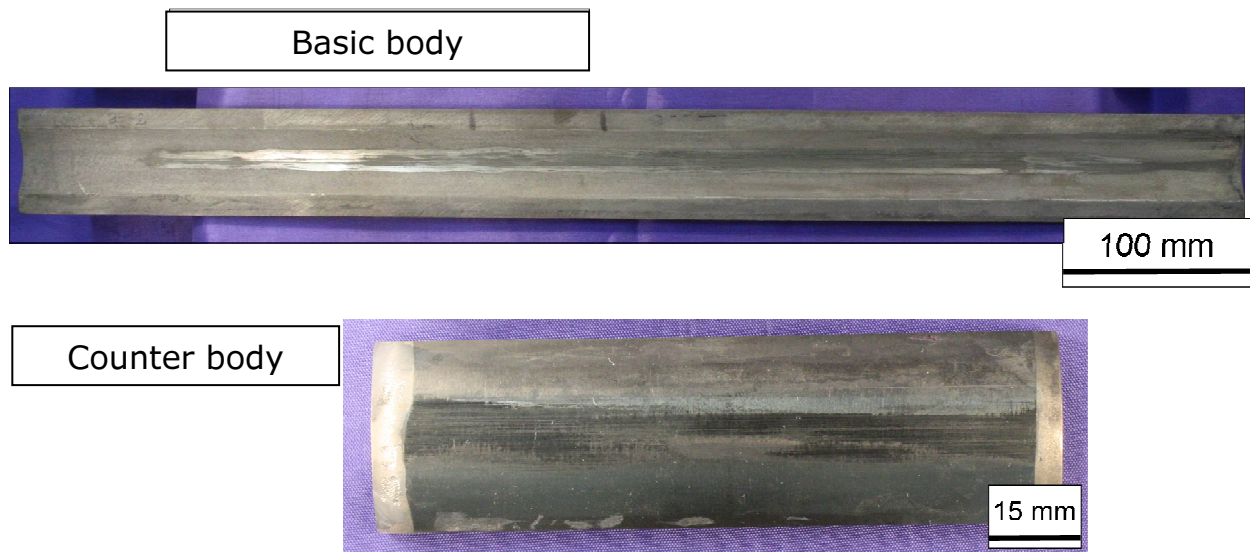The counter body samples are about 10 cm long, placed on the moveable plunger moving in up and down movement pressed against the basic body samples.

As test solution, saline medium was purged with CO_2 in order to – on one side – generate nearly oxygen free conditions, and on the other side to be added to the corrosive medium. The medium is heated to 60°C temperature. As comparison, tribological tests with distilled water purged with inert gas were performed in order to compare with the corrosively performed tests [70; 75].

The standard testing parameters chosen for the comparative tests of FP-H and M-S steel materials are given in Table 3.4:

Table 3.4: Main parameters for tribocorrosive testing [68; 74]

Parameter	Tribocorrosive testing
Basic body	FP-H and M-S steel
Counter body	Ni-base "hard" material
Testing time [h]	120
Testing cycles	56,000
CO_2 pressure [bar]	3
Medium	Sea water level saline medium

Before each test, the samples are placed in their correct place. The steel samples are placed in the outer chamber and the counter body samples in the inner sample holder. After that, the compartment is closed tightly. The medium is prepared and filled in. After that, the test rig and the measurement program are activated. [70; 75]

After the test, the medium is led out, the tank is opened and the samples are removed and cleaned for further analyses. The collected data are prepared by FlexPro® computational software to diagrams for each measured and/or desired parameter for further analysis.

3.3.3.   Sample preparation and test evaluation

For tribotest evaluation, a tribotest curve similar to one of pin-on-disc tribotesting is recorded. The recorded parameters are temperature, pressure, oxygen content and conductivity for process control, as well as friction coefficient together with pH value for evaluation of the process. A typical tribomeasurement plot is shown in Fig. 3.12. Unfortunately, it was not possible to equip a

reliable wear measurement system, so the wear loss has to be estimated after the test by optical 3D microscopy.

For the evaluation of the wear depth and width, the steel samples were measured using 3D microscopy. For this evaluation, sectional measurements were performed in the area of supposed maximal depth and width of a sample, which is the middle of the steel sample, as well as in sections close to the end of the wear track. With the software μSoft, the curved surface is flattened and then the wear depth and width of the single sectional measurements is evaluated as shown in Fig. 3.13. Out of the depth and width the average wear area of the profile can be calculated. Furthermore, by measuring profiles at different positions, knowing their distance, the wear volume can be estimated. With the gained information, conclusions on material loss per tribotest cycle and therefore on the triboperformance of the tested materials can be taken. From all samples, steel and counter bodies, macro and stereo images have been taken in order to evaluate and compare the wear images on the surface.

For the tests on the influence of hardness and microstructure, the oxide layer on the samples would only lead to insecurities on the bare metal tribobehavior. Therefore it had to be removed in a first step. In order to generate this equal metallic surface, the samples were pickled using a pickling solution out of 32 % HCl, distilled water and Dr. Vogels pickling additive. Prior to the tribotest, the whole surface of the sample is covered with anti-corrosion varnish, so that the whole sample is not affected by corrosion, only the wear track, which is formed after initial abrasion of the varnish. The counter bodies are only covered on the back with varnish, as there is the non-resistant steel matrix, whereas the Ni-base layer itself is corrosion resistant.
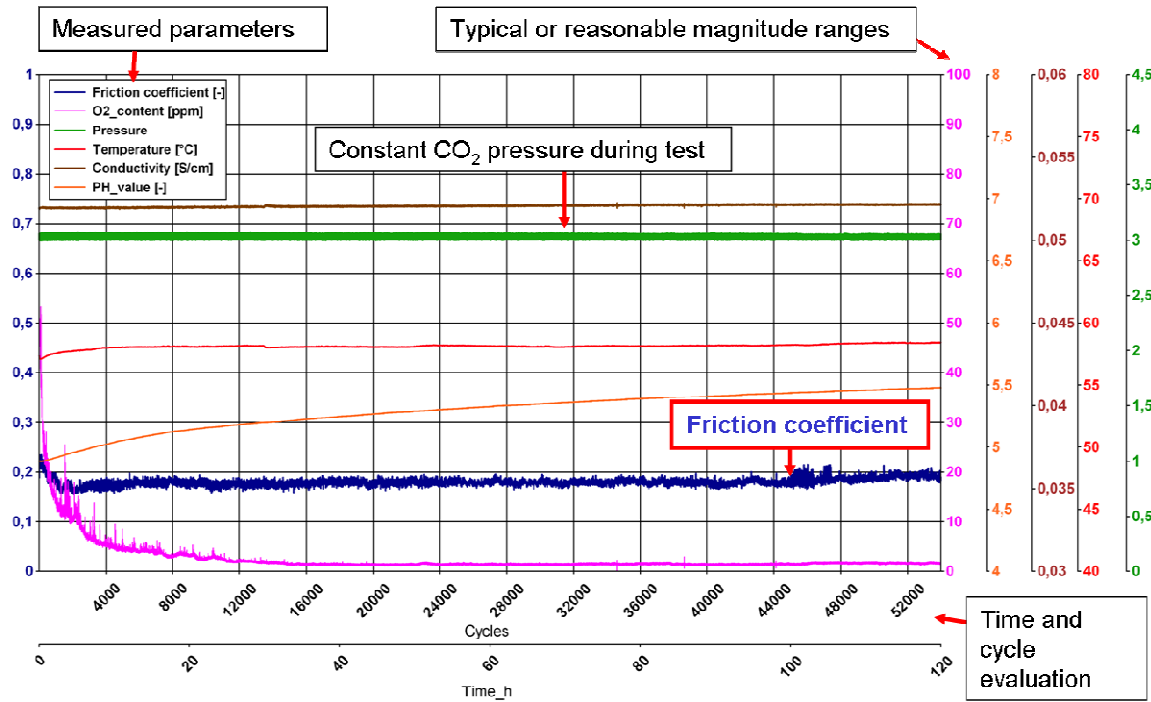
Fig. 3.12: Example for a tribotest curve collected for sliding corrosion tribotesting together with description of collected main parameters [cf. 70]
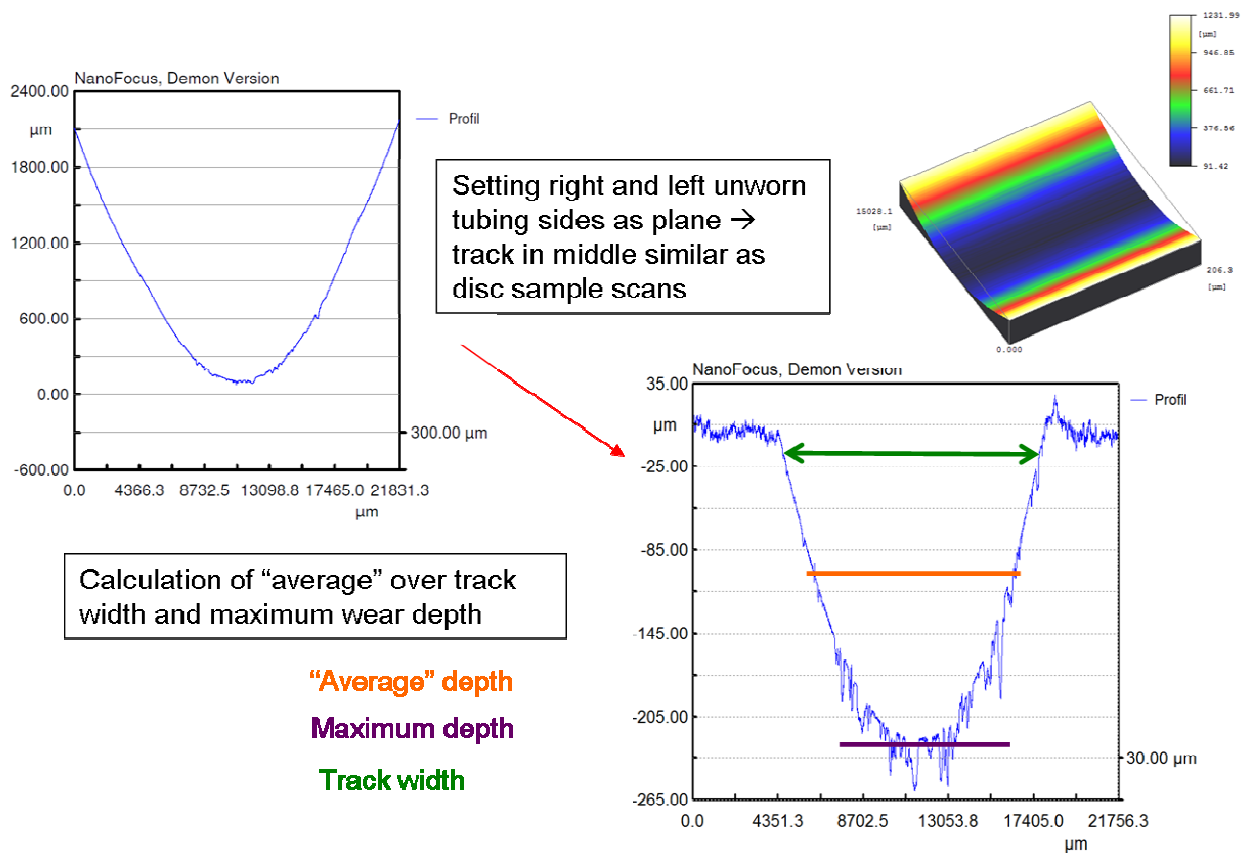

Fig. 3.13: Scheme of the evaluation of wear depth and width using 3D microscopy [cf. 70]

3.4. Instruments used for sample processing and analysis

For manufacturing the samples before the test and also after the test for further analyses, a variety of instruments has been used, which will be presented in this chapter. The methods presented here are these which were mainly used. Also, analytical methods XPS (X-ray photoelectron spectroscopy), XRD (X-ray diffraction analysis) and ICP-OES (inductively coupled plasma optical emission spectroscopy), as well as mechanical methods NI (nanoindentation) and scratch testing were used only for some single analyses and will also be presented in the following chapters.

3.4.1. Material preparation for test samples

In the steps of sample preparation, the materials were cut and grinded to the desired geometry. Also, heat treatment was applied.

3.4.2. Material preparation for metallographic investigations

For sample cutting, a cutting facility (from Struers®) was used. If needed for further analyses, the samples were embedded using an embedding machine (Struers®). Large samples were grinded with a surface grinding machine (Proth Industrial CO., LTD) in order to gain a plain and/or metallic surface free from oxides. For grinding and polishing smaller samples and/or embedded samples, as well as for the adjustment of desired roughness parameters, a grinding and polishing machine by Struers®. Heat treatment was performed in a furnace from Carbolite®. The heat treated samples were then tested with the oxide layer of heat treatment or processed with the described instruments in order to obtained plain and clean samples for further testing procedures.

3.4.3. Material analysis

For the weighting of the samples before and after the test, a scale for samples in the range of 0.5 to 1 kg, where weight changes of g were evaluated (e.g. large samples of test application) was used (Sartorius®) as well as for samples in the range of up to 210 g (Mettler Toledo®; ± 0.1 mg), where lower weighting ranges of mg are important (e.g. pin-on-disc samples, corrosion samples). For the analysis of the material hardness, a hardness tester from Future-Tech was used. Most analyses were performed optically. For the investigation of macroscopic structural phenomena on the surface, a stereo microscope was used (Olympus®). Microstructural investigations were performed using a light microscope (Leica®).

3D topographical profiles were taken using the µSurf confocal microscope (NanoFocus[®], Fig. 3.14). For the investigation of the material structure in microscale and also for elemental analyses of microstructural parts of the samples, scanning electron microscopy together with energy dispersive X-ray analysis (SEM-EDX by Philips) was used. X-ray diffraction analysis XRD (Philips) was used to identify the crystal structures on the field sample. As surface analysis method, X-ray photoelectron spectroscopy (XPS) (Thermo Scientific; Fig. 3.15) was also applied to identify elements and possible molecular structures on the formed layer of the field sample.

As the material hardness is a crucial factor for tests with differently heat treated steel materials and also for the Ni-base counter body, hardness tests were performed using the Vickers method, which is defined in the standard ASTM E384 – 11e1.

The Nanoindenter (NI, Hysitron[®], Fig. 3.16) works under the same principle as the macro hardness tester, although the applied forces are significantly smaller. With this method it is not only possible to indent on specific small phases (e.g. precipitations and material matrix separated) or to perform a hardness profile over work hardened surfaces towards the principal material, it is also possible to evaluate the Young's modulus and viscoelastic properties of a material.

For the evaluation of the mechanical properties of the formed oxide layer under constant and varied load, the Scratch tester (TRIBOtechnic[®]) was applied. This apparatus consists of an indenter, which is pressed against the load and moved across the layer. The principle is illustrated in Fig. 3.17. Acoustic emission of scratching and breaking noises can also be measured and evaluated (was not evaluated within the performed experiments).

The 3D confocal microscope can not only be used for detailed roughness calculations evaluated by the µSoft software, also is the topography of samples (e.g. wear track of pin-on-disc steel samples) important. The confocal microscope is imaging the topography of a sample height layer by height layer and is adding the information of each height step to one 3D image of the sample. With this image, it is not only possible to view the 3D appearance of a sample in microscopical scale. Also, the calculation of the wear volume can be processed by this data.
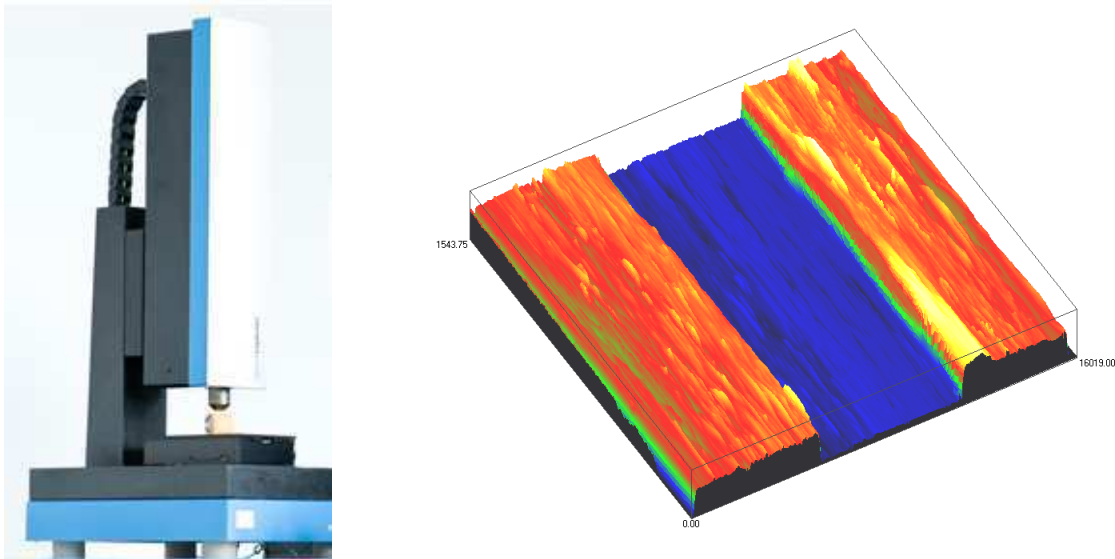
Fig. 3.14: Confocal microscope for topographical image measurements (NanoFocus®) together with an example for a topographical image (example of a wear track of pin-on-disc tribotesting) [cf. 74]

Fig. 3.15: X-ray photoelectron spectroscopy (XPS) instrument (ThermoScientific®)

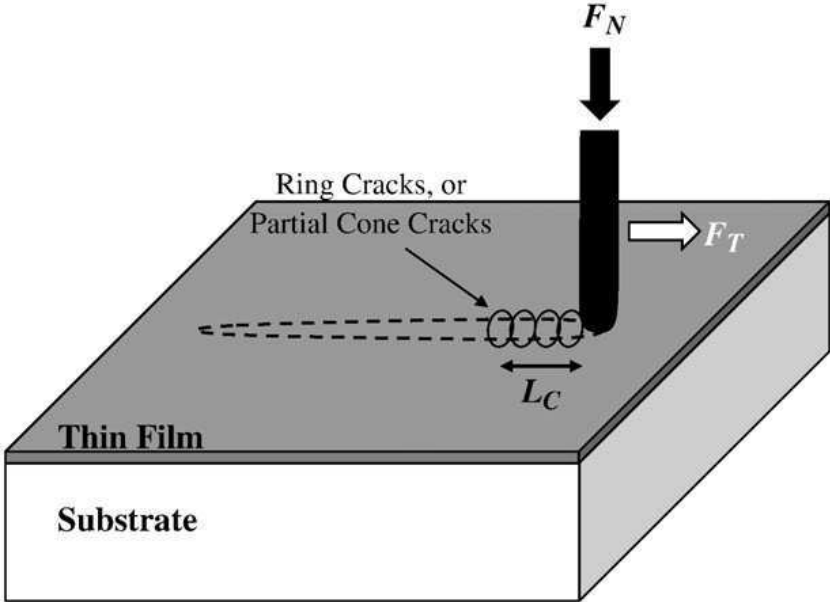Fig. 3.16: Nanoindentation NI instrument (Hysitron®)

Fig. 3.17: Principle of scratch testing [71]

3.4.4.   Roughness calculation

Out of the data obtained for the measurements with the 3D confocal microscope, roughness parameters of the samples can be calculated. On one side, the arithmetical mean roughness R_a was chosen as comparative roughness value. By the calculation of the ten-point mean roughness R_z and the smoothness depth R_p, the shape of the roughness tip can be calculated. These values were obtained by the surface imaging program itself, the calculation of the roughness parameters are as described in the following equations. In general, the roughness parameters were evaluated across the wear track at several positions.

The arithmetical mean roughness R_a represents the arithmetical mean value of the absolute values of the roughness profile over the total length lm [72].

$$R_a = \frac{1}{lm} \cdot \int_0^{lm} |y| dx \qquad\qquad\qquad (25)$$

The ten-point mean roughness R_z is calculated as the mean value of the single roughness depths of five sequential single measurement lengths.

$$R_Z = \frac{1}{5} \cdot \left(Z_1 + Z_2 + Z_3 + Z_4 + Z_5 \right) \qquad\qquad\qquad (26)$$

The smoothness depth R_p is the highest profile tip above the mean value line [72].

Fig. 3.18 shows the graphical description of the calculation of the roughness values. Out of these R_p and R_z values, the R_p/R_z ratio is calculated, which gives conclusion about the surface image of the roughness tips as shown in Fig. 3.19. Low R_p/R_z ratios mean that the roughness tips are mainly present as round hill with deep slits. Medium R_p/R_z ratios represent a triangular image of the roughness tips. High R_p/R_z ratios indicate the predominance of very sharp roughness tips.
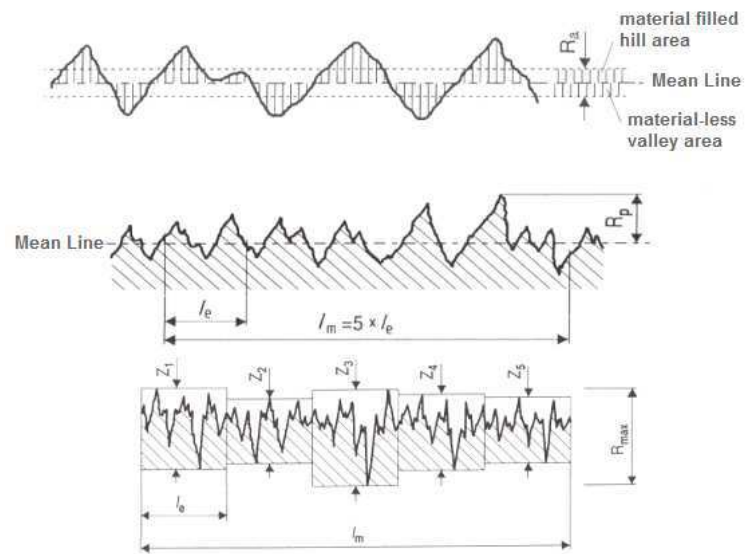
Fig. 3.18: Graphical description of the roughness values R_a, R_p and R_z [72]
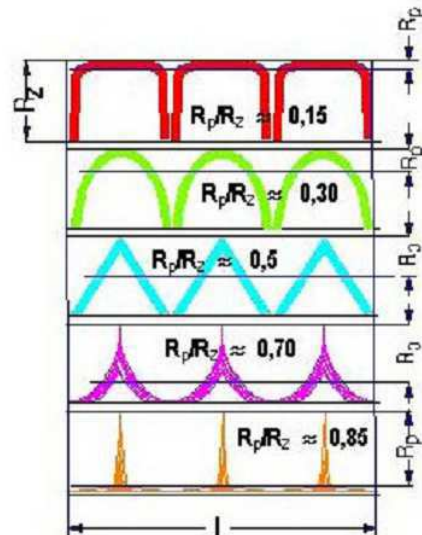
Fig. 3.19: Graphical description of the calculated R_p/R_z ratio and the corresponding surface geometry [cf. 73]

4. Results

As first step, analyses on field samples were performed to gain information about the damage images occurring for steel samples in CO_2 corrosion under tribological influence. Sliding wear tests and corrosion tests were performed in order to obtain wear mechanisms analog to the ones found for field samples. Secondly, several steel and Ni-base materials were tested in sliding wear contact for their performance under tribological and corrosive stress. Samples tested in sliding wear contact were compared to unworn samples in corrosion tests for same conditions. Results show that there is a major influence of the wear history on the corrosion performance of a steel sample and good accordance of lab tests in comparison to results obtained for field samples.

4.1. Analysis of worn and corroded materials of application

For this analysis, two steel samples which were worn and corroded within field application were obtained. On these samples, analyses were performed in order to gain information about the damaging mechanisms occurring in field applications. With that information, it was possible to establish measurement methods and schemes in order to reproduce the damage mechanisms found on the damage samples. [cf. 74]

4.1.1. Optical investigations (macroscopic, microscopic) and nanoindentation

At first, macroscopic and microscopic images were taken from the samples. Fig. 4.1 shows an overview image for both obtained samples. Fig. 4.2 shows a cut through sample 1.
From both samples, cuts have been made in order to investigate the state of the inside of the tube.

Fig. 4.1: Macroscopical images as an overview for a damaged sample [cf. 74]

Fig. 4.2: Cut through the sample [cf. 74]

The abraded surface is cleaner than the side with less abrasion. The abrasively attacked area does not show layer formation. Also cleavages occur on the abraded surface. On some areas, parts of the tube material were separated from the base material, leaving a free area of fresh steel surface, where on the other side, a layer had formed. This layer is visible as a dark rough layer, which also may contain residual liquids on its surface.

For microscopical investigations, cuts have been made for the sample 1. These cuts were taken longitudinal and sectional at highly abraded and less abraded zones of the tubing. LOM investigations of the change of the ferritic/pearlitic microstructure due to mechanical and corrosive effects have been performed. Fig. 4.3 shows LOM images of cuts for an area of high, moderate and no abrasion by the counter body.
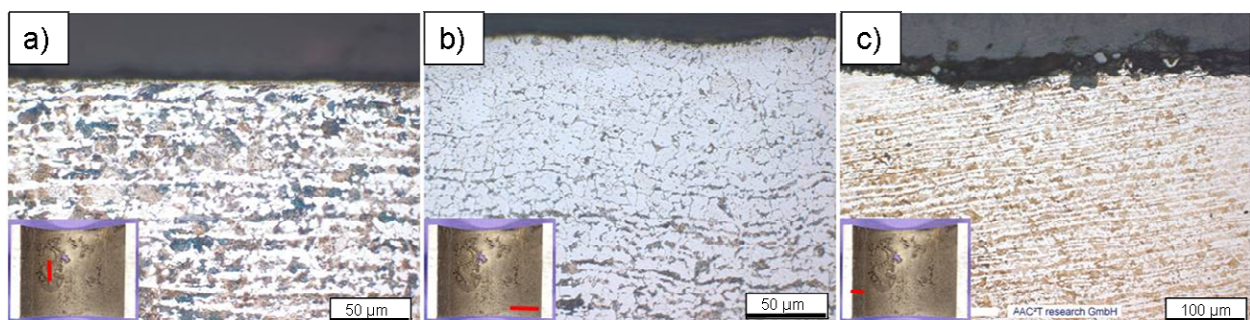

Fig. 4.3: Microstructure of tube and position of sectional cuts:

a) Longitudinal cut through area of high abrasion

b) cross-sectional cut through area of moderate abrasion and c) area of no abrasion

Fig. 4.3 a) shows a longitudinal cut in the area of high abrasion. The grains near the surface contact show deformation corresponding to the moving direction of the counter body. Fig. 4.3 b) shows a cross-sectional cut in the area of moderate abrasion. There is no layer formation visible on the surface. Fig. 4.3 c) shows a cross-sectional cut in the area of no abrasion, where a formation of a corrosion layer is visible.

In order to obtain more detailed information from the surface conditions, scanning electron microscopy (SEM) images have been performed on cut and 2-propanol washed pieces from both sample 1 and 2. Fig. 4.4 shows the pictures collected from different areas of the tube samples, going from the top of the crack into the area of less abrasion, where the protective siderite layer was allowed to be formed. EDX analysis has been performed on the sample surface. Particles found in the corrosion layer contain lots of Al and O and therefore may consist of Al_2O_3. The particles on the steel matrix contain Fe, O, Cl and most likely consist of the respective corrosion products, e.g. siderite $FeCO_3$. The layer shown in cross section in Fig. 4.4 a) is very brittle and contains in addition to the corrosion products some oil residues and sand particles from the oil production process. The layer thickness is about 100-350 μm. Fig. 4.4 b) shows the layer surface which is porous with flake structure. Fig. 4.4 c) shows abrasive wear marks and fatigue wear. Also cleavage tracks are clearly visible. Fig. 4.4 d) is taken from a sample directly cut from the tribologically stressed zone next to the crack. Cleavages as seen for Fig. 4.4 c) are clearly visible.

Also nanoindentation (NI) experiments were performed in order to investigate a change of the hardness from the stressed surface to the matrix. It was found that the hardness changes significantly from surface to core. Fig. 4.5 shows a summarizing image of the nanoindentation tests, where a line of nanoindentations was performed from close to the material surface inwards the material on a cross section of a sample part which experienced high wear influence.

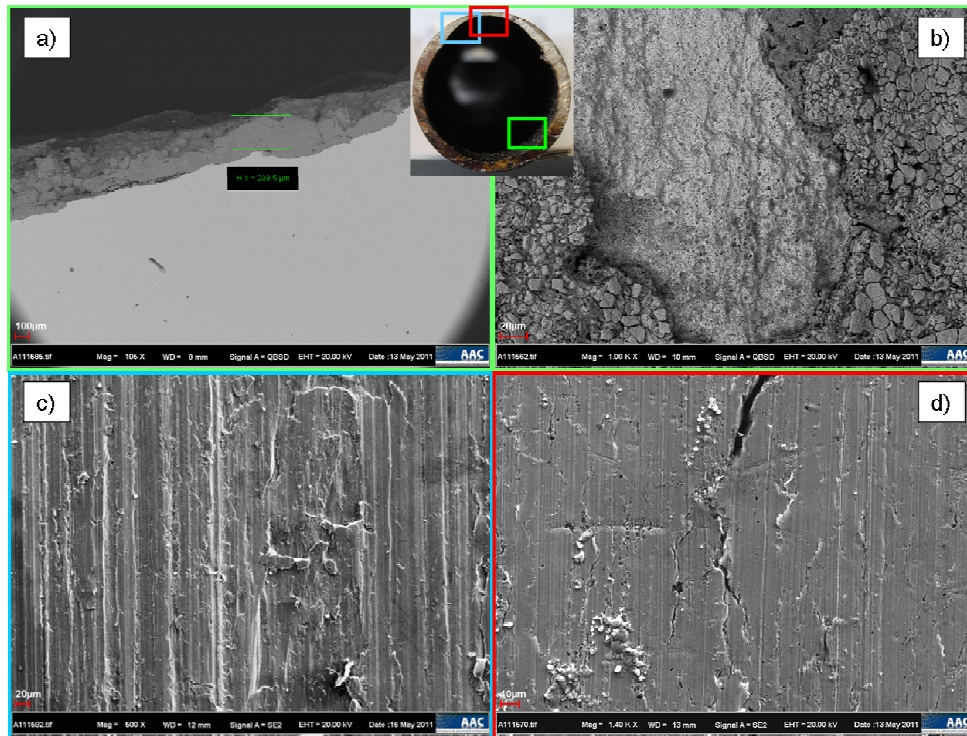Fig. 4.4: SEM images of sample 1. A) Measuring the thickness of the siderite layer (240 μm) on cross section; B) Image of the formed layer; C) Area of moderate and D) high abrasion [cf. 74]
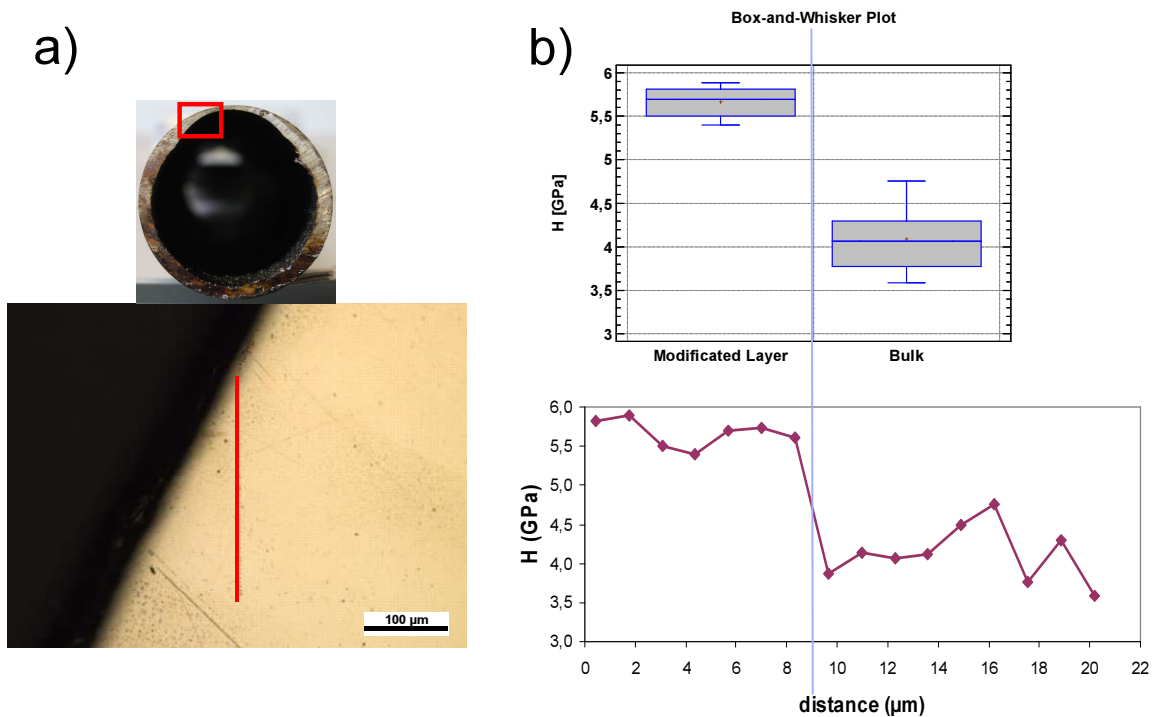

Fig. 4.5: Nanoindentation (NI) through a) longitudinal cut of the tribocorrosive stressed area (position on macro image; line scan on LOM cut – red line), b) graphs showing higher hardness for zone close to tribodamage

4.1.2.   Spectroscopical investigations

As high sophisticated method for surface analysis, X-ray photoelectron spectroscopy (XPS) was performed on the surface of the samples which were also used for the SEM measurements. Using XPS, not only the elements on the surface can be measured, also the state (oxide, carbonate etc.) can be determined. The measurements were performed measuring spots from the zone with high abrasion (crack zone) to the zone of no abrasion (siderite layer formation). Prior to the tests, the samples were cleaned with acetone to clear the samples from oil residues in order to expose the abraded surface and the formed layer on the sample surface. Inside the XPS chamber, the samples were sputtered with argon for ten seconds in order to clean it from adhesive gas molecules from the air. The measuring scheme of the XPS measurements is: zone close to crack; corroded zone close to crack; zone of moderate corrosive attack ("blank zone"); zone of increased precipitation; intensively corroded zone. As the surfaces are not the same for both samples, the obtained results are varying. With the order of measurements shown in the figure, a quasi-profile over the tube section was collected. Table 4.1 shows the results for the elemental analyses and Table 4.2 shows the state results for the determined elements as mean value over al five measurement zones.

High appearances of carbon in non-carbide or non-carbonate state are an indication for residual cracked hydrocarbons which is integrated into the surface structure. Iron is present in carbonatic and also in oxidic form, but the iron oxide also may be formed at the dismounting process and sample transportation. Sulfur and chlorine are present in lower concentrations. Corrosion due to these species is not necessarily excluded. Fig. 4.6 shows the elemental distribution from crack zone to corrosion zone for the elements carbon and iron.

The content of carbon experiences an increase from the crack towards the zone with less abrasion; iron shows an inverse behavior. Also the amounts of carbon are very high compared to them of iron. Fig. 4.7 shows the state distribution from crack zone to precipitation zone for the oxidic iron and the iron carbonate.

The oxide state decreases from the crack to the corrosion area. The distribution of the carbonate state is rather randomly. For the sample 1, a decrease of carbonate is detectable.

Table 4.1: Results of the XPS element measurements

Element	Fraction in mol%
Carbon C	69.40
Oxygen O	16.30
Iron Fe	6.05
Sulfur S	1.40
Nitrogen N	1.00
Potassium Ca	1.40
Sodium Na	0.70
Chlorine Cl	0.35
Phosphor P	0.50
Zinc Zn	0.05
Fluorine F	1.30

Table 4.2: Results of the XPS state measurements

Element	Appearance	Fraction in mol%
C	carbide	2.5
	C-C	38.0
	C=C	21.0
	C-O	4.2
	C=O	2.0
	CO_3	1.7
O	metal oxide	5.5
	O-C	10.0
	H_2O	0.8
Fe	metallic	0.9
	carbide	0.2
	oxide	4.0
	CO_3	1.0
S	sulfide	1.0
	organical	0.3
	sulfate	0.2
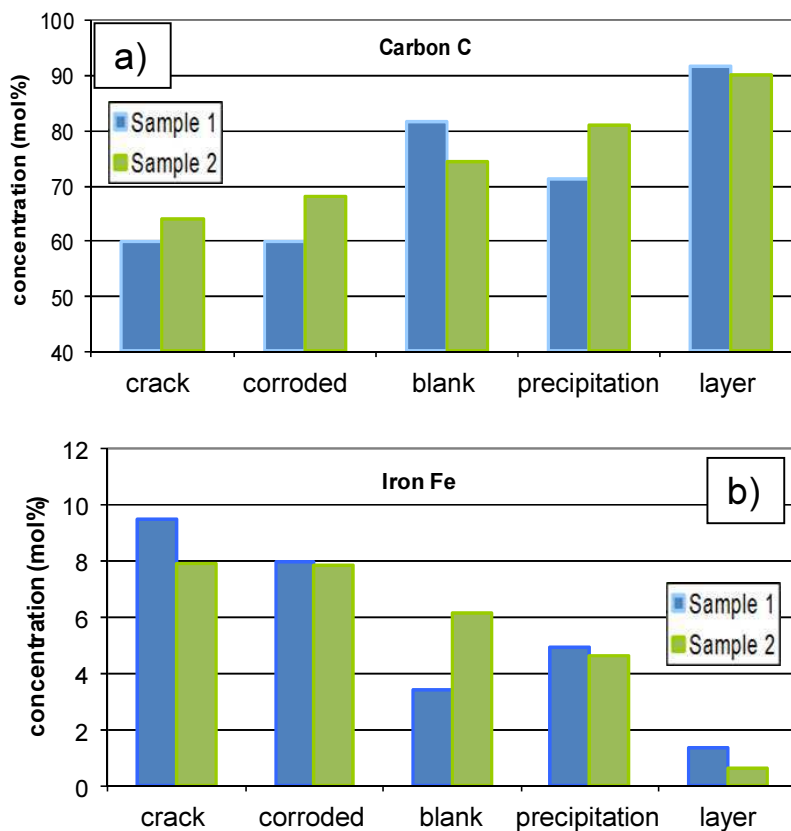
Fig. 4.6: XPS element profile results for carbon (a) and iron (b)
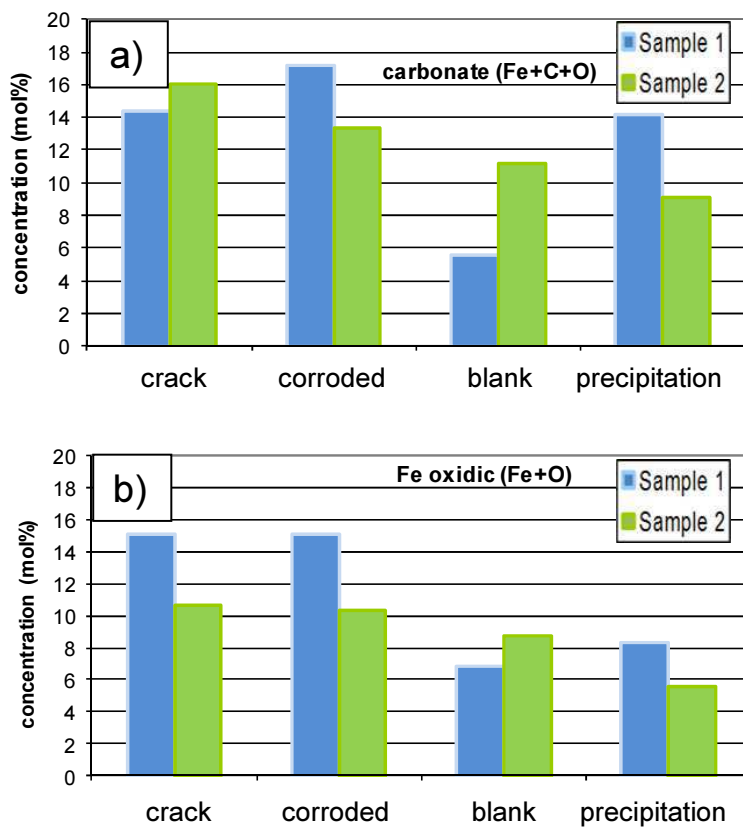
Fig. 4.7: XPS state profile results for iron carbonate (a) and oxidic iron (b)

For the investigation of the composition of the layer, XRD have been performed on both tubing samples (Fig. 4.8). Those measurements resulted that there is siderite within the corrosion layer, although it is not the only phase. Depending on the predominant conditions, other phases also develop, which are magnetite (Fe_3O_4) and wustite (FeO) for sample 1 and goethite (FeOOH) as for sample 2 (Fig. 4.8). Also the amount of the phases is different from location to location. The Fe detected might result from the base material; also as the crystallite size is calculated to be significantly higher. The siderite phase was calculated to be fine grained; the other phases are of medium size compared to the others. Fig. 4.9 shows the tables of the species amount calculated from the XRD measurements.

Table 4.3: Name and crystal structure for the found species

Species found in samples	Crystal structure
Siderite $FeCO_3$	Rhomboedral
Iron Fe	Cubic
Goethite FeOOH	Orthorhombic
Magnetite Fe_3O_4	Cubic
Wustite FeO	Cubic

Fig. 4.8: XRD measurements for sample 1 and 2 and the found phases
in the colors as seen in the diagram (performed at CEST)

Fig. 4.9: Amount for the found species calculated from XRD measurement data for

a) sample 1 and b) sample 2

4.2. Heat treatment procedure on samples

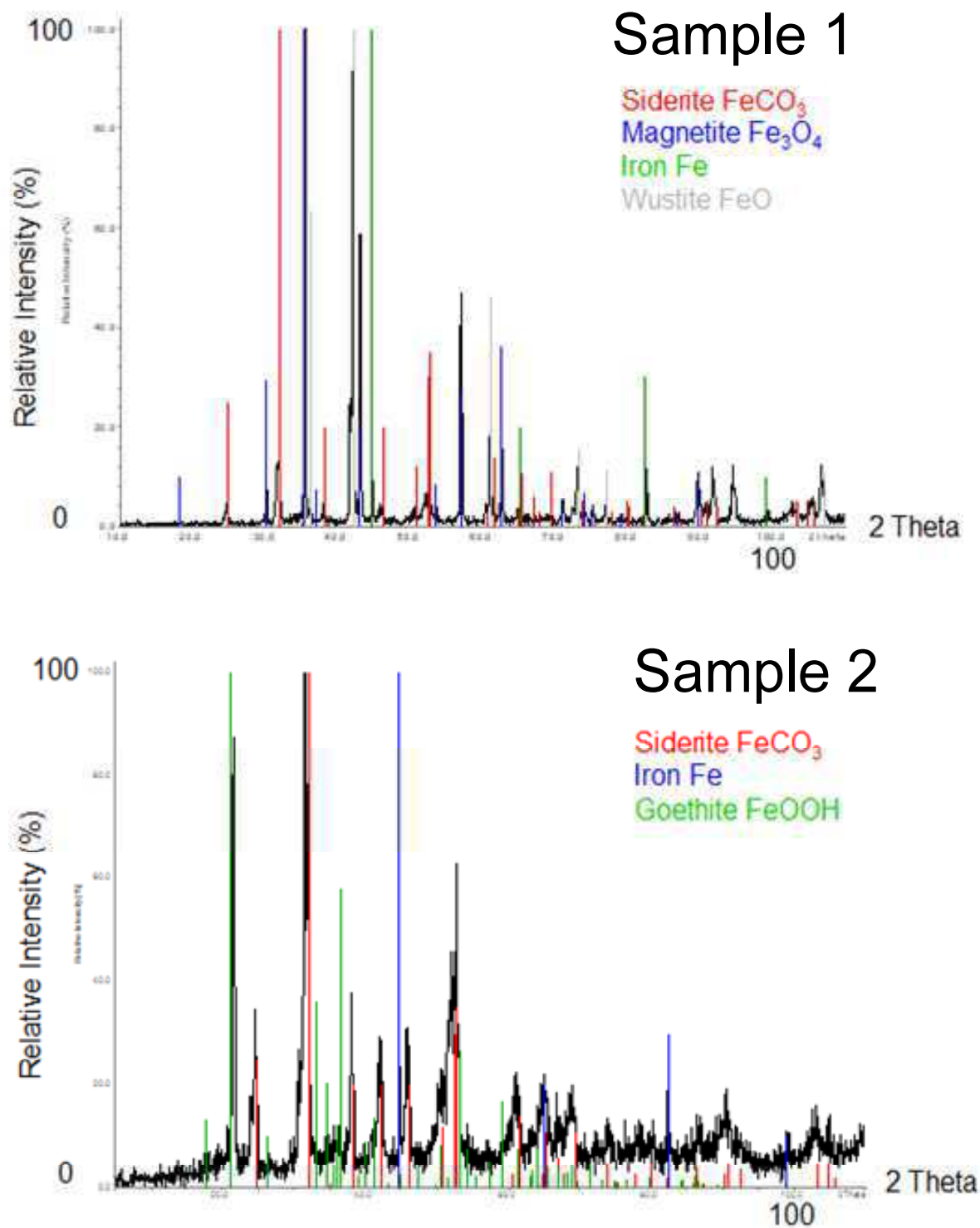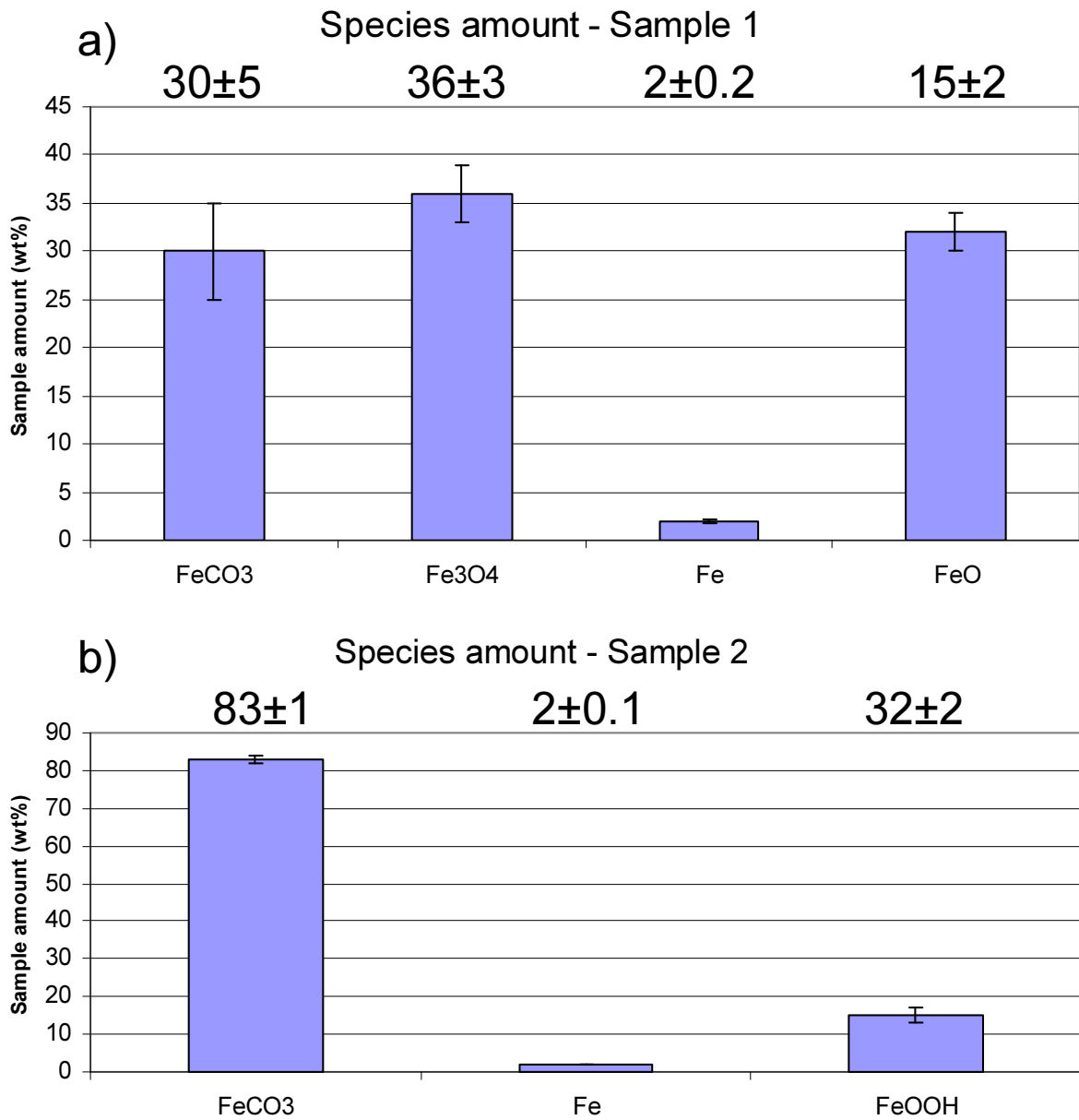Carbon steel with the chemistry as described in Table 3.1 was heat treated to generate different microstructures and hardness parameters. The main processes of the heat treatment are normalizing and quenching and tempering (Q&T). Quenching and tempering consists of a hardening step, where the steel base material is heated to the austenite area and then cooled rapidly (quenching in water bath). This leads to a distorted tetrahedral microstructure, the martensite structure. Then the samples were tempered. This step is performed in order to relax the tensed up martensitic microstructure and gain more ductility. The V1 samples were tempered at 650°C and the V2 samples were tempered at 450°C. Fig. 4.10shows the microstructure of the materials collected with light optical microscopy (LOM) after the different heat treatment procedures after etching with Nital (3 % HNO_3 in Ethanol).

The resulting hardness values after the heat treatments are given in **Fehler! Verweisquelle konnte nicht gefunden werden.**. Out of the same material as for the first heat treatment, the four steel grades, as described in chapter xx, were manufactured. An image showing the microstructure is illustrated in Fig. 4.11.

The counter body samples have been manufactured by plasma transferred arc welding. Fig. 4.12 shows the LOM images of the counter body materials together with their material hardness after etching with a solution of distilled water, ethanol 98 %, hydrochloric acid 32 % and $Cu(II)SO_4$ (5:5:5:1). The harder material shows carbide precipitations within its microstructure, which are not visible within the soft material. The layer thickness was chosen to be ~ 1 mm, as this is usual for field application counter body materials.

In order to manufacture an oxide layer similar to real sample conditions, an adapted heat treatment had to be established in order to generate oxide layers with similar thickness and appearance as found on the basic body material used in the field. While heat treatment at air entails high thickness of ~ 88 μm oxide layer, compared to 24 μm on comparable heat treated materials for field application, a fully inert atmosphere leads to low thickness values of ~ 5 μm. With mixed inert and air heat treatment, it was possible to obtain oxide layer thickness values comparable to the field material. This procedure was found for a mixture of inertal and air heat treatment as 42 min heat treatment under argon flushing, followed by air heat treatment through shutting the argon supply for another 18 min (Fig. 4.13).
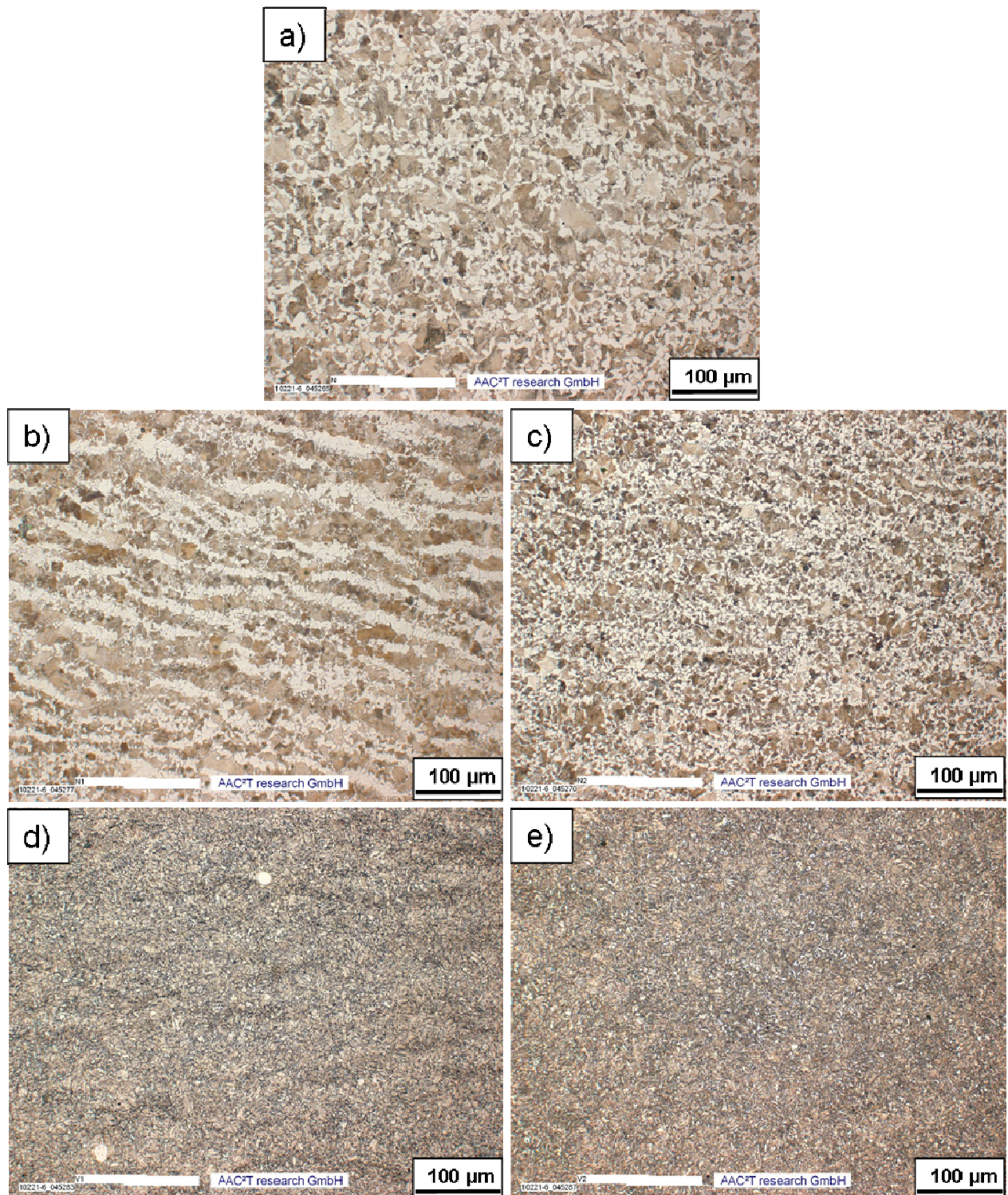
Fig. 4.10: LOM images of the microstructure of the heat treated samples:
a) steel base material N b) normalized furnace cooled N1 c) normalized air cooled N2
d) quenched and tempered V1 e) quenched and tempered V2
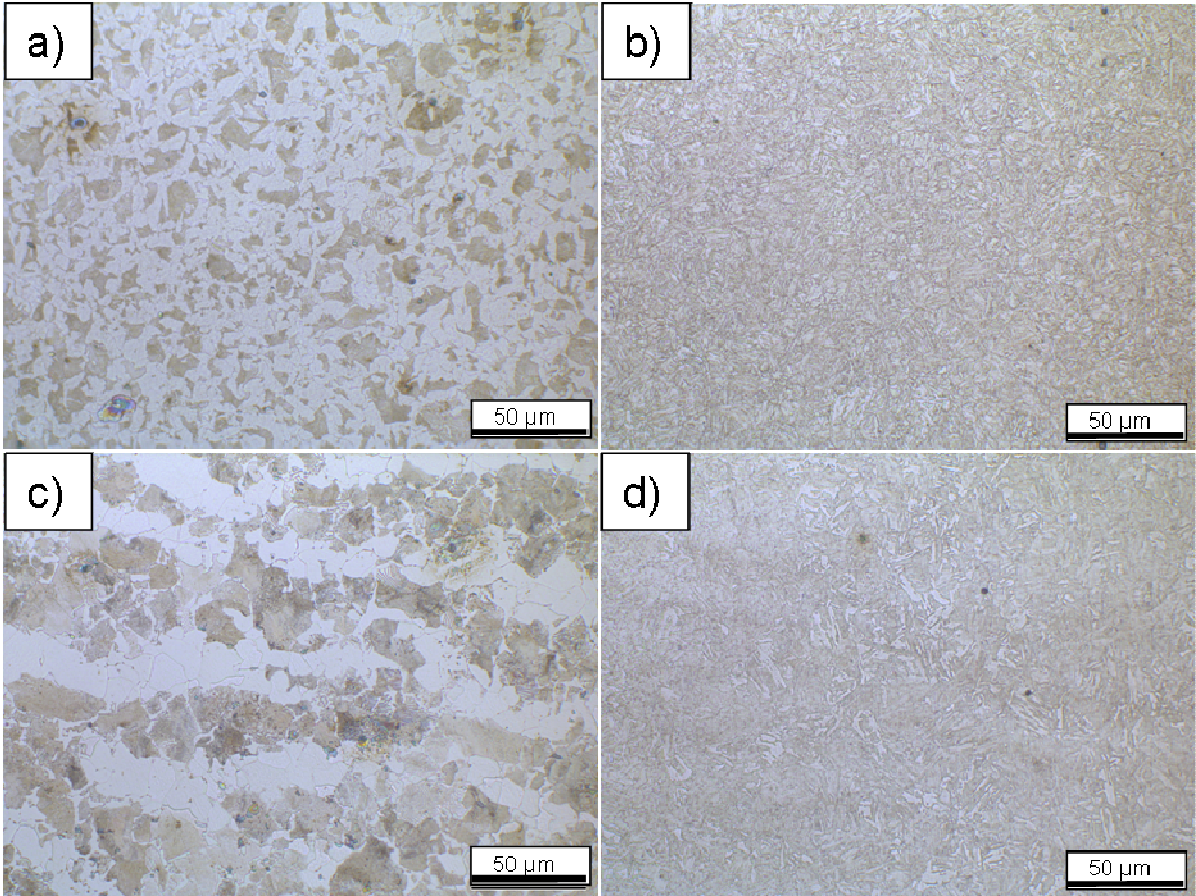
Fig. 4.11: LOM images of the microstructure of the basic body materials:
a) FP-H, b) M-H, c) FP-S, d) M-S
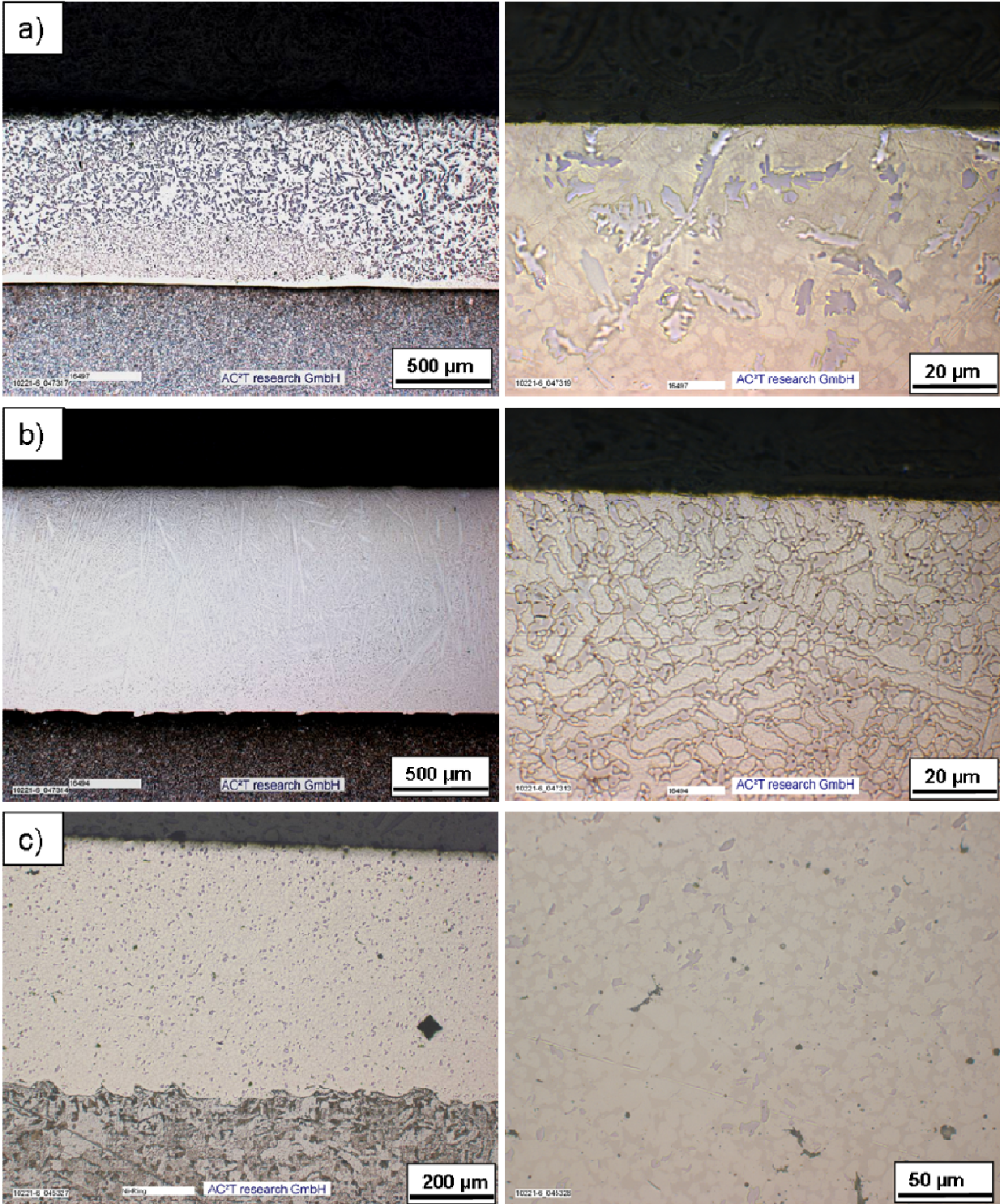
Fig. 4.12: LOM images of the cross section of the Ni-base pin materials
together with detail image: a) hard coating, b) soft coating, c) spray coating
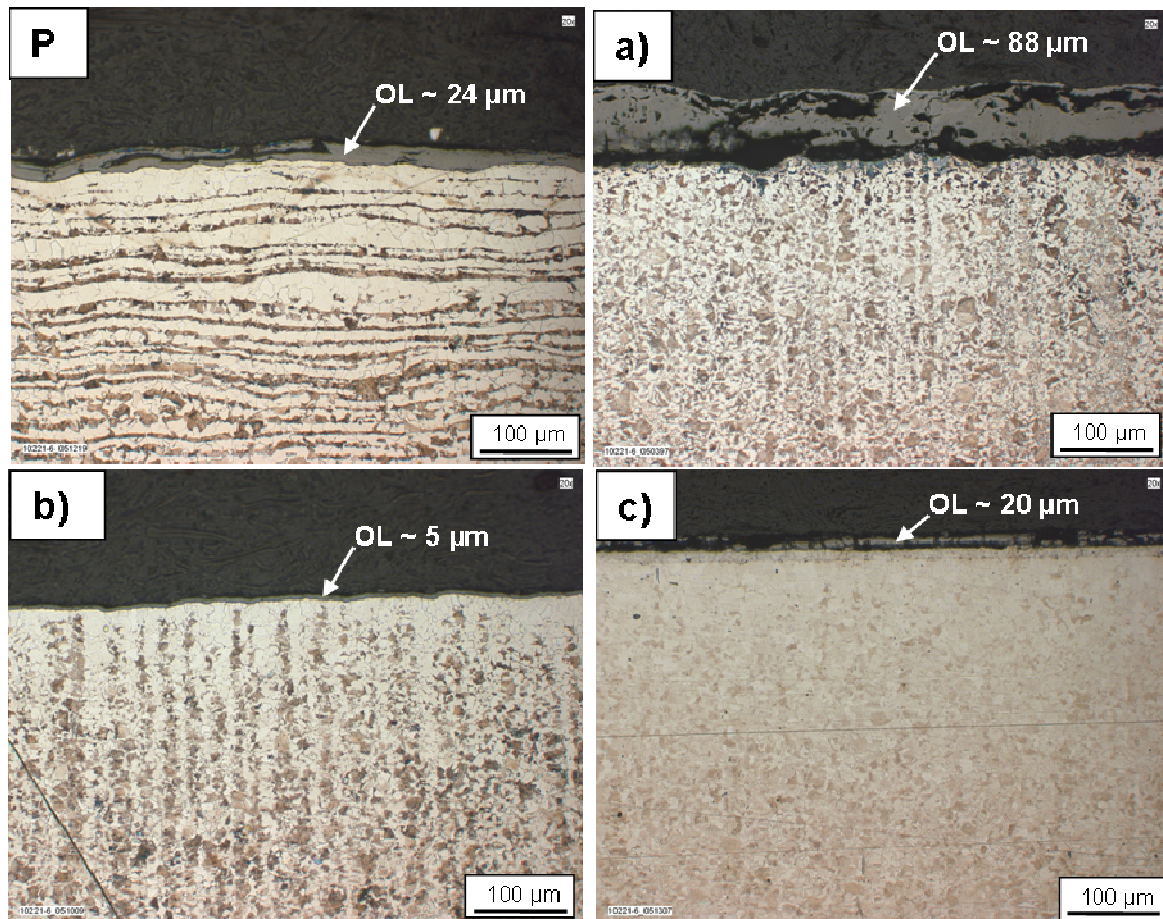
Fig. 4.13: Different oxide layer (OL) thicknesses obtained for FP-H carbon steel for different heat treatment methods compared to layer obtained for a product used in the field (P): heat treatment with air (a), argon (b), argon-air mixed (42 min argon, 18 min air) (c) [cf. 75]

4.3. Abrasive wear tests through steel-wheel testing

The steel-wheel test method was chosen in order to perform tests on the performance of the selected sample materials in three-body wear testing. In the first series, the first set of heat treatment was tested under high abrasive amounts (60 wt% sand). Also tests with low sand loads were performed for wear tests and compared to the findings for the materials of the field application. The second test series was performed with the material of specified heat treatment which is with its parameters (microstructure and hardness) closest to common field application materials (the ferritic/pearlitic material FP-H).

4.3.1. Steel-wheel two and three body abrasive tests

4.3.1.1.   Experiments performed on first heat treatment samples

The samples were worn with the steel-wheel apparatus using 45 and 130 N load in three body wear with an aqueous slurry mixture containing 60 wt% abrasive in a saline solution (1.5 wt% NaCl), tested with 0.6 m/s for 15 minutes. Three steel samples for each heat treatment state were abraded with the procedure as mentioned in the experimental sector (chapter 3.1). For the macroscopical images of the wear track, no significant difference can be seen between the different steel samples (see Fig. 4.14). Quantitative results are given in Fig. 4.15.

For the normalized samples, higher hardness is accompanied by higher wear rates. The quenched and tempered samples V1 and V2 show slightly lower wear rates than the as-rolled and natural sample, but higher wear rates than the normalized and furnace cooled sample N1 (Fig. 4.15). Higher applied loads are leading to higher wear rates.

Fig. 4.14: Macro images of the heat treated samples after the steel-wheel test:
a) steel base material N b) normalized furnace cooled N1 c) normalized air cooled N2
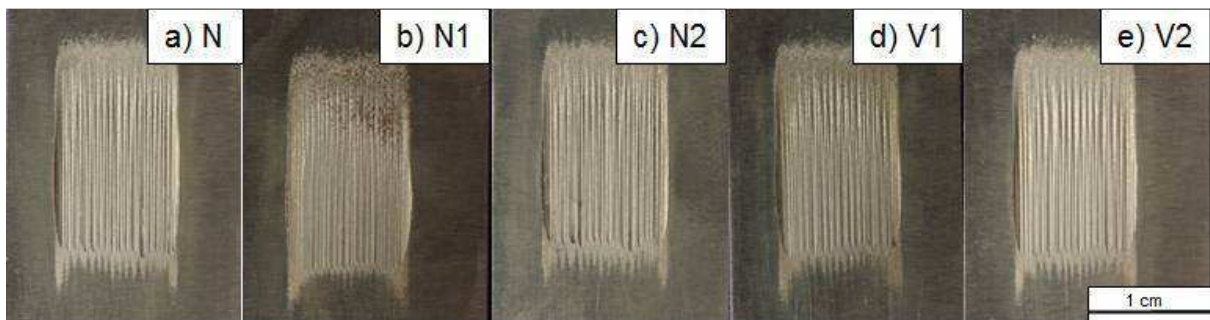d) Ni-base layer e) quenched and tempered V1 f) quenched and tempered V2
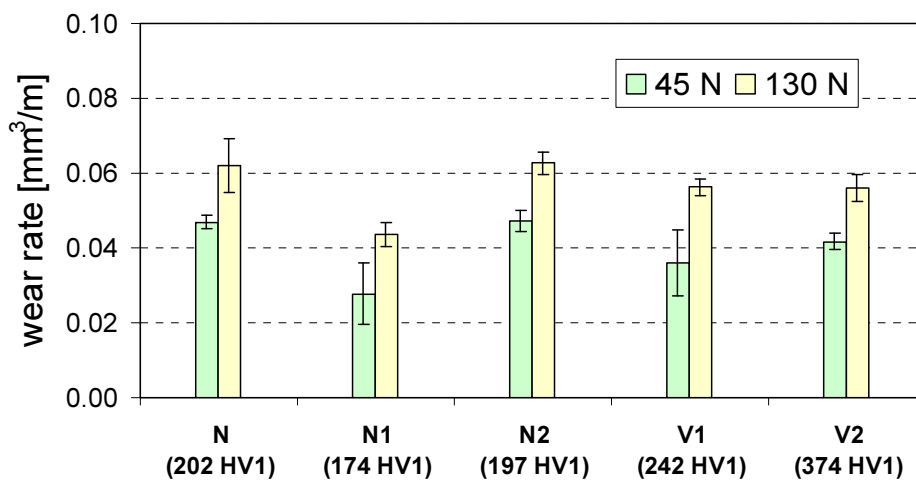
Fig. 4.15: Wear rate results for the differently heat treated steel samples

4.3.1.2. *Experiments on the influence of low abrasive content on wear*

In the second part of these first experiments, two samples of steel material N and one sample of material N1 were tested in two body wear using low (0.1 wt% sand) and no abrasive content in the saline solution. The performed tests were N with 0.1 wt% abrasive and N1 with 0.0 and 0.1 wt% abrasive (N1-a, N1-b). The other parameters were the same as for the tests with 60 wt% abrasive amount. Macroscopical image of the worn samples can be seen in Fig. 4.16. The worn samples were then investigated using SEM analysis and compared to those tested with high abrasive amount (Fig. 4.17). The wear rates were significantly lower than for high abrasive testing (Fig. 4.18).

Abrasive tests using 60 wt% abrasives clearly show dominant 3-body wear behavior. Tests using low abrasive content (0.1 wt%) mainly show grooves with less fatigue. Non-abrasive tests show no cleavage trails due to the absence of abrasive material, but the direct contact of the wheel and the sample surface lead to a high amount of adhesion or fatigue wear. The obtained wear images of these tests were also compared to those of the field sample analysis (see chapter 5.3).

Fig. 4.16: Comparison of the wear tracks after low abrasive testing:
a) Sample N with 0.1 wt%; b) N1-a without; c) N1-b with 0.1 wt% abrasive content
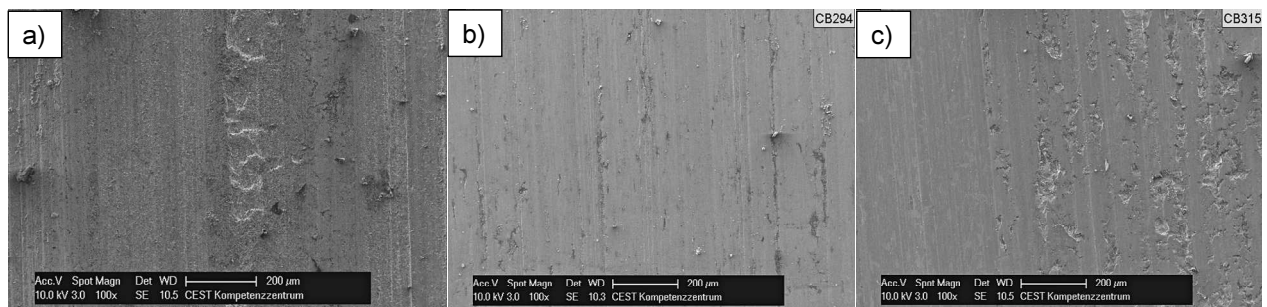
Fig. 4.17: Comparison of SEM images of the wheel friction tracks:
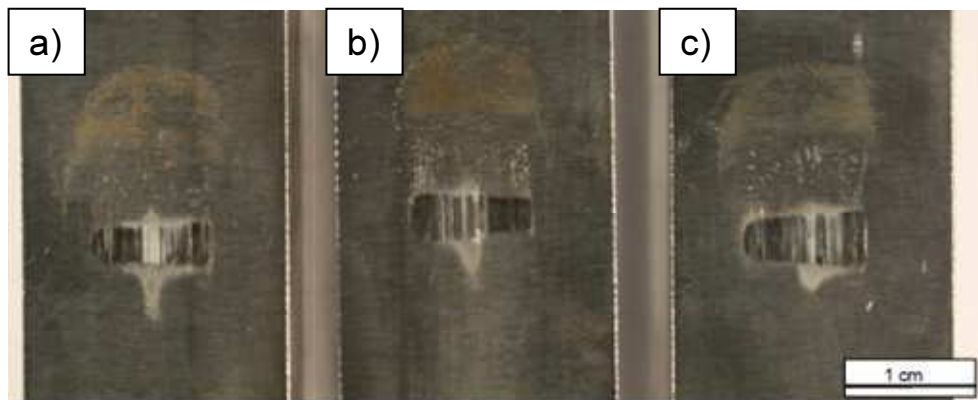a) Sample N with 60 wt%; b) N with 0.1 wt%; c) N1-b without abrasive content
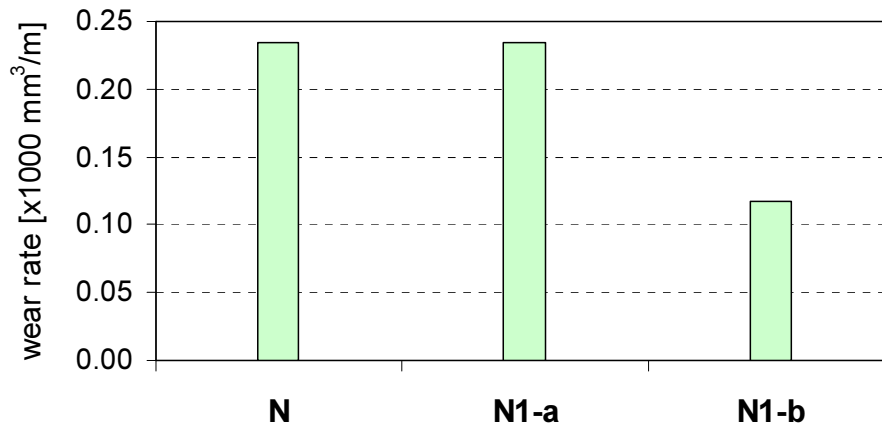
Fig. 4.18: Wear rate results for testing with 0.1 wt% abrasive amount

4.3.1.3. Experiments on the influence of different abrasive amounts and medium salinity on specific heat treated steel samples

These tests were performed using the FP-H tube material with the steel-wheel tribometer. Within these tests, the effect of the abrasive content (silica sand) and the salinity of water were tested. The tested sand amounts were 0.1, 1, 5, 10, 20 and 60 wt% silica sand in the slurry mixture. The used media were tap water without salt addition and tap water containing 1.5 wt% NaCl. So twelve different combinations of the given conditions were tested, three tests for each combination were performed.

Fig. 4.19 shows the result wear rates for saline and tap water tests. The results are similar except for 10 wt% abrasive medium. The tap water results in higher wear rates, although the standard deviation of these measurements are significantly higher than for the other measurements. Fig. 4.20 shows the worn samples for the tap water tests, Fig. 4.21 for the saline water tests. Comparing the wear tracks for 0.1, 1 and 5 wt% abrasive content, the resulted tracks are similarly small, which complies with the findings of the wear rate calculations. From 10 wt% to 60 wt% abrasive content, the size of the wear track increases significantly. Comparing of the pure and saline tap water tests, the tracks are smaller for the saline water tests for the lower four sand load values. For higher sand load values, the tracks are almost the same size and form. The appearance of the wear tracks are conforming to the results obtained for the wear rate calculations.
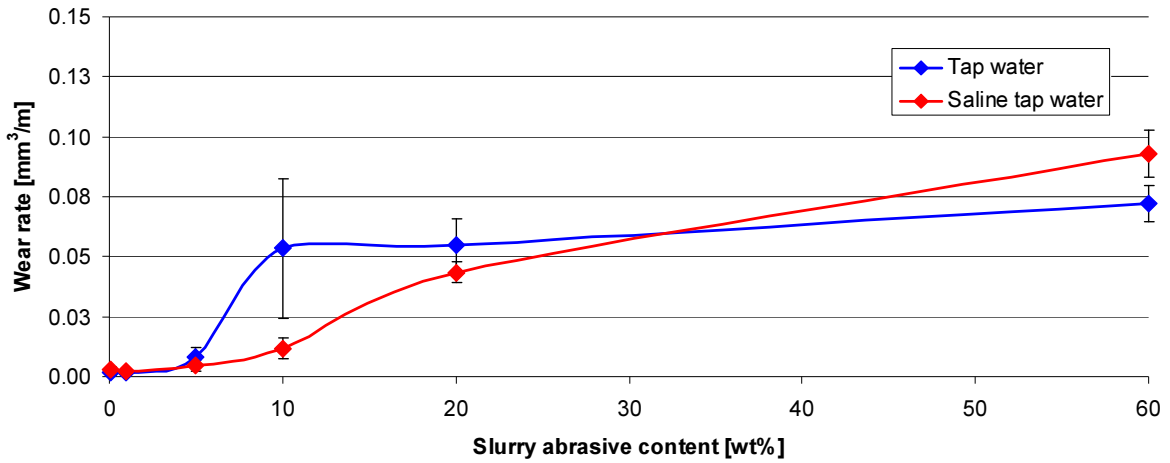
Fig. 4.19: Graphs for the wear rate of the double normalized FP-H tube steel in mm^3/m [69]
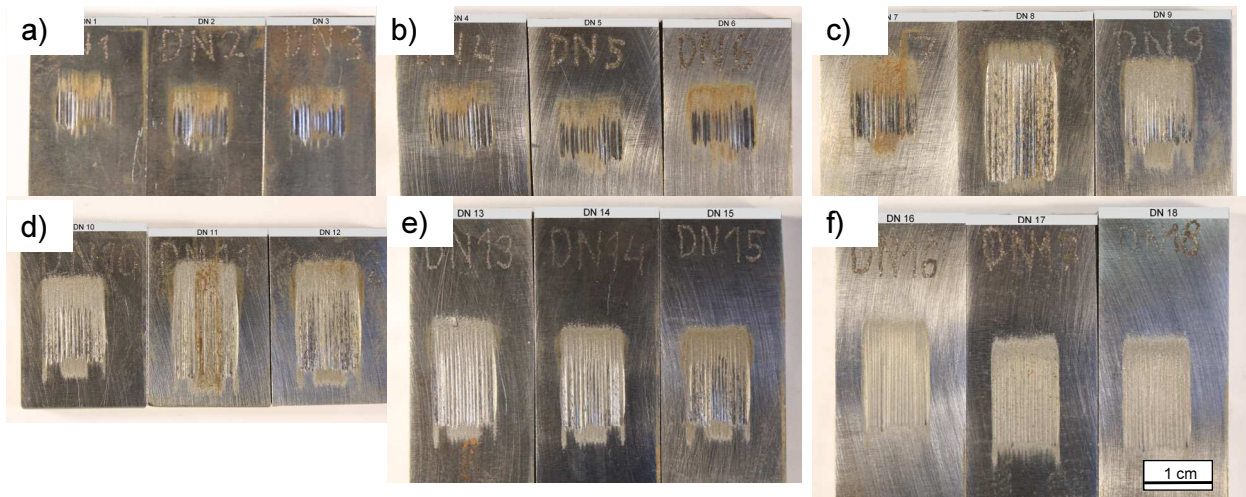
Fig. 4.20: Image of the worn samples of the pure tap water tests:
a) 0.1 wt%, b) 1 wt%, c) 5 wt%; d) 10 wt%, e) 20 wt%, f) 60 wt% abrasive content [69]
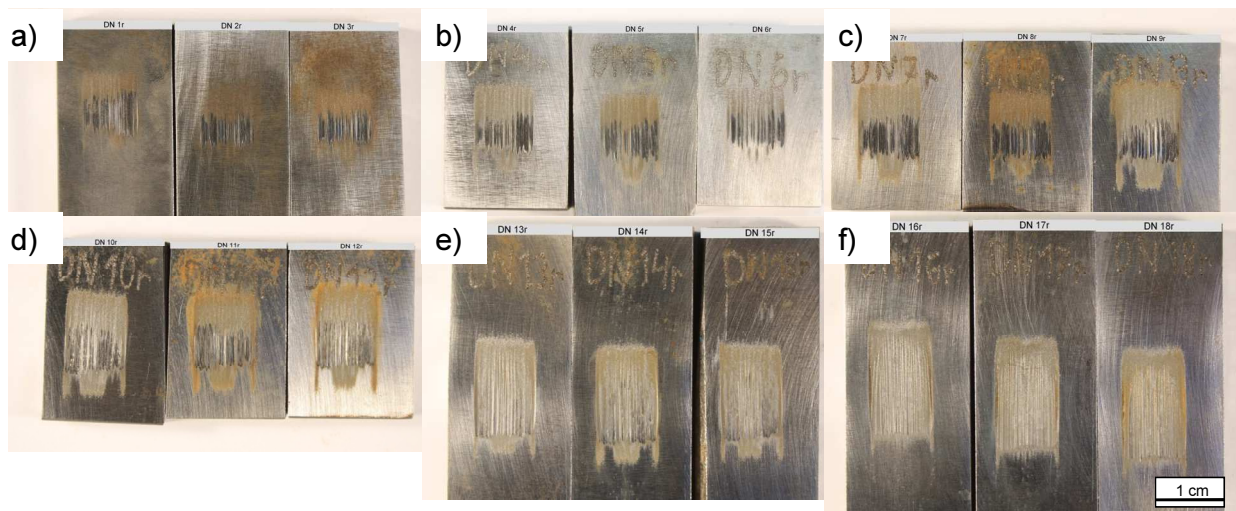
Fig. 4.21: Image of the worn samples of the saline tap water tests:
a) 0.1 wt%, b) 1 wt%, c) 5 wt%; d) 10 wt%, e) 20 wt%, f) 60 wt% abrasive content [69]

For tests with 10 wt% abrasive amount, where the change of wear response is most visible, the sample surface after the test was investigated using SEM-EDX, for one sample of each for tap water and salt water as medium was investigated (Fig. 4.22 and Fig. 4.23). On the surface of the tap water sample it can be seen that the surface experienced massive damage and much sand particles are implanted into the surface. The base material consists of the steel sample, together with some parts of the counter body (Ni in EDX measurement) and sand particles (Si in EDX measurement). The bright spots on the surface are the sand particles (high Si peak in EDX measurement, together with oxygen). The surface of the salt water worn sample on the other side shows a more regular surface with less intense wear and less sand particles on the surface. This sample is also showing Ni and Si on the surface as for the tap water sample. The high carbon content is supposed to come from carbon rich zones from the steel matrix (cementite phase) or from the sample preparation.
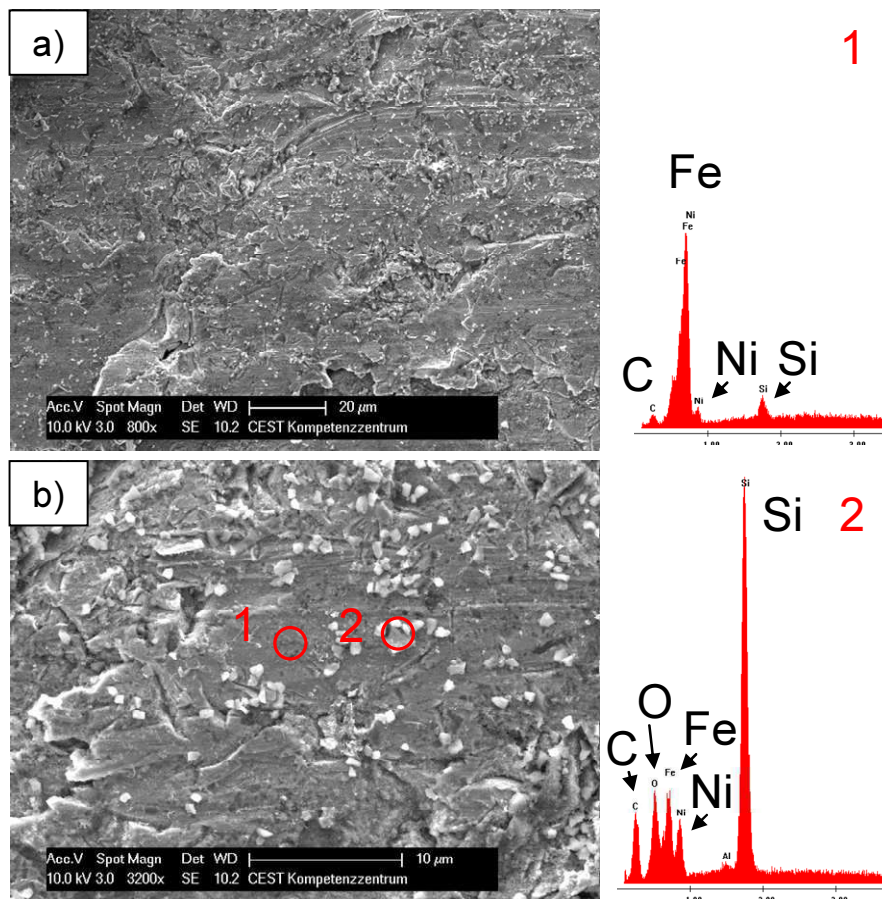
Fig. 4.22: SEM images of surface of steel sample tested with tap water and 10 wt% abrasive amount: a) worn surface, b) worn surface close-up with EDX measurement spots 1 and 2 [74]
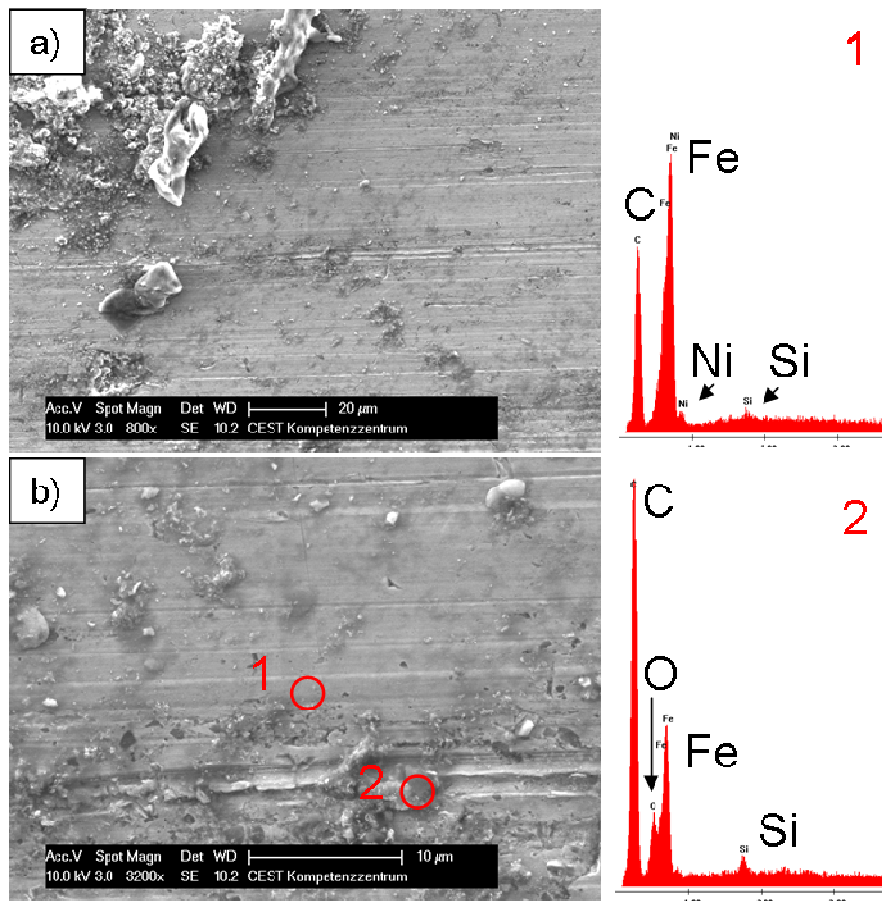
Fig. 4.23: SEM images of surface of steel sample tested with salt water and 10 wt% abrasive amount: a) worn surface, b) worn surface close-up with EDX measurement spots 1 and 2 [74]

In order to investigate the reason for the effect of reduced wear for saline medium at 10 wt% abrasive amount, which is supposed to result from a different behavior of the abrasive in the saline solution due to possible density differences, density measurements of tap water and saline water were performed. These tests resulted in 0.999 g/cm^3 for tap water and 1.009 g/cm^3 for salt water. Viscosity measurements resulted in 1.054 mPas for tap water and 1.083 mPas for salt water. So for 1.5 wt% saline solutions there exist measurable differences in density and viscosity. Different wear behavior is therefore possible.

Another hypothesis regarding the possibility of dissolution of silicon from sand through the salt water medium was disproved by performed ICP-OES measurements of tap water and salt water slurry. These showed that both liquids contain similar, very low contents of silicon (Table 4.4).

Table 4.4: Results for ICP-OES measurement of media (results in ppm)

Element	Ca	Mg	Si	Na	S
Tap water	44	11	7	50	20
Salt water	44	15	9	2800	25

4.4. Sliding wear contact of basic body and counter body materials tested in pin on disc experiments

Sliding wear tests using the pin-on-disc tribometer were performed on one side for the evaluation of the performance of different steel materials under different states. These were heat treatment, microstructural and hardness states, and also the existence of an oxide layer on the steel surface. These materials were tested against various counter bodies in order to study the tribobehavior and the results depending on the various steel and counter body conditions. Also, the samples "pre-worn" with the pin-on-disc method were used for studies on corrosion tests in comparison to unworn sample in order to investigate the influence of the tribological history on the corrosion performance.

4.4.1. Damaging of steel pins of first heat treatment set

These tests were performed using steel pins out of the samples of the lab-intern heat treatment against Ni-base coated discs under wet (tap water) conditions. The worn pins were then corroded using a saline solution with 1.5 wt% NaCl content in a beaker for 24 hours. The contact surfaces of worn and corroded samples were then analyzed using SEM-EDX. The surface of the worn pin consisted of pure steel surface, nickel worn from the disc and small dark oxides formed during the test. The corroded pin consisted of the nickel area, which was not corrosively attacked, and an oxide layer, which was formerly the free steel surface. Oxides formed during tribocontact still remained after corrosion. Fig. 4.24 shows the comparison of these two SEM images.
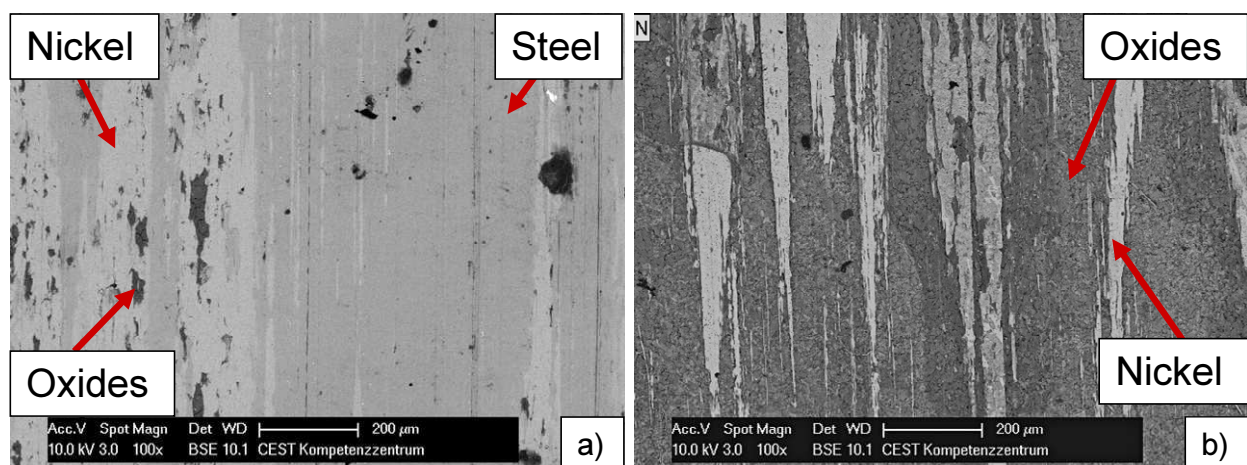

Fig. 4.24: SEM images of worn and worn plus corroded steel pin:

a) worn pin sample; b) worn and corroded pin sample

4.4.2. Performance of atmospherical heat treatment oxide layer of steel disc samples

In a first set of experiments performed on heat treated samples containing oxide layer on the surface, samples were prepared under atmospherical conditions. In order to perform experiments with oxide layers closer to real conditions, the heat treatment was adapted as described in chapter 4.2. Steel sample FP-H was coated with an oxide layer through heat treatment under atmospheric conditions. Steel discs with these oxide layers and without layers (grinded samples) were tested against rectangular Ni-base coated pin samples. These coatings consisted of two Ni-base alloys with different hardness values (535 and 775 HV1). As surface parameter, different surface parameters after polishing and grinding resulting in roughness values R_a of < 0.3 µm for the polished and > 0.6 µm for the grinded surfaces were chosen for sliding wear testing. As a result, 8 different parameter pairings were tested. The used normal force was 21.6 N, as calculated for the rectangular pin shape out of typical parameters obtained for field application. The influence of the surface and hardness on the progress of the wear test was investigated [75].

The non-oxide layer discs worn with the softer pin materials showed less wear than the ones worn with harder pin materials at macroscopical investigation (Fig. 4.25). For all performed tests, the wear track is macroscopically visible.
The disc samples with oxide layer showed high wear and a partial flaking of the oxide layer (Fig. 4.26). The wear of the layer is also macroscopically visible, especially for samples showing layer flaking. For samples without flaking effects, the wear track was harder to determine.

Of the samples, a sectional cut was performed in order to investigate the wear track using LOM (Fig. 4.27). For the disc samples without oxide layer, only wear grooves are visible on the surface. For oxide layer disc samples showing flaking of the layer, it was easy to determine the wear zone and the undamaged zone, as the abraded oxide layer and the intact layer beside the track are clearly visible.

3D microscopical images of the wear track of the disc without and with oxide layer were also investigated (Fig. 4.28). As observed for the LOM sectional cuts, only wear grooves are visible for the disc samples without oxide layer, where the oxide layer discs show a clear separation between residual border layer and abraded wear track.
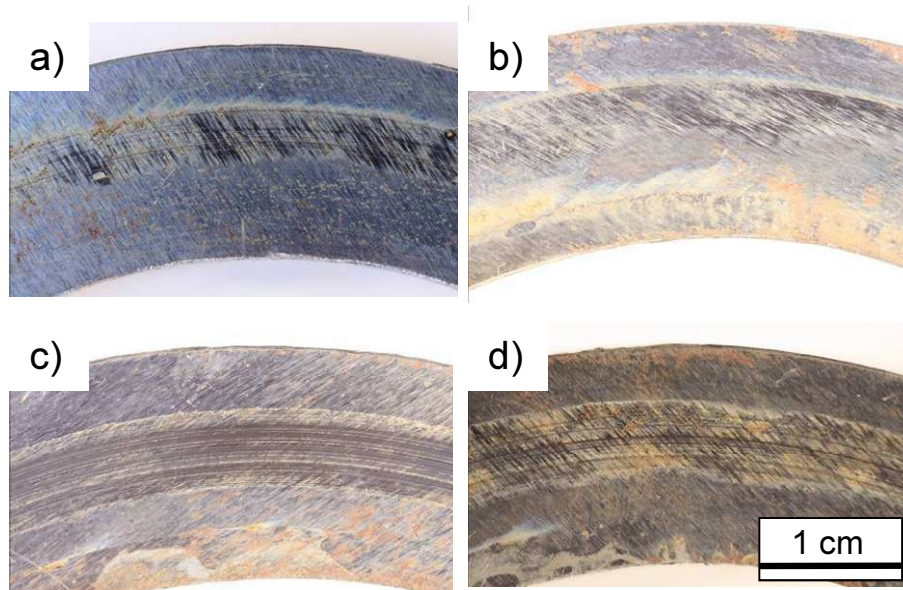
Fig. 4.25: Macroscopical images of the worn non-oxide layer disc samples worn with
a) soft pin polished, b) grinded, c) hard pin polished and d) grinded [69]
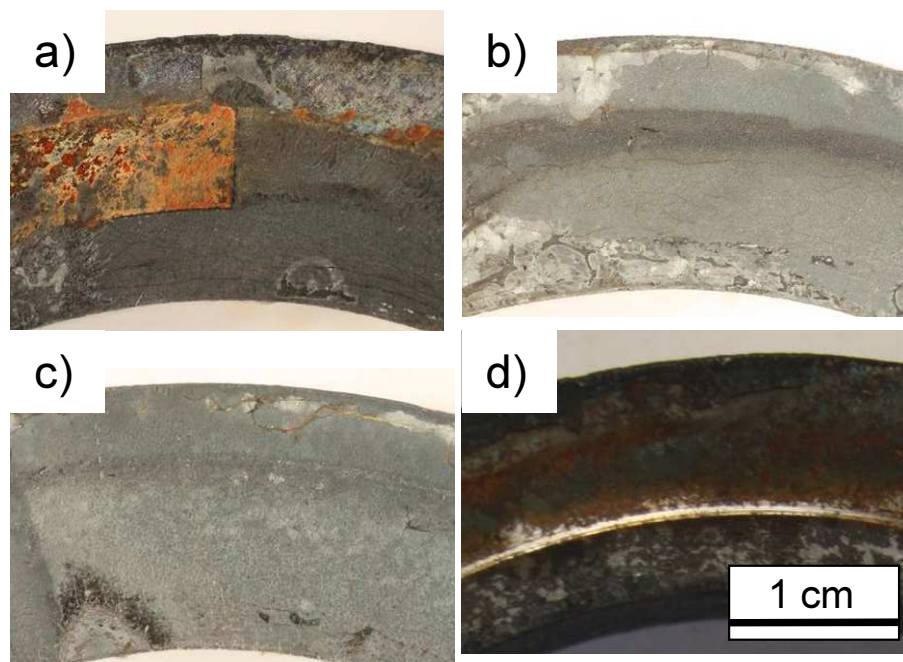
Fig. 4.26: Macroscopical images of the worn oxide layer disc samples worn with
a) soft pin polished, b) grinded, c) hard pin polished and d) grinded [69]
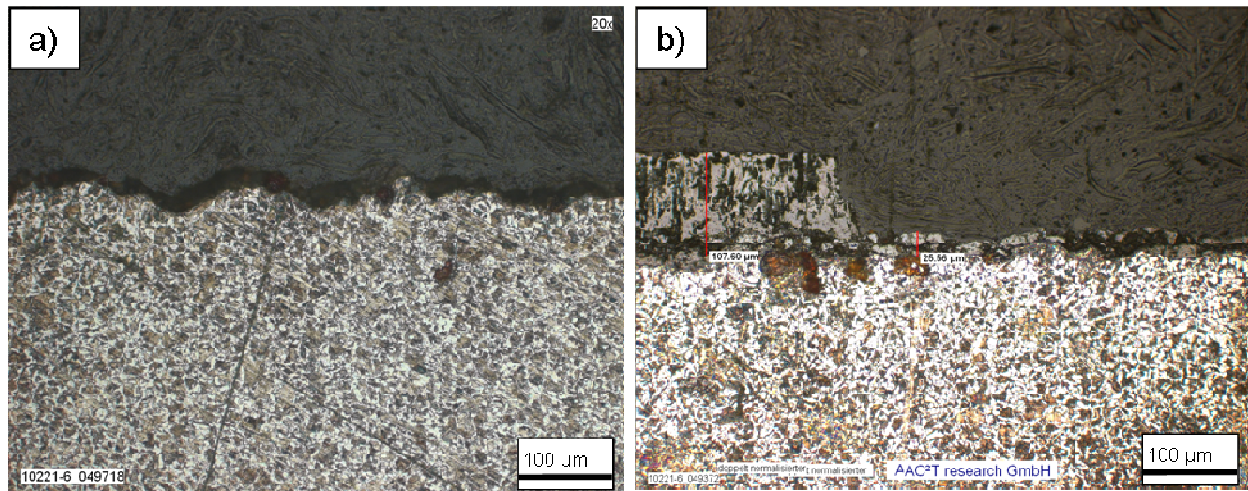
Fig. 4.27: LOM images obtained for the worn disc samples: a) worn non-oxide layer sample (soft pin, polished), b) worn oxide layer sample (soft pin, polished) [cf. 74]
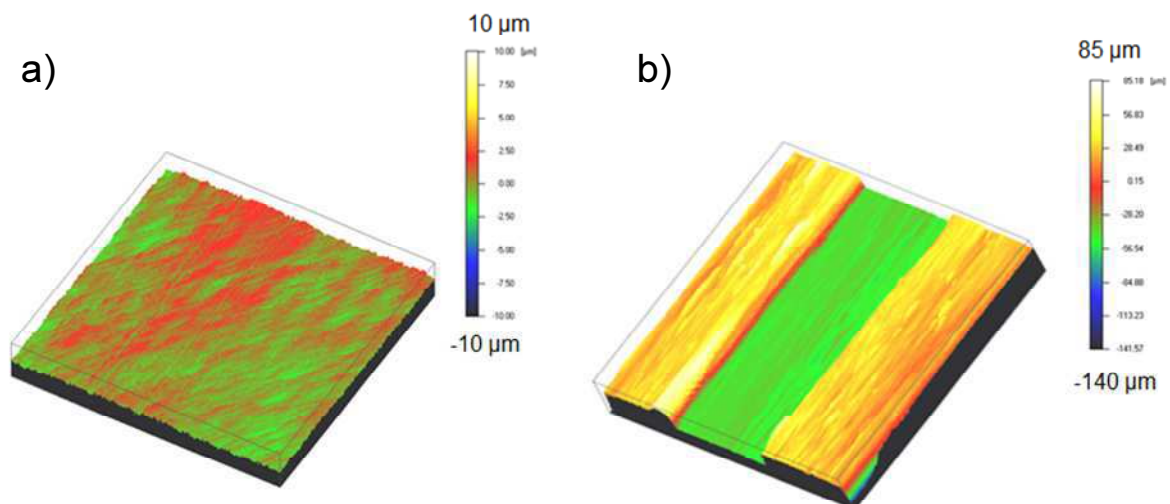
Fig. 4.28: 3D topography images, collected by a confocal microscope, were obtained for the worn disc samples: a) worn non-oxide layer sample (soft pin, polished), b) worn oxide layer sample (soft pin, polished) [69]

The rectangular shape was not ideal for pin-on-disc tribotesting. Tilting of the pin sample due to the non-circular shape led to pin sample displacements and an uneven distribution of the applied normal force. Therefore, the application was changed to circular shaped pin samples. Also the thickness and the appearance of the oxide layer (brittle) was different from the thickness of the oxide layer of the inner side of the tubings from the producer. Therefore, an adaption of the lab-scale heat treatment process was necessary.

For the used samples, nanoindentation tests were performed to investigate the hardness of the oxide layer, the steel material and the Ni-base coating phase hardness. Fig. 4.30 shows the comparison of the measured hardness values in GPa. The Ni-base materials are containing both the Ni phase (values which are at same level), together with the respective precipitations of the materials. These phases are the softer phase for the Ni soft material and the harder phase for the Ni hard material (possibly carbides).
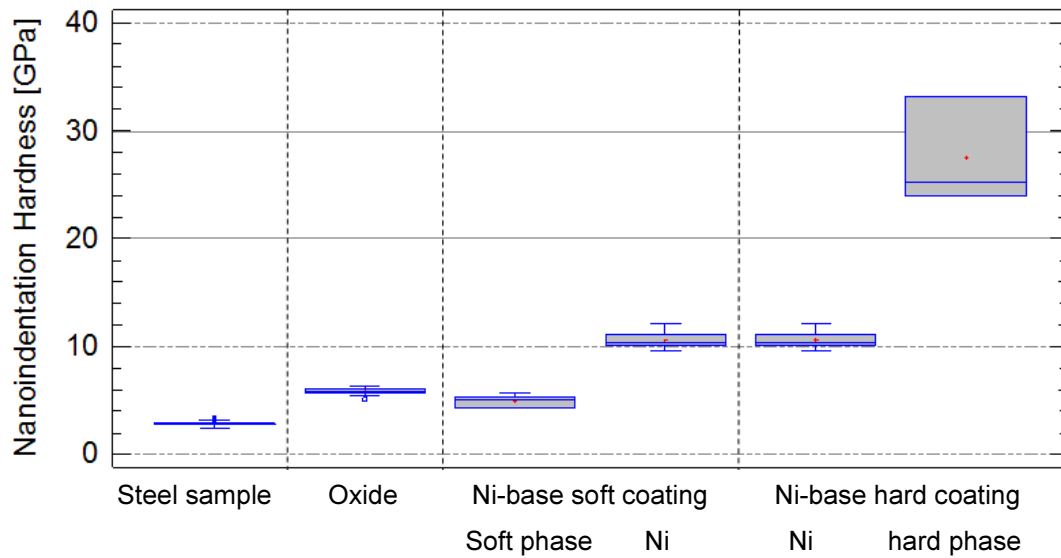
Fig. 4.29: Nanoindentation hardness measurements of steel and Ni-base materials

4.4.3. Performance of adapted heat treatment oxide layer on steel disc samples

At first, the oxide layer on the disc samples had to be generated as described in the experimental section (chapter 3.1.3). This layer was primarily tested in some screening tests. Initially, the obtained oxide layer was tested using the scratch test with different normal loads (10, 20, 30, 50 and 70 N) and a test with increasing normal load from 0 to 100 N. The layer showed brittle appearance after the tests even for 10 N applied normal load (Fig. 4.30), assumed to fail in pin-on-disc tribotest under these applied loads. In order to approve these findings, a normal load step test was performed to investigate the breakage behavior of the layer. Normal loads from 10 to 50 N performed in 5 N steps (except for last step, which was 10 N) was performed. The change in load took place after 15 min. For this test, the applied loads and durations were not sufficient to cause severe failure on the oxide layer. Tests with a longer duration of 2 hours and two normal load levels were therefore performed. Fig. 4.31 shows the tribotest curve of this test together with an image of the respective disc sample. The wear rise of each step is a result of the instrument response on the increasing load. The appearance of the layer after the pin-on-disc step test is not brittle. The oxide layer is slightly attacked and not broken. The results from the scratch test and from the pin-on-disc test are not comparable one-to-one, because the application of the load is punctual in the case of the scratch tester in contrast to the pin-on-disc tribometer, where the contact is two-dimensional on the pin surface, which results in different contact pressure and layer behavior respectively, even for similar normal loads.
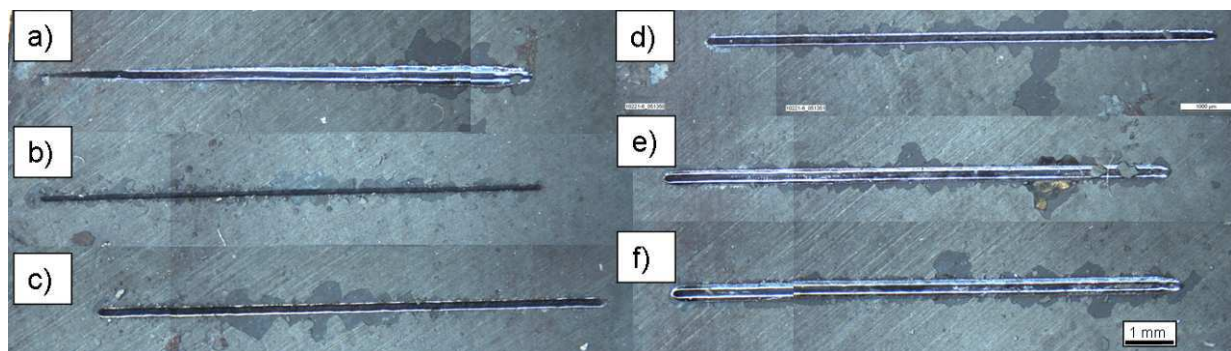
Fig. 4.30: Scratches obtained a) for continuously increasing normal load from 0-100 N and for single normal load tests using b) 10, c) 20, d) 30, e) 50 and f) 70 N constant normal load
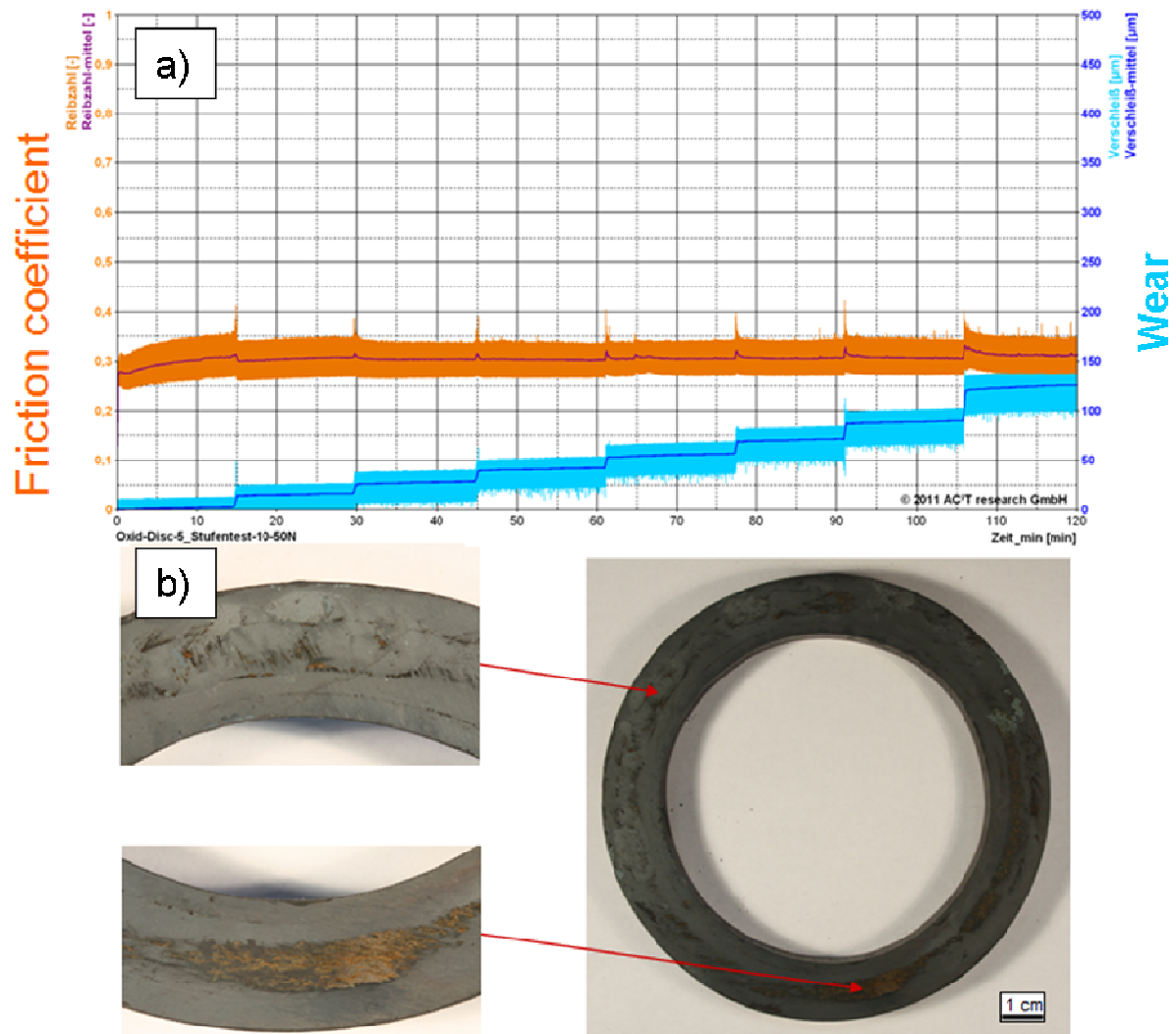
Fig. 4.31: a) Test plot for the step test (orange: friction coefficient µ; scale from 0 to 1; blue: wear; scale from 0 to 500 µm); b) macro image of disc sample with details of the wear track

4.4.4.   Running-in effects on different basic body surfaces

For these tests, the effects of the contact situation metal-metal and oxide-metal, the influence of different counter body (pin) parameters and of different normal loads were tested. Single tests for grinded and oxide layer discs were performed using the pin samples with round contact surface applying normal loads of 10 and 70 N for 2 hours test duration, or 13,500 test cycles. Fig. 4.32 shows typical results for these tests together with an image of the pin sample surface after the test.

For the metal-metal contact situation, higher noise and a less regular progress for the friction coefficient was obtained, especially for higher normal loads, whereas tests with oxide layer discs showed a less noisy progress, even for higher normal loads. Metal samples also show lower

friction coefficients than oxide layer tests (µ ~ 0.1 - 0.15 at the end of testing) using 70 N load. In comparison at the use of oxidized disc samples a higher friction coefficient of 0.2 - 0.3 was achieved which remains on a constant level till end of testing. [cf. 75]

Another difference between oxide and metal contact is the contact area of the pin after the test: the oxide layer samples were in tribocontact with the entire pin surface at the end of the test, whereas the metal contact tests mostly showed only attack on ~50 % of the original surface. With increasing normal load from 10 N to 70 N the wear increases significantly which can be seen clearly in the slope of the wear curve (compare tribotest curves c and d of Fig. 4.32).
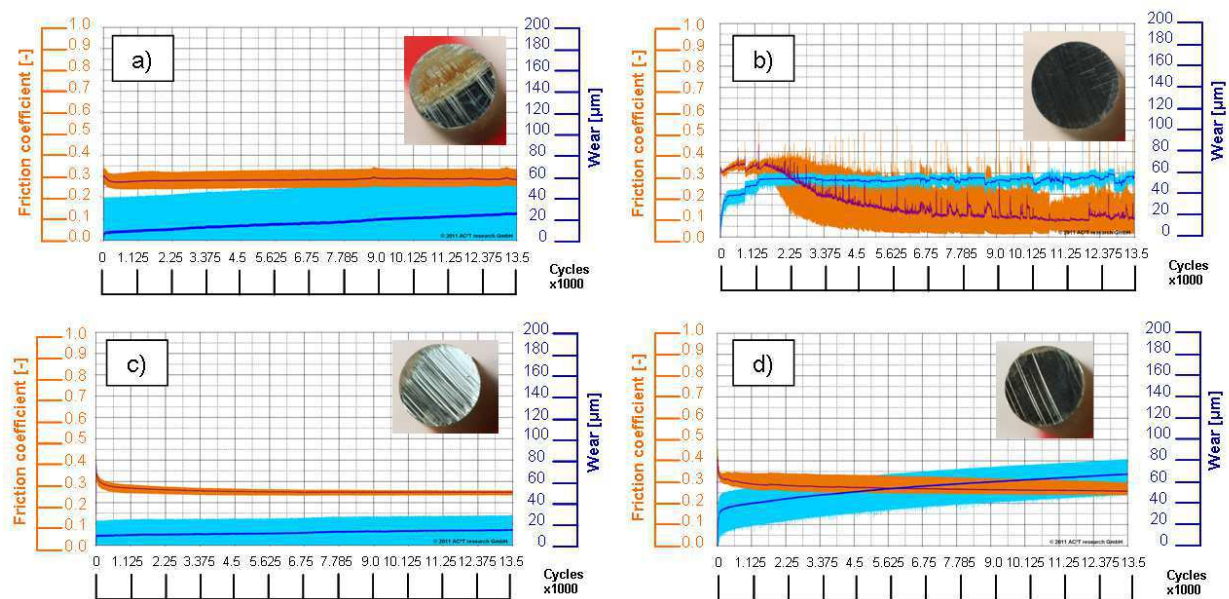
Fig. 4.32: Test plots for friction and wear with metal and oxide layer discs: metal contact at a) 10 N and b) 70 N; oxide layer tests using c) 10 N and d) 70 N (orange: friction coefficient µ; blue: total wear); including macro images of pin samples [cf. 75] [69]

4.4.5. Investigation of roughness influence for state transition

On one side, the question of the influence of the counter body roughness as R_a value came across. Also, if there is a major benefit for the use of counter bodies with less hardness, for it is more intensive to manufacture counter bodies with low roughness levels. Samples were created with smooth surface after polishing. As alternative condition, a rougher surface after grinding was manufactured and tested in an test with oxide layer discs for 8 hours testing time, which is equivalent to 54.000 test cycles, which simulates the state transition from running-in into beginning steady-state operating phase. For this experiment, three tests per parameter sets have

been performed. Fig. 4.33 shows two typical tribotest curves in direct comparison, demonstrating the severe wear increase obtained for the rougher pin material.

Calculating the mass loss for the pin samples (Fig. 4.34), it can be seen that the hard material with high roughness shows the highest mass loss of ~ 54 mg whereas the other materials show mass loss of ~ 10 - 15 mg. With respect on the pin mass loss, the Ni-base material with the grinded surface showed an unsatisfactory tribobehavior compared to the other pin materials and adjusted roughnesses. Fig. 4.35 shows exemplary tribotest curves for all tested, together with the respective samples for these tests.
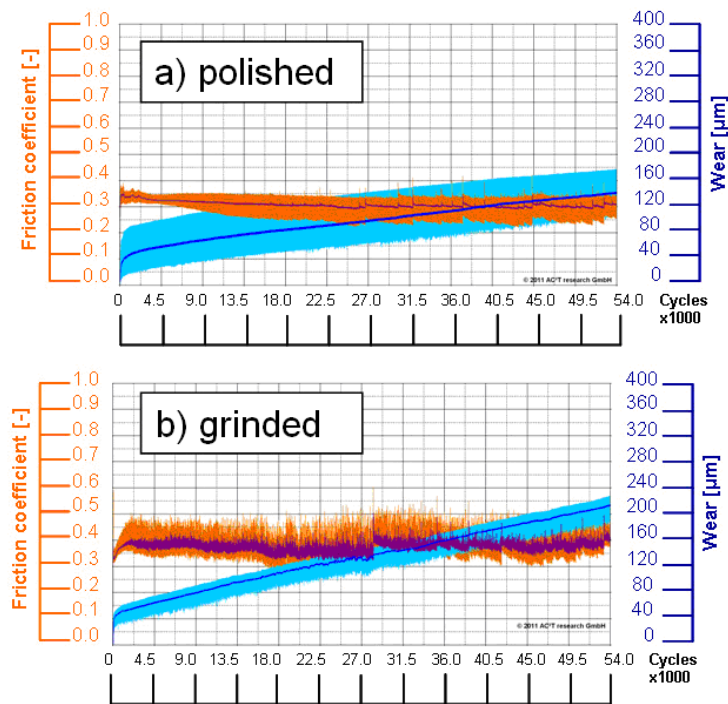
Fig. 4.33: Tribotest curves for friction and wear for oxide layer disc samples against the pin material with higher hardness: a) polished and b) grinded surface condition (orange: friction coefficient – scale 0 to 1; blue: wear – scale 0 to 400 µm) [cf. 75]
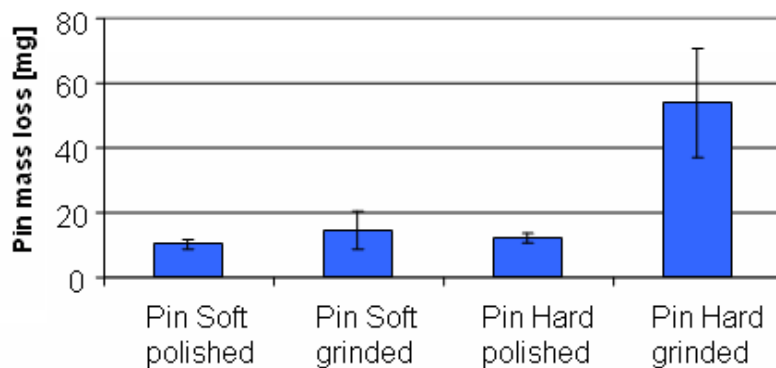
Fig. 4.34: Mass loss of pin materials under variation of hardness and roughness tested against oxide layer disc material [cf. 75]
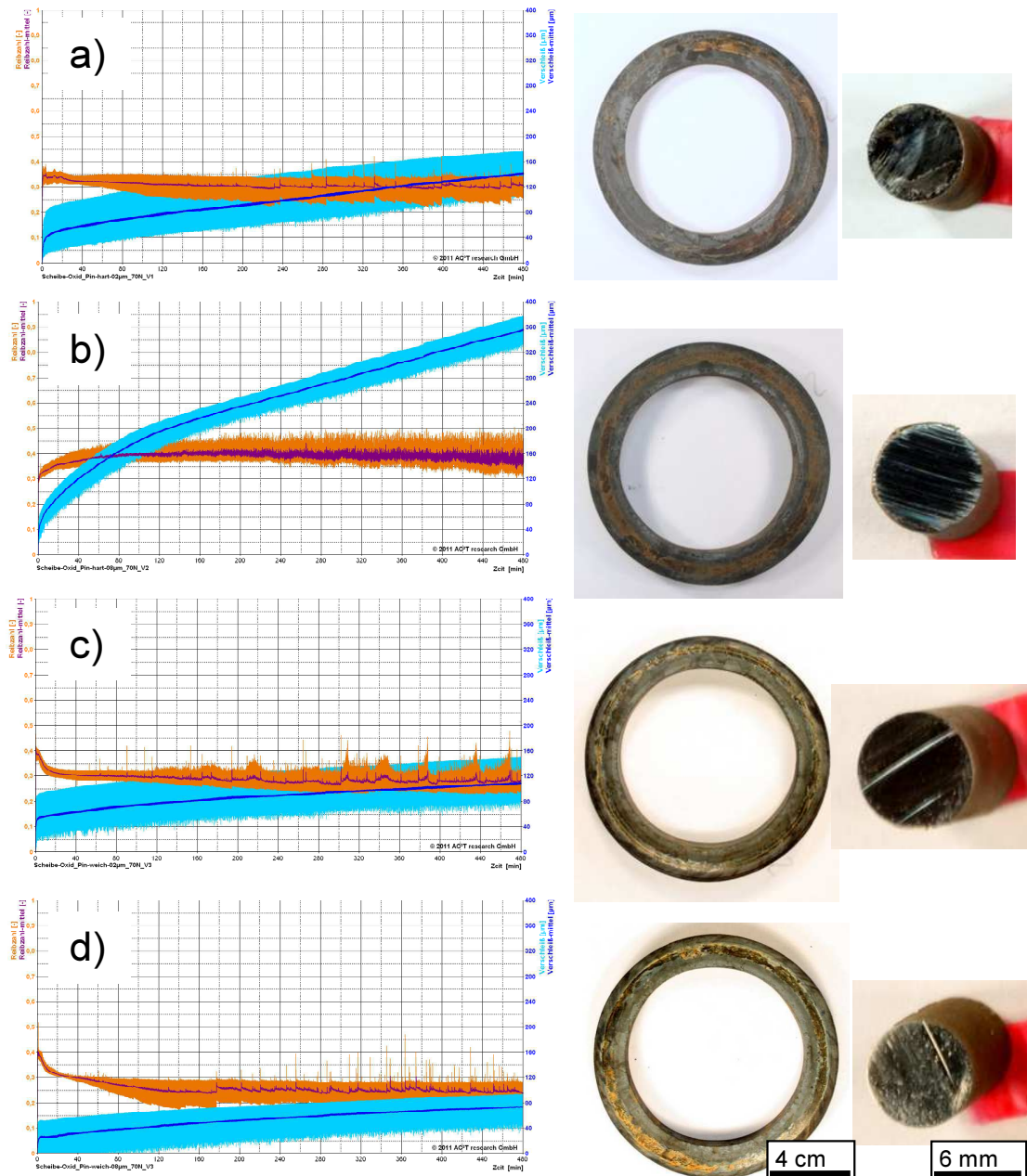
Fig. 4.35: Test curves and macro images of pin-on-disc tests with a) pin hard polished, b) grinded, c) pin soft polished, d) grinded; blue: wear; orange: friction coefficient; scales: 0-400 µm (wear), 0-1 (friction coefficient)

The pin samples were also investigated using 3D confocal microscopy in order to obtain information about the surface probabilities, especially the roughness R_a after the test. **Fehler! Verweisquelle konnte nicht gefunden werden.** shows the results for the roughness calculations of the pin samples.

The roughness after the test was measured as roughness value R_a after the tribotest across the sliding direction (wear grooves), the initial roughness was measured before the test. The difference between initial roughness and roughness after test were investigated. The samples Hard polished and Soft grinded samples show the lowest end roughness. They also show the lowest deviation of the roughness value differences. Hard polished sample seems to keep its initial roughness after the test. Soft grinded became significantly smoother compared to the initial roughness, indicated by the highest negative value. Whereas Soft polished tends to become a little rougher overtime and Hard grinded a little smoother, but the values show more deviation than the values for the other pins.

For those samples, also the R_p and R_z values have been determined before and after the test and set into relation in order to gain information about the roughness tip shape as presented in chapter 3.4.4. As the values are around 0.4 to 0.6, the results show that for the roughness geometry, the triangular tip shape is predominant. Therefore, it can be assumed that the roughness geometry is similar for the performed tests.

4.4.6. Long term 24 hour metal-metal contact to investigate the steady-state wear mechanisms

In order to study long term effects occurring in wear contact of counter body and basic body materials a specific test series was performed. For the oxide layer tests, the layer thickness was decreased to 5 μm (full inertial heat treatment) in order to guarantee an oxidic running-in with a proceeding metal-metal long term contact. As most of the interesting effects were seen for this phase, a test series of grinded basic body discs to simulate a metal-metal contact was performed for all materials three times for each material combination. As test duration, 24 hours or 162,000 rotations were chosen. The other test conditions were the same as for the 8 hour tests.

Calculating the volume loss for the pin materials, one can see that the pin volume loss is higher for tests with oxide layer disc samples than for those performed on grinded disc samples (Fig. 4.36). The hard oxide layer on the basic body leads to significantly higher pin mass loss compared to grinded metal-metal contact, except for pin hard with polished surface, where the value for the grinded test could be met within the uncertainty. The hard pin with polished surface tends to show the lowest mass loss. For oxide layer tests, the soft pin sample with initial grinded surface shows the highest mass loss, the hard pin material with initial polished surface shows the lowest mass loss.

Considering the disc volume loss together with the pin volume loss per cycle·1000, it can be shown from the results in Fig. 4.37 a), that the counter body wear is dominating whereas in steady-state metal-metal contact, the basic body wear rate is higher (Fig. 4.37 b). An example of the on-line wear measurement in Fig. 4.38 shows that the wear rate (slope of wear function) is higher for the initial oxide layer contact and is getting lower for beginning metal contact. The wear rates are calculated out of the slope of the functions of the stable test run towards the end of the experiment. For steady-state metal-metal contact, the wear rate is very low, indicated by the shallow wear increase (Fig. 4.38).

The wear zones indicated in Fig. 4.38 (colored wear increase in tribotest curve) represent the expected wear process from oxidic contact for the counter material resulting in high wear and low-noised friction coefficient progress, going through enhanced noisiness of the friction coefficient and decreasing wear to a steady-state metallic contact situation of low wear and higher noise of the friction coefficient.
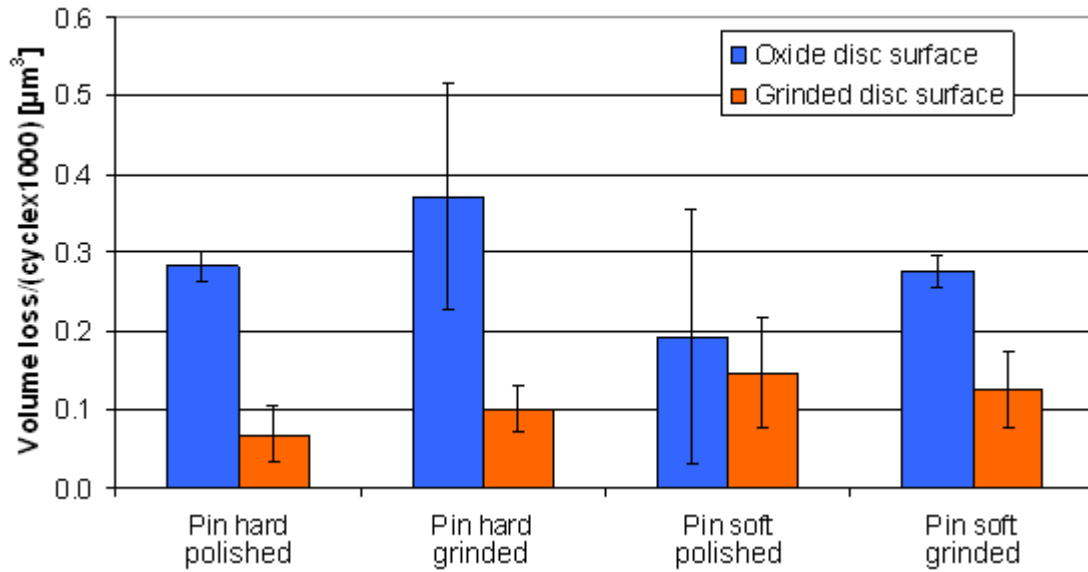
Fig. 4.36: Volume loss of pin samples after tests: a) for discs with oxide layer and
b) for grinded discs without oxide layer on the surface [cf. 75]
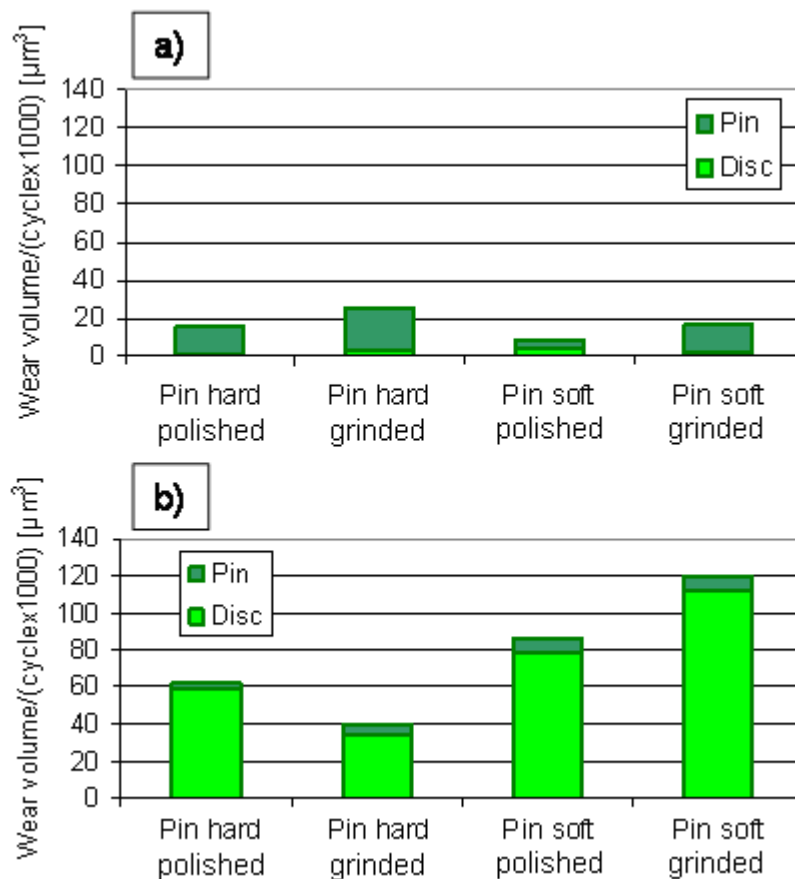
Fig. 4.37: Wear volume of basic body and counter body samples after 162 cycles·1000 testing:
a) with oxide layer on disc surface and b) with metal-metal contact without oxide layer
(in this graph the results of exemplary single tests are illustrated)
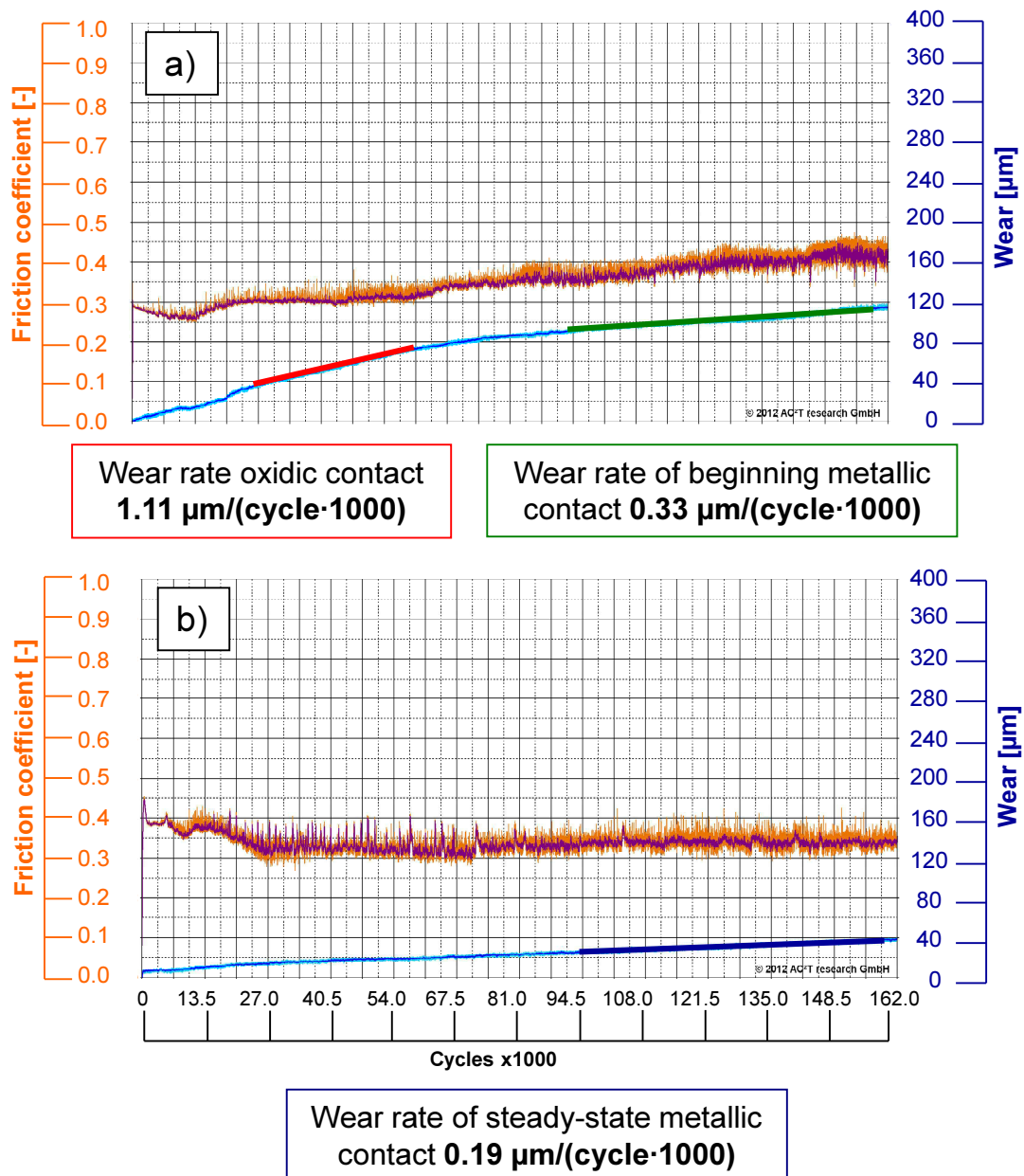
Fig. 4.38: Comparison of tribotest curves for a) basic body with oxide layer and
b) with metal-metal contact

On the use of the different pin materials, tests performed with the soft pin material resulted in a noisy progress with disturbances and peaking friction coefficients for all tested materials. Material transfer from disc to pin material was observed in SEM-EDX investigation (Fig. 4.40). Effects of adhesive wear are supposed to lead to material transfer and the noisy wear progress. For the materials FP-H and M-H, tests with hard pin materials did not result in these effects, for the other materials, nearly each test showed these adhesive effects. Fig. 4.39 shows tribotest curves for a test with hard and soft pin material, Fig. 4.40 shows the macro images of FP-H pin and disc of tests with hard and soft pin material.

In order to gain more information, SEM-EDX analyses of pin and disc samples, which showed these effects, were performed (Fig. 4.41). A material transfer from the steel disc to the Ni-base pin surface of ~5 – 10 μm thickness was evident on these samples. On the disc sample, the wear track of the disc sample clearly shows iron on the plain areas and iron oxides inside the cavities (Fig. 4.42).
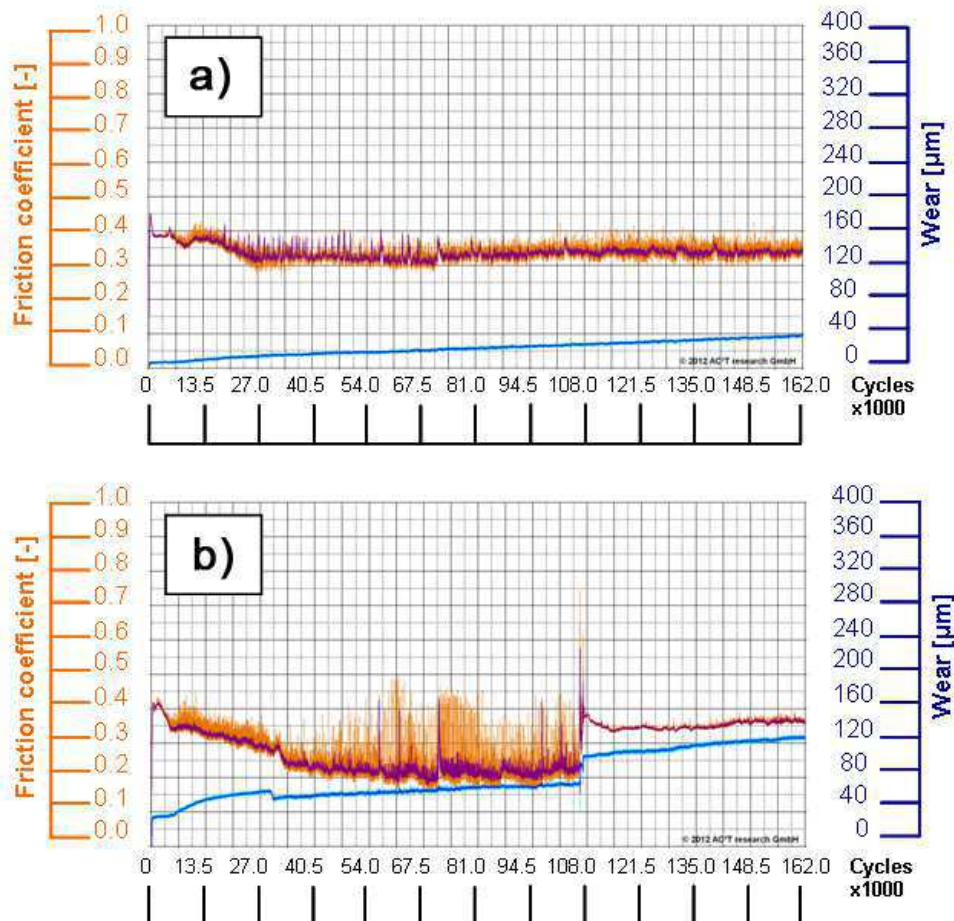
Fig. 4.39: Tribotest curves for FP-H basic body tested: a) hard pin with regular wear progress and b) soft pin material showing disturbances and irregularities coming from microwelding and 3-body-abrasive effects caused by wear particles
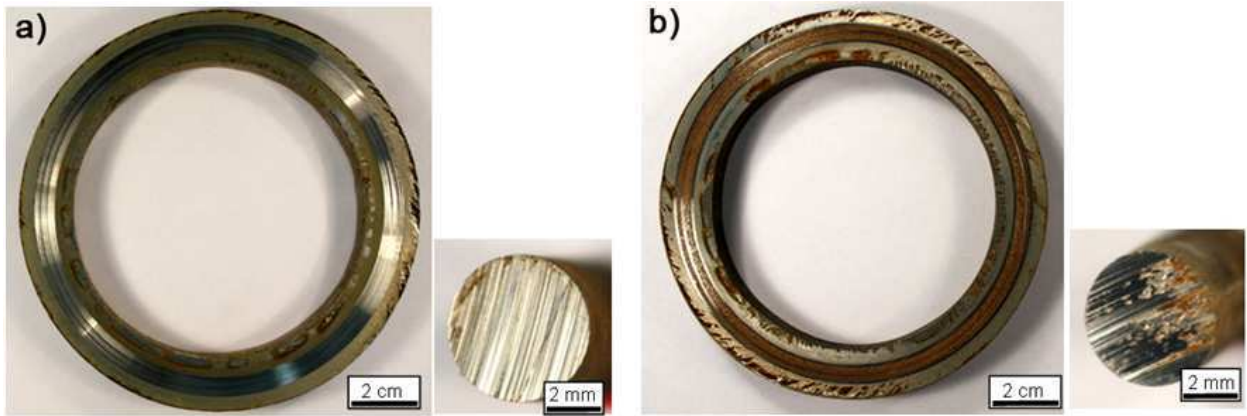
Fig. 4.40: Pin and disc samples after tribotest: a) disc sample worn with hard pin material;
b) disc sample worn with soft pin material with adhesive wear marks
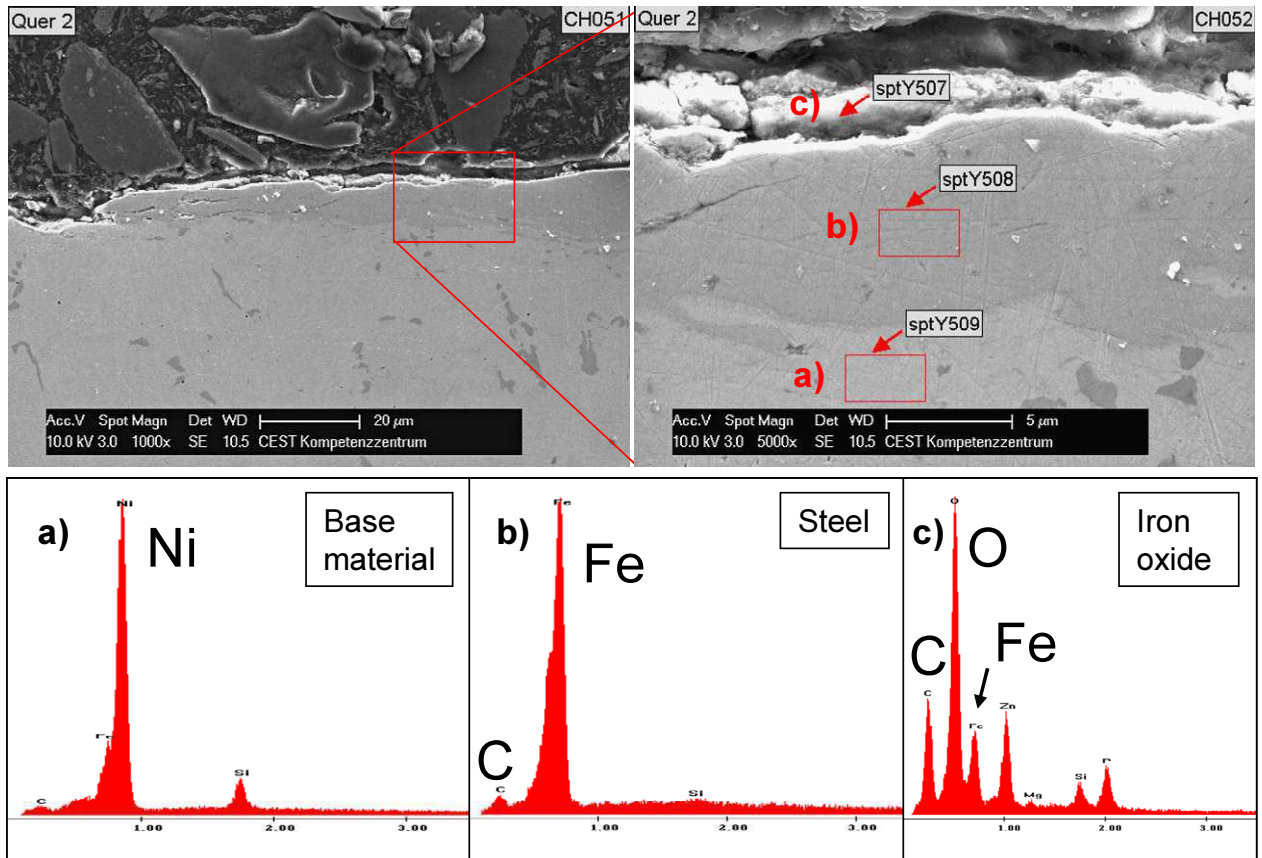
Fig. 4.41: SEM image of cross-section of soft pin material after tribotest together with EDX measurements showing material transfer of Fe-base material (spot b) disc to Ni-base pin (spot a) and oxidation (spot c) [cf. 75]
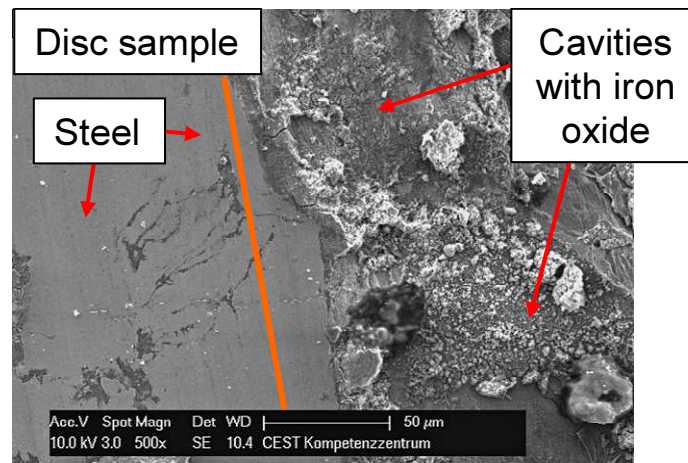
Fig. 4.42: SEM image of surface of disc sample after soft pin tribotest. Surface consists of plain base material and cavities filled with iron oxides (the orange line indicates the sliding direction)

4.4.7. Investigation of alternative basic body and counter body materials

In steady-state phase testing, selected basic body materials were tested in order to identify the behavior of these materials and their long-term effects. In sliding application, some tribotests showed high peaks in friction and wear. These effects were occurring in various cases, showing no clear trend to the roughness condition of the pin material. Tests performed with the softer counter body material type resulted on the contrary to the hard material in a noisy wear and friction coefficient progress for the ferritic/pearlitic FP-H disc material and the harder martensitic M-H material, as described in the paragraphs above. The martensitic M-S disc material and the softer ferritic/pearlitic FP-S material showed unsteadiness for nearly all tests.

For the wear rate as slope of the wear curve in the tribotest curve as μm per cycle·1000 wear increase, it can be seen that for FP-H and M-H, the hard pin material results in lower wear rates than the soft material. For the M-S basic body material, the wear rate values are highly different. In general it can be said that the hard pin material results in slightly lower wear rates (Fig. 4.43).

Comparing the total wear height of pin and disc sample for all materials and pin samples, it can be seen that the disc wear is dominant for all samples in steady-state metal-metal contact. For performed metallic contact tests, M-S showed the highest total wear together with the highest variances of test values, whereas the samples FP-H, M-H and also FP-S show lower and more regular results (Fig. 4.44). The system using M-S as basic body material is very instable and unpredictable. M-H and FP-H show same wear rates for the hard pin materials, together with acceptable deviations, whereas the softer materials show up to three times for FP-S and up to

seven times for M-S higher wear rates than the hard materials, together with high variances. Regarding the initial roughness influence, it seems that for steady-state metal-metal contact, the rougher hard pin leads to less disc wear of all tested counter body materials.

Also, the microstructure played an important role on the tribobehavior of the basic body materials. The ferritic/pearlitic FP-H surpasses the harder M-S in triboperformance, where on the other side the harder martensitic M-H surpasses the softer ferritic/pearlitic FP-S.

Fig. 4.45 shows the cross-sections for all basic body materials after wear tests with the hard pin material. Ferritic/pearlitic materials show plastic deformation, whereas martensitic materials show breaking of material, leading to cavities on the surface, especially for M-S, where the medium is able to perform corrosion. The plastic deformation and grain refinement for the ferritic/pearlitic materials is clearly visible in Fig. 4.45 a) c). The outbreaking due to adhesive wear for the soft martensitic material (Fig. 4.45 b) led to the formation of wear tracks covered with iron oxides formed during tribotest. The more wear resistant hard martensitic material does not show harsh outbreakings as observed for the softer martensitic material Fig. 4.45 d).

As the importance of the materials FP-H and M-S for applications is the highest, they have been intensively studied compared to M-H and FP-S. For FP-H basic body samples worn with soft pin material, formations of iron oxides are indicated in the cross sectional microscopic images (Fig. 4.46 c and d). The severe damage observed from the tribotest curves of tests with M-S basic body steel is also visible in the microscopic images as harsh outbreaking. Particles in the breaking areas are also visible (Fig. 4.47 b and c). The adhesive attack happening for tests with the smoother pin material was more intense, whereas for the rougher pin material, the surface suffered from less grooves.

Fig. 4.48 to Fig. 4.51 show exemplary tribotest curves together with macroscopical images for all tested material combinations. For hard ferritic/pearlitic FP-H material, regular wear process is observable for tests with hard pin material (Fig. 4.48 a, b), whereas for soft pin material with lower roughness, some disruptions due to adhesive effects are observable at the beginning and in the middle of the experiment (Fig. 4.48 c), also iron oxide formation on the wear track (macro image) is observable. Adhesive effects were observable for all soft pin tests, especially for higher initial roughnesses (Fig. 4.48 d), accompanied by intense iron oxide formation on the wear track.

For soft martensitic M-S material, most experiments resulted in adhesive wear. The exemplary results show two results for hard pin samples, where the adhesive effect has the least influence (Fig. 4.49 a, b), and for soft pin tests, which mostly led to adhesive effects with severe disruptions and rises in the friction coefficient, as it is observable in the tribotest plots and also as iron oxide formation on the disc wear tracks (Fig. 4.49 c, d).

Hard martensitic M-H mostly resulted in regular tribotests together with clean wear tracks (Fig. 4.50 a-c). For tests with the soft pin material, adhesive effects also were possible (Fig. 4.50 d). For soft ferritic/pearlitic FP-S material, nearly all tribotests resulted in adhesive wear together with the formation of iron oxides on the wear track (Fig. 4.51).
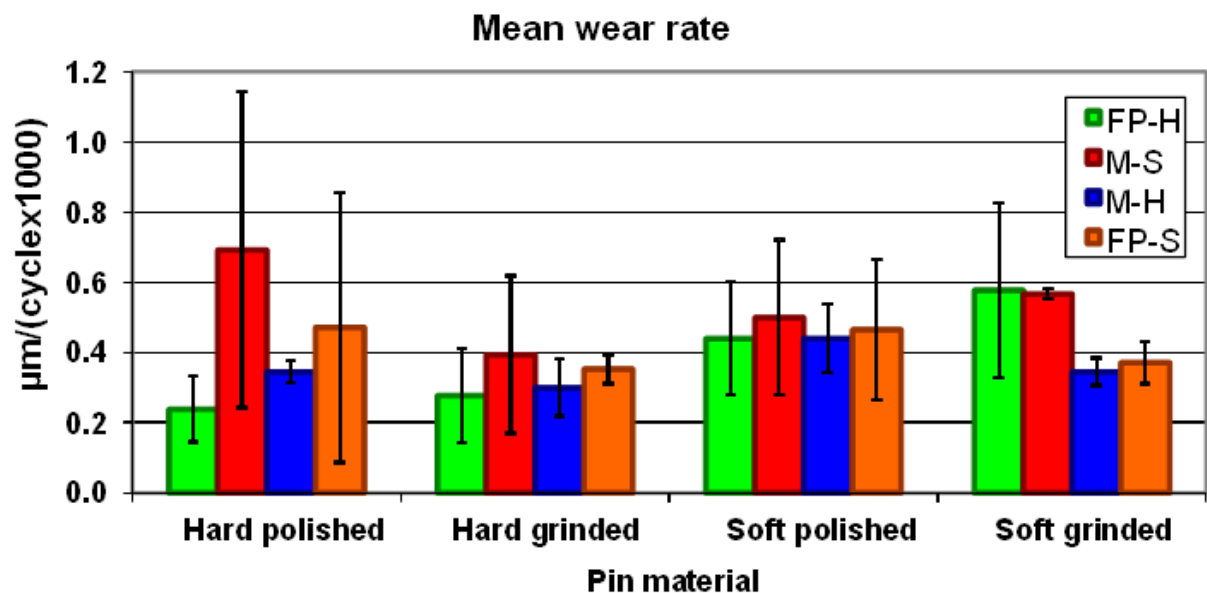
Fig. 4.43: Wear rates of disc materials calculated as slope of the tribotest curve in the stable test zone towards the end of the experiment (within the last 8 hours) in μm/ cycle·1000
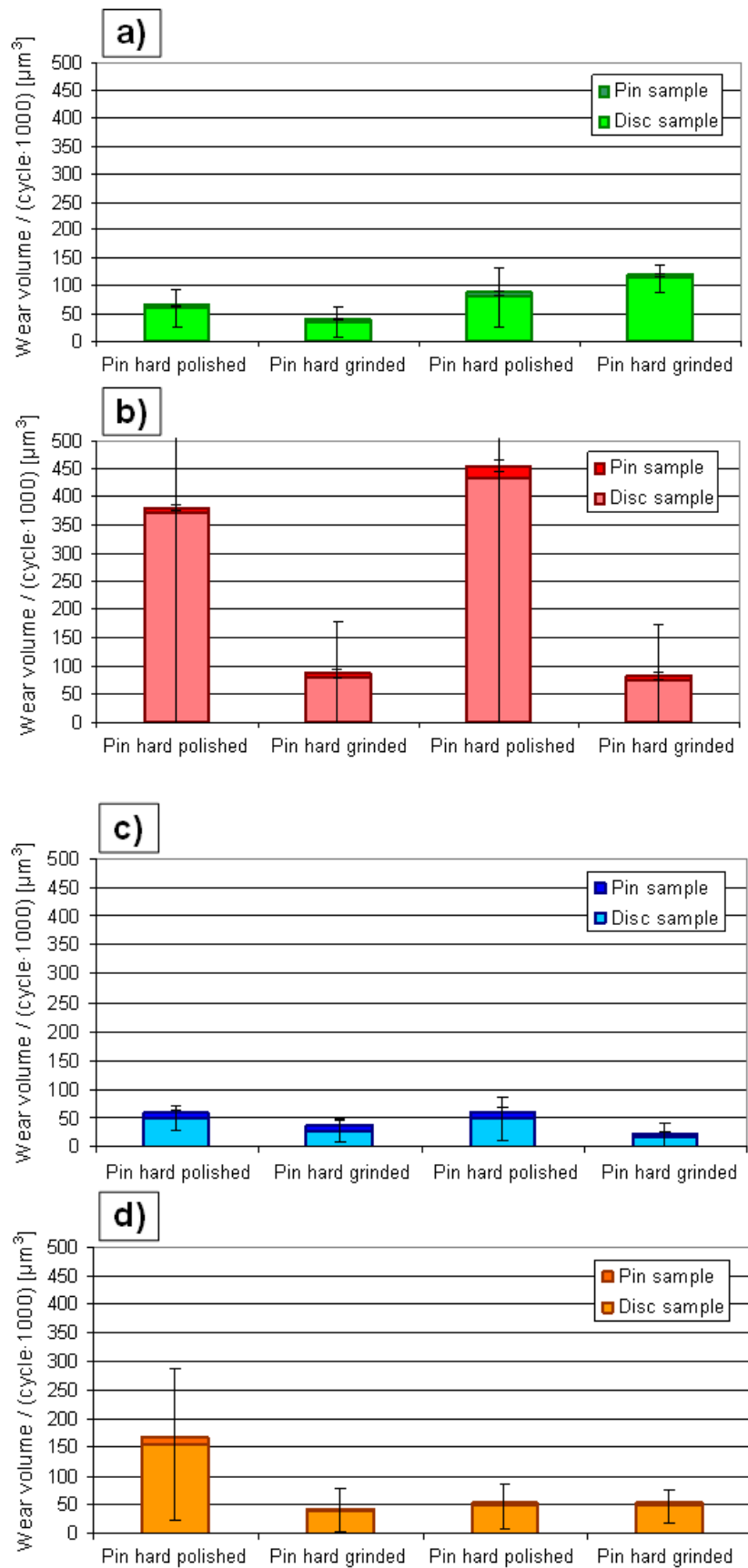
Fig. 4.44: Wear volume of selected basic body materials a) FP-H, b) M-S, c) FP-S and d) M-H
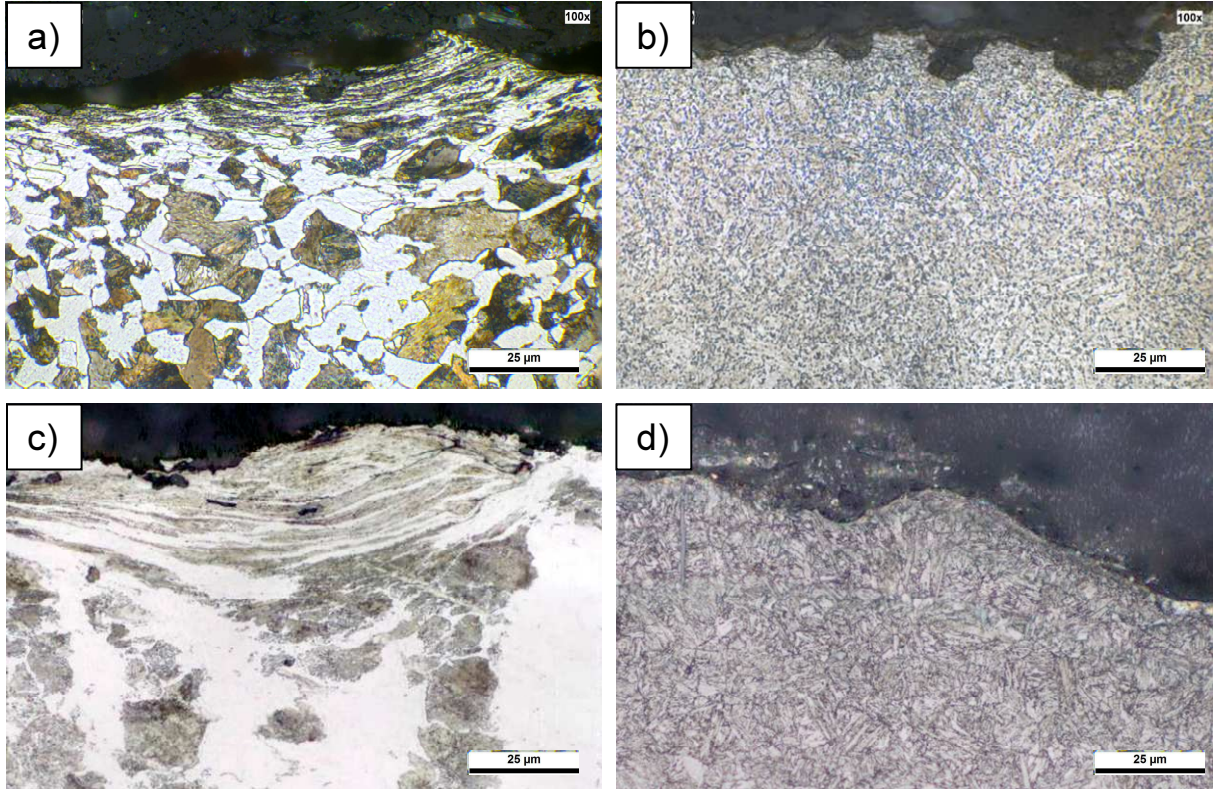
Fig. 4.45: Microstructure cross-sectional cuts of basic body materials with the tribological influence on top of the image: a) FP-H, b) M-H, c) FP-S, d) M-S) after tribotest with hard pin material
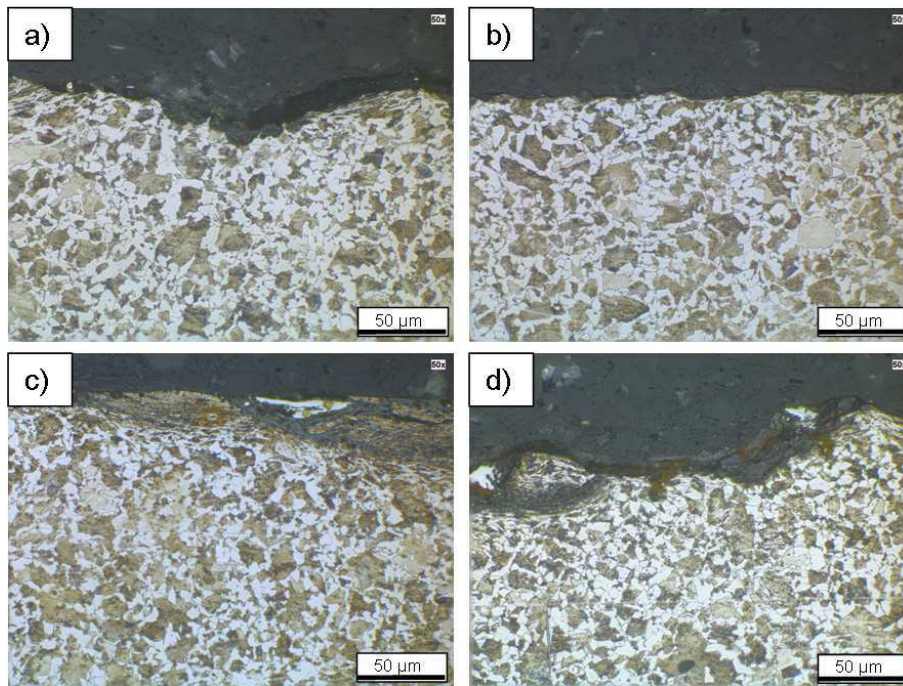
Fig. 4.46: LOM images of cross sections of wear tracks for FP-H tested with all pin materials: a) hard pin polished; b) hard pin grinded; c) soft pin polished; d) soft pin grinded
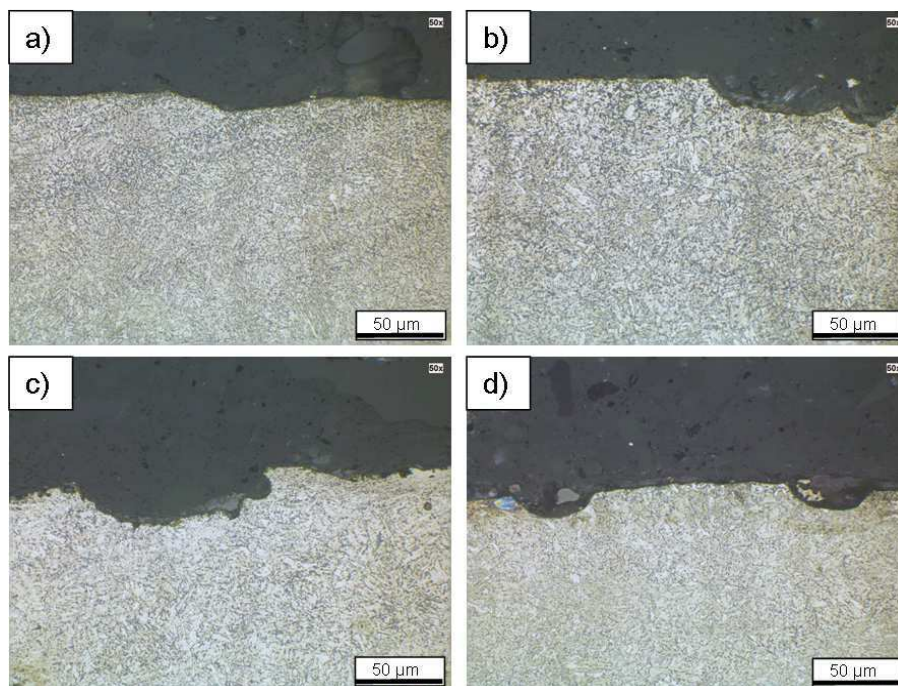
Fig. 4.47: LOM images of cross sections of wear tracks for M-S tested with all pin materials: a) hard pin polished; b) hard pin grinded; c) soft pin polished; d) soft pin grinded
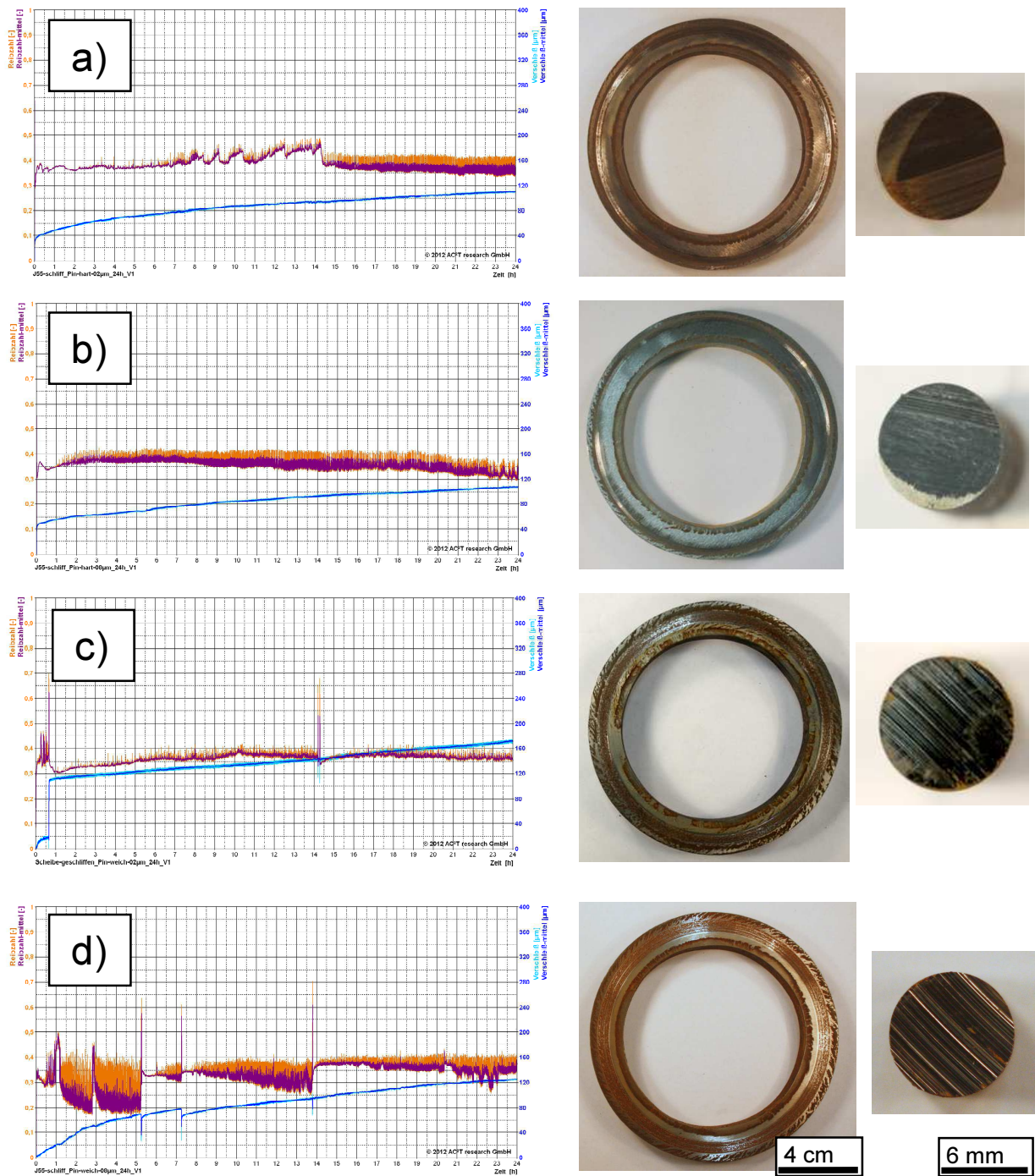
Fig. 4.48: Test curves and macro images of pin-on-disc tests for FP-H steel material with
a) pin hard polished, b) grinded, c) pin soft polished, d) grinded;
blue: wear; orange: friction coefficient; scales: 0-400 µm (wear), 0-1 (friction coefficient)
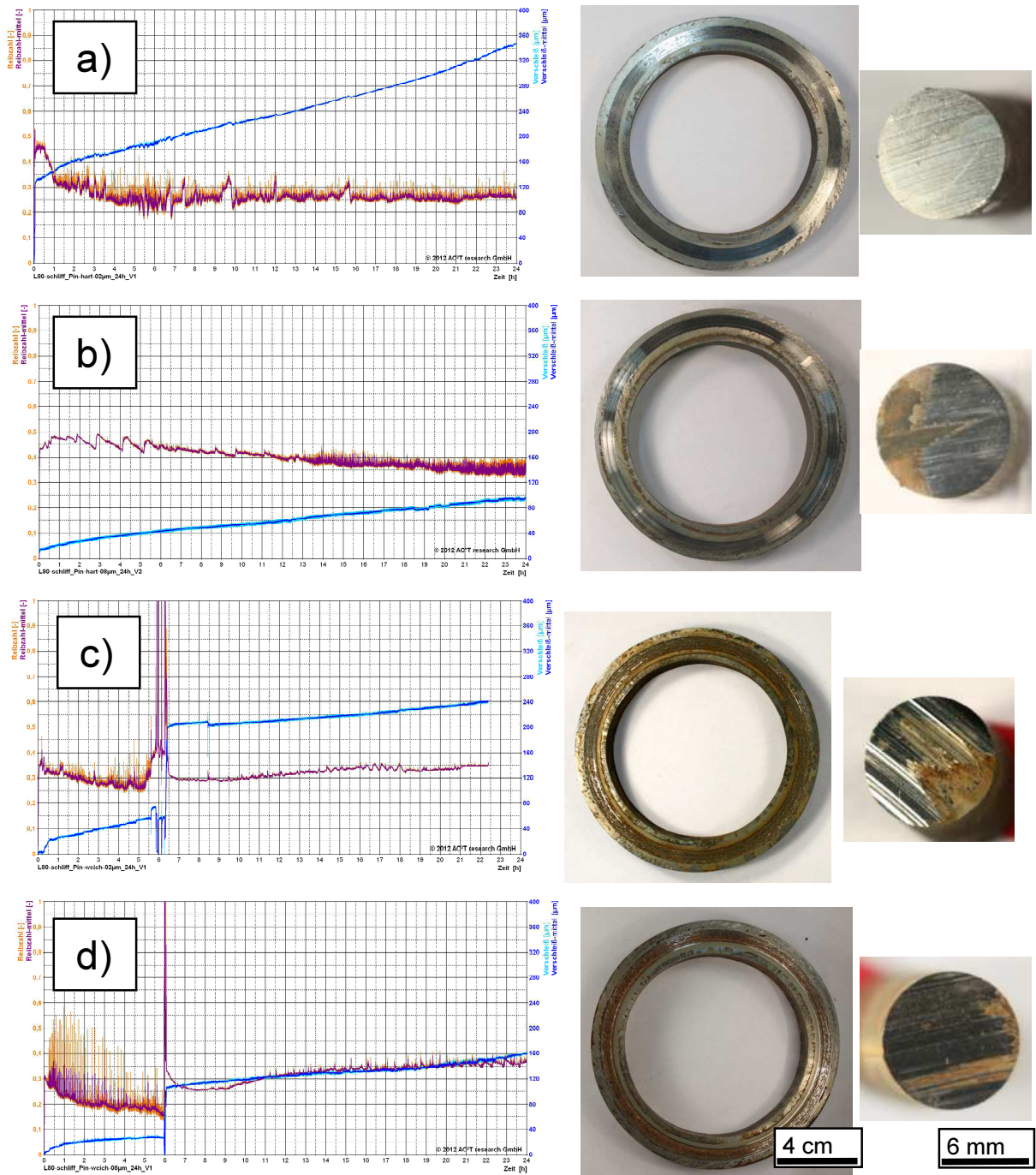
Fig. 4.49: Test curves and macro images of pin-on-disc tests for M-S steel material with

a) pin hard polished, b) grinded, c) pin soft polished, d) grinded;

blue: wear; orange: friction coefficient; scales: 0-400 µm (wear), 0-1 (friction coefficient)
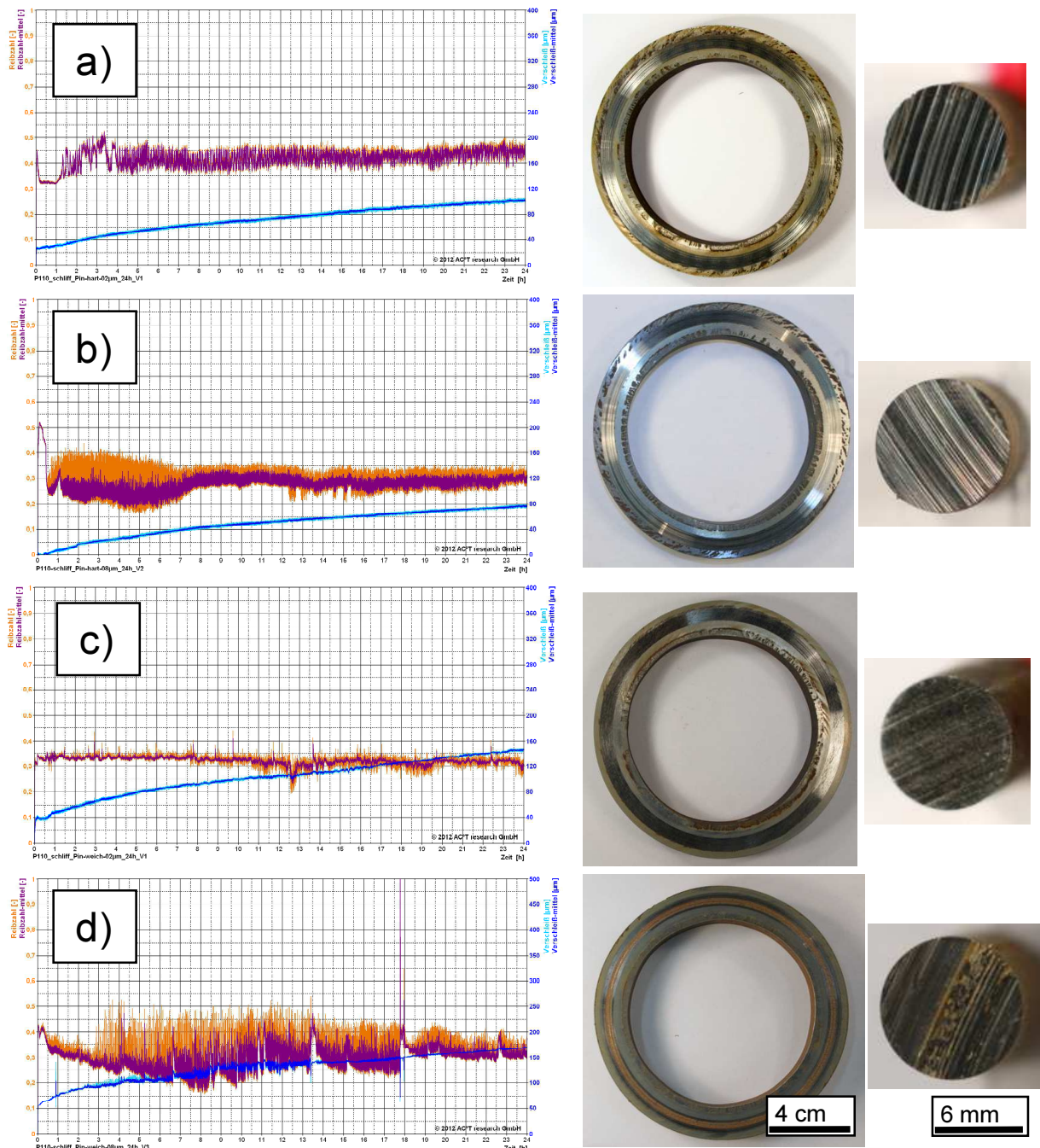
Fig. 4.50: Test curves and macro images of pin-on-disc tests for M-H steel material with
a) pin hard polished, b) grinded, c) pin soft polished, d) grinded;
blue: wear; orange: friction coefficient; scales: 0-400 µm (wear), 0-1 (friction coefficient)
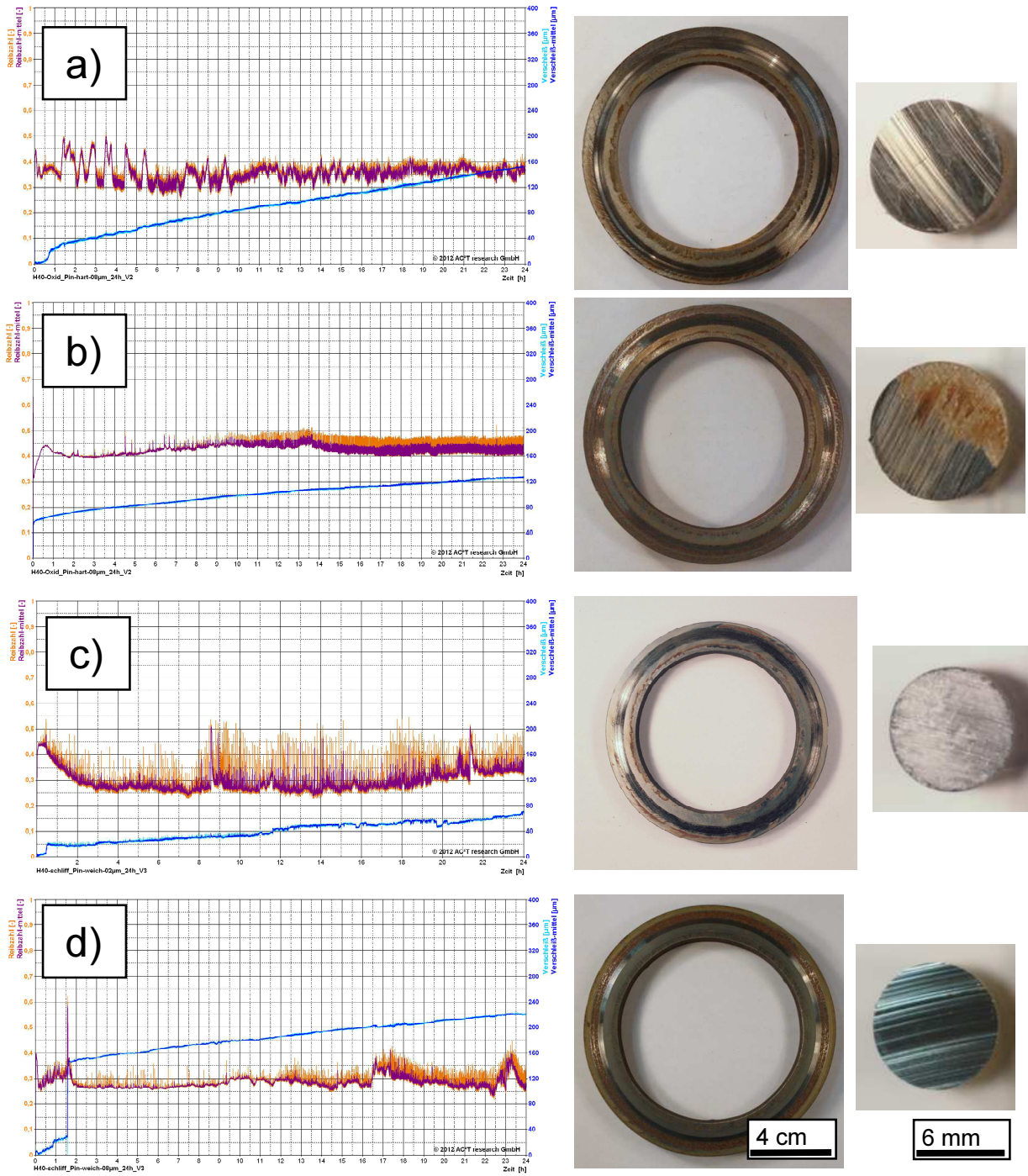
Fig. 4.51: Test curves and macro images of pin-on-disc tests for FP-S steel material with

a) pin hard polished, b) grinded, c) pin soft polished, d) grinded;

blue: wear; orange: friction coefficient; scales: 0-400 µm (wear), 0-1 (friction coefficient)

4.5. Static corrosion investigation of selected basic body samples

Static corrosion tests were performed on one side to obtain similar damage mechanisms as observed for field samples. On the other side, the influence of the wear history of the steel samples on corrosion behavior was investigated. Therefore, samples of sliding wear tests were corroded under the same conditions as unworn samples.

Results show that there is an important influence of the wear history of a steel sample on the corrosion performance. [cf. 74]

4.5.1. Introductional tests for the evaluation of the test method

At first, tests were performed in order to find out if similar corrosion behavior to the damage analysis can be obtained. The samples are placed in the medium, which is purged with CO_2 and heated to 60°C for a defined test duration. In order to simulate wear and corrosion mechanism of the real system in lab-scale, samples were first worn in steel-wheel (for comparative tests) in pin-on-disc tribometer followed by corrosive testing as described. After tribological and corrosive testing, the samples were analyzed using SEM-EDX, and compared to the analysis of the real system samples (see chapter 5.5). Fig. 4.52 shows an example for a worn and corroded steel sample, which are later compared with corroded field parts.
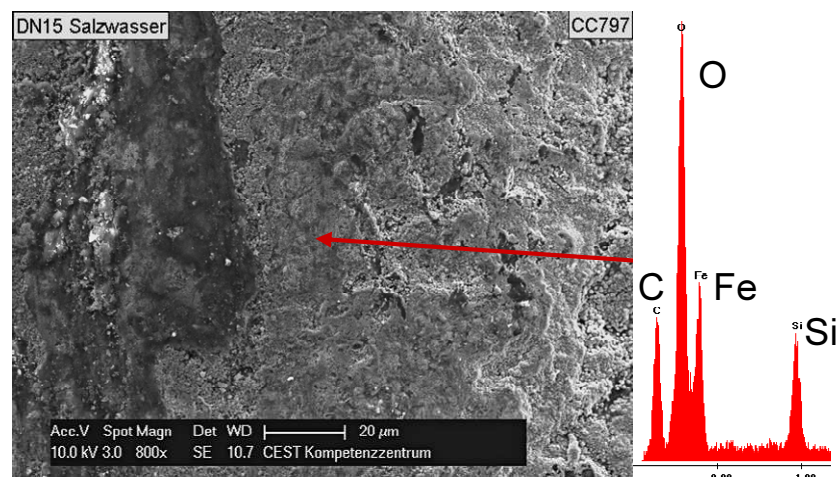
Fig. 4.52: Example for worn (steel-wheel tribotest) and corroded steel sample [cf. 74]

4.5.2.   Corrosion tests on worn and unworn basic body materials

The first corrosive tests were performed on all selected basic body steel materials (FP-H, M-S, FP-S, M-H) in unworn state after sample preparation (grinding) as well as after wear testing with pin-on-disc sliding wear test with hard pin material of initial polished surface. Corrosion tests have been performed in solutions up to 1.5 wt% sodium chloride (NaCl) solution under constant CO_2 gas purging (300 ml/min) at 60°C. Testing time was 72 hours with three tests performed. All the samples of the three corrosion tests have been weighted before and after the test. The mass loss was calculated and set to reference to the area of corrosive attack, calculating the mass loss per area in mg per cm^2 (Fig. 4.53) shows the quantitative results. The sample M-S shows high deviation. Also the FP-S shows a higher variation than FP-H and M-H. Compared to each other, no pattern of microstructure or hardness influence can be seen as FP-H shows the lowest and FP-S the highest mass loss per area. All in all, the values are approximately within the statistical insecurity. In general, the mean values for the worn samples are higher than for the plain samples, but also the deviation is higher. These values can either be within the statistical insecurity of the worn samples and the plain samples. The high differences may come from the evaluation method, because the evaluation of the area of the ring sector cuts is not trivial.
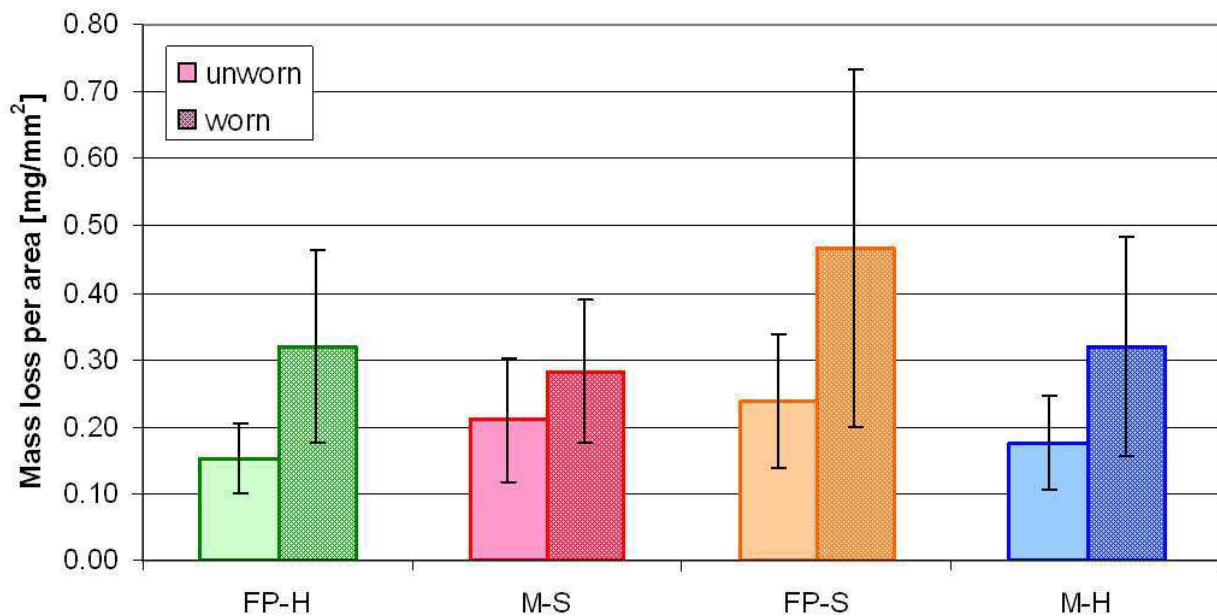
Fig. 4.53: Mean mass loss per area diagrams for unworn (light colored) and pre-worn (shaded) samples
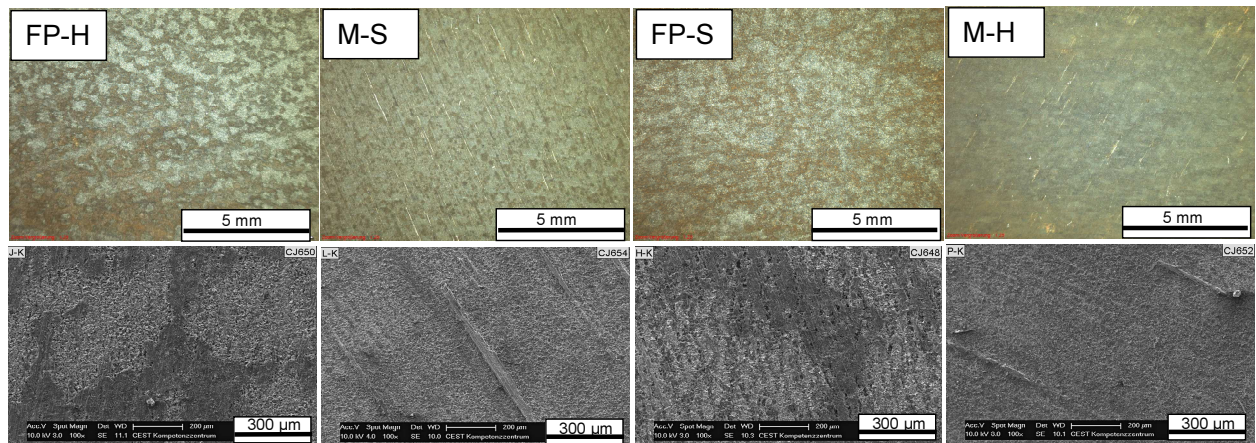
Fig. 4.54: Stereomicroscopical (upper row) and SEM images (lower row) of
unworn corroded steel materials
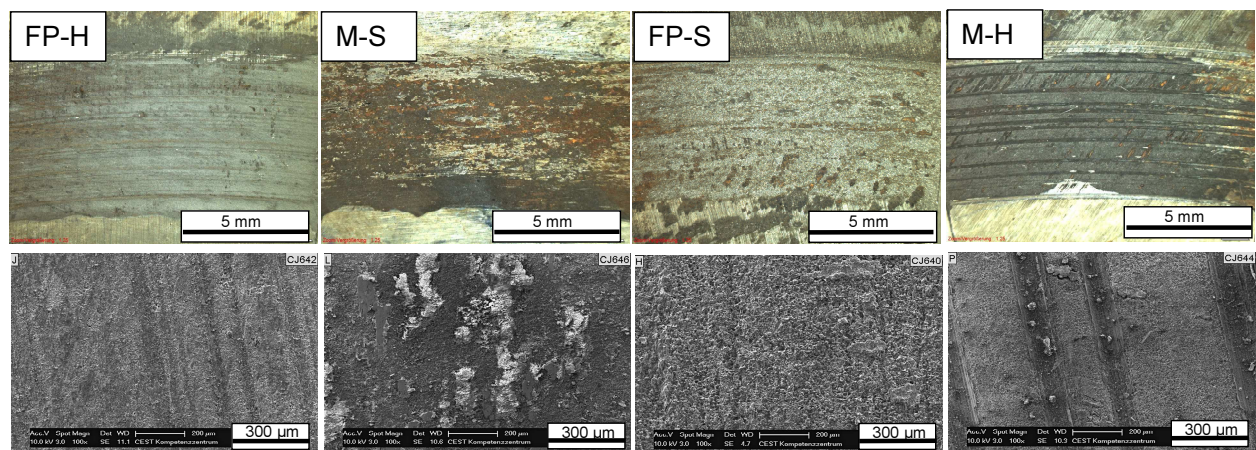
Fig. 4.55: Stereomicroscopical (upper row) and SEM images (lower row) of
pre-worn corroded steel materials

It has to be considered that to make obtained corrosion values of unworn materials comparable to them of worn materials, the unworn materials have to be brought to the same initial roughness as the worn materials, as increased roughness leads to increased surface for corrosive attack and therefore higher corrosive attack. Thereto unworn samples were preconditioned by grinding. Also, a single time span is insufficient to show the evolution in corrosiveness, hence corrosion times have been chosen for 48, 72 and 96 hours. Another convention was taken to illustrate obtained values in corrosion rate rather than mass loss per area, which simplifies the evaluation of different time spans.

The influence of the wear history of the basic body steel sample was tested within these experiments. The basic body samples FP-H, M-S, FP-S and M-H were worn with sliding wear test using a pin-on-disc tribometer. Basic body steel corrosion samples were cut out of a worn steel disc sample. The end roughness of these samples was evaluated to be a R_a of $\sim$ 2 µm. Unworn samples were grinded and brought to this roughness. Corrosion tests were performed in 3 wt% NaCl for all materials and additional tests in 1.5 wt% NaCl were performed for FP-H and M-S materials. Both conditions were done under 400 ml/min CO_2 gas flow.

Tests with 1.5 wt% salt concentration in comparison to those values obtained for 3 wt% for the same time spans were obtained and compared for FP-H and M-S basic body steel materials in unworn state with an initial roughness of $R_a \sim$ 2 µm (Fig. 4.56). From 1.5 to 3 wt% NaCl in the solution, the obtained corrosion rate values experience a significant rise for higher salt concentrations, leading to up to four times higher corrosion rates. Martensitic M-S performs significantly better than ferritic/pearlitic FP-H. The corrosion rates obtained for 3 wt% NaCl for M-S are as high as for FP-H obtained for 1.5 wt% NaCl.

On the contrary to the previous tests, pre-worn samples showed lower corrosion rates than unworn samples (Fig. 4.57). Ferritic/pearlitic materials showed up to 3-4 times higher corrosion rates than martensitic materials in unworn state. For corrosion tests with worn samples it was found that FP-H basic body samples performed better than M-S samples. In general, the samples which resulted better in corrosion test after tribotesting also resulted in better tribological behavior regarding wear behavior during wear test (no presence of adhesive effects) and wear rates together with deviations of results. Ferritic/pearlitic FP-H, which experiences plastic deformation and grain refinement during tribotest, might gain a positive effect in corrosion resistance through these plastic deformations. On the other side, martensitic M-S, which experienced the formation of many cavities due to adhesive effects experiences increasing corrosion rates. Harder martensitic M-H, which did not experience much formation of cavities and adhesive wear, respectively during tribotesting, did not result in increasing corrosion rates for samples corroded after tribotest. Softer ferritic/pearlitic FP-S material, which also showed plastic deformations after tribotesting, also experienced decreasing corrosion rates after wear testing, albeit not to a high extend as observed for FP-H material.
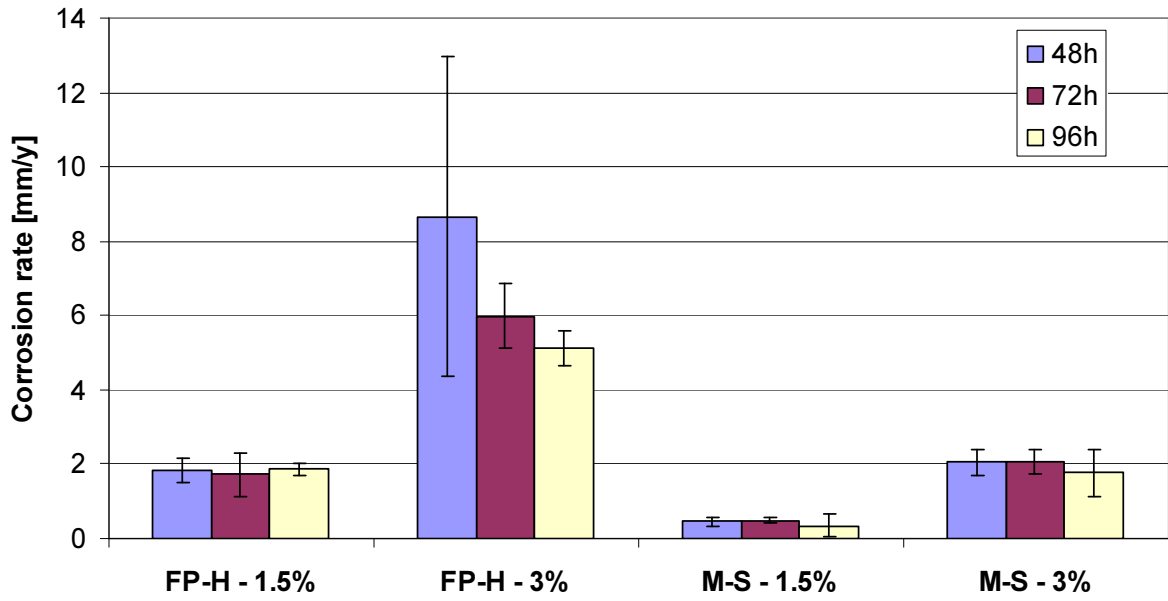
Fig. 4.56: Corrosion rate calculated for unworn FP-H and M-S samples corroded for 48, 72 and 96 hours in a 1.5 wt% and 3 wt% NaCl solution
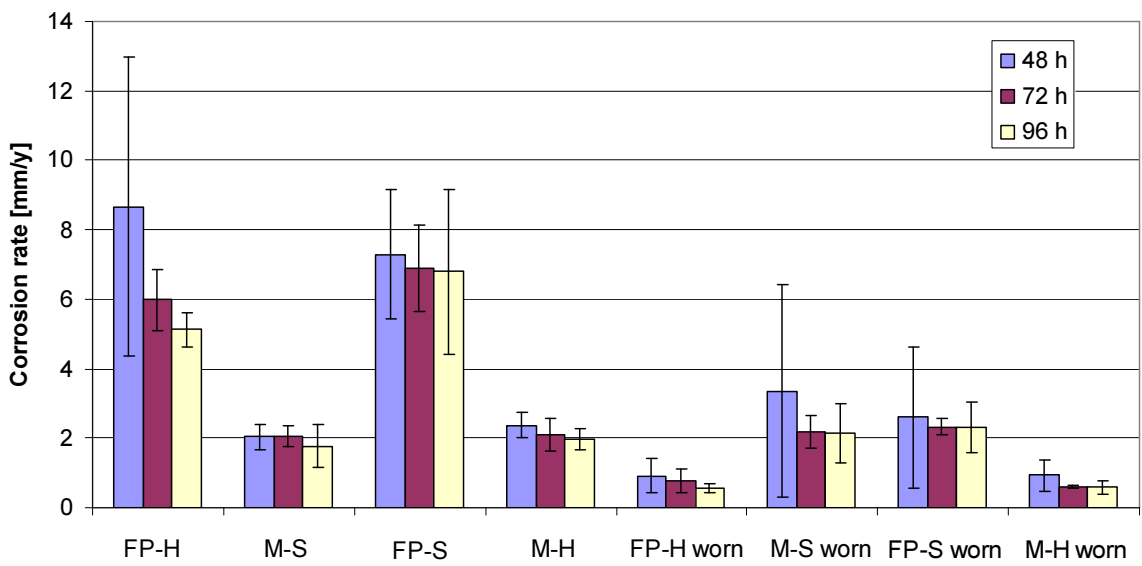
Fig. 4.57: Corrosion rates for unworn samples (left four) and pre-worn samples (right four)

4.6. Performance at combined sliding corrosion tests

In the previous chapters, tests were performed under tribological stress and then under corrosive conditions. The following tests were performed under both tribological and corrosive stress simultaneously. Effects observed for these tests are compared to previous studies. Also, tribological tests without CO_2 gas in the medium (purged with N_2) were performed to compare tribocorrosive and tribological tests of this system. [cf. 70, 76, 77]

As samples for these tests, the steel samples FP-H and M-S were chosen, as they are mostly used for real applications. First tests were performed without any sample preparation of the steel samples. For the comparison of the influence of the material microstructure, the surface was pickled first in order to gain a regular surface (see chapter 3.3.3). As counter body, Ni-base coated samples similar to the hard coating samples with polished surface were used.

The main purpose of these studies is the matching between the damage images of field samples and simulation of the damage mechanism in lab-scale, in order to optimize the tribosystem in lab-scale in the future.

4.6.1. Initial tests performed on steel samples with oxide layer

These tests were performed on steel samples of the material FP-H. Test parameters were chosen as close as possible as predominant in typical field application. CO_2 pressure was 3 bar. Temperature was 60°C. Two tests with different test duration of 2.5 and 6 days were performed. The wear depth was calculated over the wear area and volume via mass loss and density of the material in these first experiments. Fig. 4.58 shows an example for the worn steel and Ni-base layer samples.

The calculation of the wear area was performed using the freeware program ImageJ®. With this program, it is possible to draw an approximation around the wear track and calculate the area. Over the weight loss and the density of the steel (7.8 g/cm³), the wear depth was estimated. As average mass loss, 10.9 g were calculated for the steel samples of the 2.5 day test and 22.3 g for the 6 day test. As average wear depth, 0.29 mm were calculated for the 2.5 day samples and 0.46 mm for the 6 day samples. These calculations lead to an estimated average wear rate of 4.4 µm/h for the 2.5 day tests and 3.5 µm/h for the 6 day tests.
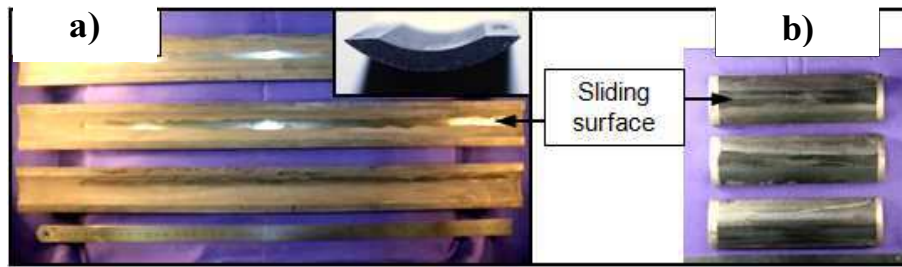
Fig. 4.58: Images of a) steel samples left image and

b) Ni-base layer samples after test [cf.76]

On one steel sample of 6 days testing period, SEM-EDX measurements have been performed. Clear abrasion marks are visible in the wear zone in Fig. 4.59 a). A detail of one of these abrasion marks is given in Fig. 4.59 b). While most of the abrasively loaded surface shows no corrosion layer formation (EDX measurements - Spot 638), deep wear tracks are covered in carbonates (Spot 639). Wear tracks are relatively shallow at this testing time, nevertheless material screening at application near conditions is possible and will be discussed in the following section.
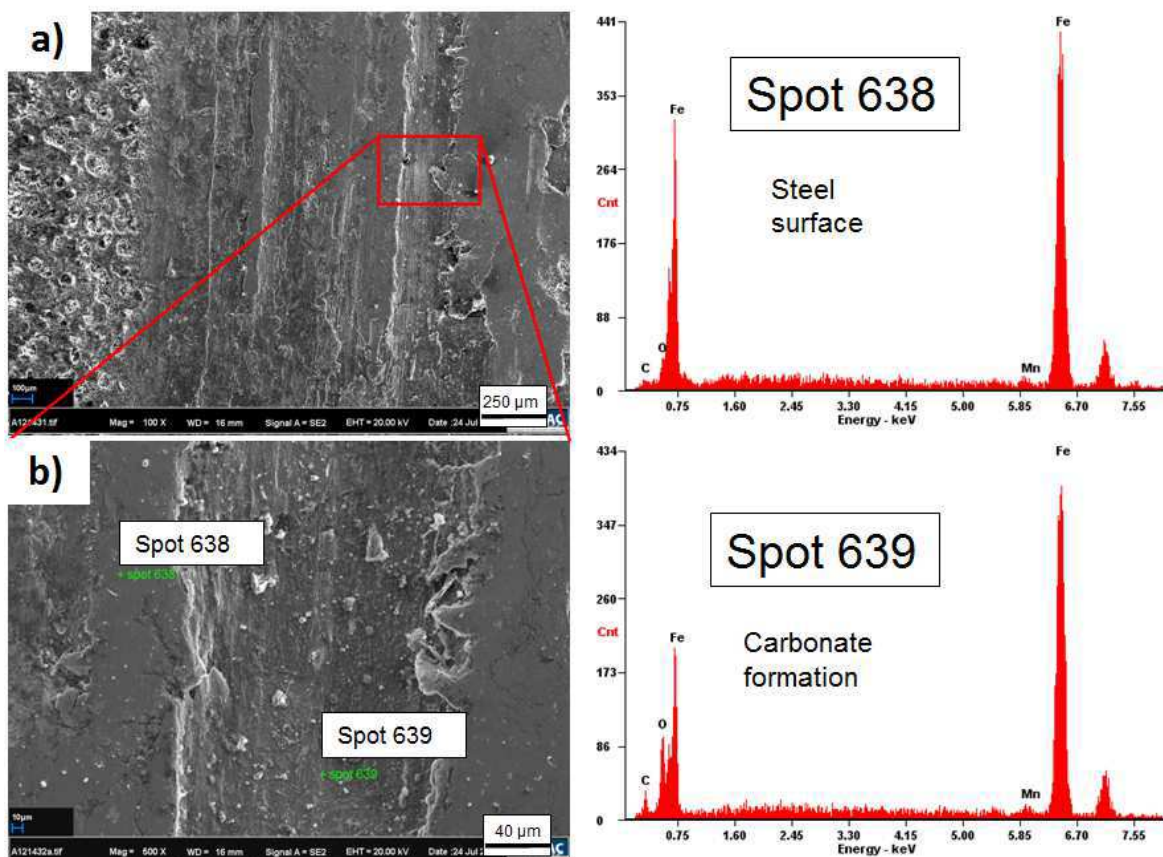
Fig. 4.59: SEM-EDX results for tested steel sample: a) overview image on sample together with

b): detail of a wear groove; EDX measurement of steel surface (spot 638) and of wear groove:

formation of carbonate due to lack of abrasion inside wear groove (spot 639) [cf. 70]

4.6.2.   Tribological and tribocorrosive tests of FP-H and M-S steel materials

For these tests, the materials FP-H and M-S were tribocorrosively and tribologically tested. In total, three test runs were performed for tribocorrosive (under combined CO_2 and NaCl) tests and two test runs for tribological (N_2 only) tests in comparison. Thereby it is possible to evaluate the influence of the corrosive medium on the tribological contact situation. Standard test parameters, which were used for these tests, are given in Table 3.4. [76]

Table 4.5 shows the wear volume results of typical samples out of the various tests. The wear volume for FP-H samples in tribocorrosive conditions is highest of all tests performed. The M-S samples show lower wear rates. The difference to pure tribological testing is significant.

Taking a closer look on the tribotest results for tribocorrosive and tribological tests, the friction coefficient is significantly lower in tribocorrosive environment (Fig. 4.60). For tribological tests, the friction coefficients are comparable to the tests performed with pin-on-disc tribotesting. [76]

Table 4.5: Average steel sample wear volume according 3D microscopical measurements on typical samples for tribological and tribocorrosive tests

Sample	Tribological wear volume under N_2	Tribocorrosive wear volume under CO_2 and NaCl
FP-H	429 ± 11 mm³	696 ± 13 mm³
M-S	413 ± 12 mm³	546 ± 20 mm³
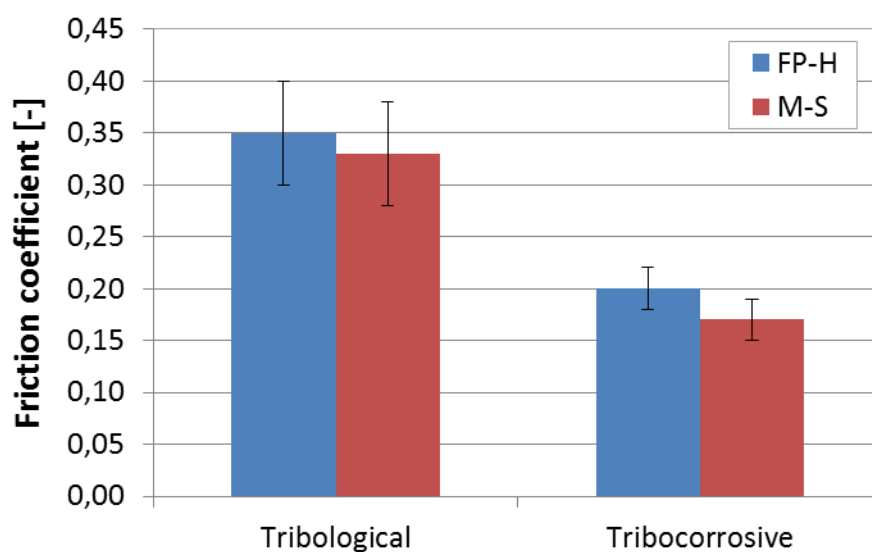
Fig. 4.60: Average friction coefficient during testing [cf. 76, 77]

For studying the surface structure of the worn steel samples, 3D microscopical measurements on the wear track in the area of highest wear attack, i.e. the middle of the sample, have been performed. Out of the data, the wear depth and wear width were calculated for the positions 25; 27.5; 30; 32.5 and 35 cm of the sample, where 30 represents the middle of the sample. The graphs in Fig. 4.61 and Fig. 4.62 show the wear depth as average and maximum depth in the measurement profile in μm, and the wear width as half width profile in mm (scaled to represent the wear track, total width is double the positive value). The results shown in these figures are representing the typical wear profile of the tribocorrosively and tribologically worn samples. Comparing the calculated wear depth and width between the FP-H tribocorrosive and tribological sample, it can be seen that the depth values of the tribocorrosively worn sample are higher and more regular pronounced than for the tribologically tested sample (Fig. 4.61). Also, the wear track is broader for the tribocorrosively tested sample. Both samples are showing an overall regular width throughout the middle of the wear track, where the measurement was performed. [70]

For the comparison of tribological and tribocorrosive wear of the M-S samples, the wear depth profile behavior is similar as for the FP-H samples, with the difference that the tribologically worn sample shows a more regular depth profile whereas the tribocorrosively worn sample shows a varying depth profile over the measured sample positions (Fig. 4.62). The track width is, as for the FP-H sample, significantly broader for the tribocorrosively worn sample.

Comparing M-S and FP-H wear depths and widths at tribocorrosive conditions the FP-H wear loss is slightly higher than for M-S samples. At tribological conditions they are quite similar.
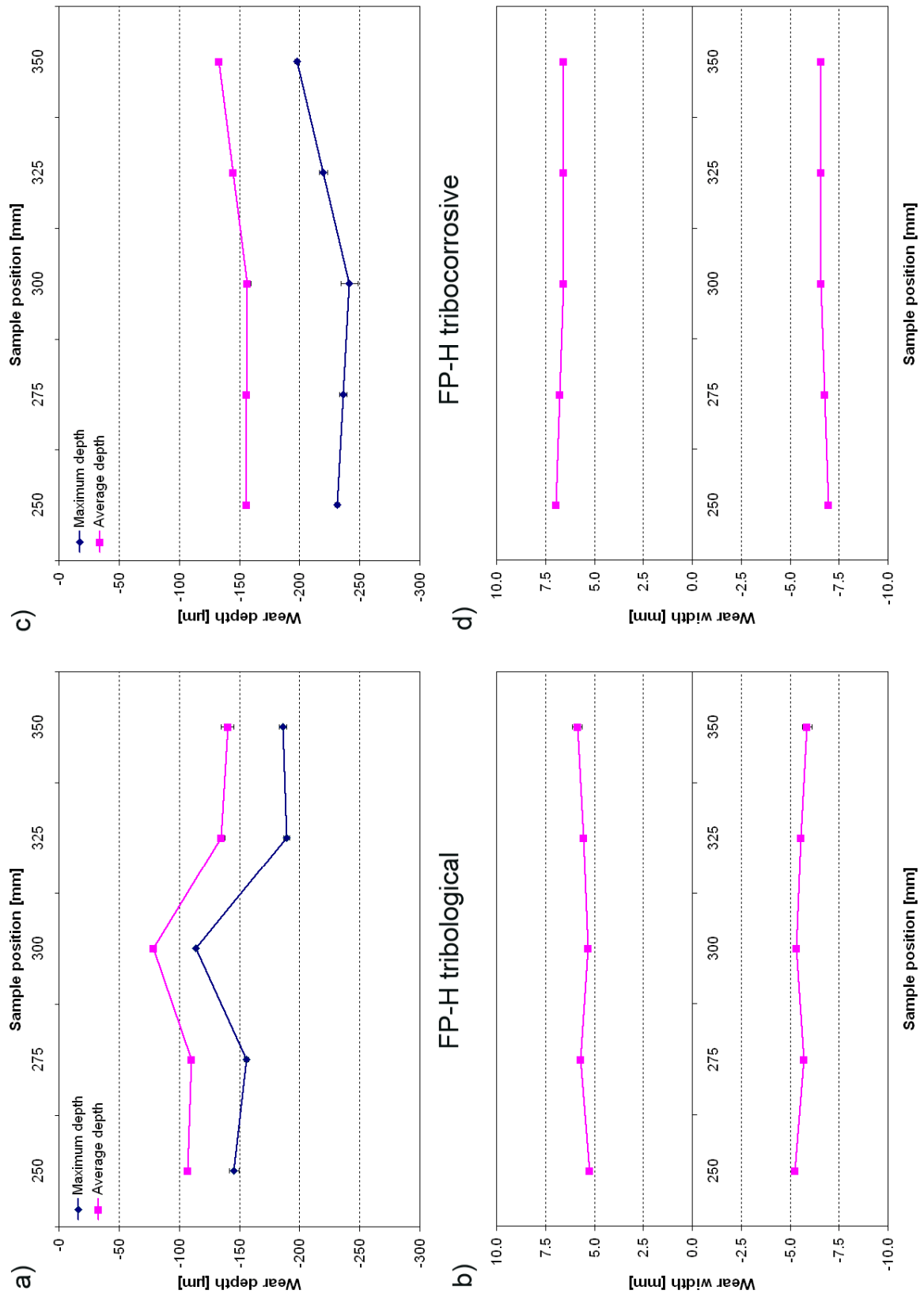
Fig. 4.61: Comparison of wear depth and track width of material FP-H tested under tribological and tribocorrosive conditions: tribological a) wear depth and b) wear width; tribocorrosive c) wear depth and d) wear width
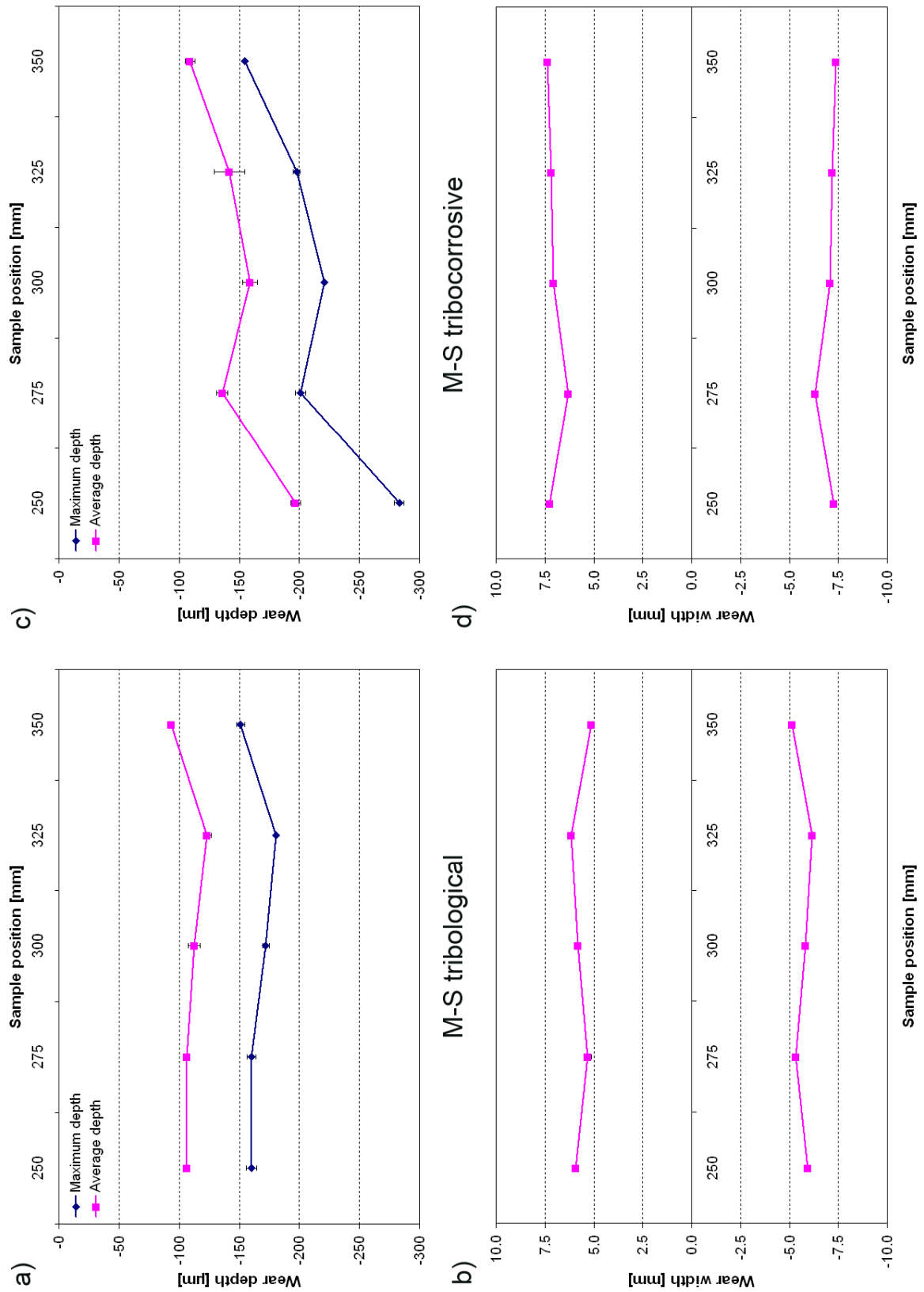
Fig. 4.62: Comparison of wear depth and track width of material M-S tested under tribological and tribocorrosive conditions: tribological a) wear depth and b) wear width; tribocorrosive c) wear depth and d) wear width

Investigating the images of the surface of the steel tubing samples, some differences between tests under tribocorrosive and tribological conditions become apparent. For FP-H surfaces (Fig. 4.63), testing without corrosives results in a surface where the center of the wear track is dominated by clear grooves, accompanied by plastic deformation towards the border between wear zone and base material. For the tribocorrosively tested samples, two dominant zones are present on the surface. The first zone shows the worn bare metallic steel surface as a result of contact with the counter body material. Grooves and wells allow the formation of corrosion products within, as they were observed for primary tests in Fig. 4.63, which are present as grey product on the surface. The same effects can be observed for M-S steel samples (Fig. 4.64), although the appearance is slightly different from FP-H samples. M-S tribologically stressed samples present a more intense grooving, tribocorrosively tested M-S samples exhibit more defined zones of tribocontact (metallic zone) and corrosion progress (grey corrosion products).

Also, cross-sectional cuts for light microscopy have been manufactured for the characterization of the wear and corrosion influence on the steel surface. For FP-H, it can be clearly seen that for tribological testing that plastic deformation and grain refinement beneath the surface is evident for ~ 30 µm depth (Fig. 4.65a). On the other side, at tribocorrosive testing, no plastic deformation or grain refinement can be observed, but a rough surface with some corrosion products in the slits and selective corrosion at pearlitic areas can be observed (Fig. 4.65 b).

For M-S steel, also severe plastic deformation occurs at tribological testing with kink formation and material deflection (Fig. 4.66). For the tribocorrosively stressed sample, similar to the one of the FP-H sample, the M-S sample does not show severe plastic deformation on the stressed surface. An intermixing of corrosion products into the surface is also possible, as partially visible in Fig. 4.66 b).

It can be concluded, that tribocorrosive testing entails other damage mechanisms as seen for sliding testing, leading to higher wear rates. The corrosion products show essential influence on the wear behavior. [76]
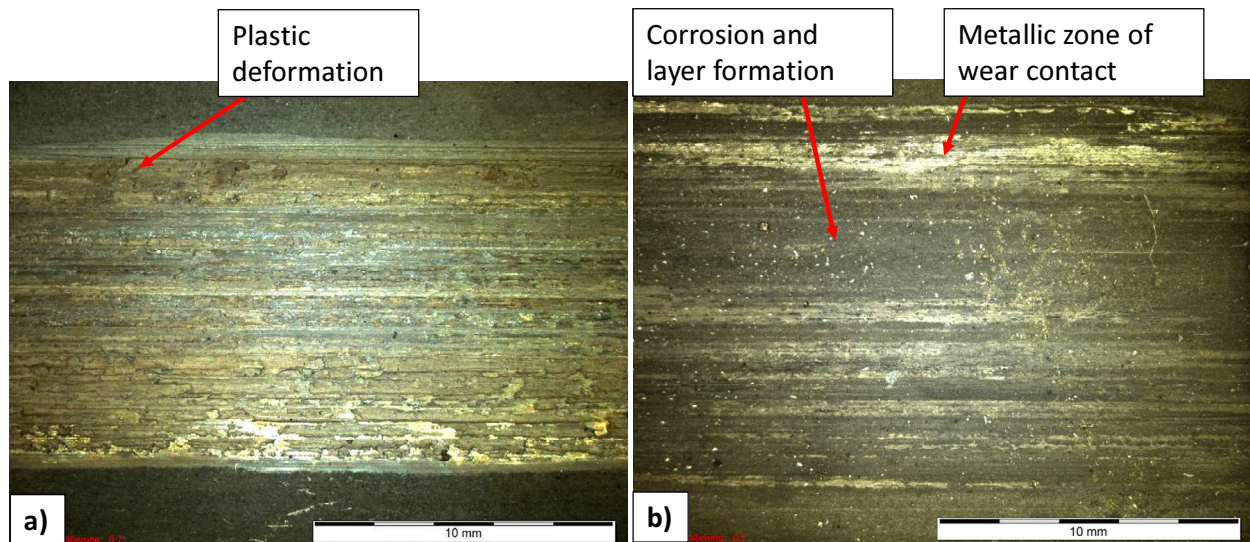
Fig. 4.63: Stereo images of the surface of sample FP-H: a) worn without corrosive medium and b) under tribocorrosive conditions [cf. 76]
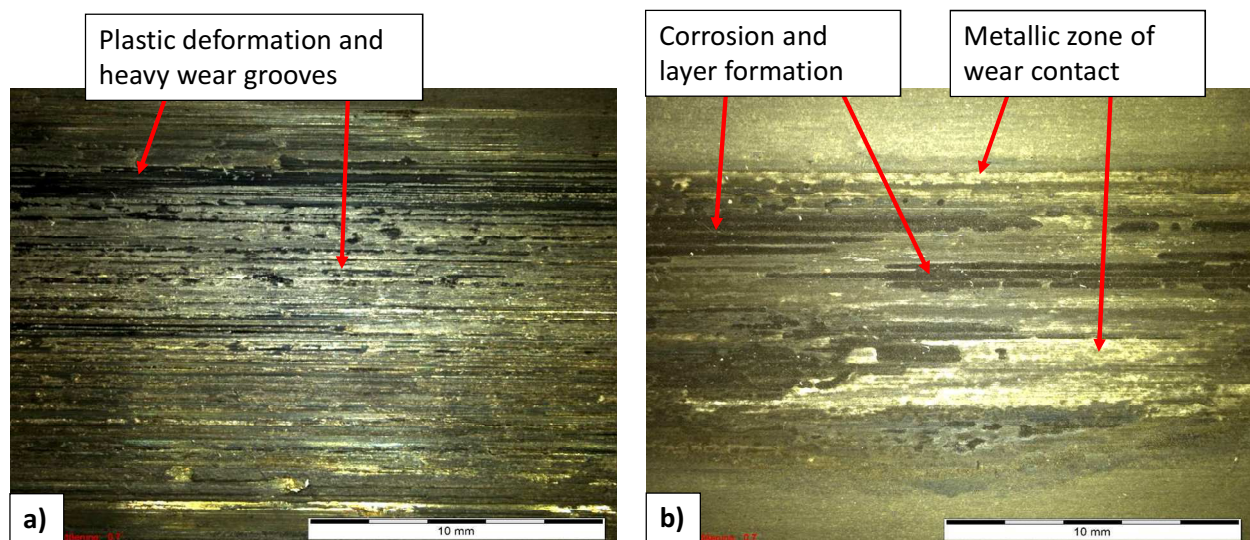
Fig. 4.64: Stereo images of the surface of sample M-S: a) worn without corrosive medium and b) under tribocorrosive conditions [cf. 76]
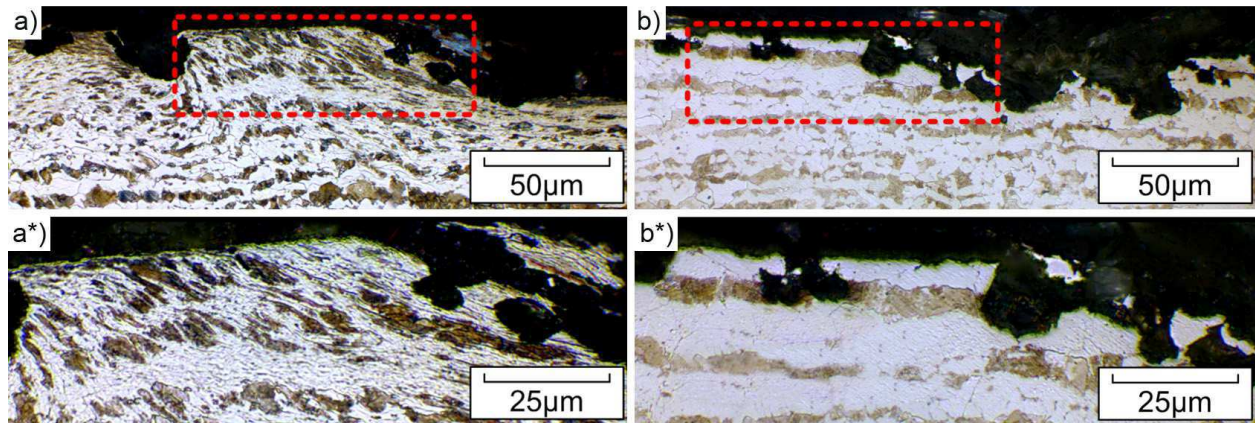
Fig. 4.65: LOM images of sectional cuts (overview plus detail *) of sample FP-H: a) worn without corrosive medium and b) under tribocorrosive conditions [cf. 76, 77]
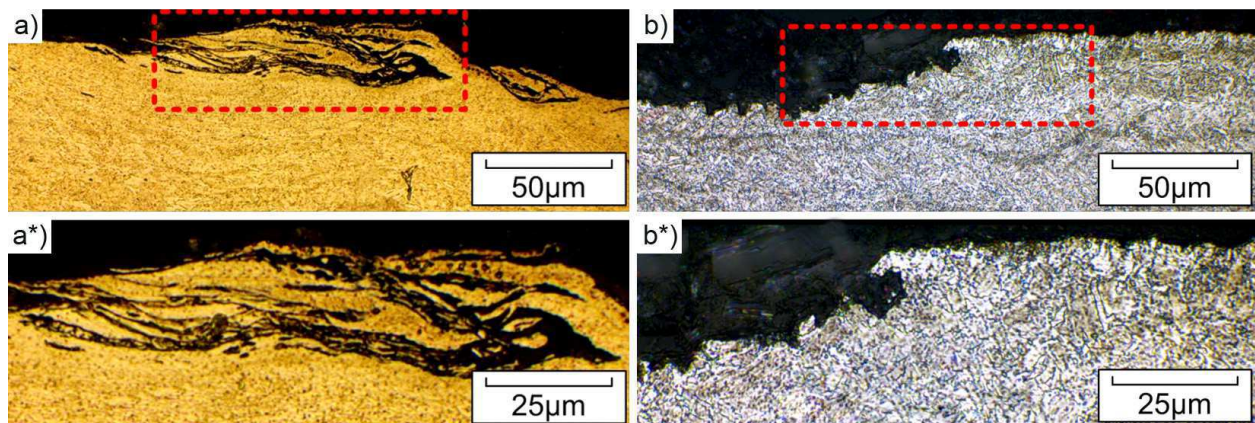
Fig. 4.66: LOM images of sectional cuts (overview plus detail *) of sample M-S: a) worn without corrosive medium and b) under tribocorrosive conditions [cf. 76,]

5. Discussion

Within this work, the influence of abrasion and corrosion on carbon steel materials, together with the influence of microstructure and hardness of steel and counter body material, was investigated. Through these performed investigations, better knowledge and deeper understanding of wear and corrosion mechanisms occurring for abrasion of steel in corrosive CO_2 media was achieved. In the following paragraphs, the results obtained for the performed investigations are summarized, discussed and also compared to the findings of the literature research. The investigation of damaged steel tube parts for a real application offered useful information for the occurring damage mechanisms. The knowledge obtained was used for the setup of the performed tests on various steel materials and other parameters influencing the results for wear and corrosion. Also, the obtained knowledge from literature research was taken as base for our investigations.

5.1. Summary for analysis of worn and corroded steel parts during application

In real application, steel tubes are often used for downhole exploration tasks, e.g. geological investigations. The used equipment is often placed on a rod, which is moving up- and downwards. Due to bending of the rods caused by high forces of the movement, parts of the equipment or joints of the single rod parts are moving against the steel tube (basic body). These joints are often made of steel covered with a wear and corrosion resistant Ni-base layer (counter body). Due to this movement of the counter body against the basic body, the basic body is abraded, exposing metallic steel surface. Therefore, the predominant corrosive medium, as in the investigated case it has been water with carbon dioxide and NaCl solved in it, is able to perform corrosive attack on this freshly exposed steel surface. The damage images of the described mechanisms are investigated and presented in the following paragraphs.

On the steel sample of field application, mechanical damage visible on the outside of the tubing occurred due to an excentric position of the equipped counter body, leading to high contact load of ~ 600 to 1200 N punctual on the basic steel body (Fig. 5.1). This pressure combined with an up- and down movement of the counter body led to abrasion on the basic body surface. The crack on the outside and the local wear on the inside of the tube are an indication for damages as a result of this combination. On the steel surface of the worn basic body, crack formation, wear grooves and delamination was observed as a result of fatigue wear. Investigations on the side

without intense abrasion were performed in order to identify the products formed on the layer on the inner side of the tubing (Fig. 5.2).

Fig. 5.1: Local wear damage on the carbon steel tube, which was used in real application, seen outside as crack [cf. 74]

Observed area of corrosive attack
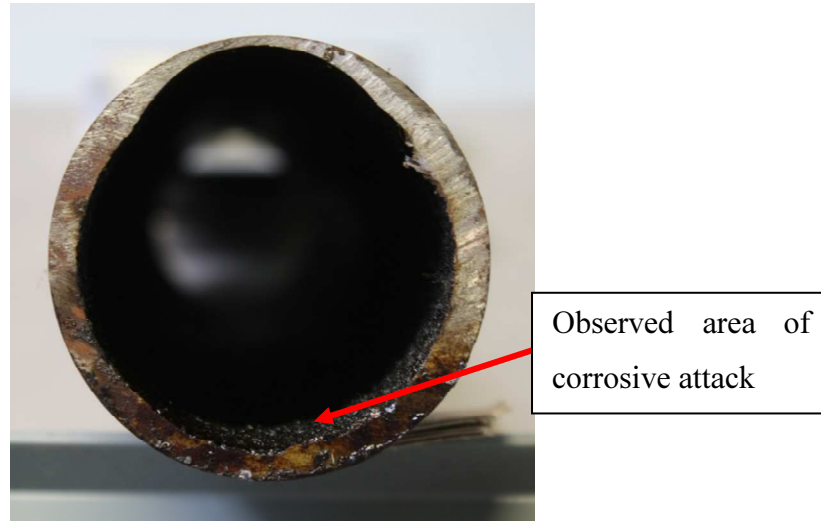
Fig. 5.2: Macroscopical investigation of layer formation for unworn side of the carbon steel tube of real application [cf. 74]

Macroscopical investigations on the inner side of the damaged part (Fig. 5.1 b) led to the conclusion that on the area of severe damage, a formation of a protective corrosion layer did not occur due to constant abrasive attack. Abrasion led to the exposure of fresh steel surface, where localized corrosion may have taken place. On the side where no abrasion occurred, the present

carbon dioxide (CO_2) in the liquid medium formed a corrosion layer on the equipped low carbon steel material without the influence of abrasion from the counter body.

On SEM images of the damaged surface, a porous structure of the formed corrosion layer was observed (Fig. 5.3 a). The layer observed showed the characteristics of a Type I scale as it was described in the literature [10]. It might offer possible protection against surface corrosion, but the porosity channels allow chlorine to perform pitting corrosion. Fig. 5.3 b) gives an indication to abrasive wear marks and fatigue wear and delamination processes. Also it is considered that the microcracks, which are formed by the stress, are contributing to the formation of visible cracks. EDX measurements showed Fe, O and C as main elements of the formed layer, which most likely consists of the respective corrosion products, e.g. siderite $FeCO_3$.
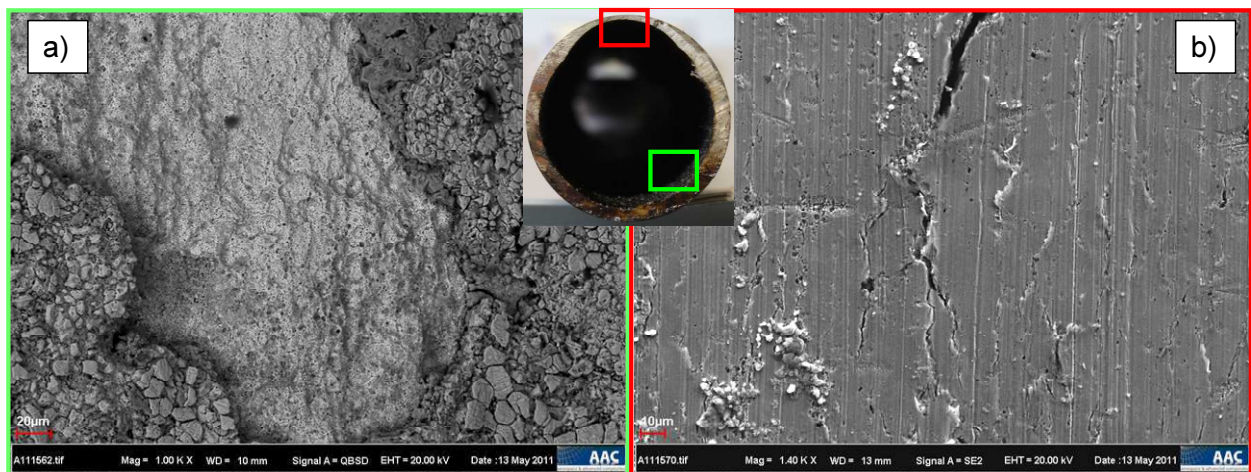
Fig. 5.3: SEM images on the surface of the carbon steel tube, which was used in real application, obtained for the area of corrosion layer formation (a) and high abrasive wear (b) [cf. 74]

Performed XPS measurement results (Fig. 4.6) showed an increase of the carbon content for measurements of areas from the crack zone towards the zone with less abrasion. On the other side, iron shows a decrease from the crack zone toward the zone with less abrasion. This goes conform with the observation made for macroscopical investigations indicating an increase of the formation of a corrosion product layer from crack to unworn area of steel sample. Carbon amounts higher than those of iron might also be an indication of residual hydrocarbons on the surface or inside the layer.

From the layer obtained on the side of no abrasion, siderite was verified to be a main component through performed XRD measurements (Fig. 4.8). Also other iron species formed, such as

magnetite, wustite or goethite, were detected. As the steel parts are used at different geological locations, the predominant corrosion product is also dependent on the conditions predominant at certain locations. Nevertheless, siderite is the main corrosion product species formed under these conditions.

In summary, in the system of the steel basic body tubing with a counter body abrading the steel wall with additional corrosive influence of liquid medium with CO_2, the damage on the basic body mainly originates of the excentric position of the counter body (often located on a moveable rod, a bending of this rod leads to a dislocation of the counter body, which therefore comes into contact with the basic body material) during its movement, which led to one-sided abrasion. In consequence of this, the tubing was worn the loaded side. On the opposite position, conditions for the growth of a corrosion layer are present. Predominant mechanisms are abrasive wear and fatigue of the material. The fatigue wear was also benefited by the harsh chemical environment containing carbon dioxide. The localized thinner wall plus the predominant pressure also have led to stress cracking corrosion. On the other tube side, the corrosion was allowed to proceed freely, precipitating the siderite layer corrosion product. SEM analysis showed a spongy surface of this siderite layer containing pits which would promote pitting corrosion. Fig. 5.4 summarizes the tube divided into the main damage zones with a description of the predominant failure mechanisms.
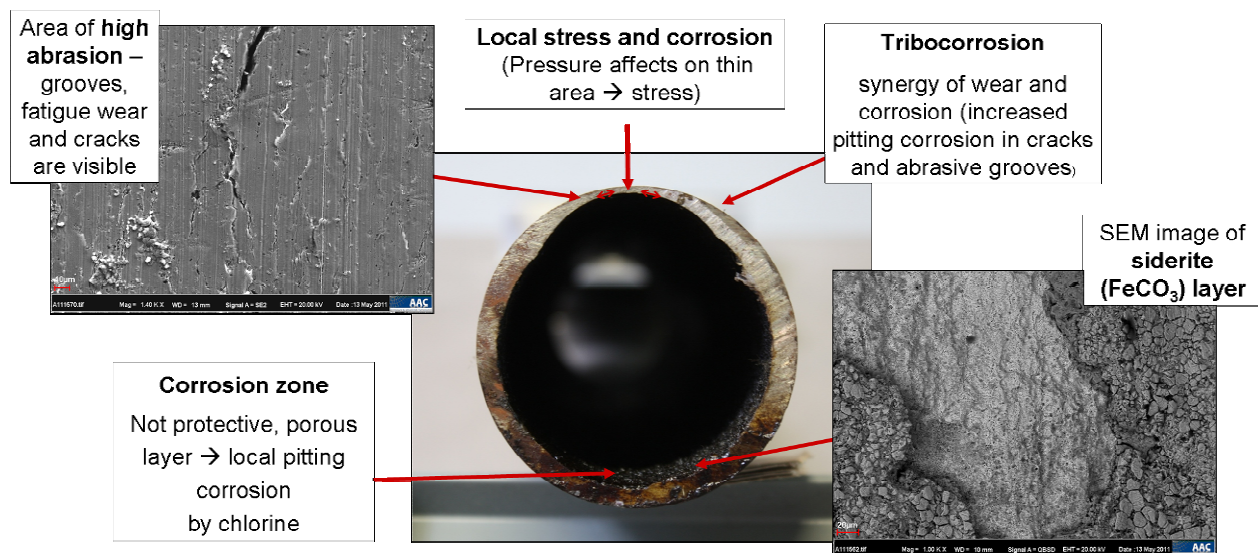
Fig. 5.4: Summary for damage analysis the carbon steel tube, which was used in real application, showing tubing in cross section and description with respective SEM images [cf. 74]

5.2. Evaluation of methods for sample preparation

Through adapted heat treatment it was possible to obtain samples showing the properties as often occurring for materials of application. Hardness and microstructure of commonly used ferritic/pearlitic and martensitic materials were successively imitated (Fig. 4.11). Also the formation of oxide layers was possible to be performed to obtain similar layer properties (Fig. 5.5). Ni-base counter body materials were possible to obtain through the plasma transferred arc welding (Fig. 4.12). With these methods, materials for specific CO_2 corrosion tests were possible to be obtained.
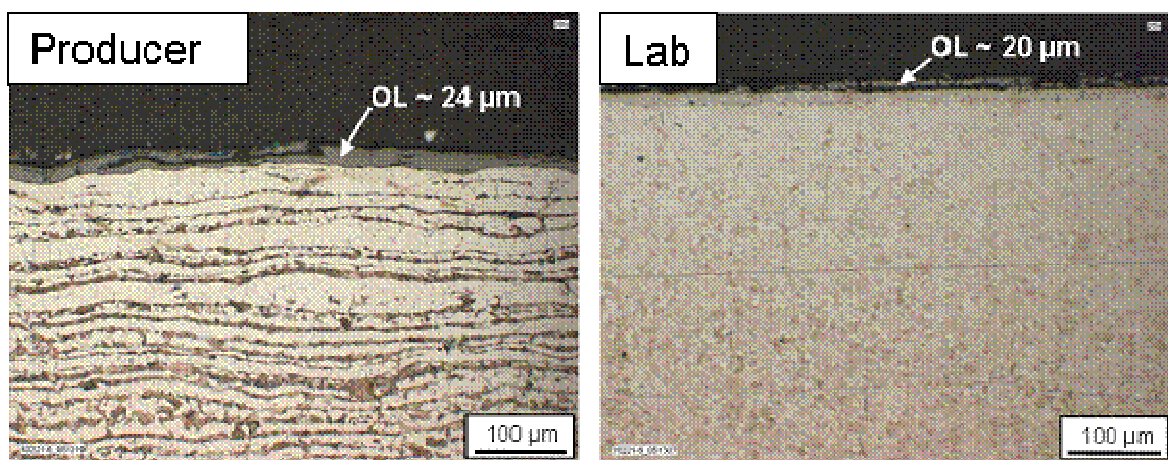
Fig. 5.5: Comparison of oxide layers of carbon steel obtained by production and by adapted laboratory heat treatment under partial inert gas and air supply [cf. 75]

5.3. Investigation of obtainable damage mechanisms through abrasive steel-wheel testing

Also beside the corrosive media and the wear caused by the moving parts of the system, abrasive particles might show an influence on the damage image. In order to test the influence of the abrasive amount, abrasive wear tests with various amounts of sand particles as abrasive under tap and salt water conditions have been performed. The caused damage was investigated via weight loss through wear and microscopical investigations of the damaged surface. Any influences of oxidation and tribolayer formation on the mass loss calculation are proven to be negligible in a previous study [78].

On the sample FP-H of the principal set of heat treatments, abrasive tests were performed using the steel-wheel tribometer in order to test the influence of the abrasive amount (sand load from

0.1 to 60 wt%) and the medium salinity (0 and 1.5 wt% NaCl) on the wear rate. Highest wear rates were measured at highest abrasive content in the slurry, albeit the differences between 10 wt% and 60 wt% are minor. The differences are much more pronounced in the region of low abrasive amount below 10 wt%. Very low abrasive contents of 1 wt% or lower show almost no abrasive attack. Abrasive amounts up to 5 wt% show little or no effect because the contact area between the steel-wheel and the sample is not influenced by these low amounts of particles. For higher amounts, the particles show higher influence, because the contact area between steel-wheel and sample is becoming covered with particles causing two- and three body wear by rolling and scratching of the sample surface.

Also at salt water slurry medium highest wear rates were measured at highest abrasive content, which are ~15 % higher than without salt water. But at lower abrasive contents salt water tests show lower wear rates, especially at 10 wt% abrasive. The sensitive region at this condition is between 5 wt% and 20 wt%, where the wear rates steadily increases. Tests at lower contents are within the range of results obtained for non-saline medium.
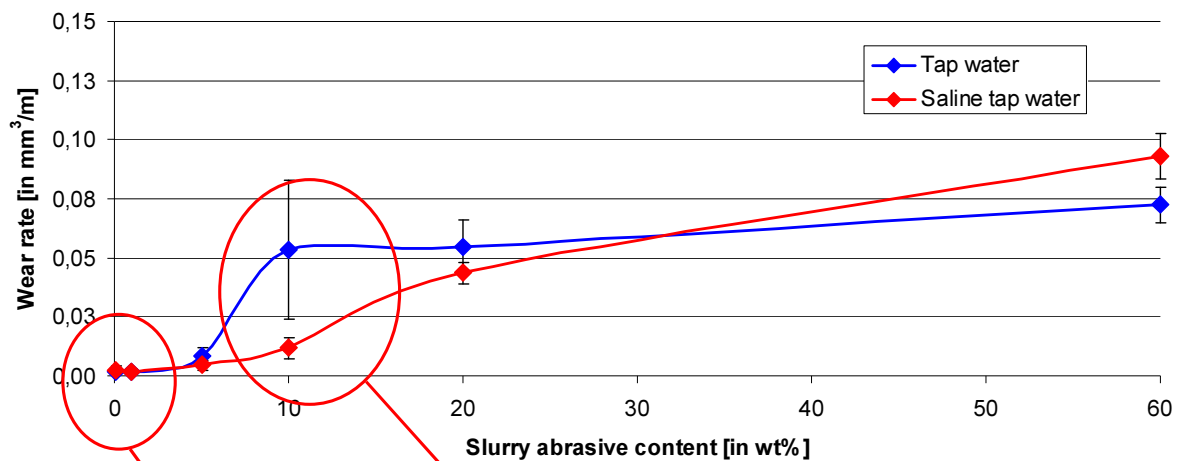
Fig. 5.6: Results for abrasive steel-wheel wear testing on FP-H carbon steel using tap water and saline tap water medium [cf. Fig. 4.19]

The salt water might show a lubricative effect and is therefore leading to lower wear rates. Differences in density and viscosity are measurable for tap water and salt water medium. These variations might contribute to the different tribobehavior in the saline medium. These findings are in accordance with the literature, where enhanced tribobehavior in saline solutions was

reported [52-54]. Garrec et al. [52] stated that saline media are reducing the friction coefficient due to boundary effects with increasing salt concentration. Sh. Hassani et al. [54] performed experiments in a flow loop on carbon steel with sand load of 1 wt% and rising NaCl content from 3 to 18 wt%, which resulted in decreasing the sand erosion due to increasing density and viscosity of the solution. The reported lubrication increase for saline solutions observed for our experiments go conform to the data acquired by literature study.

Steel-wheel tests using 60 wt% abrasive materials clearly show dominant 3-body abrasive wear behavior. Tests using low abrasive content (0.1 wt%) led to grooves and partially also fatigue wear. Non-abrasive tests of a pre-study did not lead to cleavage trails due to the absence of abrasive material, but the direct contact of the wheel and the sample surface lead to a high amount of adhesion (Fig. 5.7 a).

These first tests show a good approximation on the analysis of similar mechanisms observed for the real field samples. Cracks are visible for the lab-scale tests, albeit not in the magnitude as seen for the damage analysis sample (Fig. 5.7 b).
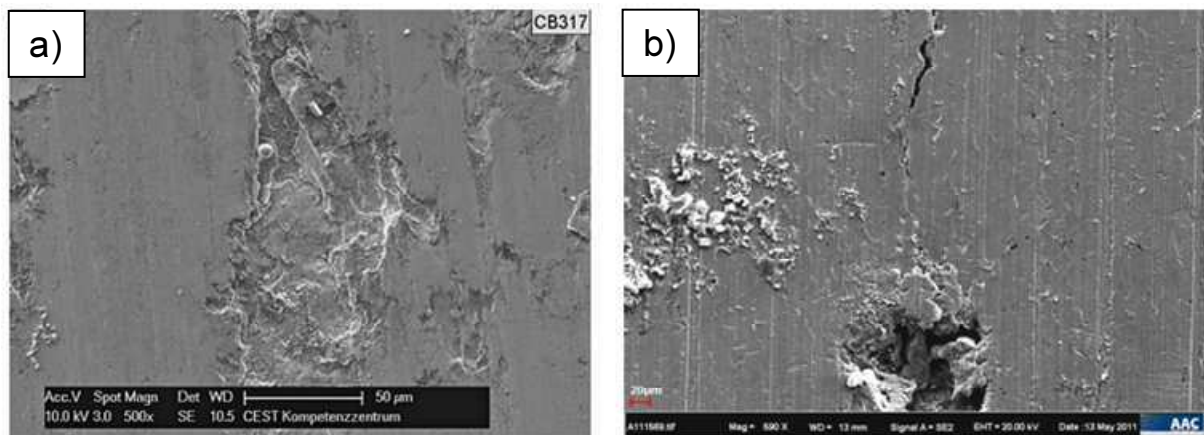
Fig. 5.7: SEM images of carbon steel after non-abrasive steel-wheel test and

field sample analysis: a) SEM image of tests with no abrasives;

b) SEM image from field sample analysis (tribocorrosive area) [cf. 74]

Differences in density and viscosity of tap and salt water shows significant influence on the wear mechanism in the sensitive region of moderate sand load (~5-10 wt%). Fig. 5.8 shows clear differences in surface damage between salt water and tap water slurry abrasive in the sensitive region of 10 wt% abrasive amount. Fig. 5.8 a) with tap water shows a very uneven surface after test, with abrasive grooves and flake formation, also abrasive can be found on the surface (bright

particles in the range <1 µm). In the work of Reza Bateni et al. [53], the formation of plate-like debris on the surface as an indicator for a delamination wear process was investigated. Surface oxidation is negligible at these conditions.

On the other hand the salt water tests show a very even surface at 10 wt%, with just small scratches in the direction of sliding (Fig. 5.8 b). But there can be found wear debris on the surface, with diameters up to 20 µm. This was classified mainly as iron oxides with just some abrasive particles by EDX measurements. Salt water lowers wear rates due to a lubrication effect on the abrasive slurry. On the other side, an increase of abrasive amounts of 20 wt% and higher result in dominating abrasive wear, so that as a result, density effects become insignificant on the wear result. For abrasive contents around 10 wt%, it is therefore supposed that density effects through different salinity of the medium have an effect on the wear result.
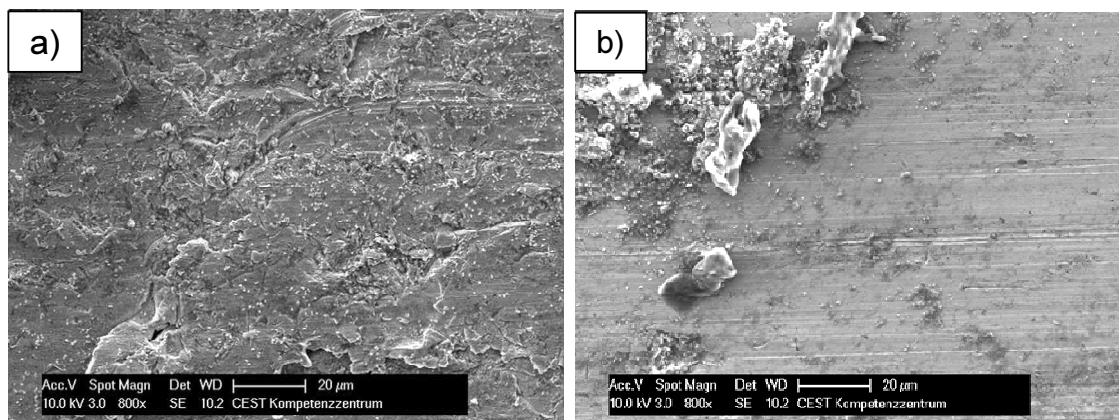
Fig. 5.8: Surface of FP-H carbon steel after steel wheel abrasive test with 10 wt% abrasive amount: a) tap water slurry medium and b) 1.5 wt% salt water slurry medium

Within the performed experiments, a change of the wear mechanism exceeding a critical value of ~10 wt% abrasive can be observed. While below this critical value, mild wear takes place, for higher values, the increase in sand particles result in a severely worn surface by abrasion. This can clearly be seen in Fig. 5.9 for tap water samples, where surface damage with increasing abrasive content is depicted.
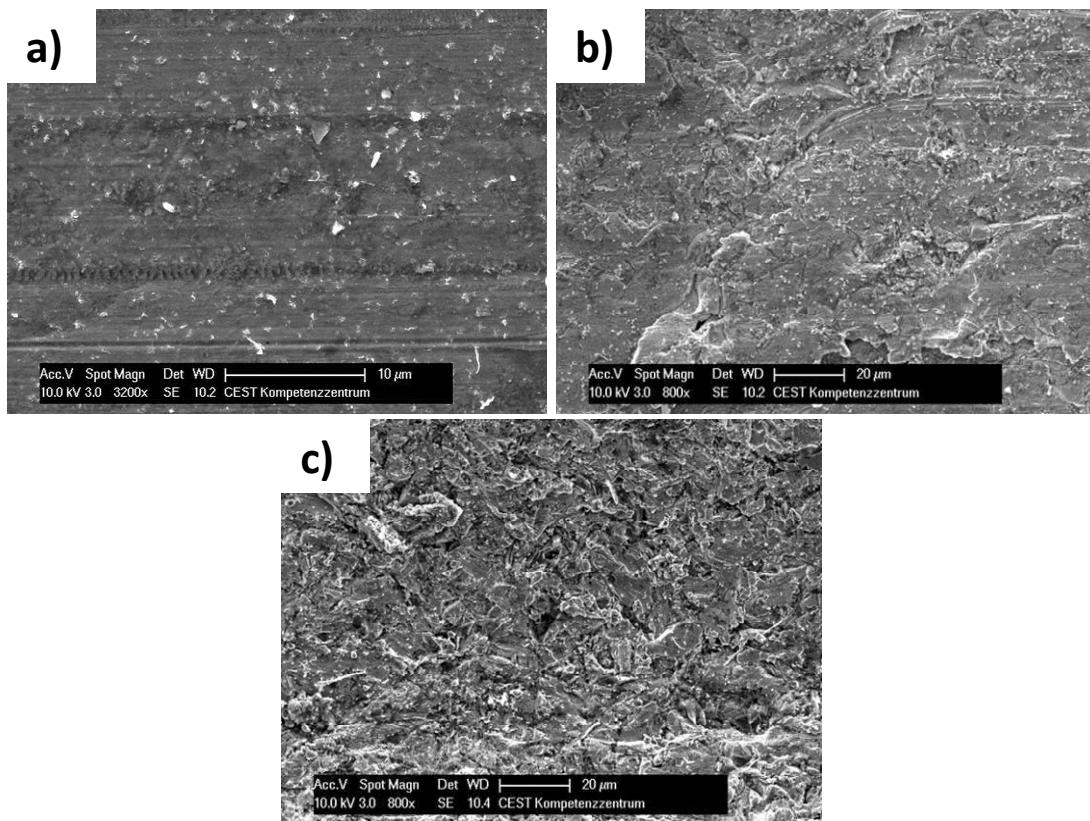
Fig. 5.9: SEM images of FP-H carbon steel after tap water abrasive test samples for

a) 0.1 wt%; b) 10 wt% and c) 20 wt% abrasive amount

5.4. Sliding wear contact of basic body and counter body materials by pin-on-disc tribotesting

In order to gain information about the tribological influence on steel and Ni-base materials, tests using a pin-on-disc tribometer were performed. The running-in, transition state and steady state phase were tested alongside effects of oxide layers on the steel material, different microstructure of the steel materials, different Ni-base materials and surface conditions. For evaluation, the wear loss per cycle was calculated and the damage image was investigating using microscopical methods. The results were then taken for the performance estimation of the used materials and properties in the above mentioned different phases of wear.

Sliding wear tests were performed on carbon steel samples of different hardness and microstructure, a softer and a harder ferritic/pearlitic (FP-S and FP-H) and a softer and harder martensitic (M-S and M-H) steel disc material. As counter body, Ni-base coatings of two hardness values ("soft" and "hard" coating) and two initial roughness states of polished and

grinded surface was applied. Tests were performed on grinded metal surface and on an oxide layer as product of a defined heat treatment procedure.

Investigations were done at increasing cycles in order to simulate running-in with effects with as delivered surfaces and long-term effects gained by prolonged use. Thereto, the running-in phase was tested at 13,500 cycles, transition at 54,000 cycles and steady-state conditions at 162,000 cycles.

Step tests performed with pin-on-disc tribotesting on oxide layer discs showed that the formed oxide layer offers a good resistance against short-term stress (see also Fig. 4.31). In order to abrade this surface and initializing metal-metal contact, high forces and/or test durations are necessary.

For the short term tests simulating running-in effects, the oxide layer leads to a better pin-disc contact situation after 13.5 cycles·1000 compared to the metal-metal contact tests. The oxide is harder as the metal disc and very abrasive. Also, the tribotest measurement diagrams show a more regular progress indicating optimal contact situation, compared to metal-metal contact tests (see Fig. 4.32). The oxide layer disc samples offer better grinding-in conditions than the pre-grinded metallic disc samples. Abrasive wear of the pin material is dominant at oxide layer tests leading to higher friction coefficients.

The transition state pin-on-disc tribotest clearly showed that higher roughness of pin of the harder Ni-base material leads to high wear rates, while the layer with lower roughness resulted in significantly lower wear rates (see Fig. 4.33). A higher roughness results in less roughness tips per area, increasing the load which is effective on the disc sample. From the evaluated R_p/R_z values before and after the test, it can be assumed that the shape of the roughness tips does not change significantly through the performed test. The roughness differences before and after the test were minimal for the pin materials with lower initial roughness, indicating that the system might reach an equilibrium roughness around an R_a value of 0.2 to 0.3 μm.

Most relevant to the field use are the steady-state long term tests. For steady-state metal-metal contact, disc wear is dominating, contrary to disc wear influenced by oxide layers (especially running-in state), where pin wear is clearly dominating. The oxide layer, which is harder than the steel matrix, is able to act as an abrasive. In metal-metal contact, the initial pin roughness plays a minor role, because with ongoing testing time, the hardness tips are either abraded or grooves are filled with wear products.

For metal-metal contact situation, it comes to noisy friction coefficient entailed by adhesive wear phenomena between base and counter material due to similar material. These phenomena are favored by similar hardness parameters of basic and counter body material, especially it is more likely to occur for the soft pin material. Once these joints have formed, they have to be broken with force through the ongoing movement of the samples. Therefore it comes to noisy behavior of the friction coefficient and material transfer between pin and disc material, which can be macroscopically seen in the disc sample as cavities filled with iron oxides produced by tap water medium during further testing (Fig. 5.10). The Fe-oxides are able to build in the tribologically not stressed areas of these cavities. Cross section investigations of the worn pin clearly show material transfer due to adhesive effects. It can be seen that iron and some formed iron oxides were joined to the Ni-base material during the tribotest. Wear particles and oxides are able to act as abrasive, causing 3-body-wear on the materials. For the materials FP-H and M-H, tests with hard pin materials did not result in these effects, for the softer material conditions FP-S and M-S with the soft Ni-base pin, nearly each test showed these adhesive effects indicated by material transfer and noisy progress of the friction coefficient.
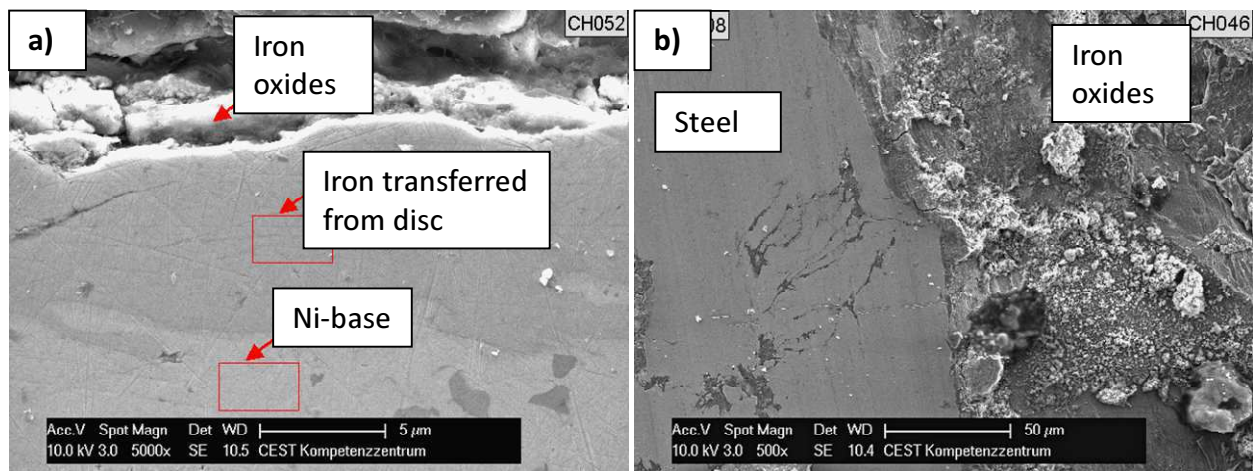
Fig. 5.10: SEM images of a) pin sample (soft Ni-base layer) with transferred iron from FP-H carbon steel disc sample and b) surface of disc sample with wear damage and iron oxides formed in cavities of material outbreak [cf. 75 (a) und Fig. 4.42 (b)]

Fig. 5.11 shows the quantitative results for the measured volume loss at all conditions investigated in steady-state situation. Least wear volume was measured for M-H material, highest wear volume, with high deviations for material M-S. Taking only wear loss into account material M-H with soft counter body at grinded surface conditions shows best behavior, but soft counter bodies tend to adhesive effects and unsteady conditions. The conditions with hard pin

material at grinded surface condition is also comparable good, as well as material FP-H with the same pin configuration. The soft disc materials show in general big distortions due to adhesive effects and behavior in field is difficult to predict.

Fig. 5.12 depicts cross sections of all materials in order to investigate wear mechanisms present at the disc samples. At the ferritic/pearlitic microstructure significant plastic deformation can be observed, while at the martensitic microstructure grooves are dominant caused by abrasion. Especially at M-S these grooves are very deep (>30 µm). Also the cavities with corrosion products can be seen. It is expected, that material transfer to the pin leads to cavities in the disc. These deep cavities are located beneath the tribological stressed area and unhindered corrosion can take place. Nevertheless, adhesion of steel material is dominant at the counter body. Material transfer from the pin was not found at the discs.
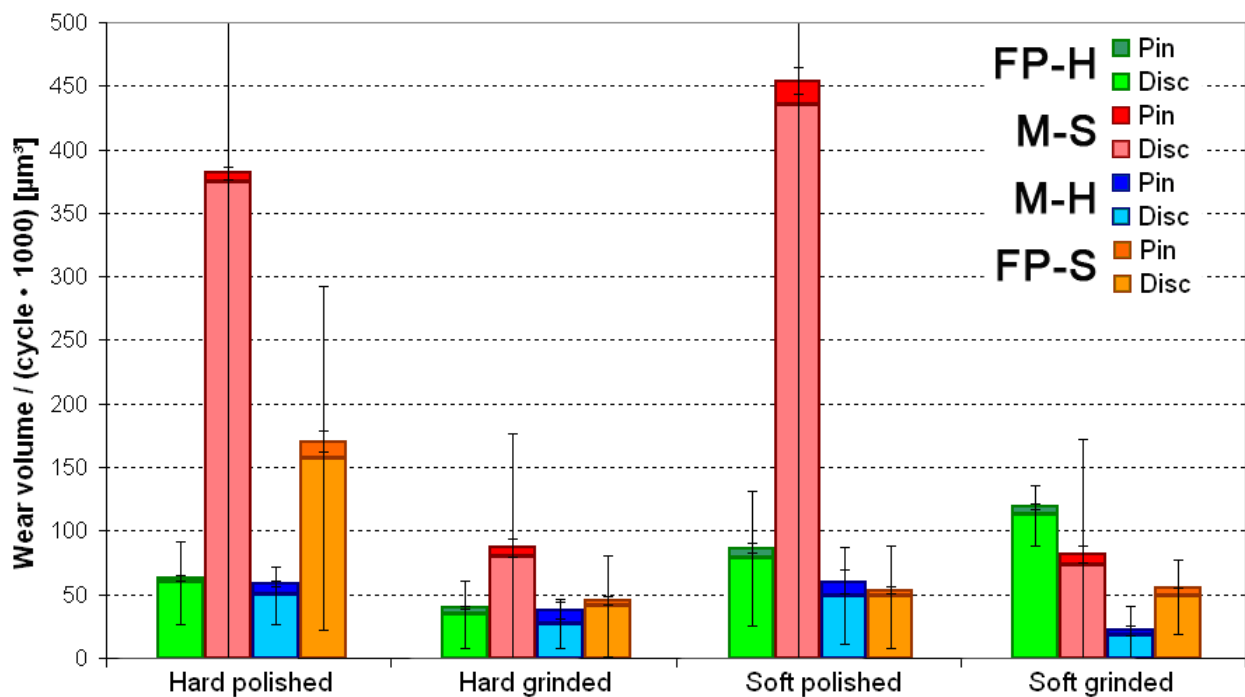
Fig. 5.11: Measured wear volume for all heat treatment carbon steel disc materials tested with all pin materials and surface conditions
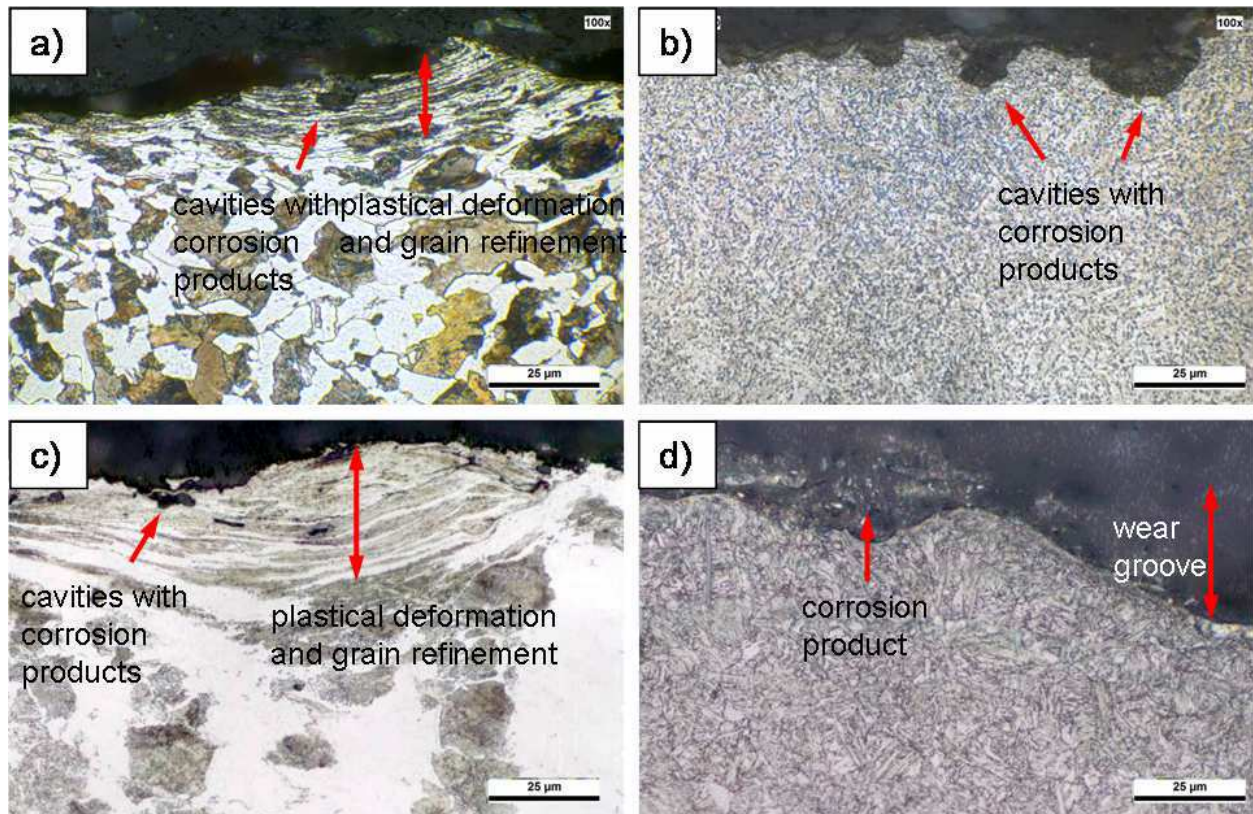
Fig. 5.12: Microstructure cross-sectional cuts of basic body carbon steel materials with the tribological influence on top of the image: a) FP-H, b) M-S, c) FP-S, d) M-H) after pin-on-disc tribotest with hard pin material [cf. Fig. 4.45]

Fig. 5.13 summarizes all the found effects for all tested time periods. At the running-in phase, an oxide layer is beneficial in order to generate a good tribocontact with smooth contact situation between the materials, albeit the initial total wear generated by oxide layer contact is higher (about two times), but metal-metal contact leads to noise in friction coefficient caused by adhesive effects. In transition to steady-state, a counter body material with low initial roughness is important for low wear. This effect is important for counter body wear in oxidic contact. For steady-state tests, it was observed that hard rough pin materials led to lower disc wear than hard smooth pin materials. Furthermore, it was observed, that soft counter body materials are unsuitable due to adhesive wear, material transfer and corrosion effects, while hard counter body materials show significantly better tribobehavior and less wear loss. For investigations on steel counter materials performed by Hedayat et al. [50], it was reported that a harder counter body material resulted on one side in more wear on the basic body, although on the other side in low wear for the counter material itself. This effect was not observed within the performed experiments on the Ni-base materials, where, to some extend, the soft counter body led to higher disc wear (Fig. 4.44).
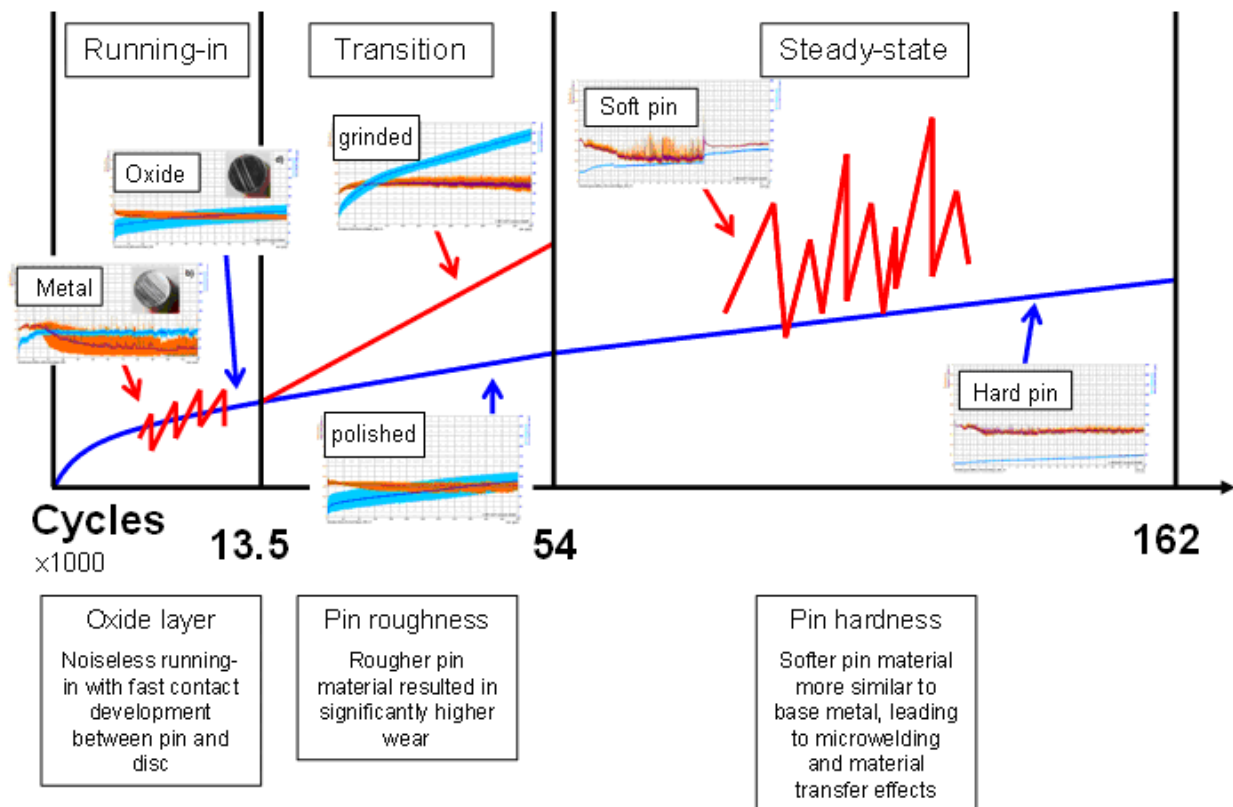
Fig. 5.13: Summarizing image over all time spans (running-in, transition and steady-state) together with the most important conclusions for sliding wear test of Ni-base layer materials on heat treated carbon steel samples

The pin-on-disc tribotest is well suited to study long-term effects such as material transfer effects and adhesion in steady-state metal-metal contact. The application of softer counter body materials resulted to be inadequate due to enhanced material similarity between counter body Ni-base layer and steel basic body material, leading to adhesion and microjunctions of the materials. An off-breaking of these junctions lead to material loss or transfer from basic body to counter body, which allows the medium to affect the material within the formed cavities, leading to corrosion by tap water and, as a result, to enhanced abrasion and corrosion effects. In the work of Chung-Woo Cho et al. [63], it was stated that cavities formed by adhesive wear are filled with oxidation products formed by the reaction with environmental oxygen. These findings go conform to the oxidation behavior experienced for the steel discs of the performed sliding wear experiments. For the Ni-base material, experiments indicated that Ni-base coatings show adhesive wear for higher loads (up to 120 N). These findings were found for Ni-base to Ni-base contact [62]. In the performed pin-on-disc experiments, adhesive wear was found for Ni-base material against steel discs for 70 N normal load.

The ferritic/pearlitic FP-H disc material resulted in more regular behavior and lower wear loss due to its higher ductility and hence its ability to adapt to the pin surface. The softer martensitic M-S disc material results in high and irregular wear rates because the martensitic microstructure is less able to adapt to the pin surface. For the microstructural groups, hardness seems to have a high influence as the harder ferritic/pearlitic FP-H and martensitic M-H basic body materials are surpassing the softer ferritic/pearlitic FP-S and martensitic M-S materials concerning wear loss and adhesive effects.

The obtained higher wear rates for FP-S compared to FP-H are in accordance to the literature [35], where it is stated that a higher and denser amount of cementite phases is less likely to result in adhesive wear than microstructures with large ferrite phases.

Summing this up the ferritic/pearlitic FP-H in contact with hard Ni-base pin material shows best performance in tribocontact, because of less adhesive effects and lowest wear loss. Lower surface roughness leads to better tribobehavior in early stages, but initial roughness gets less important at long-term use. Oxidic initial surface of basic body is important for optimal running in, hence oxide layers due to heat treatment should not be removed before usage.

5.5. Corrosion behavior of steel materials

Corrosion studies were performed on one side to obtain corrosion layers on unworn and pre-damaged samples in order to compare the acquired damage image with the results obtained for the investigated field sample. On the other side, material parameters were investigated on the corrosion performance of the investigated materials and their microstructures. Also, tests on samples damaged after tribotest (steel-wheel and pin-on-disc) were performed and compared to unworn corroded samples in order to evaluate the influence of the wear history of a steel sample on the corrosive behavior. For this purpose, the roughness of the worn samples was evaluated and the unworn samples were grinded to obtain similar roughness. This step was performed to exclude effects of surface increase due to roughness increase and to make the obtained corrosion rates for both sample types comparable. Corrosion tests were then performed on these steel samples in an aqueous solution which contained NaCl at 1.5 and 3 wt%. The samples and the corrosive medium were filled inside a reaction chamber, purged constantly with CO_2 gas and heated to 60°C. Corrosion time varied between 8 hours and five days. Before the test, the samples are weighted and the zones which should not be affected corrosively, are covered with

photoresist. After the test, the samples were cleaned and weighted. Via the mass loss, corrosion time and surface exposed the corrosion rate was calculated.

As first evaluative step, the obtained surface by tribological and corrosive damage on FP-H steel samples after steel wheel and pin-on-disc testing after corrosion testing was compared to the surface of the steel samples out of real field application. An image of the sample surfaces after the lab-scale tests compared to real system sample can be seen in Fig. 5.14. Similar wear phenomena like scratches and cracks can be found for tests with initial steel-wheel (a) and pin-on-disc tribotests (c) compared to images of the damage analysis of real field sample within the tribocorrosive area (b and d). A comparison between the steel-wheel worn (tap water, 0.1 wt% abrasive) and corroded sample (a) to the damage image in the tribocorrosive area (b) shows comparable wear grooves, delamination of material through fatigue wear and particles on the surface. Comparing the corroded sample with initial sliding wear (c) to the respective field sample (d), grooves and cracks are visible on both samples, albeit more intense on the field sample, with higher damage in the tribocorrosive zone than the lab-scale sample. The sliding wear sample (c) also shows a brittle appearing corrosion layer.

Fig. 5.15 shows the tribo-corrosion layer developed on the steel-wheel stressed and the corroded sample of lab-scale testing (a) compared to the corrosion layer of the field application (b). The appearance of the lab-scale formed layer shows similarities to the layer of the damage analysis even for shorter testing periods than the lifetime of the steel basic body in application. The EDX measurements show also similar relations for the elements C, O and Fe (Si coming from abrasive particles) which indicates the formation of similar corrosion products.

The damage images of the lab-scale samples and the field samples show a good compliance, even if the test duration - 15 minutes tribotest and 8 hours corrosion exposure of the lab-scale sample compared to half a year or more lifetime of the field application – is much different. So these lab-scale tests are a useful method for first studies of the initial damage mechanisms occurring in the field in a very short time compared to the life time of a field basic body sample.
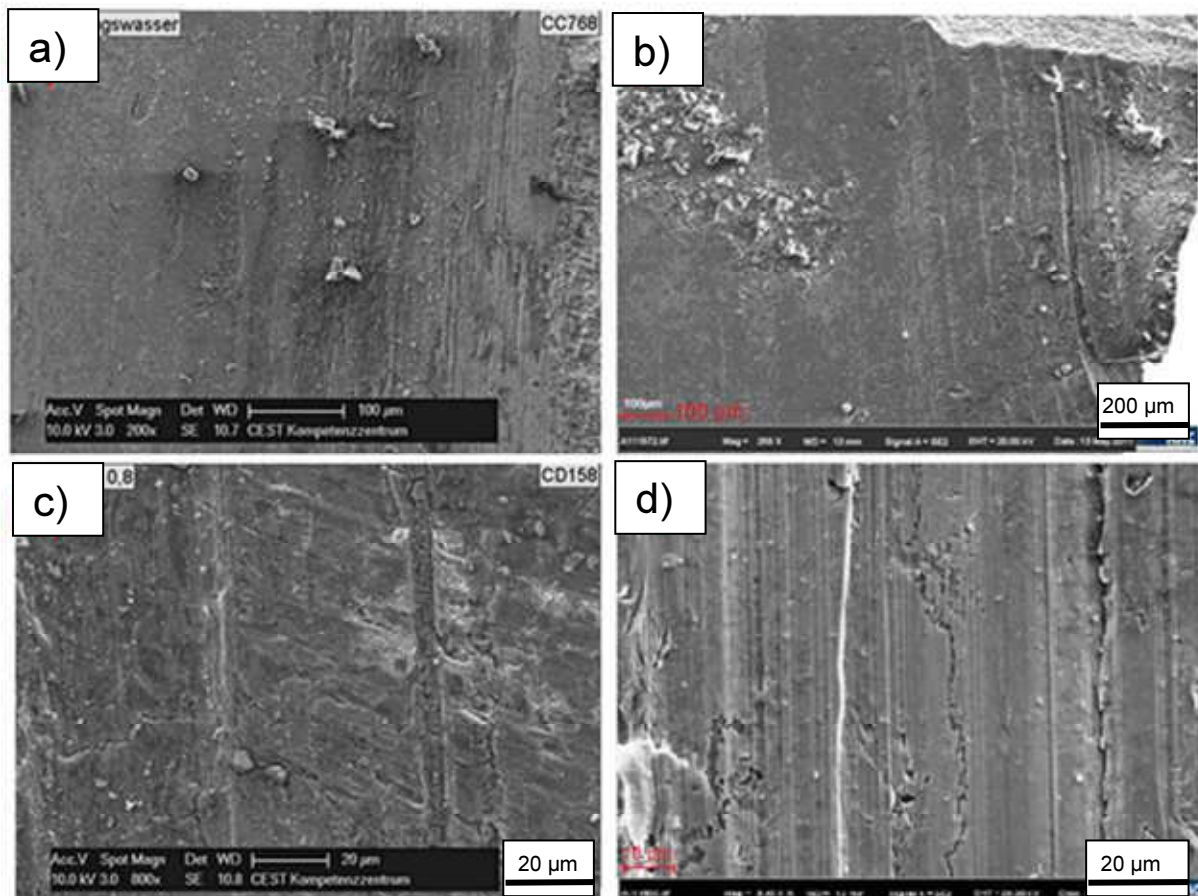
Fig. 5.14: Comparison of SEM images of lab-scale testing to damaged basic body samples:

a) steel-wheel worn (tap water, 0.1 wt% abrasive content) and corroded (1.5 wt% NaCl) FP-H

basic body steel in comparison to

b) investigated field steel sample on tribocorrosive stressed area close to crack;

c) pin-on-disc worn (hard Ni-base layer and grinded surface) and corroded (1.5 wt% NaCl) FP-H

basic body steel in comparison to

d) investigated field steel sample on tribocorrosive stressed area. [cf. 74]
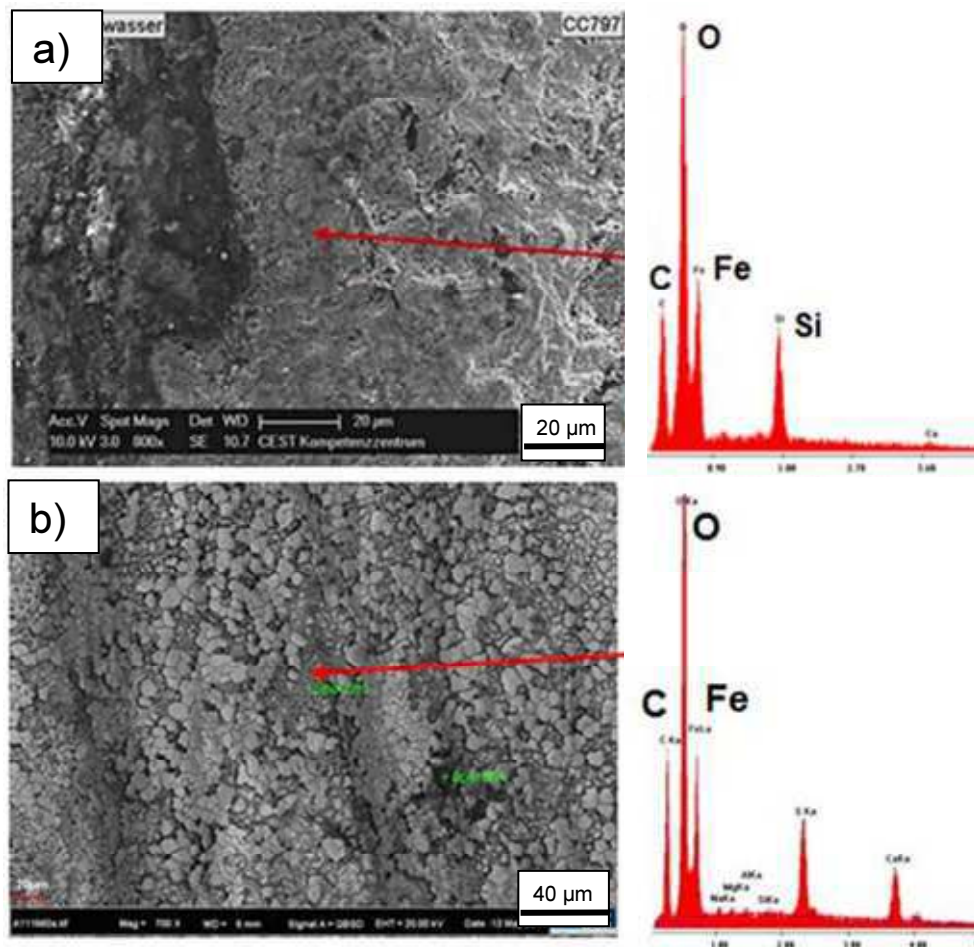
Fig. 5.15: SEM-EDX of steel-wheel worn (saline medium with 20 wt% abrasive amount) and corroded FP-H steel sample (a) compared to a SEM-EDX measurement of the corrosion layer of the investigated field material (b). [cf. 74]

The salt concentration of the medium has a high influence on the corrosion performance. From 1.5 to 3 wt% NaCl concentration the corrosion rate increases about four times for both FP-H and M-S samples (Fig. 5.16). This factor is in good compliance with the graph for increasing corrosiveness for increasing salt concentrations in these salt concentration range, as it was found in the literature [29],[Fig. 5.16].

Unworn samples show generally higher corrosion rates then pre-worn samples by pin-on-disc testing (Fig. 5.17). Also corrosion rates differ in a wide range for the different materials investigated. The microstructure of the material has a high influence on the corrosion performance. For unworn materials, ferritic/pearlitic FP-H material shows higher corrosion rates than martensitic M-S material, as it was stated in the literature [20, 22], where it is stated that ferritic/pearlitic materials show good localized corrosion resistance on one side and higher

corrosion rates than martensitic materials on the other side. The severe influence of salt for corrosion process and the better corrosive performance of M-S steel material in corrosive attack without wear attack were shown in these experiments.
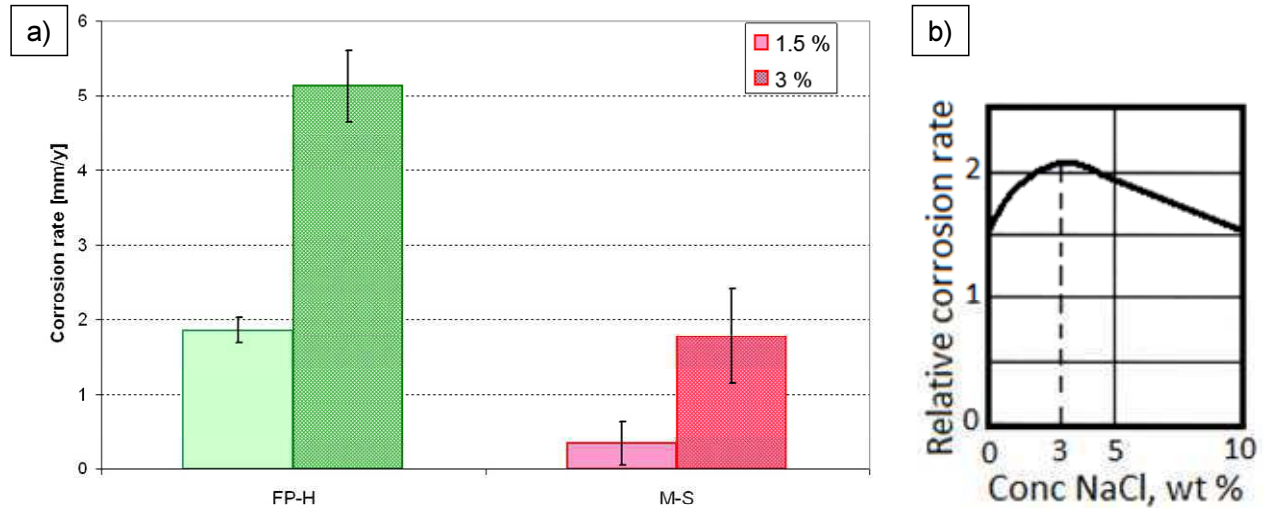
Fig. 5.16: Comparison of corrosion rates of unworn samples corroded with 1.5 and 3 wt% NaCl and CO_2 purging with corrosion rates found by H.H. Uhlig [cf. 29]
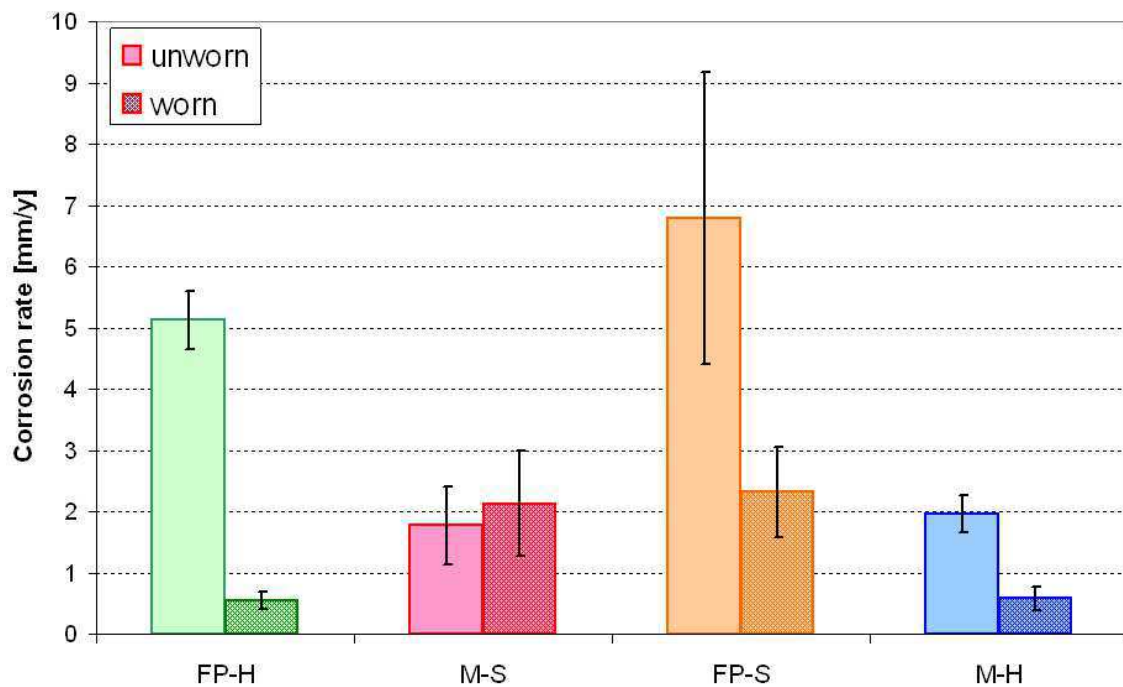
Fig. 5.17: Comparison of unworn and pre-worn (pin-on-disc tribotest with hard pin material polished) carbon steel samples at corrosion tests with 3 wt% NaCl and CO_2 purging after 96 h corrosion time

In pre-studies it was found that the surface roughness has a severe influence on corrosion rates, hence it is necessary to compare similar roughness conditions of unworn and pre-worn samples. In order to generate the same conditions for the corrosion tests for worn and unworn materials, the roughness of the unworn materials was adjusted by grinding.

For tests of worn samples, the influence of the material's surface becomes more important, the factors of hardness and ductility play an important role in material wear and are therefore determining the condition of the material and its surface, in which it is exposed to the corrosive medium afterwards. The ferritic/pearlitic samples experience a decrease in corrosion rate through plastic deformation of the surface, densifying the surface and making it more resistant against corrosive attack. The decrease in corrosion rate is higher for fine-grained FP-H than for coarse-grained FP-S. For the martensitic materials, a different behavior is observable. For the softer martensitic sample M-S, which formed many cavities on the surface due to adhesive effects during the tribotest, the corrosion rate increases slightly compared to unworn samples. The obtained corrosion rates for the M-S material are significantly higher than for the ferritic/pearlitic hard material and similar as the ferritic/pearlitic soft material. The harder martensitic material M-H shows decreasing corrosion rates for pre-worn samples compared to unworn samples, which comes from the formation of a more regular surface without cavities as seen for M-S material. In the case of tribological attack prior to corrosive attack, the worn samples of the harder materials with denser microstructure show lower corrosion rates than the softer materials. The materials FP-H and M-H both show low corrosion rates after tribological testing.

These tests clearly showed that for application of materials in tribocorrosive condition, not only the corrosive attributes are crucial, also the tribological behavior and the response of the surface has a high influence, i.e. the tribocorrosive behavior. The effect of surface alternation due to tribocontacts can be sufficiently severe to change the corrosion behavior of materials in comparison to results obtained for unworn materials as it was observed for the performed tests.

5.6. Tribocorrosive testing of FP-H and M-S steel samples

In the previous studies, tribological and corrosive effects have been tested separately. The results of these tests showed a good compliance with the analyzed real field parts. Although it was possible to obtain good results with these tests, it has to be considered that the damage analysis parts underwent tribological and corrosive attack simultaneously under specific conditions. Tribocorrosive testing together with typical predominant conditions (pressure, temperature, etc.) were tested on two common steel materials (FP-H and M-S) using a hard Ni-base layer as moving counterpart in CO_2 and NaCl saline aqueous medium under 3 bar CO_2 pressure and 60°C temperature. As results of these tests, on one side, the wear volume, wear depth, wear width and also the worn and corroded surface of the steel samples have been investigated.

Wear mechanisms established by tribocorrosive testing were compared with damage analysis of real field samples (Fig. 5.18). Abrasive grooving is the main mechanisms apparent at both samples, albeit to a much higher content at real field samples. This can be put down to the much longer period of use compared to 6 day testing (60,000 cycles). Like in the real field sample most of the surface in the tribocorrosively stressed area shows no corrosion layer formation (Fig. 5.18 a). In deep wear grooves the formation of iron carbonate is present (Fig. 5.18 b). These are very similar to the found at field application in the corrosion zone.

The samples of the performed tests showed that on the abraded area of the samples the initial damage that might occur on the real sample can be observed, indicated by grooves and plastic deformation as observed for the field samples. Where the wear grooves and fatigue wear are more pronounced on the field sample, the tested tubing represents the initial stage of CO_2 tribocorrosion within primarily deep abrasion scratches.

The total wear image is slightly different: the field analysis shows more wear grooves (Fig. 5.18 c), coming from the long period of use, allowing to develop a more regular wear track. Also, corrosion layers formed on field pars are higher developed as seen for the tribocorrosively tested parts (Fig. 5.18 d). Nevertheless, these short term tests are suitable for damage observation and material screening in much shorter time period with similar damage mechanisms like in the application.
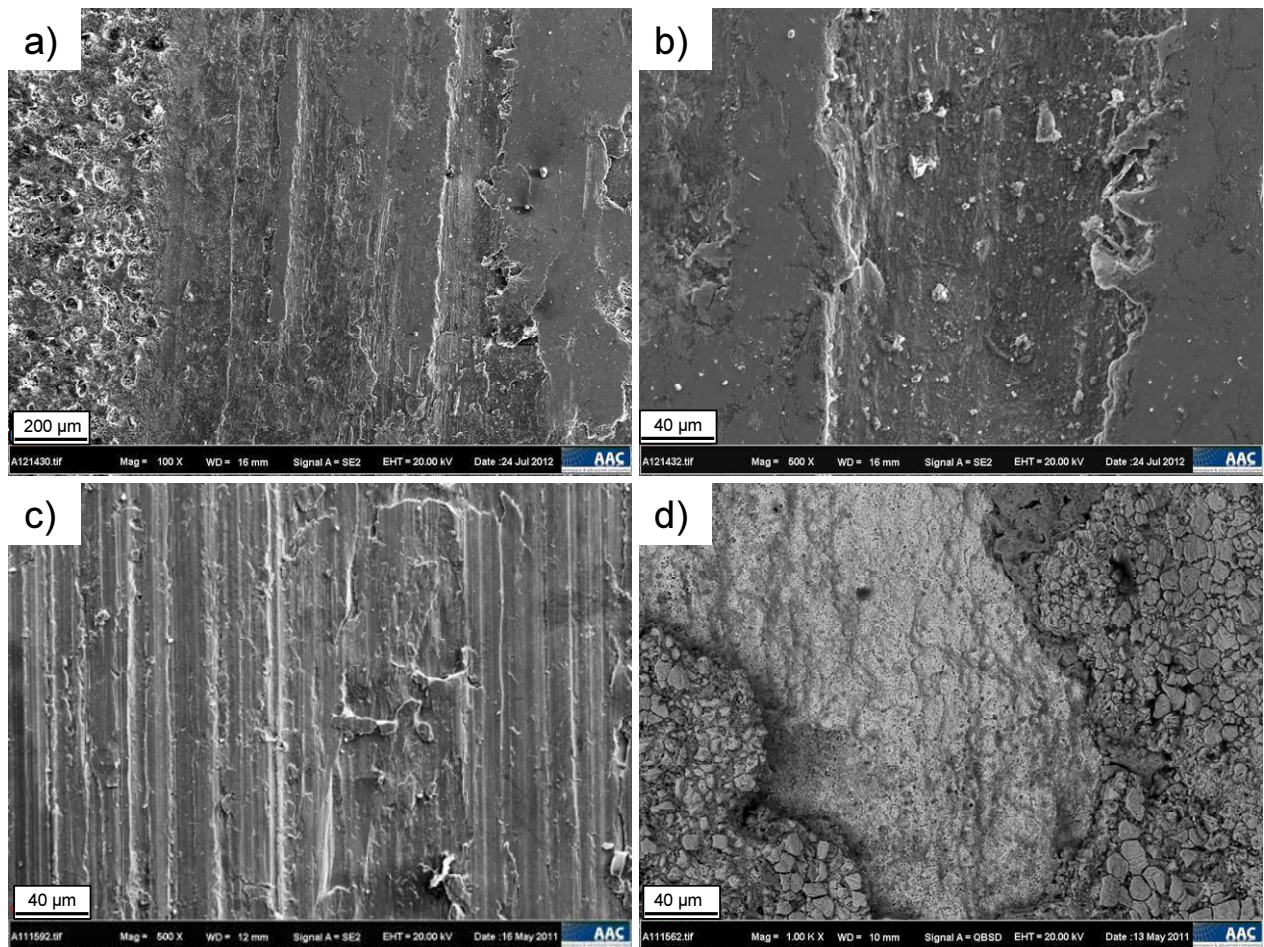
Fig. 5.18: Comparison of tribocorrosively tested FP-H carbon steel samples (a, b) with damage analysis of real field carbon steel samples (c, d) by SEM: a) overview of tribotest wear track; b): detail of deep wear groove; c) abrasion zone and d) corrosion zone of field sample [cf. 70, 74]

Tribotests under tribocorrosive application near conditions with linear oscillating sliding under corrosive medium could be established. Tests in saline solutions result in similar damage mechanisms as observed for real field application. Tests performed under tribological conditions without corrosive medium result in similar friction coefficient behavior as observed for pin-on-disc tribotesting. The friction coefficient for the FP-H basic body with hard pin counter body pin-on-disc values were μ ~0.3-0.4, same values could be obtained for tribological conditions in tribocorrosive testing (Fig. 4.60). Like in pin-on-disc testing the M-S with hard pin pairing results in slightly lower friction coefficient of ~0.3-0.35. [76]

Nevertheless, damage analysis for pin-on-disc tribotest with additional corrosion testing compared to results from tribocorrosive testing are different in their appearance. Sequential corrosive with subsequent sliding testing offers a good approximate test method to display

tribocorrosive behavior. But the sliding corrosion test offers new possibilities in application near testing and material screening in lab-scale. [76]

The Sliding corrosion-Tribotester (SCT) allows the investigation of tribobehavior both under tribological conditions as well as tribocorrosive conditions by the addition of corrosives. Fundamental different behavior was found for these two conditions. First indication is given by the friction coefficient (Fig. 4.60).

Lower friction coefficients for tribocorrosive tests compared to tribological tests show the influence of the medium composition on the tribocontact. The higher salt content may lead to lower friction coefficients. These findings would comply with those made for steel-wheel testing. Also poor sticking corrosion products may lead to the separation of the surfaces and hence lower friction coefficients.

On the other hand in pure tribological testing, adhesion and microwelding can occur, leading to higher friction coefficients.

The difference between the friction coefficients of tribocorrosive and tribological testing, as seen in the comparison (Fig. 4.60), is supposed come on one side from the added salt content [52], on the other side from a possible lubricative effect of the formed corrosion products. [76]

Differences between tribological and tribocorrosive testing are evident in the comparison of cross sections of the wear tracks (Fig. 5.19). It was observed that under tribological attack, grooving and deformation on the steel surface was prominent, indicated by the distracted surface and grain refinement beneath the wear track. The FP-H sample shows smooth surface with grain refinement up to 30 µm depth (Fig. 5.19 a). The M-S material shows severe plastical deformation and material displacement (Fig. 5.19 b). These damage mechanisms are very similar to pin-on-disc tribotesting.

Under tribocorrosive attack, the plastic deformation on the surface is minor (Fig. 5.19 c-d). The abrasion of the surface in tribocorrosive conditions is more pronounced, leading to a rough surface. Corrosion products are visible in deep wear grooves.

A possible explanation can be that under corrosive attack, the freshly exposed surface due to tribocontact is instantly corroded and then again abraded by additional hard corrosion particles. Adhesion effects like observed in pin-on-disc testing may be present in tribological SCT testing, leading to higher friction coefficients and the more plastically deformed surface. [76, 77]

Out of the performed tests, there is no significant difference in wear volume (Fig. 5.20) between these materials for the performance under pure tribological conditions without corrosive medium. Albeit damage mechanisms on micro scale are different as seen in Fig. 5.19.

Significant differences in wear volume can be determined for tribocorrosive conditions (Fig. 5.20).
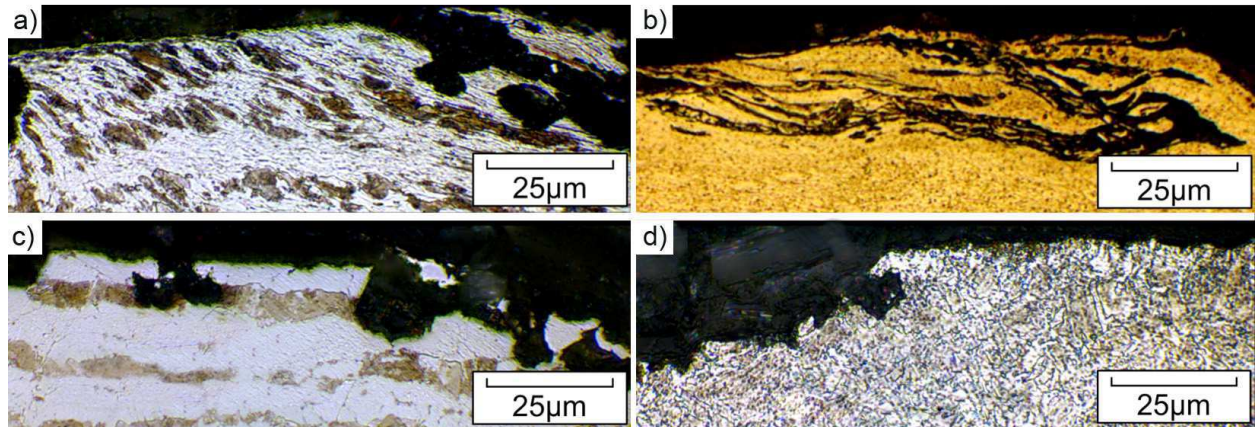
Fig. 5.19: Comparison of resulting surface: a, b) after tribological (under N_2 purging in aqueous medium) and c, d) tribocorrosive (under CO_2 purging in saline medium) testing in ACT, cross sections of FP-H (a, c) and M-S (b, d) carbon steel at 60°C [cf. Fig. 4.65 and Fig. 4.66] [76]

The two materials tested in SCT, the ferritic/pearlitic FP-H and the martensitic M-S, show different damage behavior in tribological and tribocorrosive testing [76]. The FP-H material results in higher wear volume than the M-S material. In sliding wear testing, the FP-H material performed better than the M-S material, showing fewer tendencies to result in disturbances of progresses visible on the tribotest curve as a cause of microwelding effects. Microwelding effects do not occur in combined sliding corrosion testing due to the predominant abrasion and lubrication effects caused by the saline medium and the corrosion products preventing the formation of material joints.
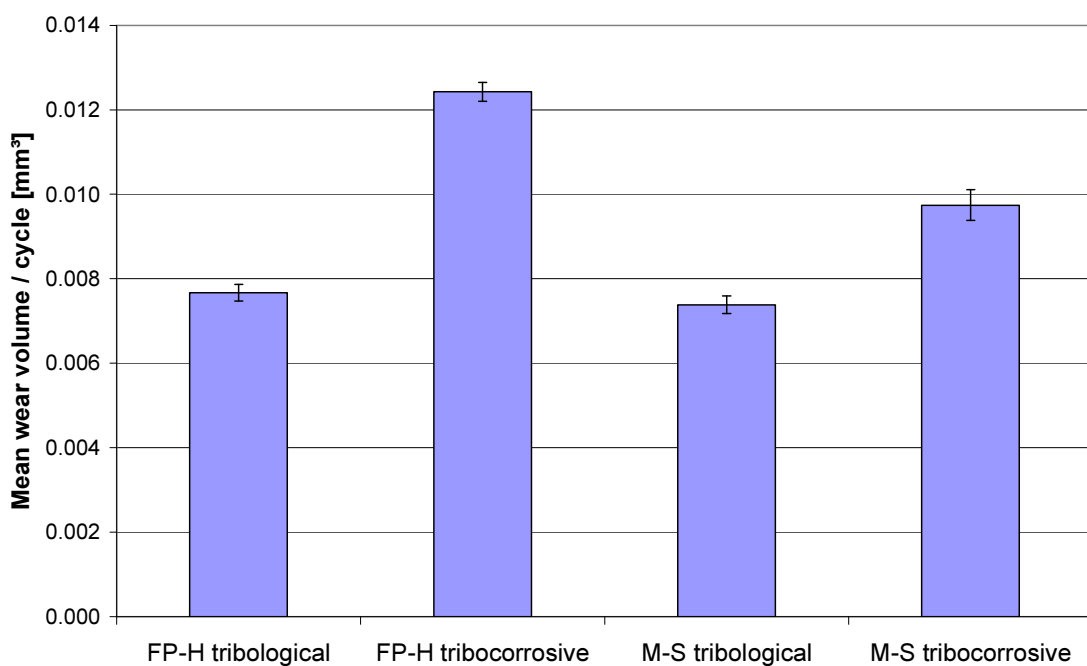
Fig. 5.20: Wear volume per cycle in SCT testing under tribological (under N_2 purging in aqueous medium) and tribocorrosive (under CO_2 purging in saline medium) conditions

Also for corrosion tests after pin-on-disc tribotests, the F-P material resulted in lower corrosion rates due to surfaces alternation prior to these tests. For tribocorrosive conditions, the M-S material performs better than the FP-H material, resulting in lower material loss. Hedayat et al. [50] investigated with similar tests as performed on the SCT that the martensitic material performs well in tribocorrosive testing, although ferritic/pearlitic materials were not tested in comparison.

It can be concluded that the combined Sliding Corrosion Tribotest allows much better approximation of real field conditions then classical tribometers. While abrasion testing with

corrosive slurry medium is mainly influenced by the abrasive, external abrasive is not dominant in application. On the other hand, pin-on-disc tribotesting is strongly affected by adhesion and microwelding effects, which do not predominate in damage analyses of field samples. Hence the material selection by these methods has to be relativized.

The damaging in real field is strongly affected by abrasion in corrosive medium and hence the formation of corrosion products during use. It was found that these corrosion products have strong influence on the wear mechanisms, leading to higher abrasion rates and prevention of adhesion. This leads to the preference of the martensitic material M-S for tribocorrosive conditions of simulated real field application. [76]

6. Summary

Aim of this thesis was the characterization of the tribocorrosive effects occurring for steel materials in tribocontact under the influence of corrosive media. The correlation between tribological and corrosive damage have been investigated. Also, the influences of the equipped material parameters in hardness and microstructure have been evaluated. The occurring abrasive and corrosive conditions have been simulated in lab-scale tests.

Based on the findings of the analyses of the field samples, a number of abrasive and corrosive experiments have been established and performed within this work, together with an analysis of damaged parts of the real field application. It was possible to investigate the occurring abrasive and corrosive mechanism in field application and to simulate these mechanisms approximately in short time by model tribotests.

Abrasion tests showed that the influence of abrasive amount shows "threshold" level for transition from low to high wear. Not only the influence of abrasives, also the lubrication potential of saline media were indicated.

In sliding wear tribotesting on a pin-on-disc tribometer, various steel materials (ferritic/pearlitic FP-H and FP-S, martensitic M-S and M-H) were tested against two counter body materials ("hard" and "soft" Ni-base layer coating) in two initial roughness conditions. For the softer Ni-base material, an unsteady tribobehavior together with adhesive effects leading to material transfer were observed. For M-S and FP-S in tribocontact with the hard Ni-base material, the formation of cavities on the steel sample was observed. Ferritic/pearlitic materials experienced a grain refinement within the subsurface due to the tribocontact, the martensitic samples did not experience these plastic deformations and changes in microstructure. M-S significantly showed cavity formation which shows disadvantageous effects in subsequent corrosion simulation. The most favorable materials in sliding contact resulted to be hard martensitic M-H or the hard ferritic/pearlitic FP-H together with a hard pin with an initial polished surface, albeit it resulted that the initial grinded surface also lead to satisfactory results.

Static corrosion tests showed the superiority in corrosion behavior of martensitic steel type M-S compared to ferritic/pearlitic steel type FP-H as result of lesser corrosion rates up to 4 times. Furthermore, the high influence of the salt amount in the medium was verified with significantly higher corrosion rates obtained for 3 wt% compared to 1.5 wt% NaCl.

The wear history of the steel samples has a significant effect in the corrosion performance. Microstructural change, i.e. grain refinement of FP-H due to sliding wear, experienced a

reduction in corrosion rate, whereas the M-S steel sample, covered with cavities due to adhesive effects after tribotest, leads to an increase in corrosion rate.

The synergistic effect of wear and corrosion is the main focus for the application of carbon steel basic bodies in sliding tribocontact with corrosive medium of field application. In this work a new tribotest is utilized to simulate the tribobehavior as application near as possible. The findings of these investigations clearly show that corrosive attack on worn surfaces is fundamentally different to a corrosive attack on plain, unworn steel surface. By the used model tests it was possible to reproduce the damage mechanisms observed for worn field application samples in lab-scale. To simulate simultaneous wear and corrosion as happening in field application, the sliding corrosion test rig was established, in which CO_2 and NaCl aqueous media can be introduced.

Tribotests performed under wear and corrosive conditions entailed similar damage mechanisms as observed for field sample parts. As the results for sequential and simultaneous wear and corrosion tests do not lead to the same results, the influence of both damaging influences together is indispensable for tests of wear and corrosion. Corrosion behavior after pre-wearing with sliding tests depends strongly on surface-structure caused by different wear mechanisms. Ferritic/pearlitic material's surface show grain refinement in tribocontact and this is increasing the local corrosion resistance. On the other hand the martensitic material shows no microstructural change, but forms cavities due to adhesive effects, which are very sensitive to corrosive attack. In synergistic testing the corrosive attack takes place immediately after tribocontact, and no pronounced surface change, which may protects the surface, can be established. Adhesive effects are prevented by the simultaneous corrosive attack, thus the martensitic materials resulted in lower tribocorrosive wear loss.

For the investigation of synergetic influences it was observed that tribological testing followed by corrosion clearly showed different results than corrosion only. Tribocorrosive tests resulted in similar damage images as observed for the real application and is therefore a powerful tool for the investigation and estimation of the wear and corrosion behavior of steel materials under CO_2 and saline tribocorrosive conditions. The field of tribological and corrosive, also tribocorrosive testing in CO_2 conditions offers a broad field for scientific research and good simulation of application by model tribotests. The sliding corrosion tester (SCT) showed high potential for further investigations in the field of tribocorrosive attack and improvement of materials used in tribocorrosive environment in the future.

7. References

[1] P. R. Roberge; "Handbook of Corrosion Engineering"; McGraw-Hill, ISBN 0-07-076516-2

[2] Z.D. Cui, S.L. Wu, C.F. Li, S.L. Zhu, X.J. Yang; "Corrosion behavior of oil tube steels under conditions of multiphase flow saturated with super-critical carbon dioxide"; Science Direct, Materials Letters 58 (2004) 1035 – 1040

[3] E. Dayalan, G. Vani, J.R. Shadley, S.A. Shirazi, E.F. Rybicki; Corrosion 95, paper no. 118; NACE International (1995)

[4] J.K. Heuer, J.F. Stubbins; „An XPS characterization of $FeCO_3$ films from CO_2 corrosion"; Corrosion Science 41, (1999) 1231-1243

[5] L. D. Benefield, J. M. Morgan: "Water Quality and Treatment: A Handbook of Community Water Supplies, Fifth Edition: Chapter 10 – Chemical Precipitation"; American Water Work Association; ISBN-13: 9780070016590

[6] L. D. Benefield, J. M. Morgan: "Water Quality and Treatment: A Handbook of Community Water Supplies, Fifth Edition: Chapter 10 – Chemical Precipitation"; American Water Work Association; ISBN-13: 9780070016590

[7] Z. Duan, R. Sun; "An improved model calculating CO_2 solubility in pure water and aqueous NaCl solutions from 273 to 533 K and from 0 to 2000 bar"; Chemical Geology 193 (2003) 257– 271

[8] Y. Liu, M. Hou, G. Yang, B. Han; "Solubility of CO_2 in aqueous solutions of NaCl, KCl, $CaCl_2$ and their mixed salts at different temperatures and pressures"; Journal of Supercritical Fluids 56 (2011) 125–129

[9] J.W. Mullin, "Crystallization", 3rd ed. (Oxford, U.K.: Oxford Press, 1993)

[10] Flavio D. de Moras, "Characterization of CO_2 corrosion product scales related to environmental conditions"; NACE CORROSION 2000, Paper No. 00030

[11] G.A. Zhang. Y. F. Cheng, "Localized corrosion of carbon steel in a CO_2-saturated oilfield formation water"; ELSEVIER Electrochimica Acta 56 (2011) 1676-1685

[12] M.H. Nazari, S.R. Allahkaram, M.B. Kermani, "The effects of temperature and pH on the characteristics of corrosion product in CO_2 corrosion of grade X70 steel"; Material and Design 31 (2010), 3559-3563

[13] S. Nesic, M. Nordsveen, R. Nyborg, A. Stangeland, "A Mechanistic Model for Carbon Dioxide Corrosion of Mild Steel in the Presence of Protective Iron Carbonate Films Part 2: A Numerical Experiment"; CORROSION, Vol. 59, No.6, 489-497

[14] M.B. Kermani, L.M. Smith, "A Working Party Report on CO_2 Corrosion Control in Oil and Gas Production"; EFC-Publications 23 (1997), 1-53

[15] D. Engels; „Einflussgrößen der Lokalkorrosion von Stahl in CO_2-haltigen Medien"; Dissertation, Aachen, 1986, 1-167

[16] B. Ingham. M. Ko. G. Kear. P. Kappen. N. Laycock. J. A. Kimpton D.E. Williams; "In situ synchrotron X-ray diffraction study of surface scale formation during CO_2 corrosion of carbon steel at temperatures up to 90 °C"; Corrosion Science 52 (2010) 3052-3061

[17] S. Nesic and K. L.-J. Lee; "A Mechanistic Model for Carbon Dioxide Corrosion of Mild Steel in the Presence of Protective Iron Carbonate Films – Part 3: Film Growth Model"; NACE Corrosion Vol. 59, No. 7; 616-628; Part III

[18] D.A. López, T. Pérez, S.N. Simison; "The influence of microstructure and chemical composition of carbon and low alloy steels in in CO_2 corrosion. A state-of-the-art appraisal"; Science Direct, Materials and Design; 24 (2003) 561-575

[19] A. Dugstad, L. Lunde, S. Nesic; „Control of internal corrosion in multi-phase oil and gas pipelines"; Prevention of Pipeline Corrosion Conference, October 17-20, 1994

[20] M.B. Kermani, A. Morshed; "Carbon Dioxide Corrosion in Oil and Gas Production - A Compendium"; Corrosion 59 (2003), 659-683

[21] M. Ueda, H. Takabe, "Effect of environmental factor and microstructure on morphology of corrosion products in CO_2 environments"; NACE CORROSION 1999, Paper No. 99013

[22] M. Ueda, A. Ikeda, "Effect of microstructure and Cr content in steel on CO_2 corrosion"; NACE CORROSION 1996. Paper No. 96013

[23] M. B. Kermani. J. C. Gonzales. C. Linne. M. Dougan; „Development of low carbon Cr-Mo steels with exceptional corrosion resistance for oilfield applications"; NACE Paper No. 01065

[24] Einar Bardal; "Corrosion and protection"; Springer-Verlag 2005

[25] C. de Waard, U. Lotz, D.E. Milliams, "Predictive model for CO_2 corrosion engineering in wet natural gas pipelines"; NACE CORROSION-DECEMBER 1991, 976-985

[26] NORSOK Standard M-506; freely available online at www.standard.no/petroleum

[27] R. Nyborg; "Overview of CO_2 Corrosion Models for Wells and Pipelines"; NACE CORROSION 2002, Paper No. 02233

[28] J. Han, J.W. Carey, J. Zhang; "A coupled electrochemical-geochemical model of corrosion for mild steel in high-pressure CO_2-saline environments"; IJGGC 397 (2011), 1-11

[29] H.H. Uhlig; "Corrosion and Corrosion Control an introduction to corrosion science and engineering"; Second Edition, John Wiley & Son Inc, NY, L, S, T, 1963, 111-113

[30] E. L. Hibner, L. E. Shoemaker: "Innovative Nickel alloys for service in critical marine applications"; CORROSION 2003, Paper No. 03259

[31] Special Metals Corporation Guideline: "High-Performance alloys for resistance to aqueous corrosion"; 2000, Publication number SMC-026

[32] Horst Czichos/Karl-Heinz Habig; "Tribologie-Handbuch – Reibung und Verschleiß" (german); Vieweg Verlag, 2. Auflage, 2003; ISBN 3-528-16354-2

[33] Karl-Heinz zum Gahr; „Microstructure and Wear of Materials"; ELSEVIER Science Publishers B.V., Vol. 10, 1987; ISBN 0-444-42754-6

[34] V. K. Gupta, S. Ray, O. P. Pandey; "Dry sliding wear characteristics of 0.13 wt.% carbon steel"; Materials Science-Poland, Vol. 26, No. 3, 2008, 617-631

[35] G.A. Fontalvo, R. Humer, C. Mitterer, K. Sammt, I. Schemmel: "Microstructural aspects determining the adhesive wear of tool steels"; Wear 260 (2006) 1028–1034

[36] P. J. Moroz Jr., "The Effects of Carbon Content, Matrix Hardness and Microstructure on the Wear of Steel Grinding Balls During Wet Copper Ore Grinding"

[37] P. J. Moroz Jr., "The Effects of Carbon Content, Matrix Hardness and Microstructure on the Wear of Steel Grinding Balls During Wet Iron Ore (Magnetite) Grinding"

[38] M.D. Bermúdez, P. Iglesias, A.E. Jiménez, G. Martínez-Nicolás: "Influence of sliding frequency on reciprocating wear of mold steel with different microstructures"; Wear 267 (2009) 1784–1790

[39] R. Oltra, B. Chapey, L. Renaud: "Abrasion-corrosion studies of passive stainless steels in acidic media: combination of acoustic emission and electrochemical techniques"; Wear 186-187 (1995) 533-541

[40] C.-W. Wu: "Corrosion-wear study of 304 stainless steel in various NaCl solutions"; Wear,162-164 (1993) 950-953

[41]   Brent W. Madsen, "Measurement of erosion-corrosion synergism with a slurry wear test apparatus"; Wear, 123 (1988) 127 – 142

[42]   X. Hu, A. Neville, "Prediction of erosion-corrosion in oil and gas – a systematic approach"; NACE Paper No. 08540

[43]   J. Han, Y. Yang, B. Brown, S. Nesic, "Electrochemical Investigation of Localized CO_2 Corrosion on Mild Steel"; NACE Paper No. 07323

[44]   G. Mori, T. Vogl, J. Haberl, W. Havlik, T. Schöberl: „Erosion corrosion and synergistic effects under high velocity multiphase conditions"; NACE Corrosion Paper No. 10382

[45]   J. Feyerl, G. Mori, S. Holzleitner, J. Haberl, M. Oberndorfer, W. Havlik, C. Monetti: „Erosion-corrosion of carbon steels in a laboratory three phase flow"; Corrosion (2008) 64, S. 175 - 186

[46]   G. Mori, J. Haberl, J. Feyerl, S. Holzleitner, M. Oberndorfer, W. Havlik: „Breakaway velocities of materials for oil and gas production"; NACE Corrosion Paper No. 07108

[47]   M. M. Stack, K. Chi, "Mapping sliding wear of steels in aqueous conditions"; Wear 255 (2003) 456-465

[48]   S. Mischler, A. Spiegel, M. Stemp, D. Landolt, "Influence of passivity on the tribocorrosion of carbon steel in aqueous solutions"; Wear 251 (2001) 1295-1307

[49]   Y. Yang, B. Brown, S. Nesic; "Mechanical strength and removal of a protective iron carbonate layer formed on mild steel in CO_2 corrosion", NACE Paper No. 10383

[50]   A. Hedayat, S. Yannacopoulos, J. Postlethwaite; "Wear and CO_2 corrosion of steel counter bodys and tubing in heavy oil screw-pump wells", Wear 209 (1997) 263-273

[51]   Z. Guanghong, D. Hongyan, Z. Yue, L. Nianlian; "Corrosion–erosion wear behaviors of 13Cr24Mn0.44N stainless steel in saline–sand slurry"; Tribology International 43 (2010) 891-896

[52]   D. A. Garrec, I. T. Norton; "Boundary lubrication by sodium salts: A Hofmeister series effect"; Journal of Colloid and Interface Science 379 (2012) 33–40

[53]   M. Reza Bateni, J.A. Szpunar, X. Wang, D.Y. Li; "Wear and corrosion wear of medium carbon steel and 304 stainless steel"; Wear 260 (2006) 116–122

[54]   Sh. Hassani, K. P. Roberts, S. A. Shirazi, J. R. Shadley, E. F. Rybicki; "Flow Loop Study of Chloride Concentration Effect on Erosion, Corrosion and Erosion-Corrosion of carbon Steel in CO_2 Saturated Systems"; NACE Paper No. 11237 (2011)

[55] P. H. Shipway, S. Wirojanupatump; "The role of lubrication and corrosion in abrasion of materials in aqueous environments", Tribology International 35 (2002) 661–667

[56] M.R. Thakare, J.A. Wharton, R.J.K.Wood, C. Menger; "Investigation of micro-scale abrasion–corrosion of WC-based sintered hardmetal and sprayed coating using in situ electrochemical current-noise measurements"; Wear 267 (2009) 1967–1977

[57] M.R. Thakare, J.A. Wharton, R.J.K. Wood, C. Menger "Exposure effects of strong alkaline conditions on the microscale abrasion–corrosion of D-gun sprayed WC–10Co–4Cr coating"; Tribology International 41 (2008) 629–639

[58] S. Birosca, G.D. West, R.L. Higginson: "Microstructural investigation of the oxide scale on low carbon steel"; METAL 2005

[59] W. Sun, A.K. Tieu, Z. Jiang, H. Zhu, Ch. Lu: "Oxide scales growth of low-carbon steel at high temperatures"; ELSEVIER Journal of Materials Processing Technology 155–156 (2004) 1300–1306

[60] B.-K. Kim: "High temperature oxidation of low carbon steel; dissertation at the Department of Mining, Metals and Materials Engineering"; McGill University; Montreal, Canada; June 2003

[61] H. Kato: "Effects of supply of fine oxide particles onto rubbing steel surfaces on severe–mild wear transition and oxide film formation"; Tribology International 41 (2008) 735–742

[62] Chen Guoqing, Fu Xuesong, Wei Yanhui, Li Shan, Zhou Wenlong: "Microstructure and wear properties of nickel-based surfacing deposited by plasma transferred arc welding; Surface & Coatings Technology http://dx.doi.org/10.1016/j.surfcoat.2012.05.125

[63] Chung-Woo Cho, Young-Ze Lee: "Effects of oxide layer on the friction characteristics between TiN coated ball and steel disk in dry sliding"; Wear 254 (2003) 383–390

[64] P. Zhang, L. Ma, Z. Liang, J. Zhao: „Preparation and mechanical properties of two nickel base alloy coatings achieved by electrospark deposition"; Acta Metall. Sin.(Engl. Lett.)Vol.24 No.4 pp309-314 August 2011

[65] ASM Handbook, Volume 03 - Alloy Phase Diagrams; ASM International, 1992

[66] Patent: "WO 2009/080556 A1; well tubings with polymer liners"; World Intellectual Property Organization

[67] "OMV-Petrom Specification for sucker rods, pony rods and polished rods"; 2010

[68] ASTM G65 – Standard test method for measuring abrasion using the dry sand/rubber wheel apparatus

[69] A. Proyer, R. Kalzin; "Analysis of the wear behaviour of different kinds of steel in corrrosive media"; HTL thesis, Eisenstadt, 2012

[70] E. Badisch, A. Trausmuth N. Zwazl, R. Jahn, T. Vogl, G. Zehethofer: "Close-to-reality abrasion/corrosion tribotesting: Introduction of a novel testing system for oilfield application" Proceedings ITS 2013, Luleå University of Technology (2013) 58

[71] O. Borrero-López, M. Hoffmann, A. Bendavid, P. J. Martin: "The use of the scratch test to measure the fracture strength of brittle thin films"; Thin Solid Films 518 (2010) 4911-4917

[72] DIN 4762 [2.7]

[73] F. Franek: "Tribometrie und Tribosensorik"; lecture script, Technical University Vienna, 2012

[74] N. Zwazl, S. Ilo, R. Sonnleitner, G. Zehethofer, E. Badisch: "Investigation of tubing failures in oil production due to tribocorrosion"; Proceedings Eurocorr, NACE (2012) 158

[75] N. Zwazl, S. Ilo, E. Badisch, R. Sonnleitner, G. Zehethofer: "Fundamental investigation of material parameter influence on the tribosystem J55 carbon steel tubing and Ni-base coated coupling in pin-on-disc-tribotesting"; Proceedings ÖTG Symposium, ÖTG (2012), 121-128

[76] A. Trausmuth, E. Badisch, F. Weigel, G. Zehethofer, T. Vogl: "Sliding/ corrosive wear phenomena of C-steel against Ni-based coating"; Proceedings MaTri, AC²T research GmbH (2014) 13-19

[77] A. Trausmuth, E. Badisch, F. Weigel, R. Jahn, G. Zehethofer, T. Vogl: "Tribocorrosive wear phenomena occurring in oilfield application"; World Tribology Congress 2013

[78] M. Varga, H. Rojacz, H. Winkelmann, H. Mayer, E. Badisch: "Wear reducing effects and temperature dependence of tribolayer formation in harsh environment"; Tribology International, 65 (2013) 190-199

Lebenslauf

Persönliche Daten

Name	Dipl.-Ing. Nina Zwazl
Geburtsdaten	15.09.1986 in Neunkirchen, NÖ
Wohnadresse	Goethestraße 1/5/12, 2620 Neunkirchen
Telefon	0699 11935424
E-Mail	nina.z@gmx.at
Staatsangehörigkeit	Österreich

Ausbildung

April 2011 – September 2014	**Doktoratsstudium Technische Chemie** an der Technischen Universität Wien
Oktober 2004 – Jänner 2011	**Studium Technische Chemie** **Masterstudium Werkstofftechnologie und -analytik** an der Technischen Universität Wien Diplomprüfung 31.Jänner 2011
September 1996 – Juni 2004	**BG/BRG Neunkirchen mit Schwerpunkt Mathematik** Maturaprüfung 03.Juni 2004 mit Sehr Gut in Mathematik und Chemie

Berufliche Tätigkeiten

Seit August 2013	**JCT Analysentechnik GmbH, Wr. Neustadt** Forschungstechniker im Bereich Messgasaufbereitung
Feber 2011 – Juni 2013	**Austrian Competence Center for Tribology (AC²T research GmbH), Wr. Neustadt** Junior Scientist im Bereich Werkstoffwissenschaften und Korrosion
Feber / August / September 2009	**Semperit Technische Produkte GmbH, Wimpassing** Ferialtätigkeit im Bereich chemische Analytik
August / September 2009	**Borealis Polyolefine GmbH, Schwechat-Mannswörth** Ferialtätigkeit im Qualitätssicherungslabor

Sprachkenntnisse

Englisch	Sehr gute Kenntnisse in Wort und Schrift
Spanisch	Grundkenntnisse in Wort und Schrift

Computerkenntnisse

Applikationen	MS Word, Excel, PowerPoint

Hobbys

Hobbys	Gymnastik, Radfahren, Krafttraining, Lesen, Zeichnen